# THÈSE

**En vue de l'obtention du**

## DOCTORAT DE L'UNIVERSITÉ DE TOULOUSE

**Délivré par :**

Institut National Polytechnique de Toulouse (INP Toulouse)

**Discipline ou spécialité :**

Hydrologie, Hydrochimie, Sols, Environnement

---

**Présentée et soutenue par :**

M. MILOUD MOUZOURI

le lundi 7 novembre 2016

**Titre :**

Non-Newtonian Flow Modelling Through A Venturi Flume

---

**Ecole doctorale :**

Sciences de l'Univers de l'Environnement et de l'Espace (SDUEE)

**Unité de recherche :**

Institut de Mécanique des Fluides de Toulouse (I.M.F.T.)

**Directeur(s) de Thèse :**

M. OLIVIER THUAL

M. LAURENT LACAZE

**Rapporteurs :**

Mme NICOLE GOUTAL, EDF CHATOU

M. PIERRE-YVES LAGREE, UNIVERSITE PIERRE ET MARIE CURIE

**Membre(s) du jury :**

M. DAVID NERON, ECOLE NORMALE SUPERIEURE DE CACHAN, Président

M. LAURENT LACAZE, CNRS TOULOUSE, Membre

M. MAURICE RINGER, GEOSERVICES, Membre

M. OLIVIER THUAL, INP TOULOUSE, Membre

# ABSTRACT

NON-NEWTONIAN FLOW MODELLING THROUGH VENTURI FLUMES

by

Miloud Mouzouri

During a drilling operation, a certain number of unexpected events, related to the flow of drilling fluid in the well, may happen rather quickly. Examples of such events are formation fluid influx (kick) and mud loss to the formation. An uncontrolled kick that increases in intensity may result in what is known as a blowout (e.g. the Deepwater Horizon incident in 2010). Influxes and kicks are traditionally detected by monitoring the drilling mud balance in the well, in particular, by monitoring the flow out the well and comparing it to the incoming flow induced by the pumps. Most methods of monitoring the flow out of the well while drilling consists in using a simple paddle (sensor that measures the height of drilling fluid with the inclination of a paddle) in the return flow line, or in using a Coriolis flow meter (flow meter known for its accuracy but expensive and requires a complex installation by adding a bypass). There is a clear need of a new accurate flow meter, but easy to install and inexpensive.

The Venturi flume has been used as flow meter for years in water industry. It appears as a cheap but accurate solution to measure large flow rates. Many people have worked on this solution to improve its accuracy and to expand its scope. They have developed models, based on a calibration process, to relate the upstream height to the flow rate. This means that current models, as ISO NORM 4359 [1], can be used only for water flow and specific geometry. As known, muds have non-Newtonian behavior and water models cannot be used with this kind of fluids. For our application, trapezoidal shape appears as a good compromise between accuracy and range of flow rate measurements.

Thus, we built a model able to compute the flow rate with taking into account fluid properties and geometrical parameters. This model is simplified in 1D form by using the Shallow Water theory, and completed by a friction model taking into account the variation of fluid properties and geometry along the open channel. It have been validated by series of experiments with both Newtonian and non-Newtonian fluids, where we measured the flow rate and heights of the flow at different locations along the trapezoidal Venturi flume. It have been also completed by 3D CFD which has been simulated both Newtonian and non-Newtonian flows along the flume. To generalized this study, the work was extended to another shape of Venturi more suited to some rig design.

The correlations and models developed and experimentally validated during this research can be used to extend the use of Venturi flume flow meters for any fluids : Newtonian and non-Newtonian. It is an opportunity for industries to propose a cheap but accurate solution to measure flow rates in open channels with any kind of fluids.

# RESUME

Lors d'une opération de forage, un certain nombre d'événements imprévus par rapport à l'écoulement du fluide de forage dans le puits, peuvent se produire assez rapidement. Des exemples de tels événements sont les afflux de pétrole ("kick") ainsi que les pertes de boue dans la formation. Un "kick" qui augmente en intensité peut entraîner, par ce que l'on nomme, un "blowout" (par exemple l'incident Deepwater Horizon en 2010). Les pertes et les gains sont habituellement détectés en contrôlant l'équilibre de la boue de forage dans le puits, en particulier en contrôlant le débit sortant du puits et en le comparant au débit entrant induit par les pompes. La plupart des méthodes de surveillance, de l'écoulement du puits en cours de forage, est d'utiliser un simple "paddle" (capteur qui mesure la hauteur du fluide de forage avec l'inclinaison d'une pagaie) dans la ligne d'écoulement de retour, ou d'utiliser un débitmètre de Coriolis (débitmètre connu pour sa précision, mais coûteux et nécessite une installation complexe en ajoutant un "by-pass"). Il y a un besoin évident d'un nouveau débitmètre précis, mais facile à installer et peu coûteux.

Le canal Venturi a été utilisé comme débitmètre pendant des années dans l'industrie des eaux. Il apparaît comme une solution peu chère mais précise pour mesurer des débits importants. Beaucoup de personnes ont travaillé sur cette solution pour améliorer sa précision et élargir son champ d'application. Ils ont développé des modèles, sur la base d'un processus d'étalonnage, permettant de relier la hauteur en amont au débit. Cela signifie que les modèles actuels, comme ISO NORM 4359 [1], peuvent être uniquement utilisés pour l'écoulement d'eau et pour une géométrie bien spécifique. Comme nous le savons, les boues ont des comportement non-Newtonien, et donc ces modèles établis ne

peuvent pas être utilisés avec ce type de fluides. Pour notre application, la forme trapézoïdale apparaît comme un bon compromis entre la précision et la portée des mesures de débit.

Ainsi, nous avons développé un modèle capable de calculer le débit en prenant en compte les propriétés du fluide ainsi que les paramètres géométriques du canal. Ce modèle a été simplifié sous forme 1D en utilisant la théorie des eaux peux profondes, et a été complété par un modèle de friction tenant en compte de la variation des propriétés des fluides et de la géométrie du canal. Ce modèle a été validé par une série d'expériences avec les deux types de fluides: Newtonien et non-Newtonien, où nous avons mesuré le débit et la hauteur de l'écoulement à différents endroits le long du canal Venturi. Nous avons également réalisé des simulations 3D, en simulant des écoulements Newtoniens et non-Newtonien le long du canal. Pour généraliser cette étude, cette démarche a été étendue à une autre forme de Venturi plus adapté à un certain design de plate-forme pétrolière.

Les corrélations et les modèles développés et validés expérimentalement au cours de cette étude peuvent être utilisés pour étendre l'utilisation des canaux Venturi à tous les fluides Newtonien mais aussi non-Newtonien. Il est maintenant l'occasion pour les industries de proposer une solution, peu chère mais précise pour mesurer les débits dans des canaux ouverts et pour tous types de fluides.

# مُقَدِّمَ

أَتهنَأ االمَلِات الهِفر، وَئادَد مُـيَن مِن الأَهدَته گهير المَتوقِت، تَتَئالَّق تَدَفُّق سَيل الهَفر فِ البِرِ، قَد يَهدُته بَدَلَان بِسرِات. وَمِن الأَمتهلَت االَا هَدهِه الأَهدَته هِ تَسهكِل السَّيل تَدَفُّق (ركِل) وَفُقدَن التِّن لتسهكِل. رَكلَت گهير المُندَبِت الدهي يَزِد فِ سهَدَّت قَد يُادِّ إِ اللَا مَ يُـرَف بِاسم اليَنفِجَر (متهَل هَدِته دِب وَوَتر هُرَيزِن فِ االم ٢٠١٠). تَمّ الكَسهف االن تَدَفُّقَت وَلرَّكلَت تَقلِدِاَن رَسد التَّوَزُن تِن الهَفر فِ البِرِ، اِالَا وَجه الكهُسُسِ، مِن كهِلَل رَسد تَدَفُّق مِن البِر وَمَقرَنَتِهَ تَدَفُّق وَرِدَت النَّجِمَت االن المُدَكهكهَتِ. مِزم وَسَيل رَسد تَدَفُّق مِن البِر أَتهنَأ الهَفر هُ ا اسـتِكهدَم مجدَف بَسِت (جهَز اَيستِسهار يُقِس ا ارتِفَئ سَيل الهَفر مَئ مِل مُجدَف) فِ كهَتّ تَدَفُّق الِاودَتَ، أَو ا اسـتِكهدَم تَدَفُّق مِتر كُرِيُلَيس (تدَفَق مِتر وَلمـئرُف االن دِقتِهَ وَلَكنَّهَ مُكَلَّفَت وَتَتَلَّب تَركِب مُـقَّد بِئِـدَفَت اَللتَّفَفِاتِ). هُنَك هَجَت وَدِهَت مِن المِتر تَدَفُّق دَقِق جَدِدِن، وَلَكُن مِن السَّهل تَهبِت وَگهَير مَكَلَّفَت.

وَقَد ا اسـتَكهدَم المَسَيل بِكهَكه كَمَ تَدَفُّق مِتر لِسَنَوَت فِ سِنَئات المَيَه. يبدو كَمَ هَلّ رَكهِس وَدَقِقَت لِقِاس مُـدَّلَت التَّدَفُّق الكَبِرَتِ. وَقَد االمِلَت الِديد مِن النَّس االَا هَدهَ الهَلّ لِتَهسِن دِقتِهَ وَتَوسِـا نِتَقِه. وَقَد تَوَرَت هَدهِه النُّمَدهِجَ، اَيستِنَدَان إِ اللَا االمَلِات المِـيرت، لِرَبت ا ارتِفَئ المُنبِـا إِ اللَا مُـدَّل التَّدَفِّق. وَهُدهَ يَئنِ أَن النَّمَدهِج الهَلِاتَ، يمكن أَن تُستَكهدَم إِلَّ لِتَدَفُّق المِاه وَلهِندَسَت مَهَدِّدَت. كَمَ هُ مَئرُفن، اَلتَيَن لَهَ السُّلُك وَلِاه نَمدهِج گهير النُّيُتُنِات لَ يُمكِن ا اسـتِكهدَمُهَ مَئ هدهَ النَّوِ مِن السَّوَيل. لِتَلَبِنَ، يُزهِر سهَكَّل سهبه مُنهَرِفِن، بِوَسفِهَ هَلَّان تَوفِقِاَن بَين الدّقَّت وَمَجمُـمَت مِن القِاسَت مُـدَّل التَّدَفُّق.

وَبِالتَّلِ، فَئِتَّنَ بِنَا نَمُدهَجَان قَدِرَان االَا هِسَب مُـَدَّل التَّدَفُّق مَئ الأَكهَده بِـَين كهَسَيِس السَّيِل الهِسَب وَلمَئايِر الهَندَسِاتِ. يتم تَبسِت هدهَ النَّمُدهَج فِ سهَكل ١■ بِاستِكهدَم نَزَرِات المِاه الدَّهلَتِ، وَلَيتِهَأ مِن نَمُدهَج الَيهتِكَك مَئ الأَكهَده بِـَين الَيـتِبَر الَيكهتِلَف فِ كهَسَيِس السَّوَيِل وَلهِندَسَت االَا تُل القنَت المَفتُهَتِ. وَقَد تَمّ التَّهَقُّق مِن سِهتِهَ مِن قِبَل سِلسِلَت مِن التَّجَرِب مَئ كل السَّوَيِل النُّيُتُنِات وَكهَير النِّـتُنِاتِ، هَيته قُمنَ بِقِاس مُـَدَّل التَّدَفُّق وَيرتِفَئ تَدَفُّق فِ مَوَقِا مُكهتَلِفَت االَا تُل سهبه مُنهَرَف بِكهَكه المَسَيِل. وَقَد تَمّ الَيتِهَأ أَيدَان مِن قِبَل ٣■ ■■ الدهي مُهَكَت كل مِن التَّدَفُّقَت نِـتُن وَكهَير النُّيُتُنِات االَا تُل المَسَيِل. إِ■لَا تَئمِ هَدهِه الدِّرَستِ، تَمّ تَمدِد الِامَل إِ■لَا سهَكَّل اكهَر مِن بِكهَكه أَكتهَر مُلَئِمَتَن لِبَئد تَسمِ تَلَئـب.

اَلَيرتِبَتَت وَلنَّمَدهِج المُتَقَدِّمَت وَتَجرِبَان التَّهَقُّق مِن سِهَّت كهِلَل هدهَ البَهته يمكن أَن تُستَكهدَم لِتَوسِا ا■ستِكهدَم بِكهَكه تَدَفُّق مِتر المَسَيِل اان أَي سوَيل: نِـتُن وَكهَير النِّـتُنِاتِ. إِنَّهَ فُرَست لِلسِّنَئات ا■قتِرَه هَلّ رَكهِس وَدَقِقَت لِقِاس مُـَدَّلَت التَّدَفُّق فِ القَنَوَت المَفتُهَت مَئ أَي نَوِ مِن السَّوَيِل.

# DEDICATION

To my Mom and my Dad.

# ACKNOWLEDGEMENTS

I am very grateful to:

- My supervisors, Olivier THUAL and Laurent LACAZE, for their guidance, motivation and patience.
- The FLAG team from Geoservices, especially Maurice RINGER and Prasanna A. VARADARAJAN, for their guidance in the special world of industry.
- The technician, Yann AUDRAN, who helped me in the interesting experimental part.
- The Institut de Mecanique des Fluides de Toulouse and Geoservices for funding the research.
- The Geoservices soccer and babyfoot teams for all these moments of fun which allowed me to create a lot of friendship with Geoservices colleagues.

I also would like to present my gratitude to:

- My parents, Youssef and Kheira MOUZOURI, for all their patience and encouragement. I owe everything to them.
- My wife, Linda MOUZOURI, for all her patience, encouragement and motivation. She was always there for me.
- All my familly, sisters and brothers, but also nieces and nephews.

# TABLE OF CONTENTS

# LIST OF FIGURES

**Figure**

# LIST OF TABLES

**Table**

# LIST OF SYMBOLS

| Symbol | Description | Units |
|---|---|---|
| a | cross-sectional area of flow | $m^2$ |
| b | width of the channel | m |
| Bn | Bingham number | - |
| $B_1$ | width of flume throat | m |
| $B_2$ | width of the approach channel | m |
| $\beta$ | momentum coefficient | - |
| d | flume depth | m |
| $D_h$ | hydraulic diameter | m |
| f | Fanning friction factor | f |
| Fr | Froude number | - |
| g | acceleration due to gravity | $m/s^2$ |
| $\dot{\gamma}$ | shear rate | $s^{-1}$ |
| h | flow depth | m |
| K | shape factor | - |
| k | consistency index | $Pa.s^n$ |
| $k_s$ | roughness height | m |
| L | length of the trapezoidal section of the Venturi flume contraction | m |
| m | side slope of the trapezoidal section | - |
| $\mu$ | dynamic viscosity | Pa.s |
| $\mu_{app}$ | apparent viscosity | Pa.s |
| n | fluid behaviour index | Pa.s |
| $P_w$ | wetted perimeter | m |
| Q | flow rate | L/min |
| $Re_g$ | generalized Reynolds number | m |
| $R_h$ | hydraulic radius | m |
| $\rho$ | density | $kg/m^3$ |
| $\sigma_\eta$ | surface width | m |
| $\tau_w$ | wall shear stress | Pa |
| $\tau_y$ | yield stress | Pa |

## CHAPTER I

# Introduction

The Venturi effect is named after Giovanni Battista Venturi (1746 – 1822)

## 1.1 Introduction to Venturi flume

A Venturi flume is a critical-flow open flume with a constriction which causes a drop in the hydraulic grade line, creating a critical depth : $h_c$ shown in Figure 1.1.

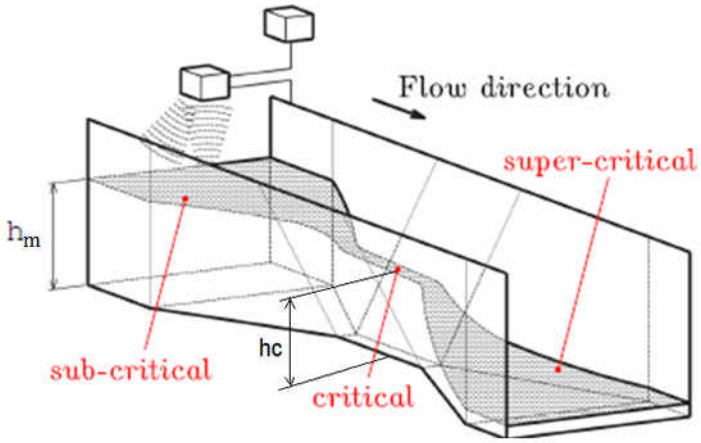


Figure 1.1: Venturi flume

It is used in flow measurement of large flow rates where the critical height $h_c$ can be related to the flow rate $Q$. Commonly, flumes are designed to pass the flow from sub critical to supercritical state while passing through the throat, which in this case becomes a critical section with a critical height $h_c$. This specific transition is named a transcritical transition, as opposed to hydraulic jump. This critical height may be sufficient for computation of discharge, but due to the uncertainty in its location and on its measurement, a method consists of relating the critical height $h_c$ to an upstream height, $h_m$, where the level of the fluid is horizontal and easier to conduct.

To ensure the occurrence of critical depth at the throat, the flumes are usually designed in such way as to form a hydraulic jump on the downstream side of the structure. When the downstream depth is so high that the subcritical flow enters the throat, then the hydraulic jump disappears, the flume is operating in a submerged flow regime, and the discharge need to be corrected. This correction may be found using predetermined tables for a particular flume geometry, or may be done by adding a second height mea-

surement.

Weirs are using the same Venturi principle, but Venturi flumes have two advantages over weirs where the critical depth is created by a vertical constriction. First, the hydraulic head loss, which means the energy dissipated by friction, is smaller in flumes than in weirs. Second, there is no dead zone in flumes where sediment and debris can accumulate, such a dead zone exists upstream of the weirs. Since 1928, different versions of Venturi flumes have been developed, and the main ones are described in the next section.

## 1.2 Kinds of Venturi flumes

The measurement of water flow rate in open channels is a matter of importance throughout the irrigation industry. The cost of the measuring structures faces a lot of problems, as well as the fact that the particular device installed may not be well suited to the conditions under which it must operate. Accumulations of debris in many devices have made the measurements either questionable or even not valuable. Such failures have encouraged the installation of devices better suited to the conditions.

For the measurement of water flow rate in open channels, the weir (Figure 1.2) has been most generally used for small-to-moderate flow rates. Laboratory tests indicated that it was the most accurate practical method for measuring water flow discharge. Nevertheless, if the pool or channel section immediately upstream from the weir crest accumulates sediment, the required vertical depth of water $h_m$ above the crast is correspondingly reduced, thus interfering with the accuracy of the measurement.

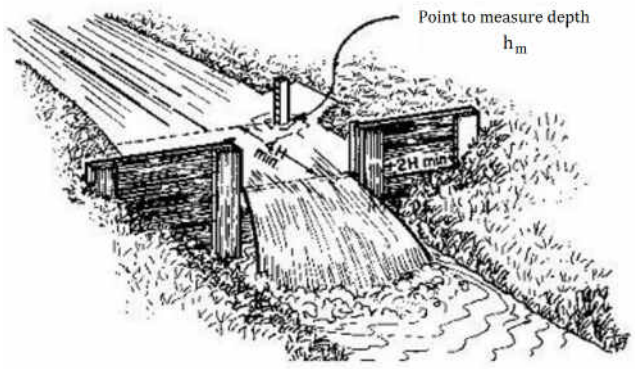


Figure 1.2: Rectangular weir

Where the size of the channel is not sufficient to permit the use of standard weirs, orifices (Figure 1.3) have been used. Experiments seemed to indicate that the relation which applies to give the true discharges is affected by the shape of the orifice, thus rendering the practical application of device uncertain. However, its property of indicating the discharge with a relatively small loss in head is an advantage.

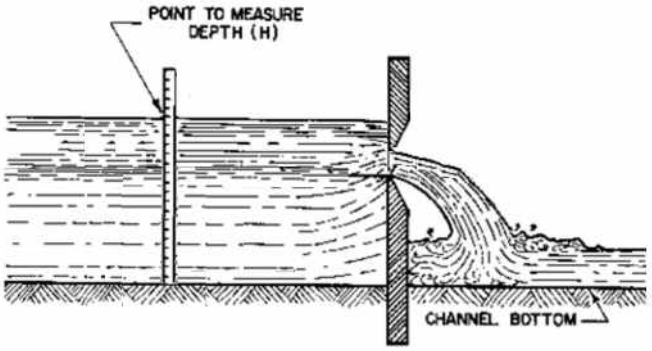


Figure 1.3: Orifice

One of the devices most commonly used to measure large flows is the rating flume, which is a simple structure built in the channel where the floor is level and with its side walls either vertical or inclined. This flume is calibrated by current meter measurements or by other means, where the rate of discharge varies with the depth of the stream, indicated by a staff gage set on the inside face of the flume. The standard rating flume is not altogether reliable. A sediment deposit often accumulates at the bottom of the

device, thus cutting down the cross section of the water prism, which in turn affects the velocity. Flow conditions downstream the rating flume are therefore modified. The previously calibrated relationship between water height and flow discharge is not valid anymore, leading to an erroneous measurement of the discharge. Trailing grass, weeds or willows in the water may also affect the flow rate, which causes error in the discharge measurements.

The improved Venturi flume (Figure 1.4), as described by R. L. Parshall [45], is believed to possess such characteristics as will obviate many of the objections to the weir, orifice, rating flume or other devices which was in general use. The use of the word "Venturi" is justified, since the flume, by having a contracted section between a converging and diverging section, is somewhat similar in principle to the Venturi tube or meter. The improved Venturi flume, under certain conditions of flow, operates in accordance with the Venturi principle. The design of the Parshall flume consists of a uniformly converging upstream section, a short parallel throat section (the width of which determines the flume size), and a uniformly diverging downstream section. The bottom of the flume is horizontal in the upstream section: zone (1), slopes downward in the throat: zone (2), then rises in the downstream section: zone (3) and ending with a downstream elevation below that of the upstream elevation: zone (4), see Figure 1.4. The greatest particularity is a drop in elevation through the throat of the flume. The drop produces supercritical flow through the throat of the flume. With a transcritical transition, only one head measurement is necessary to determine the flow rate, greatly simplifying the use of the flume.

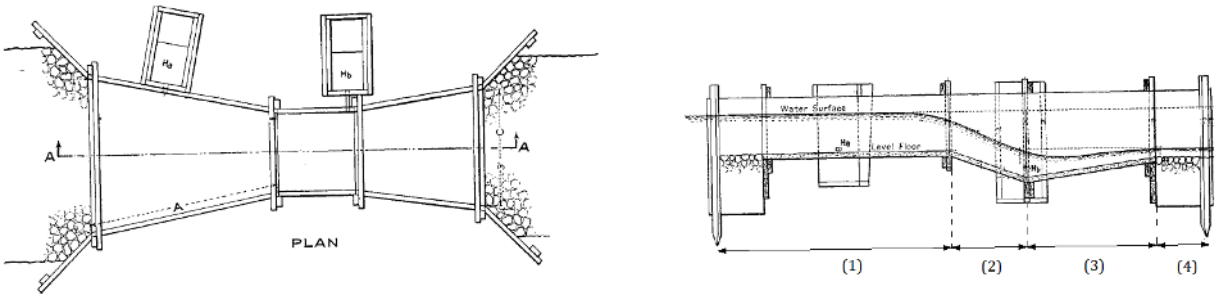


Figure 1.4: Parshall flume geometry proposed by Radalph Parshall in 1928 [45]

After Parshall, many works have started to adapt Venturi effect to open channel flow. The Palmer-Bowlus flume, shown in Figure 1.5, was the results of one of them in the 1930s. The goal of their work was to develop a simple, low cost flume which can be easily adapted to the round pipes and U-channels found in sanitary sewer applications. Designed for installation in existing manhole channels and inline with sewer piping, Palmer-Bowlus flumes have a U-shaped cross section. The throat of a Palmer-Bowlus flume is created by a raised trapezoidal ramp section. As the bottom of the flume raises, the sidewalls also get closer and the cross section is therefore contracted. The result is that flow is accelerated through the throat by the combination of change in floor elevation and vertical constriction of the sidewalls. Unlike the more common Parshall flume, there is no need to accommodate a change in elevation. Both the inlet and outlet of the Palmer-Bowlus flume are at the same elevation.

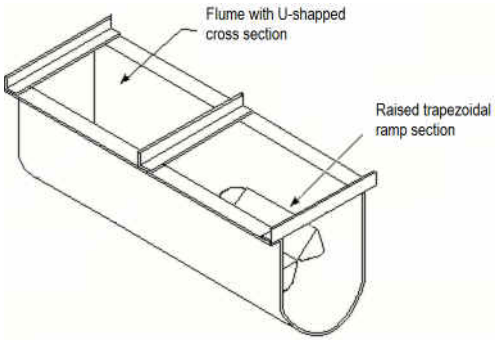


Figure 1.5: Palmer-Bowlus flume

In the 1930s, another work was carried out on a simple flume to measure run-off from small plots and experimental catchments by the Soil Conservation Service, U.S. Department of Agriculture. The H flume (Figure 1.6), so called as it was the eighth design in a series starting with "A", combines the sensitivity of a sharp-crested weir with the self-cleaning properties of a flume. The H Type flume consists of a uniformly converging section, rectangular in cross-section, and an horizontal bottom. The throat is formed by sloping the tops of the sidewalls downwards in the direction of the flow. Thus, as the level in the flume increases, the point at which the flow overtops the sidewalls moves further upstream, so that the effective crest width also increases. The result is that H Type flumes are able to accurately measure flow rates lower than other flumes, including the popular Parshall flume, while still being capable of measuring high flows.

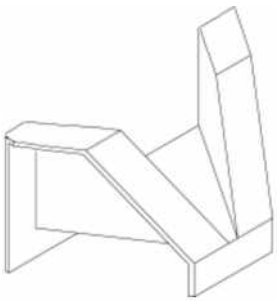

Figure 1.6: H flume

Without a change in floor elevation (as for a Parshall flume) or the need for a free spilling discharge off the end of the flume (as with a H Type flume), the trapezoidal flume (Figure 1.7) consists of outward sloping walls of varying widths and an horizontal bottom. The throat of the flume is defined as the narrowest section of the flume. As the flow rate increases in the trapezoidal flume, the effective width (width of the free surface at the throat) increases as the sidewalls slope outwards. The result of this is that the trapezoidal flume has the sensitivity to measure low flows and the capacity to measure high flows. The minimization of amount of transition needed to direct flow and the flat floor of the flume allows it to be easily retrofitted into existing channels.

Both of these features serve to reduce installation costs. An additional advantage of the flat floor is that the flume is substantially self-cleaning; able to pass trash and debris quite readily. This reduces the maintenance associated with the operation of the flume while also allowing it to operate quite satisfactorily in applications where the flow can be flashy or ephemeral, with solids present.

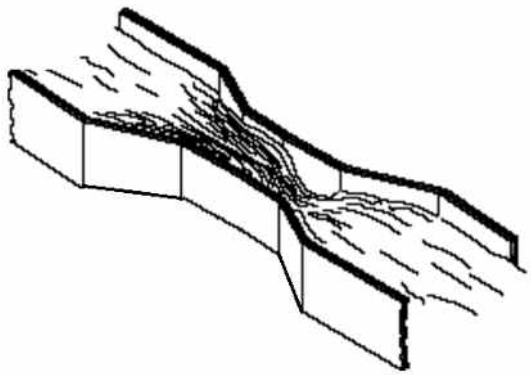

Figure 1.7: Trapezoidal flume

In the 1960's, Gaylord Skogerboe, Leon Hyatt, Ross Anderson, and Keith Eggleston, backed by funding from the United States Department of the Interior, Office of Water Resources Research, developed a flume that was suitable to installation on flat bottoms. Up until their research into what would become the Cutthroat flume (Figure 1.8), the common approach to measuring flows in horizontal bottom applications was to use a Parshall flume with the throat sections removed (which eliminated the need to raise the flume to accomodate the drop through the flume). As the flume has no throat length, it was given the name Cutthroat by its developers.

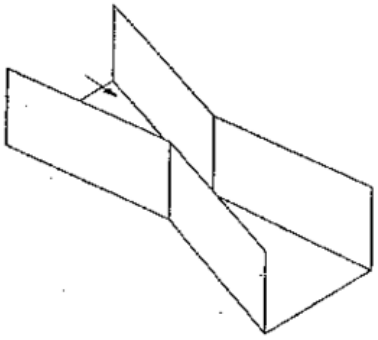

Figure 1.8: Cutthroat flume

The Montana flume (Figure 1.9) is a lesser-known modification of the popular Parshall flume. Its primary use is the measurement of irrigation flows, but has gained popularity in certain municipal sewage applications where free-fall conditions occur. The form of a Montana flume is the same as the uniformly converging section of a regular Parshall flume. The floor of the flume is flat, retaining the same self-cleaning characteristic of the Parshall flume. The throat of the flume is the narrowest, discharge end of the flume. Like the Parshall flume that it is based on, the Montana flume is sized by the throat width alone.

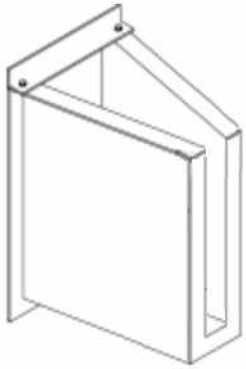

Figure 1.9: Montana flume

The RBC (Replogle, Bos, Clemmens) flumes (Figure 1.10) are a series of portable long-throated flumes developed in 1984 by scientists at the U.S. Department of Agriculture (USDA) and the International Institute for Land Reclamation & Improvement (IRLI) for the measurement of flows in furrow and earthen channels. The RBC flume is trapezoidal in cross-section with a sloped ramp in the flume throat (similar to a Palmer-Bowlus flume). The cross-sectional area is constant in shape through the flume (unlike Trapezoidal flumes) and does not necessarily have to conform to the upstream / downstream channels. A primary advantage of the RBC series of flumes is that they can be calibrated by computer analysis, enabling the design of custom flumes that meet specific site requirements or development of rating tables for non-standard dimension flumes. The floor allows it to be more easily retrofitted into existing channels, reducing installation costs and eliminating the need to either set the flume above the channel floor or modifying the downstream channel. But making the installation easier by adding a floor increases accumulation of debris.

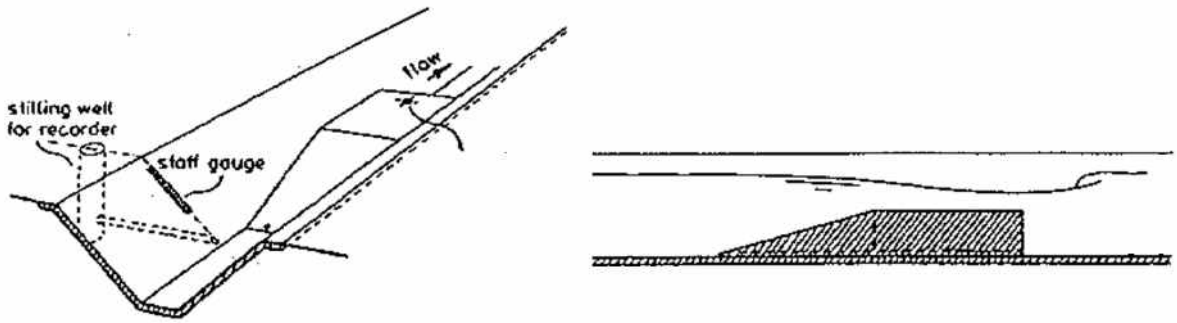


Figure 1.10: RBC flume

## 1.3 Oil & Gas industry motivations

### 1.3.1 Overview of drilling operation

Oil and gas wells are drilled to depths of several hundred to more than 5,000 meters, as described Zoveidavianpoor [39]. Figure 1.11 shows a schematic of typical drilling rig, which uses a rotating drill bit attached to the end of a drill pipe. Drilling fluids (muds) are pumped down through the hollow drill pipe, through the drill bit nozzles and up the annular space between the drill pipe and the hole. Drilling mud mixture is particularly related to site and hole condition; it used to lubricate and cool the drill bit, maintains pressure control of the well as it is being drilled, and helps to removes the cuttings from the hole to the surface, among other functions.

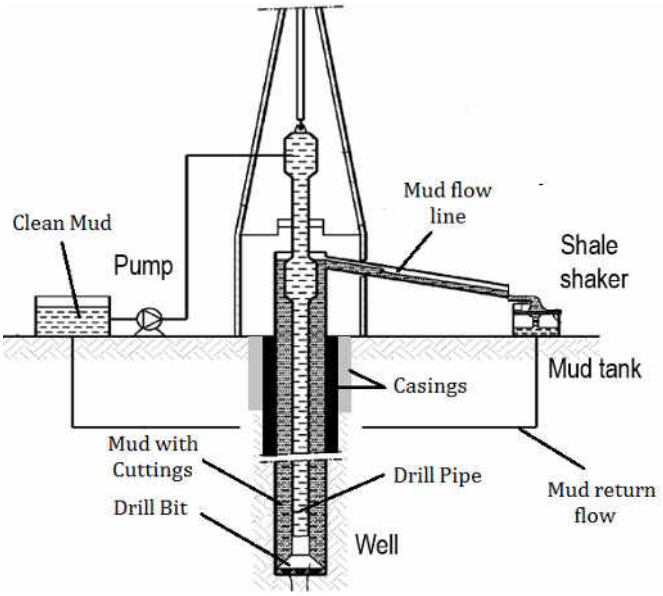


Figure 1.11: Drilling installation

Mud and drill cuttings are separated by circulating the mixture over vibrating screens called shale shakers. As the bit turns, it generates fragments of rock (cuttings), which will be separated from the mud by shale shakers that will moves the accumulated cuttings over the screen to a point for further treatment or management. Consequently, additional

lengths of pipe are added to the drill string as necessary. As a common practice in drilling of oil and gas wells, when a target depth has been reached according to the drilling plan, the drill string is removed and the exposed section of the borehole is permanently stabilized and lined with casing that is slightly smaller than the diameter of the hole. The main function is to maintain well-bore stability and pressure integrity. (Two sizes of casing depicted in Figure 1.11). Cement is then is pumped into the space between the wall of the drilled hole and the outside of the casing to secure the casing and seal off the upper part of the borehole. Each new portion of casing is smaller in diameter than the previous portion through which it is installed. The final number of casing strings depends on the total depth of the well and the sensitivity of the formations through which the well passes. The process of drilling and adding sections of casing continues until final well depth is reached.

### 1.3.2 Fluid gain and loss in drilling operation

During a drilling operation, a certain number of unexpected events, related to the flow of drilling fluid in the well, may happen rather quickly. Examples of such events are formation fluid influx (kick), mud loss to the formation, pipe washout, plugging of the drill-string or bridging of the annulus. To minimize the impact of such incidents on the drilling operation, it is important to detect and classify them as soon as possible, in order to initiate counter actions that can reduce the risk of escalation of an abnormal situation.

During a kick, the pressure found within the drilled rock is higher than the mud hydrostatic pressure acting on the borehole or rock face. When this occurs, the greater formation pressure has a tendency to force formation fluids into the wellbore. This forced fluid flow is called a kick. An uncontrolled kick that increases in intensity may result in what is known as a blowout (e.g. the Deepwater Horizon incident in 2010).

Maintaining well control is the first priority of every drilling operation. Early detection of influxes from the formation before they develop into dangerous kicks can avoid potentially losing the well, the rig and lives.

Influxes and kicks are traditionally detected by monitoring the drilling mud balance in the well, in particular, by monitoring the flow out the well and comparing it to the incoming flow induced by the pumps. The most basic method of monitoring the flow out of the well while drilling is to use a simple paddle (sensor that measures the height of drilling fluid with the inclinaison of a paddle) in the return flow line, see solution 1 in Figure 1.12. This is an inaccurate measurement which limits the resolution of kick/loss detection. The other solution of monitoring the flow out the well is using a Coriolis flow meter. This flow meter is known for its accuracy but it is an expensive solution which requires a complex installation by adding a bypass, see solution 2 in Figure 1.12. This solution is then only used in a few rigs.

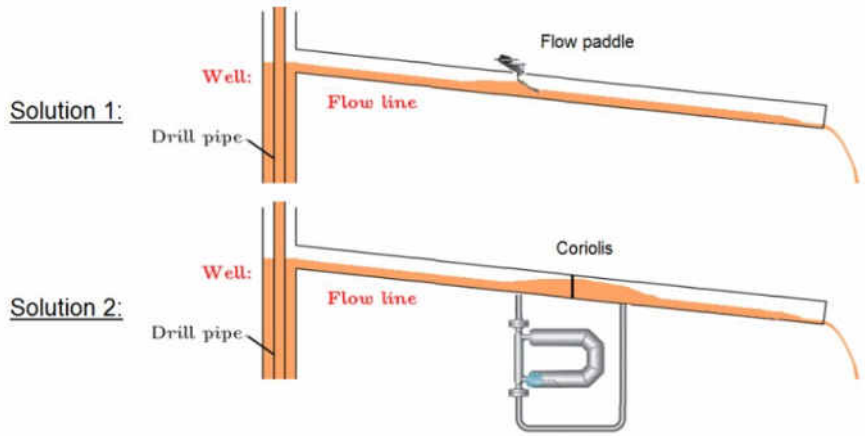


Figure 1.12: Flow paddle (solution 1) and Coriolis (solution 2) sensors installed in return lines

An alternative accurate and cheap solution can be a Venturi flume. In order to monitor the flow rate out the well and to increase the reactivity of kick/loss detection, we have to put the Venturi flume should be placed as close as possible to the well. Its place would then be on the return flow line just before the shale shaker and the mud tank (Figure 1.13).

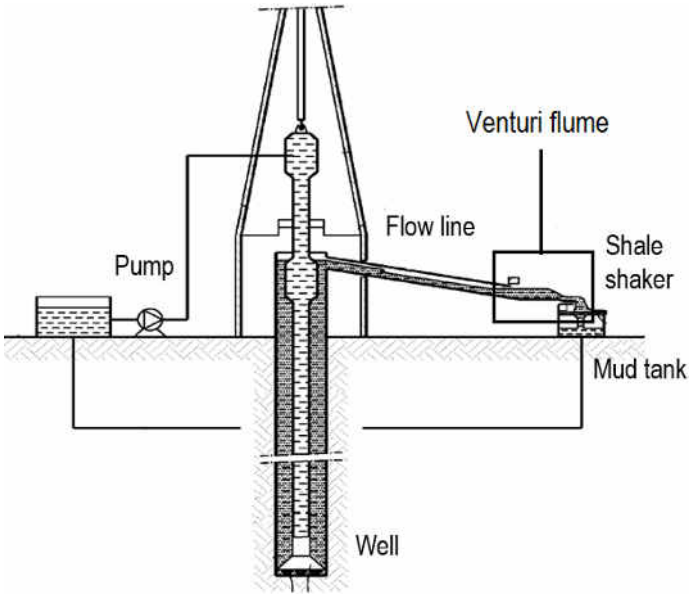


Figure 1.13: Drlling installation

## 1.4 Research & Engineering challenges

The Venturi flume has been used for years in water industry. It appears as a cheap but accurate solution to measure large flow rates. Many people have worked on this solution to improve its accuracy and to expand its scope. They have developed models, based on a calibration process, to relate the upstream height to the flow rate. This means that current models (as ISO NORM 4359 [1]) can be used only for water flow and specific geometry. In the present study, we extend this solution to other fluids and all types of geometry. To do this, we have to built a model able to take to account for the fluid properties and the geometric parameters. This model is able to compute flow rates

in real time based on upstream height measurements for any types of fluid (Newtonian and Non-Newtonian).

While flow of water in open channels has been well researched, non-Newtonian flow in open channel is still a research topic that attracts more and more attention (Haldenwang [28]). Datasets were published for non-Newtonian flow in rectangular open channels by Coussot [15], Naik [40], Haldenwang [28], and Haldenwang & Slatter [48] ,Fitton [20] for non-Newtonian flow in semi-circular open channels. Burger [8] published a set of experiments for non-Newtonian flow in rectangular, triangular, semi-circular and trapezoidal cross sectional shaped. They have demonstrated the effect of shape on Newtonian and non-Newtonian flow but these results were established for specific and constant section channels. The purpose of this study is also to generalize these studies to non-Newtonian flows in any types of open channel with varying cross sections.

## 1.5 Venturi flume set-up

### 1.5.1 Venturi flume shape and geometry

For our application, we prefer to avoid flume with change in floor elevation. The change in floor elevation enhance cuttings deposit which can affect the measurements. In drilling conditions, the flow rate has to be high but during the start and stop of pumps, flow rates are low, so the flow rate sweep a large range of values and we need good accuracy to measure low and high flow rates. Thus, we have chosen a trapezoidal Venturi flume (Figure 1.14). This flume consists on consecutive sections : a converging section, a throat section and a diverging section. So, this specific shape that under free-flow conditions forces flow to accelerate from sub-critical to super-critical flow. This transcritical transition may be characterized by a known relationship between the height at the critical point and the flow rate. However, such a relationship needs the critical height to be measured with good accuracy to estimate the flow rate. Such a measurement is very difficult due to the rapid evolution of the free surface height around the transition location and the uncertainty on the streamwise position of this transition due to the complex 3D fluid flow in the Venturi flume.

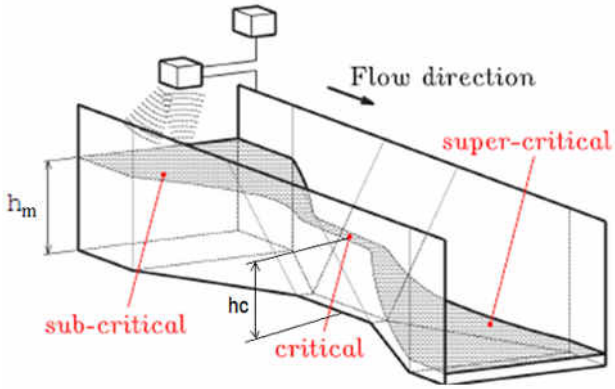


Figure 1.14: Trapezoidal Venturi flume

### 1.5.2 Venturi flume design

The iso standard 4359 [1] describes a way to size a trapezoidal Venturi flume related to the range of flow rates measured. This method is based on the relation between the height measured and the flow rate (1.1) established by a norm. This relation also depends on geometric parameters, described on Figure 1.15, and is given below.

$$Q = \left(\frac{2}{3}\right)^{\frac{3}{2}} \sqrt{g}\ C_V\ C_S\ C_D\ B_1\ h_m^{\frac{3}{2}} \tag{1.1}$$

With:

- $Q$ : flow rate ($m^3/s$)
- $C_V$ : dimensionless coefficient accounting for the influence of the incoming flow velocity on the measured fluid level upstream
- $C_S$ : dimensionless numerical coefficient accounting for the non rectangular cross section
- $C_D$ : dimensionless coefficient of discharge;
- $B_1$ : width of flume throat (m)
- $h_m$ : height measured (m)

The coefficients $C_V$, $C_S$ and $C_D$ are related to the height measured and others geometric parameters as $B_1$, $B_2$, $m$ and $L$ where :

- $B_2$ : width of the approach channel (m)
- $m$ : side slope of the trapezoidal section ($m$ horizontal length to a unit vertical length)
- $L$ : length of trapezoidal section of the contraction at the flume (m)

The ISO standard 4359 imposes different constraints for the Venturi dimensions to maintain performances such as:

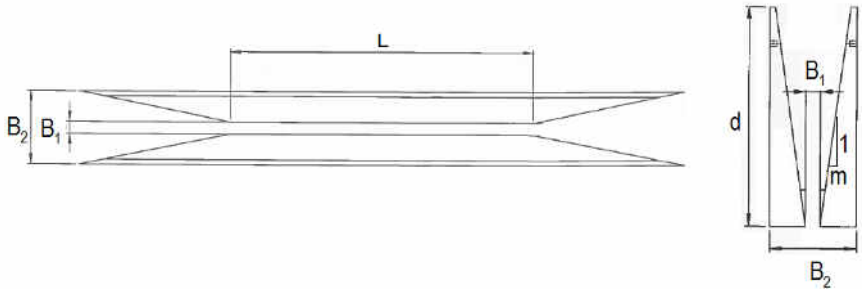


Figure 1.15: Trapezoidal Venturi flume shape end geometrical parameters

- $0.05\text{m} < h < 2\text{m}$
- $h/L < 0.5$
- $B_1 > 0.1\text{m}$

The limitaion on $B_1$ results from the lack of experimental data, but J. Vazquez [32] has extended the iso standard 4359 for trapezoidal Venturi flume with $B_1$ down to 0.02 m. We introduce $d$ which is the depth of the Venturi flume and relates to the maximum of upstream height in order to avoid overflow.

### 1.5.3 Size optimization

The objective of this section is to study the sensitivity of geometrical parameters on the flow rate $Q$ for $Q$<500L/min. The optimization parameters are :

- $B_2$ : imposed by application constraints at 0.12 m;
- $d$ : evaluated by the maximum flow rate;
- $m$ : evaluated by the maximum upstream height and increased by 30% to avoid overflow risk on the Venturi flume;
- $L$ : evaluated by two time the maximum upstream height;
- $B_1$ : minimum of 0.1m, but down to 0.02m by J. Vazquez [32].

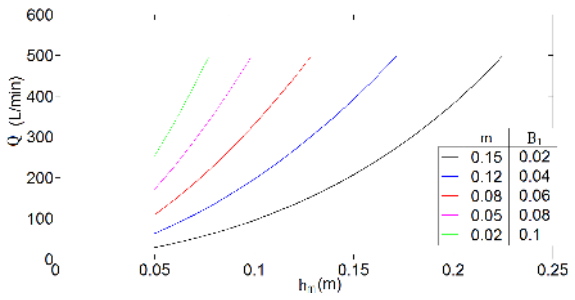


Figure 1.16: Flow rate $Q$ vs. height measured $h_m$ for different configurations of $B_1$ and $m$, based on the ISO standard 4359

We notice that the trapezoidal Venturi flume which have the larger range of validity is one that have the smaller width of flume throat $B_1$. Then, we have selected geometrical values as follows:

- $B_1 = 0.02$m
- $B_2 = 0.12$m
- $m = 0.15$
- $L = 0.5$m
- $d = 0.3$m

## 1.6 Organisation of the dissertation

The overall aim of this work was to extend the use of Venturi flume as flow meter to non-Newtonian fluids. The study is subdivided into the following chapters :

- Chapter 1 : it serves as an overall introduction, providing the background and motivation for this study. It introduces the Venturi principle with different shapes of flumes, as well as the shape of Venturi flume chosen.
- Chapter 2 : it shows the experiments conducted with our Venturi flume at reduced scale, for different kinds of fluids.
- Chapter 3 : it contains a CFD study with our Venturi flume geometry, with different kinds of fluids.
- Chapter 4 : it explains the 1D simplications made to model the flow along our Venturi flume.
- Chapter 5 : it introduces a new model of friction in open channel flows.
- Chapter 6 : it compares all results from experiments and computations.
- Chapter 7 : it generalizes this study to a new Venturi flume shape.
- Chapter 8 : it presents the overall conclusions and recommendations.

## 1.7 Introduction générale

Au cours des opérations de forage, le débit de boue sortant du puits doit être surveillé. Ainsi, un débitmètre doit être installé dans la conduite de retour. En raison du marché actuel, un canal Venturi peut être une solution précise et peu couteuse intéressante pour surveiller le débit de boue sortant du puits.

Un canal venturi est une portion de canal munie d'un étranglement et éventuellement d'une élévation du radier, voir Figure 1.17. Ce canal permet de mesurer le débit de liquide traversant le canal. Cette méthode de détermination des débits est fréquemment utilisée, le plus souvent comme mesure du débit entrant ou sortant d'une station de traitement des eaux usées. La réduction de la section du canal entraîne un changement de régime hydraulique via un passage critique. L'écoulement fluvial change en un écoulement torrentiel. Le niveau d'eau passe alors au-dessous de la hauteur critique $h_c$. Ainsi il existe une relation entre la hauteur en amont $h$ et le débit $Q$.

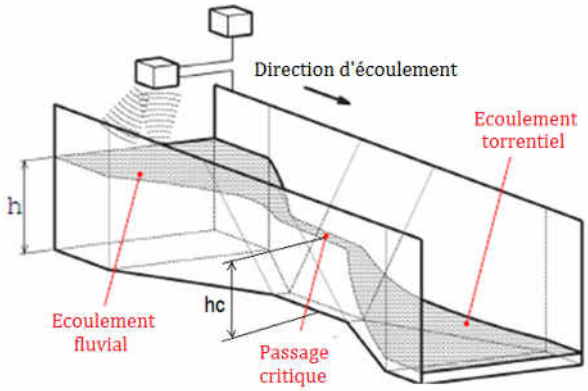


Figure 1.17: Canal Venturi

Même si le canal Venturi apparaît comme une très bonne solution, ce dispositif est utilisé uniquement pour mesurer les débits d'eau. Ainsi, nous avons développé différents travaux, expériences et modélisations, afin d'étendre cette solution à des écoulements de boue.

# CHAPTER II

# Experimental flow through a Venturi flume

*The only source of knowledge is experience.*

Albert Einstein (1879 - 1955)

## 2.1 Fluid rheology

### 2.1.1 Introduction to rheology

Rheology is the science of the deformation and flow behaviour of materials ranging from ordinary liquids to elastic solids. This general definition of rheology was drawn up by Bingham. Today, the term "rheology" is mainly used to denote the study of complex fluids.

A fluid can be characterized according to its behaviour under the action of external pressure or shear stress. The first type of behaviour distinguishes between compressibility and incompressibility depending on whether a fluid element reacts to the applied pressure or not. Most of the time, liquids can be considered as incompressible, whereas gases are compressible media. This assumption is used to set up the continuity equation for a fluid element. In the case of a liquid, the response of the fluid to an applied shear stress is usually more significant. In particular, the shear stress of a liquid can be expressed by different rheological constitutive laws. They describe the fluid behavior associated with flow curves which give the shear stress $\tau$ to shear rate $\dot{\gamma}$ relationship. Note that the rheological behaviour of a liquid can be more complex, i.e. the shear stress could depends upon the pressure, temperature or even history for instance. In the present study, we focus on the case for which the shear stress is a function of the only shear rate $\dot{\gamma}$. For this reason only generalized Newtonian fluid models will be discussed in the following and will be referred as non-Newtonian fluid for sake of simplicity. Examples of popular rheological models which satisfy this assumption are shown in Figure 2.1. There are two elementary fluid behaviors, known as the Newtonian and non-Newtonian. A Newtonian fluid is defined by the linear dependence of the shear stress with the shear rate, and viscosity as the constant of proportionality. Newtonian fluids are homogeneous and isotropic, for example water. The viscosity of the materials in simple shear (one

dimensional shear) is defined as

$$\tau = \mu\dot{\gamma} \ . \tag{2.1}$$

Non-Newtonian fluids have a non-linear flow curve and/or can have a yield stress $\tau_y$. Above the yield stress, the fluid has a viscous behaviour while it becomes solid when the applied shear stress does not overcome the yield. In the solid state, elastic behaviour can be observed in most of these viscoplastic fluids. The most simple model accounting for a yield stress is the Bingham model which reads as

$$\tau = \tau_y + \mu_p\dot{\gamma} \ , \tag{2.2}$$

with $\tau_y$ the yield stress and $\mu_p$ the plastic viscosity. A more complex model has been proposed to mimic the rheological behaviour of many visco plastic fluids, the Herschel-Bulkley model which reads

$$\tau = \tau_y + k\dot{\gamma}^n \ , \tag{2.3}$$

with with $\tau_y$ the yield stress, $k$ the consistency index and $n$ the flow index. If $\tau < \tau_y$ the Herschel-Bulkley fluid behaves as a solid, otherwise it behaves as a fluid. For $n < 1$ the fluid is shear-thinning, whereas for $n > 1$ the fluid is shear-thickening. If $n = 1$ and $\tau_y = 0$ , this model reduces to the Newtonian fluid.

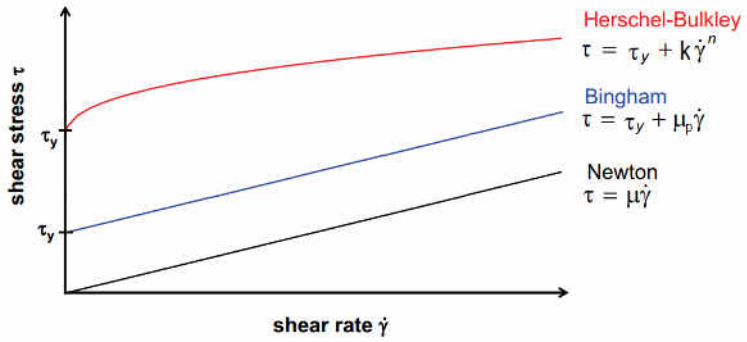


Figure 2.1: Rheological constitutive laws

### 2.1.2 Rheological characteristics of muds

#### 2.1.2.1 Drilling muds functions

Drilling muds fulfill several purposes for the drilling operation, as described by Coussot [42]. First the circulation of a viscous mud allows to evacuate rock cuttings from the bottom hole to the surface, where the solids are separated from the fluid.

Muds also maintain the cuttings in suspension when the circulation is stopped: indeed, in order to add tubings to the drill string, the fluid circulation is regularly stopped. During this rest time, solid cuttings may sediment to the bottom hole and lead to plugging of the well. Drilling muds are therefore thixotropic and develop a gel (yield stress) when not circulated.

The fluid circulated will generate a certain pressure (addition of the hydrostatic and the frictional pressure) which is maintained at a value superior to the pressure of the rock formation (in overbalanced drilling conditions). This helps to maintain the well walls, to prevent destabilization of the ground and to control the venue of fluids from the formation. Due to this pressure difference, the mud will filtrate in the permeable rock formation and will form a filtration cake at the wall. Finally, the circulation of the mud helps to cool down and lubricate the drill bit.

#### 2.1.2.2 Drilling muds compositions

Drilling muds may be classified in two main families:

- **Water based muds** are principally aqueous solutions of polymers and clays in brines with different types of solids and additives.
- **Oil based muds** are invert emulsions of brine into an oil phase stabilized by surfactants. Various additives are added as organophilic polymers, organophilic surface modified clays, solids and other additives.

The choice of the mud formulation will depend on the nature of the rock formation, the environmental and economic constraints as well as the possibility of supplying on site. Different formulations may be used for a same drilling operation depending on the geological nature of the different layers drilled. Oil based Muds can give better performances but are generally more expensive and less ecologically friendly.

#### 2.1.2.3 Drilling muds model

The fluids used in the experiments are aqueous solutions for which additives allow to obtain the various desired rheological behavior. Drilling fluids such as mud have shear-thinning properties (their effective viscosity decreases with shear rate) and present a yield stress. The rheological behaviour of these muds is well represented by the Herschel Bulkley model. The properties that determine the operational performance of these fluids are their apparent viscosity and yield stress. Efficient pumping requires a sufficiently low viscosity, while a minimum yield stress is required to maintain the suspended solids in these fluids. Structure and the resulting properties typically cause a thixotropic nature (fluid sensitivity to the history of shear). We carried out experiments using different fluids, with similar density, to focus on the influence of rheological parameters on the flow.

### 2.1.3 Fluids used during experiments

Three types of fluids were used in our different experiments allowing us to validate our model for different regimes and also to reproduce real drilling muds behaviour.

- **Experiments with water :** this starting point is very important to validate the experimental device with standard models used in the litterature for the case of a water flow in trapezoidal Venturi flumes. In this case, the flow regime is always turbulent. This case will be used to validate the 1D approach for this kind of flow.

- **Experiments with Newtonian viscous fluids :** this step is important to generilized the the 1D Saint Venant approach taking into account of the friction of the fluid, but still for Newtonian fluids. The main regime desires is the laminar regime. Indeed, friction will have a big impact on laminar regime and then we need robust friction and momentum models. To do this experiments, we choose mixtures of glycerine. These mixtures are known for their simple protocol of preparation with a fortuitous balance of physical properties, viscous and stable.
- **Experiments with non-Newtonian fluids :** this step is the last one to conclude on the validity of the model to compute the flow along the trapezoidal Venturi flume. In order to explore the different regimes (laminar and turbulent), different mixtures of Carbopol will be used. Carbopol polymers are water soluble vinyl polymers consisting of chains of cross-linked poly acrylic acid. Their solutions often exhibit a yield stress and are widely used for making emulsions, for thickening and gelation in many industries. As muds, these mixtures have an Herschel Bulkley behaviour after the addition of a base [54]. Values of the yield stress and the consistency of the fluid mostly depends on the concentration of Carbopol mixed in the solution.

### 2.1.4 Fluids preparation

Mixtures used in the experiments are mainly aqueous solutions for which additives are added to obtain the various desired rheological behavior.

- **Water:** we fill the tank directly with tap water ensuring that the flow loop is clean. We have only to be careful with the proliferation of algae, and regularly put anti algae chlorine solution.
- **Mixtures of glycerin:** these Newtonian mixtures are obtained by mixing glycerin and water. Glycerin is available in the laboratory in an hermetic tank of

$1000L$. The pure glycerin is very viscous and is denser than water. We prepared 10 different mixtures of glycerin with different concentrations. We started experiments with pure glycerin and diluate the mixture by adding a volume of water desired. Then, the solution is slowly stirred in order to obtain an homogeneous solution of glycerin/water mixture without air bubbles trapped in the fluid. Note that the viscosity of the fluid is very sensitive to the variation of the temperature and also to the variation of the concentration. Then, we have to be careful during tests with the temperature and the density of the fluid. Different mixtures selected for this study are presented in Table 6.1 .

- **Mixtures of carbopol:** these non-Newtonian mixtures are obtained by mixing Carbopol 940 resin and water. These mixtures are yield stress fluids and are caracterized by Herschel-Bulkley laws. One difficulty will be on the dissolution of the carbopol resin. So it is better to divide the all volume of mixture into small volume and dissolved carbopol slowly. The mixing need to be slow to minimize air bubbles formations which will be trapped into the mixture because of the yield stress. When the Carbopol is homogenously mixed in the water tank, the pH of the solution is around 4, because of the acid groups attached to the base link of the polymer. This solution is brought to a pH of 7 by neutralization with a sodium hydroxide solution. This adding sodium hydroxide leads to an instantaneous thickening and a sol-gel transition when the pH of the solution is close to 7. Beyond the neutralization phase, i.e. when pH $> 9$, there are no more links between the chains and the gel is destructured. Finally, three zones can be distinguished: a pH less than 5, the solution is in a state of pre-gelling, to a pH between 5 and 8, the solution is in the form of a gel and finally, for a pH greater than 9 begins the breakdown. This fluid was chosen because it has the properties to be transparent, non-toxic and keeps its homogeneity even under the action of

large deformations [24]. Note that the rheology of the fluid is very sensitive to the variation of the pH and also to the variation of the concentration. Then, we have to be careful during tests with the pH, the density and the temperature of the fluid. Different mixtures selected for this study are presented in Table 6.1.

### 2.1.5 Rheology measurements

We used the rheometer RheolabQC, from Anton Paar, to measure the rheology of our fluids. We can select between controlled shear rate $\dot{\gamma}$ by imposing a rotational speed and measure the torque or controlled shear stress $\tau$ by imposing a torque and measure the rotational speed. With this two methods, we can determine the evolution of the shear stress $\tau$ with the shear rate $\dot{\gamma}$, and then decuce the viscosity $\eta$ as

$$\eta = \frac{\tau}{\dot{\gamma}} \, . \tag{2.4}$$

We have a Couette geometry, as shown in Figure 2.2, composed by two coaxial cylinders with two different radius. The inner cylinder rotates at a rotational speed so that the outer cylinder is fixed. Therefore, the fluid is sheared between these two cylinders.

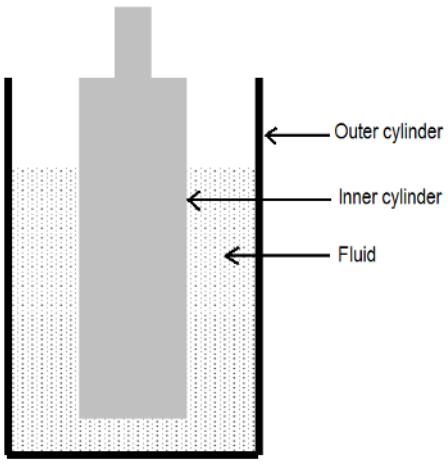


Figure 2.2: Couette geometry of the rheometer RheolabQC

The RheolabQC is connected to a PC and is equipped with a temperature device to accurately control the temperature in the range of 10 °C to 50°C, with cooling system. Different strategies are used to determine the rheology of each mixtures on real configurations.

**Water:** water viscosity is well known and is taken equal to $1Pa.s$ in our configuration, as found by Kestin [31] for instance.

**Mixtures of glycerin:** these mixtures are still Newtonian, in which shear stress is directly proportional to the shear rate. The viscosity measurement characterizes these mixtures, but these mixtures are known to have viscosity very dependent on temperature. During experiments, the temperature of the mixture increase because of pump system. Therefore, we have to characterized mixtures viscosities for the range of temperature in our configuration. We decided to measure six different viscosities at $20°C$, $22°C$, $24°C$, $26°C$, $28°C$ and $30°C$ for each mixtures of glycerin. The measured viscosity is plotted as function of shear rate $\dot{\gamma}$ for different values of $T$ in Figure 2.3. In Figure 2.3, we can see that the viscosity is shear independant as expected for Newtonian fluid, and only depedents on the temperature $T$. Figure 2.3 shows the six different measurements of viscosities as a function of $T$ for the case Gly.3. Data are fitted with a second order polynomial function which corresponds to Equation (2.5).

$$\mu_{Gly.3}(T) = 0.0006\ T^2 - 0.0447\ T + 0.943 \tag{2.5}$$

where $\mu_{Gly.3}$ is the viscosity of the mixture Gly.3 and T the temperature of the fluid.

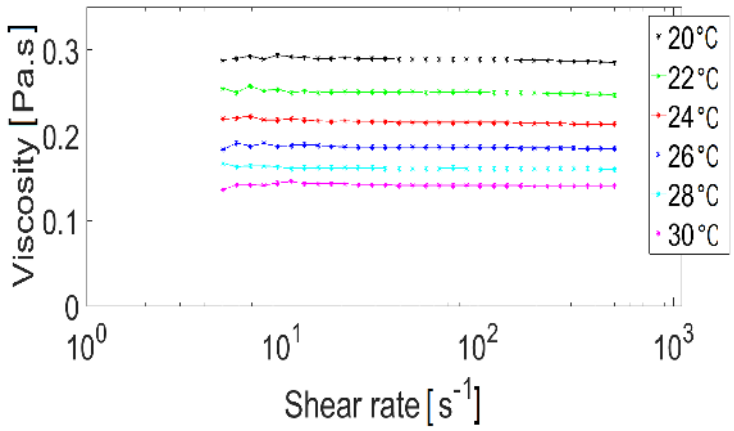


Figure 2.3: Viscosity of the mixture with 90% of glycerin at different temperatures in function of the shear rate with log scale

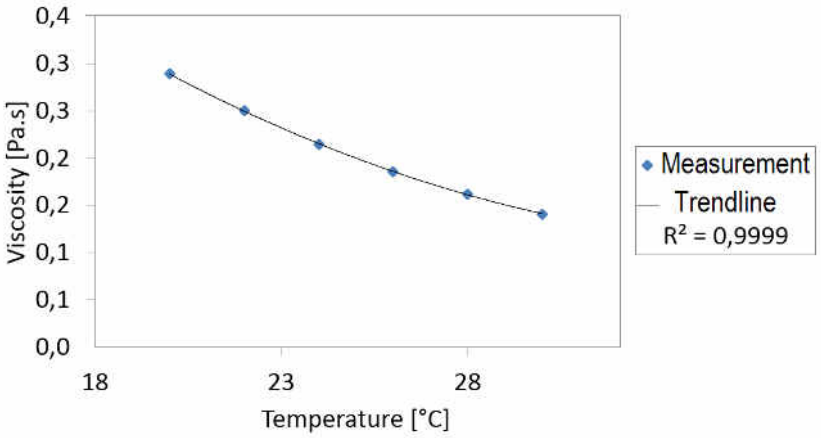


Figure 2.4: Trendline of the viscosity and temperature of the mixture with 90% of glycerin

We used this fit polynomial function to estimate the evolution of the viscosity during the experiment by measuring the temperature as function of time. Notice that we fixed a range of shear rate measurement equal to $[5s^{-1}, 500s^{-1}]$, based on the recommended practice on the rheology and hydraulics of oil-well drilling fluids [29], to be close to what range is chosen in field.

**Mixtures of carbopol:** these mixtures are non-Newtonian, in which the shear stress is related to the shear rate by the Herschel-Bulkley law, as described in Equation

(2.3). The purpose of the rheological measurement is to characterize the three parameters of the law : $\tau_y$, $k$ and $n$. For this purpose, we plotted the measurements of the shear stress as a function of the shear rate and found the three parameters of the Herschel Bulkley law from the trendline using an algorithm from the RheolabQC software, as shown on Figure 2.5 .

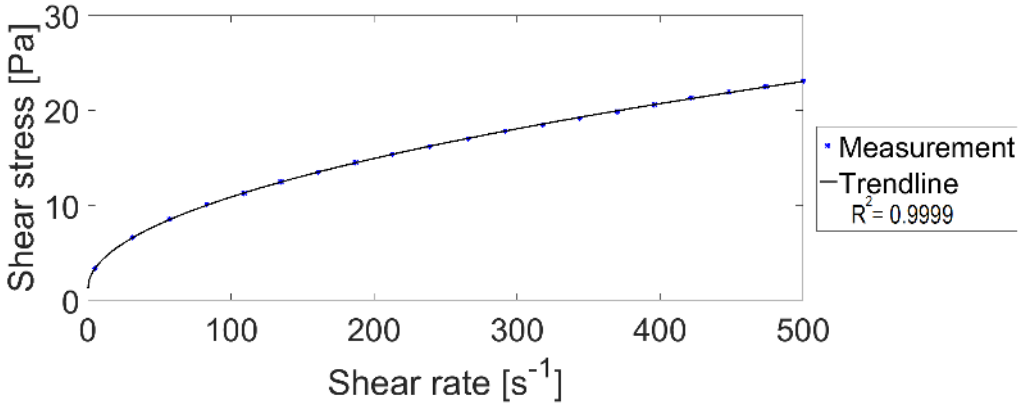


Figure 2.5: Trendline of the rheology of the mixture with 0.13% of carbopol, where the three parameters of the Herschel Bulkley law are equal to : $\tau_y = 1.315Pa$, $k = 0.913Pa.s^n$ and $n = 0.51$.

Another method allows to determine more accurately the yield stress value of the carbopol mixtures by slow linear temporal variation of the shear stress. It imposes a constraint, which the viscosity and the deformation of the fluid are recorded. The slow and continuous increase of the shear stress led to the collapse of the fluid gel structure when the yield stress value is reached and then exceeded. The viscosity collapses and deformation abruptly diverge: the fluid, previously in gel form, begins to flow. This method allows to determine accurately the yield stress value, as described by Gabard [24] and shown here in Figure 2.6.

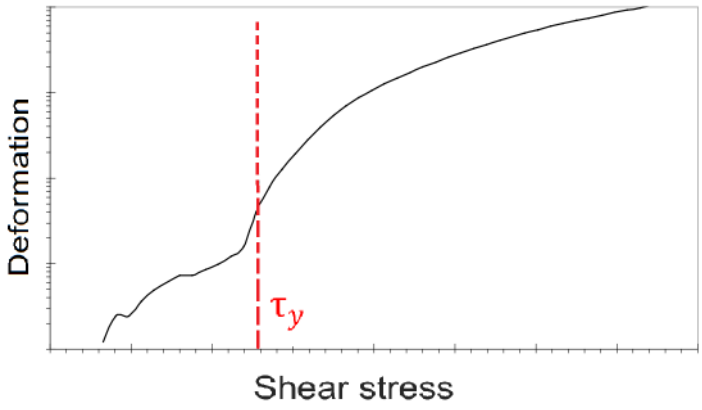


Figure 2.6: Deformation method to determine accurately the yield stress value

These carbopol mixtures are very slightly thixotropic, their rheological characterizations are simple, reliable and reproducible. Those resumed their jelly structure almost instantly after being sheared. These mixtures can be very viscous but with not a large yield stress, one solution to have more yield stress, as mud behaviour, could be to add a yield stress fluid as laponite but it was not studied here. Carbopol mixtures are not very dependent on temperature variation but even with low yield stress, air bubble can be stuck in the gel. Rather than establishing a relation between the three parameters of each fluid rheology and the temperature, as well as the influence of the air bubbles, we prefered to make a rheology characterization of the fluid regularly by taking off several samples during experiments.

### 2.1.6 Fluids properties used

Table 6.1 summarizes all fluids used with their properties, and the number of different flow rates established. Each values on Table 6.1 are mean values during the day. Indeed during the day, viscosity of the fluid changes due to change in temperature or air bubbles trapped. All details of accurate measurements for all fluids can be found in the Appendix.

| **Design −ation** | **Concen −tration** [%] | **Tempe −rature** [$°C$] | **Density** [$kg/m^3$] | **Rheology** | | | **Number of different flowrates** |
|---|---|---|---|---|---|---|---|
| | | | | $\tau$ [$Pa$] | $k$ [$Pa.s^n$] | $n$ [-] | |
| Water | 100 | 22 | 1000 | 0 | 0.001 | 1 | 25 |
| Gly.1 | 100 | 24 | 1256 | 0 | 0.747 | 1 | 14 |
| Gly.2 | 95 | 23 | 1249 | 0 | 0.429 | 1 | 9 |
| Gly.3 | 90 | 25 | 1237 | 0 | 0.203 | 1 | 21 |
| Gly.4 | 87.5 | 27 | 1230 | 0 | 0.128 | 1 | 22 |
| Gly.5 | 82.5 | 27.4 | 1220 | 0 | 0.074 | 1 | 23 |
| Gly.6 | 80 | 27.2 | 1215 | 0 | 0.059 | 1 | 22 |
| Gly.7 | 77.5 | 27.8 | 1209 | 0 | 0.045 | 1 | 24 |
| Gly.8 | 72.5 | 28.7 | 1197 | 0 | 0.027 | 1 | 25 |
| Gly.9 | 70 | 28 | 1215 | 0 | 0.024 | 1 | 25 |
| Gly.10 | 65 | 28.1 | 1192 | 0 | 0.016 | 1 | 25 |
| Carb.1 | 0.13 | 21 | 999.3 | 1.55 | 0.81 | 0.53 | 23 |
| Carb.2 | 0.12 | 24 | 1000.1 | 1.15 | 0.59 | 0.54 | 24 |
| Carb.3 | 0.118 | 22 | 999 | 0.83 | 0.57 | 0.55 | 21 |
| Carb.4 | 0.115 | 22 | 999 | 0.84 | 0.51 | 0.54 | 21 |
| Carb.5 | 0.11 | 23 | 1000.2 | 0.56 | 0.40 | 0.56 | 13 |
| Carb.6 | 0.10 | 22 | 999.4 | 0.01 | 0.16 | 0.61 | 24 |
| Carb.7 | 0.095 | 22 | 999.8 | 0 | 0.01 | 0.64 | 21 |
| | | | | | | **Total** : | 382 |

Table 2.1: Fluids properties used during experiments

## 2.2 Experimental device

### 2.2.1 Scale down

In order to perform experiments which reproduce as much as possible field applications, a scaling between laboratory experiments and field application is done based on similitude concept of the pertinent dimensionless numbers.

The first dimensionless number is the Reynolds number $Re$. It is used to characterize different flow regimes within a similar fluid, such as laminar or turbulent flow. The Reynolds number is defined as the ratio of inertial forces to viscous forces. It is written in generalized form by Haldenwang [28] for Newtonian and non-Newtonian fluids as

$$Re_g = \frac{8\rho u^2}{\tau_y + k\left(\frac{8u}{D_h}\right)^n} \ . \tag{2.6}$$

The second one dimensionless number is the Froude number $Fr$. It is used to characterize different flow regimes within a similar fluid, such as subcritical or supercritical flow. The Froude number is defined as the ratio of inertial forces to gravitational forces. In open channel flow, it is written in generalized form by Chow [13] as

$$Fr = \frac{u}{\sqrt{g\frac{a}{\sigma_\eta}}} \ . \tag{2.7}$$

The last one dimensionless number is the Bingham number $Bm$. The Bingham number is defined as the ratio of yield stress to viscous stress. It is written in generalized form as

$$Bm = \frac{\tau_y}{k\left(\frac{8u}{D_h}\right)^n} \ . \tag{2.8}$$

The flow fields are exactly the same when considered with translation of the scales by preserving the non dimension numbers. We shall get the generic expressions for the scaling so that the real size setup could be translated to the experimental setup. Let us

consider the terms given by the subscript "exp" for the experimental bench setup scales and the terms given by the subscript "real" to the real size dimension on the field. We then define all the scale ratio as

- the flow rate ratio

$$\frac{Q_{real}}{Q_{exp}} = r_Q \ , \tag{2.9}$$

- the length ratio

$$\frac{b_{real}}{b_{exp}} = \frac{h_{real}}{h_{exp}} = \frac{L_{real}}{L_{exp}} = r_L \ , \tag{2.10}$$

- the velocity ratio

$$\frac{u_{real}}{u_{exp}} = r_u \ , \tag{2.11}$$

- the density ratio

$$\frac{\rho_{real}}{\rho_{exp}} = r_\rho \ , \tag{2.12}$$

- the yield stress ratio

$$\frac{\tau_{yreal}}{\tau_{yexp}} = r_{\tau_y} \ , \tag{2.13}$$

- the consistency index ratio

$$\frac{k_{real}}{k_{exp}} = r_k \ , \tag{2.14}$$

- the index ratio

$$\frac{n_{real}}{n_{exp}} = r_n \ . \tag{2.15}$$

We have to preserve all dimensionless numbers. Note that there are other dimensionless numbers in our problem. First there is the side slope $m$, and then there is the power index $n$. These numbers have not dimension and have to be taking into account. So first, we impose

$$m_{real} = m_{exp} \tag{2.16}$$

$$n_{real} = n_{exp} \ . \tag{2.17}$$

Then, we consider the Froude number for both the real scenario and the bench case as:

$$\begin{aligned} Fr_{real} &= Fr_{exp} \\ \Leftrightarrow \frac{u_{real}}{\sqrt{g\frac{a_{real}}{\sigma_{\eta real}}}} &= \frac{u_{exp}}{\sqrt{g\frac{a_{exp}}{\sigma_{\eta exp}}}} \\ \Leftrightarrow \left(\frac{u_{real}}{u_{exp}}\right)^2 &= \left(\frac{a_{real}}{a_{exp}}\right)\left(\frac{\sigma_{\eta exp}}{\sigma_{\eta real}}\right) \\ \Leftrightarrow r_u^2 &= r_L \ . \end{aligned}$$

Next, we consider the generalized Reynolds number for both the real scenario and the bench case as :

$$\begin{aligned} Re_{greal} &= Re_{gexp} \\ \Leftrightarrow \frac{8\rho_{real}u_{real}^2}{\tau_{yreal} + k_{real}.\left(\frac{8u_{real}}{D_{hreal}}\right)^{n_{real}}} &= \frac{8\rho_{exp}u_{exp}^2}{\tau_{yexp} + k_{exp}.\left(\frac{8u_{exp}}{D_{hexp}}\right)^{n_{exp}}} \\ \Leftrightarrow \frac{\rho_{real}u_{real}^2}{\tau_{yreal}\left(1+\frac{1}{Bn_{real}}\right)} &= \frac{\rho_{exp}u_{exp}^2}{\tau_{yexp}\left(1+\frac{1}{Bn_{exp}}\right)} \\ \Leftrightarrow \frac{\rho_{real}u_{real}^2}{\tau_{yreal}} &= \frac{\rho_{exp}u_{exp}^2}{\tau_{yexp}} \\ \Leftrightarrow r_{\tau_y} &= r_\rho r_u^2 \ . \end{aligned}$$

After, we consider the Bingham number for both the real scenario and the bench case

as :

$$
\begin{aligned}
Bn_{real} &= Bn_{exp} \\
\Leftrightarrow \frac{\tau_{yreal}}{k_{real}.\left(\frac{8u_{real}}{D_{hreal}}\right)^{n_{real}}} &= \frac{\tau_{yexp}}{k_{exp}.\left(\frac{8u_{exp}}{D_{hexp}}\right)^{n_{exp}}} \\
\Leftrightarrow r_k &= r_{\tau_y}\frac{\left(\frac{8u_{exp}}{L_{2exp}}\right)^{n_{real}}}{\left(\frac{8u_{real}}{L_{2real}}\right)^{n_{exp}}} \\
\Leftrightarrow r_k &= r_{\tau_y}\frac{\left(\frac{8u_{exp}}{L_{2exp}}\right)^{n_{real}}}{\left(\frac{8u_{real}}{L_{2real}}\right)^{n_{exp}}} \\
\Leftrightarrow r_k &= r_{\tau_y}\left(\frac{r_L}{r_u}\right)^{n} \ .
\end{aligned}
$$

The last ratio needed for the scale similitude is to consider the conservation of the mass for the two scales, as

$$
\begin{aligned}
Q_{exp/real} &= a_{exp/real}u_{exp/real} \\
\Leftrightarrow r_Q &= r_L^2 r_u \ .
\end{aligned}
$$

To summarize,

- To maintain the same side slope number for the scaling means to impose the ratio:

$$r_m = 1 \ . \tag{2.18}$$

- To maintain the same index number for the scaling means to impose the ratio:

$$r_n = 1 \ . \tag{2.19}$$

- To maintain the same Froude number for the scaling means to impose the ratio:

$$r_u^2 = r_L \ . \tag{2.20}$$

- To maintain the same Reynolds number for the scaling means to impose the ratio:

$$r_{\tau_y} = r_\rho r_U^2 \ . \tag{2.21}$$

- To maintain the same Bingham number for the scaling means to impose the ratio:

$$r_k = r_{\tau_y} \left( \frac{r_L}{r_u} \right)^n \ . \tag{2.22}$$

- To maintain the same flow rate for the scaling means impose to impose the ratio:

$$r_Q = r_L^2 r_u \ . \tag{2.23}$$

Therefore we have 6 equations and 8 unknown ratios, so we have to impose 2 other relations. Because of technical tools, the first relation to be imposed is on the flow rate ratio. During drilling, the typical range of flow rate in the field is [ $0L/min$ ; $6000L/min$ ], so we want to reduce it to [ $0L/min$ ; $500L/min$ ] by imposing the ratio $r_Q = 12$. The second relation to impose is the density ratio. Since the typical range of density is [ $1000\text{kg/m}^3$ ; $2000\text{kg/m}^3$ ] for fluids in the field or in the laboratory, it is relevant to impose the ratio $r_\rho = 1$. Then, we can estimate all ratios as:

$$\frac{Q_{real}}{Q_{exp}} = 12 \tag{2.24}$$

$$\frac{L_{real}}{L_{exp}} = 12^{\frac{2}{5}} \ (\approx 2.7) \tag{2.25}$$

$$\frac{u_{real}}{u_{exp}} = 12^{\frac{1}{5}} \ (\approx 1.6) \tag{2.26}$$

$$\frac{\rho_{real}}{\rho_{exp}} = 1 \tag{2.27}$$

$$\frac{\tau_{0real}}{\tau_{0exp}} = 12^{\frac{2}{5}} \ (\approx 2.7) \tag{2.28}$$

$$\frac{k_{real}}{k_{exp}} = 12^{\frac{2+n}{5}} \ (\approx 4.4 \ if \ n = 1) \tag{2.29}$$

$$\frac{n_{real}}{n_{exp}} = 1 \ . \tag{2.30}$$

It means that, based on similitude of the dimensionless numbers which govern the flow, at the lengths at the lab scale are decreased by a factor of 2.7, velocities at the lab scale are decreased by a factor of 1.6, flow rates at the lab scale are decreased by a factor of 12, densities are the same and for Newtonien fluids viscosities at the lab scale are decreased by a factor of 4.4. Based on this study, we built a flow loop able to reproduce real flow conditions at reduced scale.

### 2.2.2 Flow loop

To study the flow of non-Newtonian fluids into trapezoidal Venturi flume during drilling, we made fluid flow laboratory experiments along a Venturi flume at reduced scale. The geometry size, the range of flow rates, the rheology and the density of the fluid have been chosen to match to real scenarios during drilling at reduced scale. The principle of this experiments is to circulate a fluid, with a rheology known, into the Venturi flume at a flow rate known, and measure the height profile into the flume.

A flow loop was built, see Figure 2.7, at reduced scale and able to circulate different fluids at different flow rates into the Venturi flume. This flow loop is composed by

- (1) : a tank able to contain $700L$ of fluid
- (2) : two helical screw pumps able to provide together a maximum flow rate of $500L/min$
- (3) : a valve system to achieve small flow rates
- (4) : a Coriolis and an electromagnetic flowmeters able to measure the flow rate accurately
- (5) : a column which brings the flow into the open channel
- (6) : the trapezoidal Venturi flume with 8 height sensors willing all along

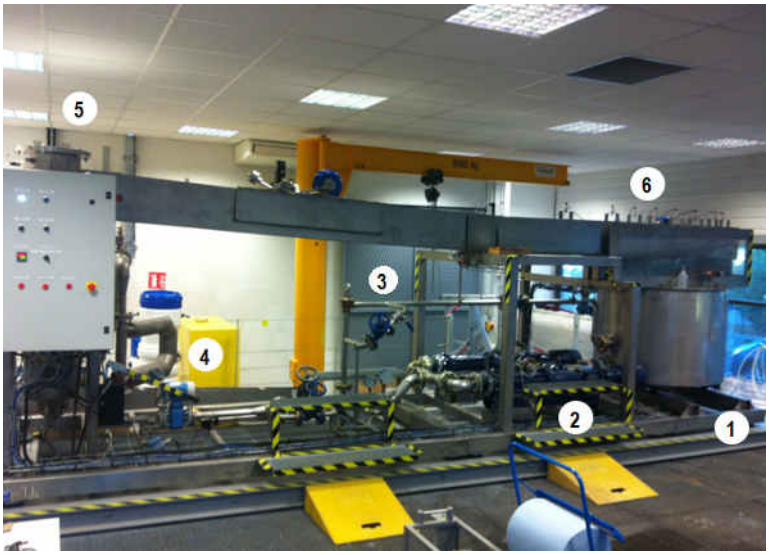


Figure 2.7: Flow loop at Geoservices

The flow loop is also equipped with several security systems as a maximum level alarm into the open channel and also a maximum pressure alarm into the pipe just after the pumps. We have also a mixer into the tank to allow us to blend continuously the mixture. The temperature and the pH are also monitoring in real time to keep an eye on the fluid properties.

Following, 3 different configurations of the flow loop

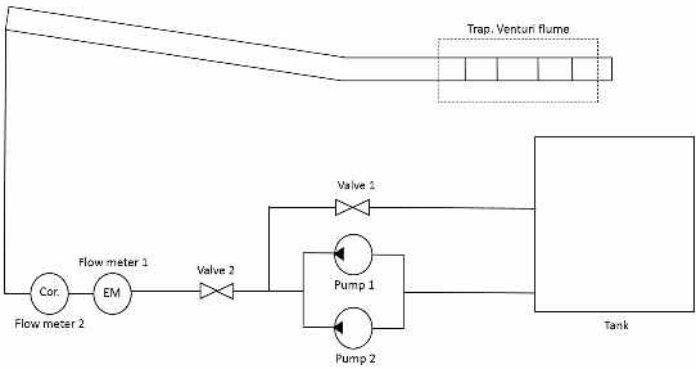


Figure 2.8: Empty flow loop

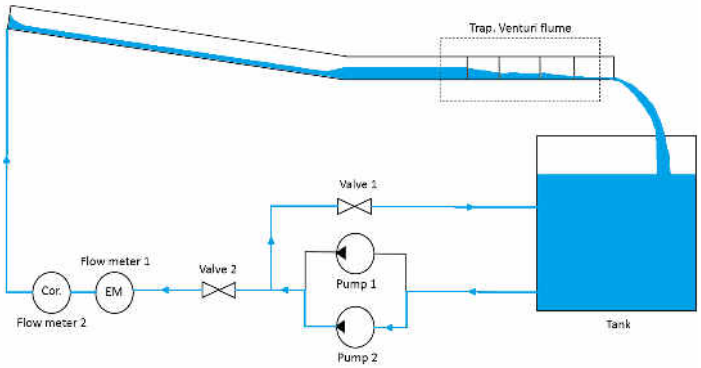


Figure 2.9: Flow loop with low flow rate, the valve 1 is open and only 1 pump is turned on

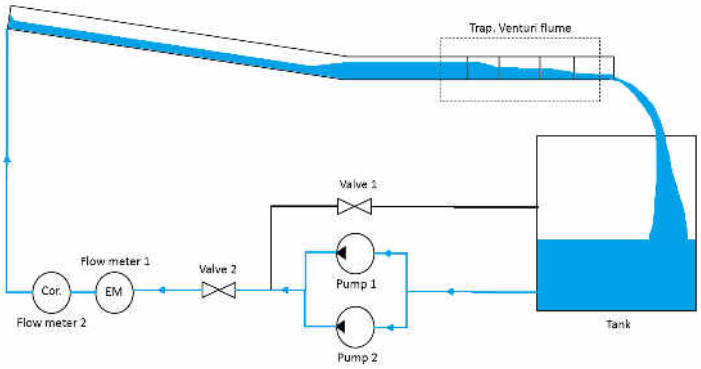


Figure 2.10: Flow loop with high flow rate, the valve 1 is closed and the 2 pumps are turned on

### 2.2.3 Sensors in the flow loop

Table 2.2 summarizes main sensors installed in the flow loop and their performances.

| Sensor | Designation | Technology | Measurement | Accuracy |
|---|---|---|---|---|
|  | CMF200 | Coriolis | Volume flow | ± 0.1 % |
| | | | Mass flow | ± 0.05 % |
| | | | Density | ± 0.2 $kg/m^3$ |
| | | | Temperature | ± 1 $°C$ ± 0.5 % of reading |
|  | Promag 53P | Eletromagnetic | Volume flow | ± 0.2 % |
|  | UNAM 200 | Ultrasonic | Height | ± 1 $mm$ |

Table 2.2: Sensors characteristics

Figure 2.11 shows the location of the 8 height sensors along the Venturi flume. The locations have been chosen to cover the all height profile along the Venturi flume, and at specific locations. Sensors US-1 and US-2 are upstream the Venturi flume, at stable and subcritical flow. Sensors US-3 and US-4 quantifie the decreasing of height due to the convergente part. Sensors US-5 and US-6 are in the throat and before the divergent part, where may be the critical transition. Sensors US-7 and US-8 are downstream, and may confirmed the supercritical flow.

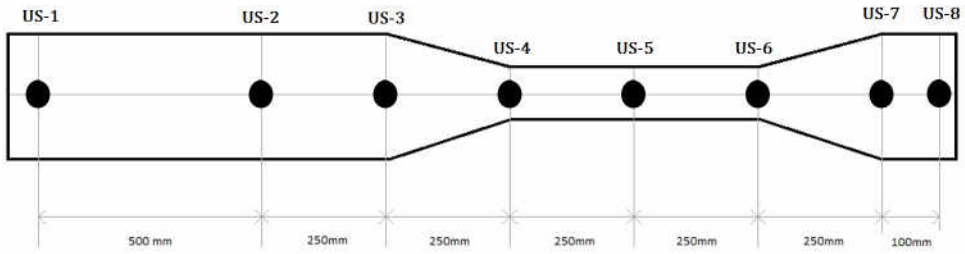


Figure 2.11: Location of the 8 ultrasonic height sensors along the trapezoidal Venturi flume

Let us consider the height $h_1$, the height measured by the sensor US-1, and the same for all sensors.

### 2.2.4 Protocol of experiments

The protocol of experiments is decomposed into different steps

- **Step 1:** preparation of the mixture

All the mixture preparations are done as described previous part. Generally, we make mixtures and wait 1 or 2 days to start the experiments and to let it rest.

- **Step 2:** calibration of the sensors

The Coriolis and the EM sensors have their own factory calibration. But for the US sensors, we have to calibrate them. These calibrations are done by using adjusting shims with a tolerance of $1\mu m$. This technology is dependent of the temperature, therefore we confined the area of measurements by installed a cover and controlled the temperature inside. These calibrations were controlled every days before started the experiments.

- **Step 3:** circulation of the fluid with a fixed and chosen flow rate

We controlled flow rates by controlling the frequency of the pumps. It was the best way to have constant and stable flow rates for all fluids. The small flow rates were obtained by using the 2 valves, because the pumps are not made to go to low frequencies. Notice that for high flow rates, pumps heated and so do fluids, so generally we heated fluids before to start experiments by keep running pumps.

- **Step 4:** wait until steady state is reached

Indeed, we waited until steady states were reached. Generally, steady states were reached after few minutes, this was depending on the viscosity of the fluid and also on how much we increased the flow rate.

- **Step 5:** take 1 minutes of all measurements

All the measurements were done by averaging them during 1 minute. The standard deviations were also taken to quantify the stability of the measurements.

- **Step 6:** change the flow rate and go to the step 4

When the flow was stabilized and when the measurements were made, we changed the flow rate and restarted from the step 4.

- **Step 7:** change the fluid

When we make all ranges of flow rates desired, we change the fluids by adding water. Indeed, we started by the more viscous mixtures and diluted them by adding water, and also waited the mixture homogenizations.

## 2.3 Dataset

### 2.3.1 Flow rate vs. height

We are interested by the relation between an upstream height from the Venturi flume and the flow rate. The upstream height has been chosen where the height is relatively horizontal. Knowing that $h_1$ and $h_2$ are very close, we choose $h_2$ as the selected height due to space optimization. We plotted these two parameters, $h_2$ vs. $Q$, on two plots : Figure 2.12 for Newtonian fluids and Figure 2.13 for non-Newtonian fluids.

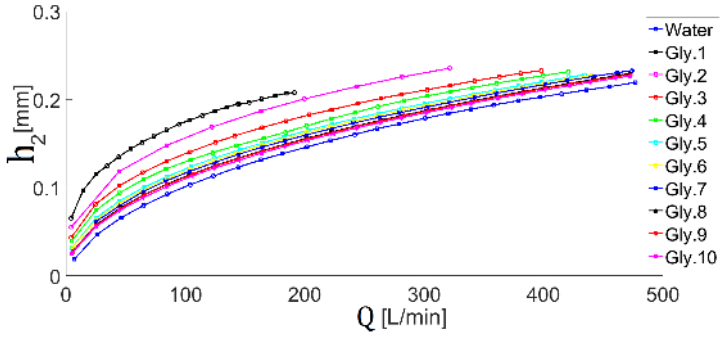


Figure 2.12: Height $h_2$ versus flow rate $Q$ for all Newtonian fluids from experiments

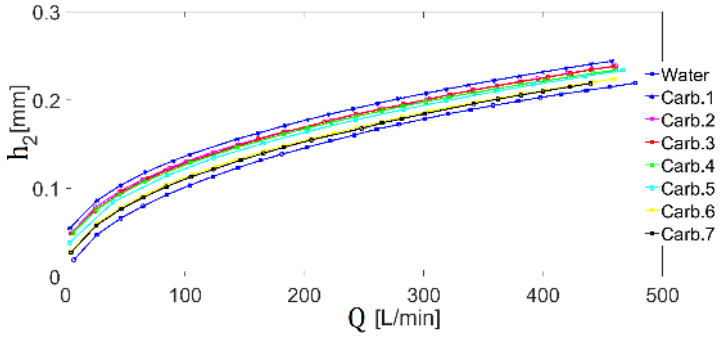


Figure 2.13: Height $h_2$ versus flow rate $Q$ for all non-Newtonian fluids from experiments (and for water to have a reference)

### 2.3.2 Equivalent displacement thickness vs. Reynolds number

#### 2.3.2.1 Boundary layer theory

For the boundary layer theory, we Consider a stationary body with a fluid flowing around it, like the semi-infinite flat plate with fluid flowing over the top of the plate (assume the flow and the plate extends to infinity in the positive/negative direction perpendicular to the x-y plane), as shown in Figure 2.14. At the solid walls of the body the fluid satisfies a no-slip boundary condition and has zero velocity, but as you move away from the wall, the velocity of the flow asymptotically approaches the free stream mean velocity.

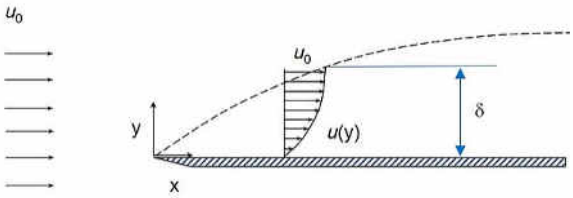


Figure 2.14: Schematic drawing depicting fluid flow over a flat plate

The boundary layer thickness, $\delta$, is the distance across a boundary layer from the wall to a point where the flow velocity has essentially reached the 'free stream' velocity $u_0$. This distance is defined normal to the wall. It is customarily defined as the point $y$

where :

$$u(y) = 0.99u_0 \tag{2.31}$$

at a point on the wall $x$. For laminar boundary layers over a flat plate, as described H. Schlichting [53] , the Blasius solution to the flow governing equations gives :

$$\frac{\delta}{x} = \frac{4.91}{Re_x^{0.5}} \tag{2.32}$$

where the Reynolds number $Re_x = \rho u_0 x/\mu$. The displacement thickness, $\delta^*$, is the distance a streamline just outside the boundary layer is displaced away from the wall compared to the inviscid solution, as shown in Figure 2.15.

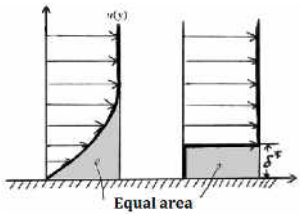


Figure 2.15: Displacement thickness

Based on the Blasius solution, Equation (2.32), we can determine the displacement thickness :

$$\frac{\delta^*}{x} = \frac{1.721}{Re_x^{0.5}} \tag{2.33}$$

#### 2.3.2.2 Analogy with the boundary layer theory

The purpose of this section is to find a way to model the increase of height based on the boundary layer theory. Indeed, this increase of height may be compared to the displacement thickness, and therefore may be related to a Reynolds number taking into account the viscosity of the fluid. We want to quantify the increase of height from a water flow to a more viscous flow. We start from the relation height vs. flow rate for water, as shown in Figure 2.16, which represents 26 points from experiments.

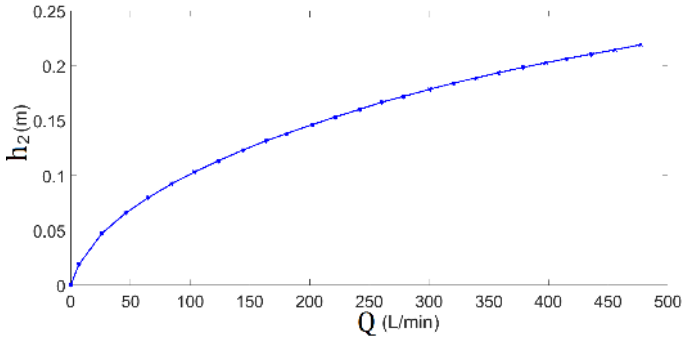


Figure 2.16: Height $h_2$ versus flow rate $Q$ for water

We create a function $f_w$ which returns interpolated values at specific experimental points using linear interpolation. This function is created only by experimental values. On Figure 2.17, we plotted the height for water and for the fluid Gly.3 and we can see the increase on height $dH$ for a same flow rate $Q_0$.

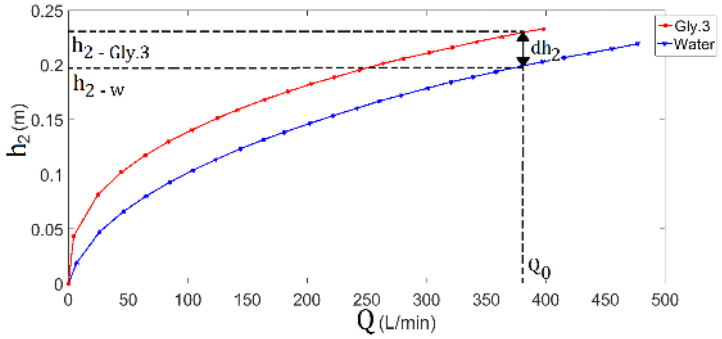


Figure 2.17: Height $h_2$ versus flow rate $Q$ for water and Gly.3 fluids, with the representation of $dh_2$

Therefore, the purpose is to relate this $dh$ to a Reynolds number following Equation (2.33).

**Newtonian fluids** For Newtonian fluids, we choose a typical Reynolds number, taking the characteristic length as the hydraulic mean depth $h_m$, and defined as :

$$Re_N = \frac{\rho u h_m}{\mu} \tag{2.34}$$

where $h_m$ is the hydraulic mean depth and is equal to the depth $h_2$ for our rectangular section at this location ($h_m = a/\sigma = Bh/B = h_2$). In Figure 2.18, we can plot the relative equivalent displacement thickness at le location 2 as $dh_2/h_{2-w}$ in function of the typical Reynolds number $Re_N$, for experimental Newtonian fluids.

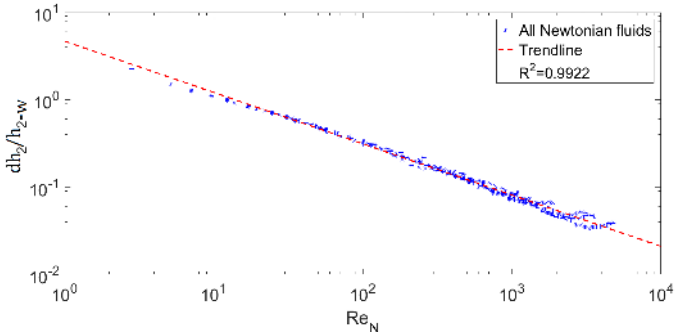


Figure 2.18: Relative equivalent displacement thickness $dh_2/h_{2-w}$ in function of the typical Reynolds number based on the hydraulic mean depth $Re_N$ for all experimental Newtonian fluids

Therefore, we find the relation for the trendline from Figure 2.18 :

$$\frac{dh_2}{h_{2-w}} = \frac{4.6835}{Re_N^{0.587}} \tag{2.35}$$

with a R squared close to 1. This means that we can estimate directly and accurately the height $h_2$ for our Newtonian fluids by the computed height $h_{2-c}$ based on water data $h_{2-w}$, the flow rate $Q$, the density $\rho$, the viscosity $\mu$ of the fluid and the width of the channel $B$ as :

$$h_{2-c} = \frac{4.6835\ h_{2-w}}{\left(\frac{\rho Q}{B\mu}\right)^{0.587}} + h_{2-w} \tag{2.36}$$

**Non-Newtonian fluids** For non-Newtonian fluids, we choose a generalized Reynolds number defined by Haldenwang [28] and used by Burger [8], but taking the characteristic

length as the hydraulic mean depth $h_m$, and defined as :

$$Re_g = \frac{8\rho u^2}{\tau_y + k\left(\frac{8u}{h_m}\right)^n} \tag{2.37}$$

where $h_m$ is the hydraulic mean depth and is equal to the depth $h_2$ for our rectangular section at this location ($h_m = a/\sigma = Bh/B = h_2$). In Figure 2.19, we can plot the relative equivalent displacement thickness $dh_2/h_{2-w}$ in function of the generalized Reynolds number $Re_g$, for all experimental data : Newtonian and non-Newtonian fluids.

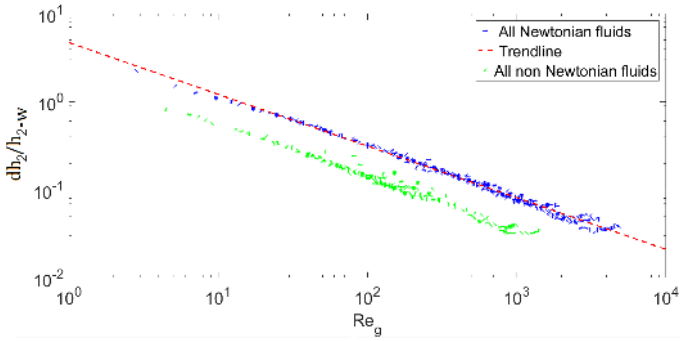


Figure 2.19: Relative equivalent displacement thickness $dh_2/h_{2-w}$ in function of the generalized Reynolds number $Re_g$ based on the hydraulic mean depth, for all experimental fluids

As shown on Figure 2.19 there is an offset between Newtonian and non-Newtonian data, indeed a parameter from non-Newtonian behaviour is not taking into account. Kozicki and Tiu [56] who generalised the Rabinowitsch-Mooney equation for pipe flow and together with the corresponding expression for non-Newtonian flow between parallel plates, proposed a single equation of a generalized Reynolds number, $Re^*$, containing two factors a and b to account for different channel shapes. Kozicki and Tiu [56] presented expressions for laminar flow of power law, Equation (2.38), and Bingham fluids in rectangular, semicircular and triangular open channels. Kozicki and Tiu did not experimentally verify their work.

$$Re^* = \frac{8\rho u^2}{k\left(\frac{a+bn}{n}\frac{8u}{D_h}\right)^n} \tag{2.38}$$

where a and b are constants for various cross-sectional shapes. For pipe flow, $a = 0.25$, $b = 0.75$ and for slit flow, $a = 0.5$ and $b = 1$. Based on this theory, we decided to introduce in the generalized Reynolds number, from Equation (2.37), a coefficient $c$ which was fine tune. This coefficient is also added on the numerator, as shown as Equation (2.39), to refind the typical Reynolds number for Newtonian fluids from Equation (2.34).

$$Re_c = \frac{8c\rho u^2}{\tau_y + k\left(c\frac{8u}{h_m}\right)^n} \tag{2.39}$$

A minimization study was done to find the better value of $c$ to minimize the discrepency between Newtonian and non-Newtonian data : $c = 10$. Therefore, we can plot on Figure 2.20

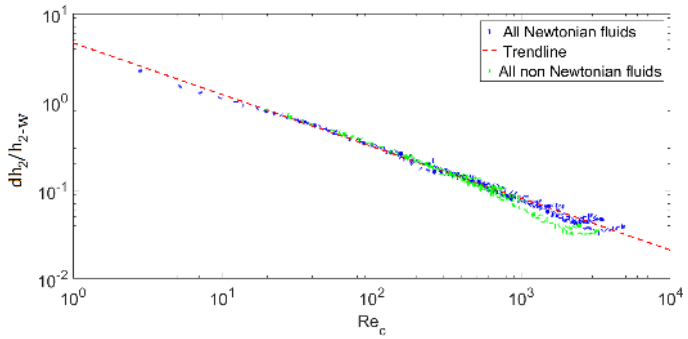


Figure 2.20: Relative equivalent displacement thickness $dh_2/h_{2-w}$ in function of the calibrated Reynolds number $Re_c$ with $c = 10$, based on the hydraulic mean depth, and for all experimental fluids

We have the same expression of the trendline but with the calibrated Reynolds number as

$$\frac{dh_2}{h_{2-w}} = \frac{4.6835}{Re_c{}^{0.587}} \tag{2.40}$$

with a R squared still close to 1.

**All fluids:** The generalization for non-Newtonian fluids was done. Therefore, we can estimate directly and accurately the height $h_2$, for Newtonian or non-Newtonian, by the computed height $h_{2-c}$ based on water data $h_{2-w}$, flow rate $Q$, density $\rho$, fluid property ($\tau_y$, $k$, $n$) and width of the channel $B$ by the implicite relation:

$$h_{2-c} = \frac{4.6835\ h_{2-w}}{\left(\frac{80\rho Q^2}{\tau_y B^2 h_{2-c}^2 + k(80Q)^n B^{2-n} h_{2-c}^{2-2n}}\right)^{0.587}} + h_{2-w}\ . \tag{2.41}$$

To quantify the accuracy of this relation, we compared the height computed $h_{2-c}$ using Equation (2.41) with the height measured during experiments $h_2$, by introducing the relative error on height as:

$$error_h = \frac{h_{2-c} - h_2}{h_2} \times 100\ . \tag{2.42}$$

The estimation of the relative error on height is shown on Figure 2.21, and confirmed an accurate estimation of the relation (2.41) around 2%. Therefore, this method can be used to estimate accurately the upstream height of any fluid based on the fluid property and water data.

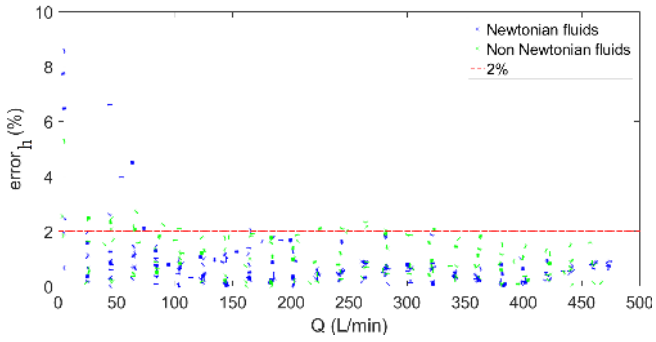


Figure 2.21: Relative error on height, using Equation (2.41) and the experiments, in function of flow rate Q

## CHAPTER III

# 3D simulation of flow through a Venturi flume

*The world's an exciting place when you know CFD.*

John Shadid

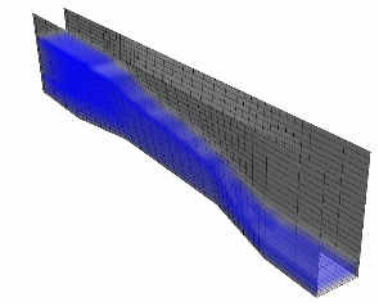

## 3.1 Introduction to CFD

### 3.1.1 Computational Fluid Dynamics

Computational Fluid Dynamics (CFD) is the analysis of systems which produces quantitative predictions of fluid motion based on conservation laws of mass, momentum and energy, together with its associated phenomena such as chemical reactions, by means of computer-based simulation. The simulation generally takes place by utilizing numerical approximation techniques. The conditions of flow geometry, the physical properties of a fluid, the boundary and initial conditions of a flow field are defined to provide solution sets of the flow variables either at selected locations or for overall behavior in the computational domain at specific times.

Due to the availability of affordable and advanced computing hardware, CFD has become more common in petroleum engineering, as well as other fields of engineering, after it was originally developed mechanical engineering, specifically in aerospace industries, Versteeg and Malalasekera [26]. Furthermore, a number of distinct advantages of CFD include its time and cost effectiveness compared to those of a high-quality experimental facility. More comprehensive information of all relevant flow variables can be obtained conveniently with CFD. With a validated CFD model, flexible ability to change parameters defining the flow conditions could be achieved for analyzing a problem with different flow parameters under «what-if» scenarios.

### 3.1.2 CFD softwares

The market of commercial CFD softwares is currently dominated by four codes: PHOENICS, FLUENT, FLOW3D and STAR-CD. The perpetual licence fee for a commercial software is typically ranges from $10000 to $50000 depending on the number of "added extras" required.

An alternative to these commercial CFD softwares would be free ones. Main current

free CFD codes are : OpenFOAM, SU2, PyFR, Code Saturn, FEniCS, Gerris Flow Solver, Clawpack, FEATFLOW, Channelflow and others. These open source softwares are often written in $C++$ and are delivered with full source code access. OpenFOAM appears as a general purpose open-source CFD code and the most widespread with a large community of users, therefore we chose it for the rest of the study.

### 3.1.3 OpenFoam

OpenFOAM is a free, open source CFD software developed primarily by OpenCFD Ltd since 2004, distributed by OpenCFD Ltd and the OpenFOAM Foundation. It has a large user base across most areas of engineering and science, from both commercial and academic organisations. OpenFOAM has an extensive range of features to solve open channel flow with both Newtonian & non-Newtonian fluids, and for both turbulent & laminar regimes. OpenFoam is using with a tools to process the results of simulation cases and includes a plugin to interface with Paraview.

## 3.2 Numerical model

### 3.2.1 Numerical solver : interFoam

InterFoam is a solver for 2 incompressible fluids, which tracks the interface and includes the option of mesh motion. The governing equations are based on the conservation laws of mass and momentum for incompressible homogeneous fluid flow. In the interFoam solver, the conventional VOF method presented by Hirt and Nichols [9] is applied. It uses the volume fraction as an indicator function ($\alpha$ in OpenFOAMTM code) to define which portion of the cell is occupied by the fluid. For a water channel flow,

$$\alpha(x,y,z,t) = \begin{cases} 1 & \text{for a place (x,y,z,t) occupied by water} \\ 0 < \alpha < 1 & \text{for a place (x,y,z,t) in the interface} \\ 0 & \text{for a place (x,y,z,t) occupied air} \end{cases} \tag{3.1}$$

InterFoam solves the governing equations using finite volume approximations. A computational domain is subdivided into a mesh of computational cells. For each computational cell, average values for flow parameters are computed at discrete times

### 3.2.2 Geometry & mesh

CFD applies numerical methods (called discretization) to develop approximations of the governing equations of fluid mechanics in the fluid region of interest. Therefore, the first step would be to define the fluid region of interest. the fluid region would be the region into the trapezoidal Venturi flume defined chapter II. For computation time issue, we use the symetry of the problem on the plane (x,z) and then study only the half of the region as shows on Figure 3.1.

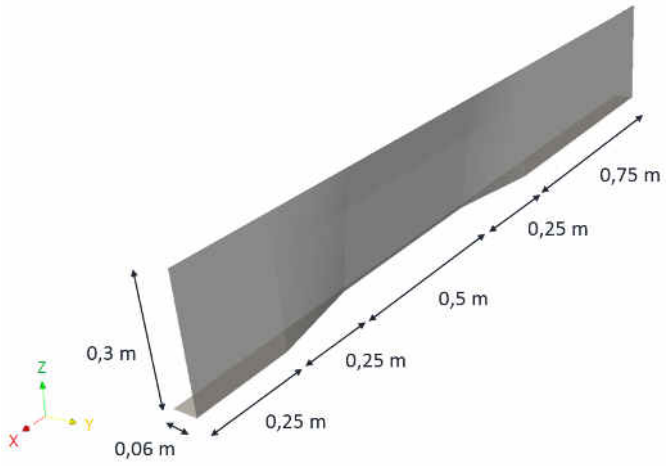


Figure 3.1: Computational domain for the Trapezoidal Venturi flume modeling

After defining the computational domain, we have to define the mesh of the domain. In this study, The mesh is generated from a dictionary file named *blockMeshDict* on

OpenFoam directory. The principle behind blockMesh is to decompose the domain geometry into a set of three dimensional, hexahedral blocks. Edges of the blocks are straight lines. The mesh is ostensibly specified as a number of cells in each direction of the block, sufficient information for blockMesh to generate the mesh data. We choose to specify in the

- x direction : 500 cells
- y direction : 15 cells
- z direction : 75 cells

Therefore, we built a mesh with 562500 cells, and a size of mesh of $4mm$ in each directions as shows on Figure 3.2.


Figure 3.2: Mesh for the Trapezoidal Venturi flume modeling

The mesh is checked with a dictionary file named *checkMesh*. This function checks validity of the mesh with checking the geometry and the topology. This function is usable when the geometry and the mesh are complicated, but here it still simple.

### 3.2.3 Boundary conditions

All CFD problems are defined in terms of initial and boundary conditions. It is important that we specify these correctly. In transient problems the initial values of all the flow variables need to be specified at all solution points in the flow domain. In our case, we start from an empty channel so all initial values are zero.

The boundary conditions for the fluid in the computational domain were defined as shown in Figure 3.3, by adopting different colors for the seven faces of the three-dimensional fluid element in CFD. At the bottom, south and the up east faces of the computational domain which represented to the flume floor and walls (in gray), the wall boundaries were specified with a no-slip wall condition. At the north face of the computational domain (in green), the symmetry boundarie was defined. At the top of the computational domain (in yellow), the atmospheric pressure condition was specified. At the east and west faces of the computational domain (in blue and red), which represented the inlet and outlet of the Venturi flume structure, pressure boundaries with specified fluid heights (at the inlet) were specified. The inlet fluid height imposed accross the full red face was choose as lesser than the final height of the flow after stabilization, as a result, the final value of the height fluid is not imposed. At the outlet of the flume, it was also assumed that a inlet-outlet condition of fluid velocity existed across the boundary, as a result, the flow did not reflect when leaving the computational domain. It was also assumed that a zero normal-derivative condition of height existed across the boundary, as a result, no height value was imposed at outlet.

### 3.2.4 Numerical parameters

**Time step:** The appropriate time-step increment was automatically controlled by OpenFoam, activating the function *adjestTimeStep*, to avoid numerical instabilities and maintain computationally accurate results.

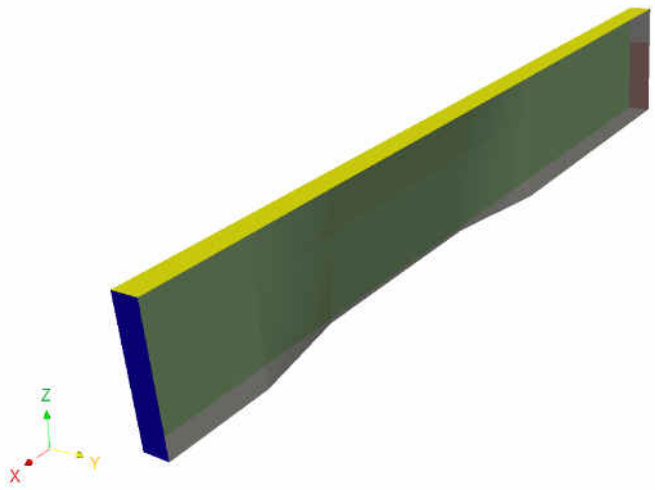


Figure 3.3: Computational domain and boundary conditions for the trapezoidal Venturi flume modeling

**Steady-state condition:** The simulation was set to be terminated either at a simulation time of $60s$, or when reaching a steady-state condition. The height quantities represented in the computational domain were monitored for the steady-state terminating condition.

**Numerical schemes:** The *fvSchemes* dictionary in the *system* directory sets the numerical schemes for terms, such as derivatives in equations, that appear in applications being run. We set *default* schemes from derivative in OpenFoam as *Euler* or *Gauss linear* schemes.

**Turbulence modelling:** Different turbulence models for Newtonian flow are available in OpenFoam but we choose the numerical model: standard two-equation $k - \epsilon$.

**Gravity:** Since this type of flow condition is expected to be influenced primarily by inertia and gravitational forces with viscous effects, the gravitation physical model was activated with a gravitational acceleration of $9.81 m/s^2$.

**Parallel computing:** OpenFOAM is able to run cases in parallel on distributed processors. The method of parallel computing used by OpenFOAM is known as domain decomposition, in which the geometry and associated fields are broken into pieces and allocated to separate processors for solution. This method was used here and allocated to 4 processors.

**Iterative convergence:** All residuals are checked to ensure solution convergence. The iterative convergence error has an order of $10^{-8}$ for each quantities.

## 3.3 Results for water flow

### 3.3.1 Numerical parameters

We simulated a water flow along the trapezoidal Venturi flume using the 3D model defined before. Table 3.1 is a summary of all parameters defined in input

| Input | Value |
|---|---|
| Fluid | Water |
| Density | $\rho = 1000Kg/m^3$ |
| Viscosity | $\mu = 0.001Pa.s$ |
| Flow rate | $Q = 477L/min$ |
| Inlet fluid height | $h_0 = 0.2m$ |

Table 3.1: Input of the 3D water flow computation

### 3.3.2 Numerical results for the trapezoidal Venturi flume with the 3D unsteady flow model

Figure 7.9 represents the evolution of a water flow through the trapezoidal Venturi flume using CFD. We captured the height profile of the flow $h$ from the symmetrical face, in function of the $x$ position at different time $t$. We started with an empty channel. For $t$=1s, the flow is still fully supercritical and we can see the formation of an hydraulic

jump at $t$=15s. The hydraulic jump will go upstream the flume and makes appear a subcritical regime upstream. After 10s, the flow reached steady state and the Venturi flume works with upstream subcritical condition, and imposed a transcritical transition through the throat.

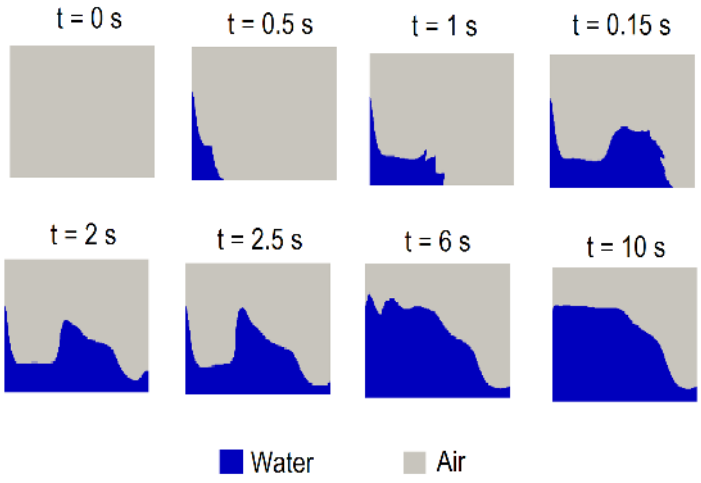


Figure 3.4: Capture at different time of a water flow along the trapezoidale Venturi flume with the 3D model

## CHAPTER IV

# 1D Model for open channel flow through a Venturi flume

*All models are wrong, but some models are useful.*

George P. E. Box (1919 - 2013)

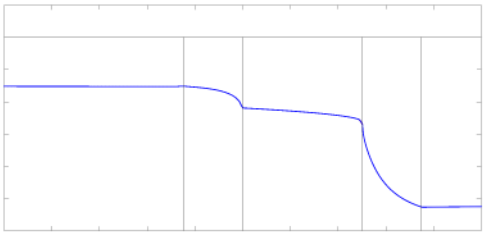

## 4.1 1D Saint Venant Equations (SVE) adapted to the trapezoidal Venturi flume

### 4.1.1 Introduction to Saint Venant Equations

A general fluid-flow problem involves the dynamics of different fields: the fluid pressure, the temperature, the density and the flow velocity. The modelling of these dynamics involves six fundamental equations: the continuity equation based on the law of conservation of mass, the momentum equations along three orthogonal directions (derived from Newton's second law of motion), the Thermal Energy equation obtained from the first law of thermodynamics and equation of state, which is an empirical relation among fluid pressure, temperature and density.

In the case of incompressible fluids and isothermal flows, the last two equations are not required, and therefore can be solved by the continuity equation and by the momentum equations assuming that both density and temperature are constant.

Throughout this section, channel flows are described with one-dimensional model, which are simplifications of the full 3D model. Assuming one-dimensional flow does not mean that velocities on others directions are zero. This is an important distinction because, for an horizontal flow example, the vertical velocity cannot be zero when depth changes.

The basic one-dimensional equations expressing hydraulic principles are called the Saint Venant Equations [16] and were formulated in the 19th century by two mathematicians: Saint Venant and Boussinesq.

These equations can be derived by averaging the Naviers Stockes eqtions (conservation of mass and conservation of momentum mentioned previously) over the cross-section of the channel as it is presented in the following sections. Note that in the case of a flow mostly oriented in the streamwise direction along the channel, these equations reduce

to a one dimensional system.

The basic assumptions for the analytical derivation of the Saint Venant Equations are the following:

- the flow is one-dimensional, i.e. the velocity is uniform over the cross-section and the fluid level across the section is represented by a horizontal line
- the streamline curvature is small and the vertical accelerations are negligible, so that the pressure can be taken as hydrostatic
- the effects of boundary friction and turbulence can be accounted for through resistance laws analogous to those used for steady state flow

Mentioned by E. Aldrighetti [3], these hypotheses do not impose any restriction on the shape of the cross-section of the channel and on its variation along the channel axis, although the latter is limited by the condition of small streamline curvature. Then, we will develop this equations to our trapezoidal Venturi flume geometry even if the validity of assuming small streamline curvature for the flow along this geometry can be discussed.

### 4.1.2 Definition of the 1D problem

A sketch of the geometry is shown in Figure 4.1. The geometry depends on the following parameters:

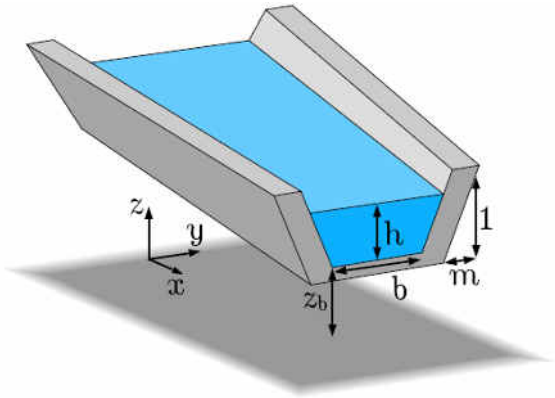


Figure 4.1: Parameters of the trapezoidal Venturi flume, y=0 at the streamwise axis of symmetry

- $h$ : the height of the fluid though the Venturi flume
- $b$ : the width of the Venturi flume
- $m$ : the side slope of the Venturi flume
- $z_b$ : the bottom level of the Venturi flume (inclined by $\theta$ with the horizontal)

For a trapezoidal flume, the channel width depth $z > z_b$ and position $x$ is given by $\sigma(x,z) = b(x) + 2m(x)(z - z_b)$. For $a > 0$ there exist a unique fluid height ($h > 0$) in the channel. The surface depth is $\eta = z_b + h$ and the surface width is $\sigma_\eta = b(x) + 2m(x)h(x)$. Thus, the cross section occupied by the fluid is expressed with the following non linear formula:

$$a(x) = \int_{z_b}^{\eta} \sigma(x,z)dz = bh + mh^2 \tag{4.1}$$

Before to entering into formulation of the 1D model equations, one needs to define the mathematical tool, that is the Leibniz integral rule:

$$\frac{\partial}{\partial x}\left(\int_{z_b(x)}^{\eta(x)} g(x,z)dz\right) = \int_{z_b(x)}^{\eta(x)} \frac{\partial g(x,z)}{\partial x}dz + g(x,\eta)\frac{\partial \eta}{\partial x} - g(x,z_b)\frac{\partial z_b}{\partial x} \tag{4.2}$$

showing that the partial derivative of the integral can be written as the integral of the partial derivative and accounting for the variation of the limits of the integral.

### 4.1.3 1D Saint Venant Equations

The starting point are the Navier Stokes equations for incompressible fluids. They describe local mass and momentum equations:

$$\nabla.(\vec{v}) = 0 \tag{4.3}$$

$$\rho\frac{\partial \vec{v}}{\partial t} + \rho(\vec{v}.\nabla)\vec{v} = -\vec{\nabla}p + \vec{\nabla}\tau + \rho\vec{g} \tag{4.4}$$

with $\rho$ the density, $\vec{v} = (u, v, w)$ the velocity, $p$ the pressure, $\vec{g}$ the gravity, and $\tau$ the stress tensor. So we make the following hypothesis:

- 2D ($x$,$z$) flow : $\vec{v} = (u(x,z), w(x,z))$
- zero slope : $\theta = 0$ and then $\frac{\partial z_b}{\partial x} = 0$
- gravity : $\vec{g} = (0, 0, -g)$
- considering only friction at walls (depending on y): $\tau_{11} = 0$
- characteristic horizontal length scale much larger than the characteristic vertical length scale ($L >> h$)
- characteristic horizontal velocity much larger than the characteristic vertical velocity ($u >> w$)

Notice that with these assumptions, neither viscous or inviscid boundary conditions are satisfied by the flow at side walls, at y=-$\sigma/2$ and y=-$\sigma/2$ . Within theses hypothesis, the Naviers Stockes equations read:

$$u_x + w_z = 0 \tag{4.5}$$

$$\rho u_t + \rho u u_x + \rho w u_z = -p_x + (\tau_{12})_y + (\tau_{13})_z \tag{4.6}$$

$$0 = -p_z - g \tag{4.7}$$

These asumptions allow that the convective and the viscous terms in the third momentum equation can be neglected. Therefore, the following equation for pressure results as an hydrostatic pressure :

$$p(x, z, t) = \rho g \left[\eta(x, t) - z\right] + p_{atm} \ . \tag{4.8}$$

Moreover, assuming that the free surface can be expressed as a single valued function $z = \eta(x, t)$, the kinematics condition of the free surface is given by:

$$\eta_t + u(\eta)\frac{\partial \eta}{\partial x} = w(\eta) \ . \tag{4.9}$$

Integrating the mass conservation equation along $z$, we have :

$$\int_{z_b}^{\eta} (u_x + w_z)\, dz = 0 \ . \tag{4.10}$$

$$\int_{z_b}^{\eta} u_x dz + w(\eta) - w(z_b) = 0 \ . \tag{4.11}$$

Using the Leibniz integral and the no slip condition, we can write :

$$\frac{\partial}{\partial x}\left(\int_{z_b}^{\eta} u dz\right) + w(\eta) - u(\eta)\frac{\partial \eta}{\partial x} = 0 \ . \tag{4.12}$$

And then, using the (4.9) with kinematics condition of the free surface

$$\eta_t + \frac{\partial}{\partial x}\left(\int_{z_b}^{\eta} u dz\right) = 0 \ . \tag{4.13}$$

Integrating along $y$

$$\int_{-\frac{\sigma}{2}}^{\frac{\sigma}{2}} \eta_t dy + \frac{\partial}{\partial x}\left(\int_{z_b}^{\eta}\int_{-\frac{\sigma}{2}}^{\frac{\sigma}{2}} u dy dz\right) = 0 \ , \tag{4.14}$$

we found finally for the mass conservation :

$$a_t + (a\bar{u})_x = 0 \ , \tag{4.15}$$

with $a$ the cross section and $\bar{u}$ the cross sectional averaged velocity defined as :

$$\bar{u} = \frac{1}{h}\int_{z_b}^{\eta} u dz \tag{4.16}$$

Now, we rewrite the momentum equation (4.6) in conservative form

$$\rho u_t + \rho(uu)_x + \rho(wu)_z = -p_x + (\tau_{12})_y + (\tau_{13})_z \tag{4.17}$$

Using the kinematics condition at the free surface with Equation (4.9), the no slip condition at the bottom of the channel, the expression of the hydrostatic pressure with Equation (4.8) and integrating over the section Equation (4.9) then reads

$$\rho a\bar{u}_t + \rho\left(\beta a\bar{u}^2\right)_x = -\rho g a h_x - P_w\tau_w \ , \tag{4.18}$$

where $P_w$ is the wetted perimeter defined in the Annexe D.1 for different shape cross section. The momentum coefficient $\beta$ is defined by

$$\beta = \frac{\frac{1}{h}\int_{z_b}^{\eta} u^2 dz}{\left(\frac{1}{h}\int_{z_b}^{\eta} u dz\right)^2} \ , \tag{4.19}$$

and $\tau_w$ the shear stress at walls and bottom is defined by

$$\tau_w = \frac{1}{2} f \rho \bar{u}^2 \ , \tag{4.20}$$

where $f$ is modelled as the Fanning friction factor, Liggett J. A. [36]. Finally, we obtain the momentum conservation equation as

$$(a\bar{u})_t + \left(\beta a \bar{u}^2\right)_x = -gah_x - \frac{1}{2} P_w f \bar{u}^2 \ , \tag{4.21}$$

where

- $(a\bar{u})_t$ is the local acceleration term
- $(\beta a\bar{u}^2)_x$ is the convective acceleration term
- $gah_x$ is the pressure gradient term
- $\frac{1}{2}P_w f\bar{u}^2$ is the friction term

Note that Equation (4.21) is often written in the conservative form as (see [10] for instance)

$$(a\bar{u})_t + \left(\beta a\bar{u}^2 + g\xi(h)\right)_x = g\Sigma(h) - \frac{1}{2} P_w f \bar{u}^2 \tag{4.22}$$

Here, the pressure gradient has been decomposed as

$$gah_x = g\xi_x(h) - g\Sigma(h) \tag{4.23}$$

where

$$\xi(h) = \frac{1}{2}bh^2 + \frac{1}{3}mh^3 \tag{4.24}$$

$$\Sigma(h) = \frac{1}{2}b_x h^2 + \frac{1}{3}m_x h^3 \tag{4.25}$$

Equations (4.15) and (4.21) are called the Saint Venant Equations. For sake of clarity, $\bar{u}$ will be replaced by $u$ in the following of this work.

### 4.1.4 Hyperbolicity and the Saint Venant system

The Saint Venant Equations are systems of PDEs that can be written in the form

$$\mathbf{W}_t + \mathbf{F}\left(\mathbf{W}\right)_x = \mathbf{b}\left(x, \mathbf{W}\right) \tag{4.26}$$

where $\mathbf{W}$ is the vector of the conserved quantities, $\mathbf{F}$ is the flux function and $\mathbf{b}$ the source term

$$\mathbf{W} = \begin{pmatrix} a \\ au \end{pmatrix}, \quad \mathbf{F} = \begin{pmatrix} au \\ \beta au^2 + g\xi(h) \end{pmatrix}, \quad \mathbf{b} = \begin{pmatrix} 0 \\ g\Sigma(h) - \frac{1}{2}P_w f u^2 \end{pmatrix} \tag{4.27}$$

We can define the matrix $\mathbf{J} = \frac{\partial \mathbf{F}}{\partial \mathbf{W}}$ as the Jacobian of the flux $\mathbf{F}\left(\mathbf{W}\right)$ which is equal to

$$\mathbf{J} = \begin{pmatrix} 0 & 1 \\ c^2 - \beta u^2 & 2\beta u \end{pmatrix} \tag{4.28}$$

where $c$ is the celerity of the gravity wave at the free surface, and given by

$$c = \sqrt{\frac{ga}{\sigma_\eta}} \tag{4.29}$$

Studying the characteristic polynomial of **J**, one can prove that system (**??**) is hyperbolic. With eigenvalues which are real, distinct and read

$$\lambda_1 = \beta u + \sqrt{c^2 + \beta(\beta - 1))u^2} \tag{4.30}$$

$$\lambda_2 = \beta u - \sqrt{c^2 + \beta(\beta - 1))u^2}\ , \tag{4.31}$$

and the corresponding eigen vectors as

$$\mathbf{v_1} = \begin{pmatrix} 1 \\ \beta u + \sqrt{c^2 + \beta(\beta - 1))u^2} \end{pmatrix}, \quad \mathbf{v_2} = \begin{pmatrix} 1 \\ \beta u - \sqrt{c^2 + \beta(\beta - 1))u^2} \end{pmatrix} \tag{4.32}$$

Therefore, the Saint Venant system can be decomposed in two ODEs that hold along the two characteristic curves given by

$$\frac{dx}{dt} = \lambda_{1,2} \tag{4.33}$$

### 4.1.5 Flow classification & flow conditions

Given the characteristic speeds and $\beta = 1$ (knowing that extension to $\beta \neq 1$ can be made), one can classify the flow according to a dimensionless number called the Froude number and defined as

$$Fr = \frac{\mid u \mid}{c} \tag{4.34}$$

According to the value of the dimensionless Fr number, three different regimes can be defined

- **Fr** $< \mathbf{1}$ : that means $\mid u \mid < c$, the two characteristic speeds have opposite directions. Therefore, the information is transmitted along these curves both upstream and downstream. This kind of flow is known as subcritical flow and occurs when the gravitational forces are dominant over the inertial ones

- **Fr = 1** : that means $\mid u \mid = c$, one characteristic speed is vertical and the other has the same direction of u. This kind of flow is known as critical flow and occurs when the inertial forces and the gravitational forces are perfectly balanced.

- **Fr > 1** : that means $\mid u \mid > c$, the two characteristic speeds have the same direction of u. Therefore the information is only transmitted downstream. This kind of flow is known as supercritical flow and it occurs when the inertial forces are dominant over the gravitational ones.

The current flumes principle is to impose a transcritical transition, where we capture the transition from a subcritical flow to supercritical flow. These current flumes are designed based on ISO standard 4359 and are applied to so-called subcritical upstream conditions. Figure 4.2 shows the three different regimes found along a Parshall flume with subcritical upstream condition.

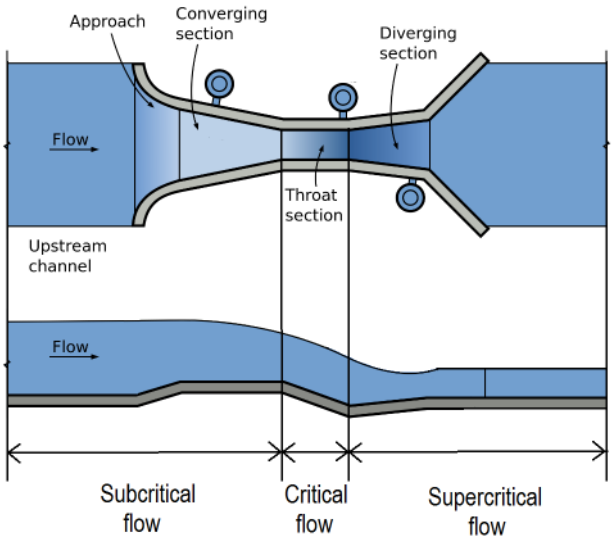


Figure 4.2: Different regimes along a Parshall flume.

Note that supercritical upstream flumes also exhist but are more likely used for flow rate measurements in the case of heavy sediment load condition (see [49] for instance). In order to highlight the major difference between a subcritical upstream flume and a

supercritcal usptream flume, the sensitivity parameters can be considered. It is defined as

$$s(Q) = \frac{dh_m}{dQ} \tag{4.35}$$

where $Q$ is the flow rate and $h$ the measured depth. Thus, equation (4.35) states that sensitivity is a measure of the relative change in depth with a unit change in discharge. In order to obtain a good accuracy on the flow rate estimation from height measurement, the bigger value of $s$ should be considered as it corresponds to a small variation of $Q$ associated with a big variation of $h_m$.

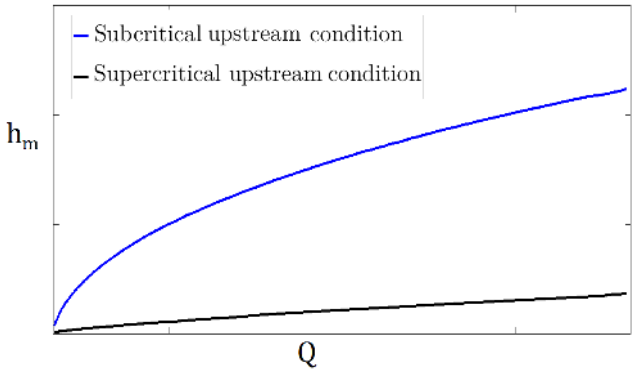


Figure 4.3: Qualitative relation between $h_m$ and $Q$ for subcritical and supercritical upstream condition for a trapezoidal Venturi flume

As shown in Figure 4.3, the upstream condition causes the bigger value of $s$ is the subcritical upstream condition. Therefore, we decide to develop a Venturi flume solution based on subcritical upstream condition.

### 4.1.6 The friction and momentum models

#### 4.1.6.1 Friction model

The average shear stress on the surface in contact with the fluid, or local shear stress, equals to:

$$\tau_w = \frac{1}{2}\rho f u^2 \ , \tag{4.36}$$

where $f$ is the Fanning friction factor and $u$ is the mean velocity. In open channel flow, it is common to use the Darcy friction factor $C_d$, which is related to the Fanning friction factor by:

$$C_d = 4f \ . \tag{4.37}$$

As for pipe flows, the flow regime in open channels can be either laminar or turbulent. In industrial applications with Newtonian fluids, it is commonly accepted that the flow becomes turbulent for Reynolds numbers larger than 2000-3000, Chanson [10], the Reynolds number being defined for pipe and open channel flows as:

$$Re = \frac{\rho u D_h}{\mu} \tag{4.38}$$

where $\mu$ is the dynamic viscosity of the fluid, $D_h$ is the hydraulic diameter and $u$ is the mean flow velocity. Most open channel flows with water are turbulent, because of the relatively small viscosity of water and with large flow rates. In most practical cases, open channel flows are turbulent and the friction factor (with Darcy coefficient) may be estimated from the Colebrook–White formula, Colebrook [14]

$$\frac{1}{\sqrt{C_d}} = -2log_{10}\left(\frac{k_s}{3.71D_h} + \frac{2.51}{Re\sqrt{C_d}}\right) \tag{4.39}$$

where $ks$ is the equivalent roughness height of the surface over which the flow takes place. Equation (4.39) is a non-linear equation. Numerical solutions of Equation (4.39) for different ratios $k_s/D_h$ are given in Figure 4.4, known as the Moody diagram (Moody, 1994).

As mentioned before, Equation (4.39) is a non-linear equation and is usually solved numerically due to its implicit nature. Lot of works have been employed to obtain explicit reformulation of the Colebrook equation. But there are also various explicit

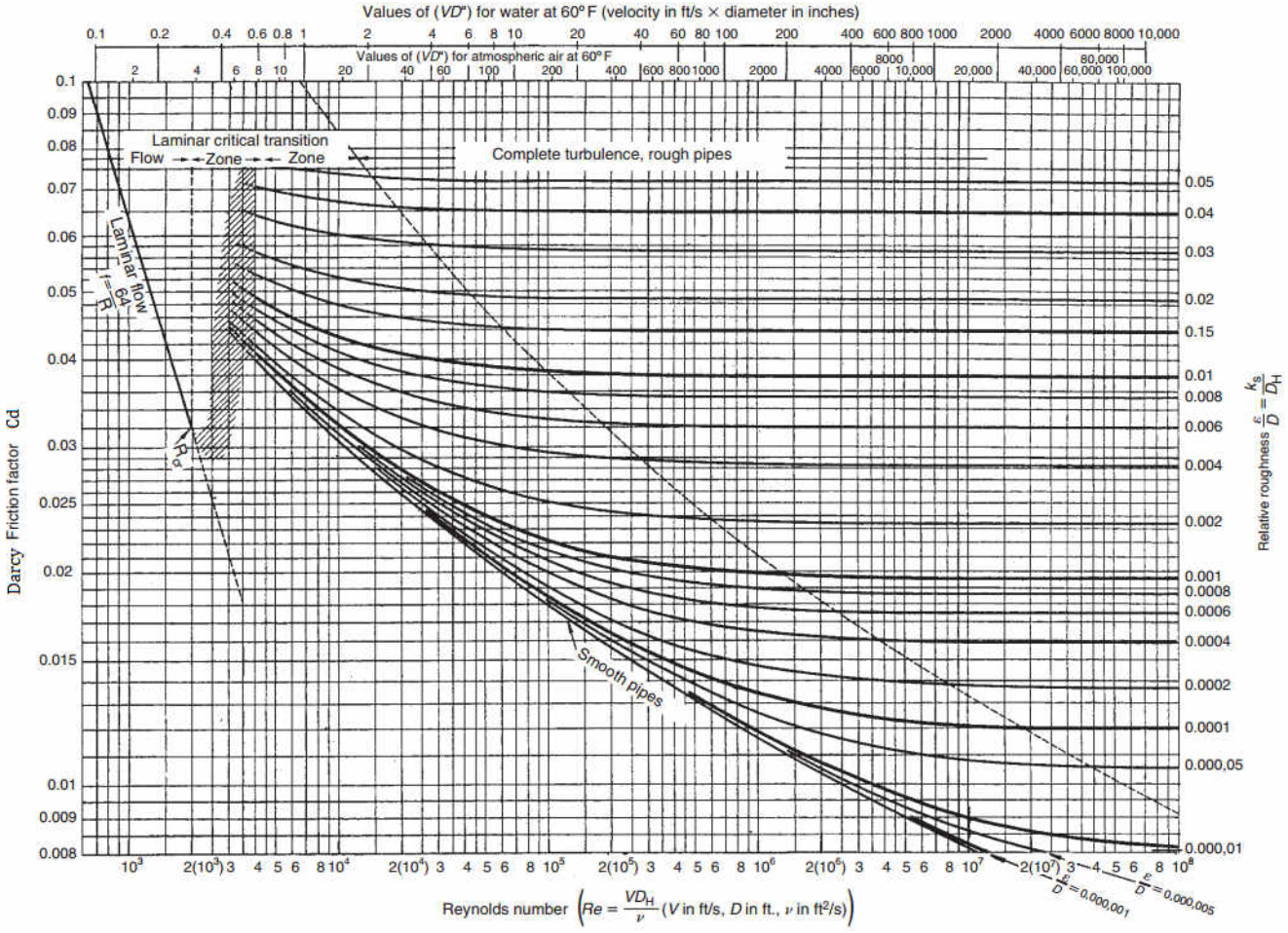


Figure 4.4: Moody diagram (after Moody, 1944, with permission of the American Society of Mechanical Engineers)

approximation of the related Darcy friction factor for turbulent flow as Haaland [27]

$$\frac{1}{\sqrt{C_d}} = -1.8 log_{10}\left(\left(\frac{k_s}{3.7D_h}\right)^{1.11} + \frac{6.9}{Re}\right) \tag{4.40}$$

The different friction formulae (4.39) and (4.40) account for the roughness parameter $k_s$. Typicale values of $k_s$ are given in Table 5.5.

| $\mathbf{k_s}$(mm) | Material |
|---|---|
| 0.01–0.02 | PVC (plastic) |
| 0.02 | Painted pipe |
| 1–10 | Riveted steel |
| 0.25 | Cast iron (new) |
| 1–1.5 | Cast iron (rusted) |
| 0.3–3 | Concrete |
| 3–10 | Untreated shot-concrete |
| 0.6–2 | Planed wood |
| 5–10 | Rubble masonry |
| 3 | Straight uniform earth channel |

Table 4.1: Typical roughness heights

#### 4.1.6.2 Momentum model

Velocity profiles are usually not uniform over the cross section, therefore average velocity can be used by introducing the momentum coefficient or Boussinesq coefficient, after Boussinesq [7]

$$\beta = \frac{\frac{1}{a}\int_a u^2 da}{u^2} \ , \tag{4.41}$$

where $a$ is the cross-sectional area (normal to the flow direction) and $u$ is the mean flow velocity ($u = Q/a$). The momentum coefficient is always larger than unity and $\beta = 1$ implies an uniform velocity distribution as shown in Figure 4.5 .

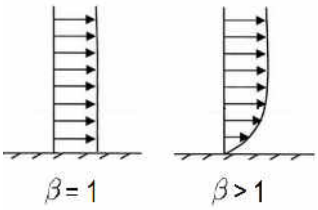


Figure 4.5: Values of momentum coefficient for uniform and non uniform velocity profiles

This coefficient was studied by Chow [13] who gives values for different channels for water flow in turbulent regime, as described in Table 4.2.

For approximate values, the momentum coefficient can be computed by Equation

| **Channels** | **Value of $\beta$** | | |
|---|---|---|---|
| | Min. | Av. | Max. |
| Regular channels, flumes, spillways | 1.03 | 1.05 | 1.07 |
| Natural streams and torrents | 1.05 | 1.10 | 1.17 |
| Rivers under ice cover | 1.07 | 1.17 | 1.33 |
| Rivers wallays, overflooded | 1.17 | 1.25 | 1.33 |

Table 4.2: Values of momentum coefficient $\beta$ for different channels

(4.42) assuming a logarithmic distribution of velocity.

$$\beta = 1 + \epsilon^2 \ , \tag{4.42}$$

or can be approximated by Equation (4.43) assuming a linear distribution of velocity as Rehbock [50] obtained.

$$\beta = 1 + \frac{\epsilon^2}{3} \tag{4.43}$$

where $\epsilon = u_{max}/u - 1$, $u_{max}$ being the maximum velocity and $u$ being the mean velocity. The coefficient $\epsilon$ can be estimate using the relation

$$\epsilon = \frac{9.5n}{R_h^{1/6}} \tag{4.44}$$

where $n$ is Manning's roughness coefficient and $R_h$ the hydraulic radius. The Manning's roughness can be estimate with Table 5.18.

| **Channels** | **Manning′s n** |
|---|---|
| Very smooth concrete and planed timber | 0.011 |
| Smooth concrete | 0.012 |
| Ordinary concrete lining | 0.013 |
| Wood | 0.014 |
| Straight unlined earth canals in good condition | 0.02 |
| Mountain streams with rocky beds | 0.05 |

Table 4.3: Manning's roughness coefficients for various boundaries

It is well known that the flow velocity distribution across any flow cross-section of

open channel is not uniform. The nature of flow velocity distribution in the cross section of a channel flow is shown in Figure 4.6, as reported by Chaudhry [11].

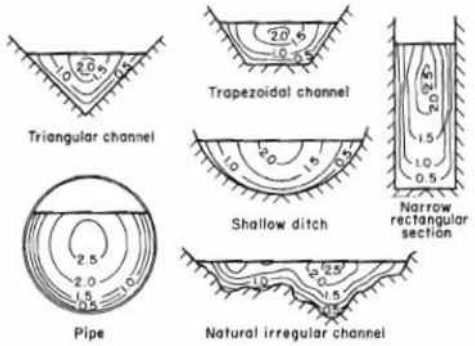


Figure 4.6: Velocity distribution in open channel flow

Numerous sources confirme the practical consideration of momentum (or Boussinesq) coefficient $\beta$ as unity in hydraulic problem analysis, though the same sources indicate that the values are not equal to unity. Experiments done by U. G. Wali [57], using the traditional approach of determining momentum coefficients with numerical integration, demonstrates that even for a small prismatic canal the value $\beta$ is different from unity. The findings presented by U. G. Wali are in agreement with what was reported by Chow [13], which stated that for a regular canal the value of $\beta$ range from 1.03 to 1.07. Fenton [19], reported that neglecting this coefficient, i.e. $\beta$=1, in pipe flow and channel flow modelling can introduce an error on height profile up to 5-10%. For this reason, he encourages the use of the integral forms of the momentum equation in practical problems of hydraulics to ensure the proper consideration of this factor.

## 4.2 A 1D first order scheme for UNSTEADY flows through a Venturi flume

### 4.2.1 Introduction to numerical methods

The current literature describes several numerical techniques that are suitable for solving Equations (4.26). These include the method of characteristics, explicit difference methods, fully implicit methods, Godunov methods [25] and semi-implicit methods. The Godunov's type methods, require the solution of local Riemann problems and, consequently, are very effective on simple channel geometries. For space varying bottom or width, source terms may generate artifical flows unless specific treatments of the geometrical source terms are implemented [43], [55]. Moreover, Godunov's type methods are explicit in time and, accordingly, the allowed time step is restricted by a C.F.L. stability condition, which relates the time step to the spatial discretization and the wave speed.

### 4.2.2 Finite volume method

The finite-volume method (FVM) is a method for representing and evaluating partial differential equations in the form of algebraic equations [35]. Similar to the finite difference method or finite element method, values are calculated at discrete places on a meshed geometry. Finite volume refers to the small volume surrounding each node point on a mesh. In the finite volume method, volume integrals in a partial differential equation that contain a divergence term are converted to surface integrals, using the divergence theorem. These terms are then evaluated as fluxes at the surfaces of each finite volume. Because the flux entering a given volume is identical to that leaving the adjacent volume, these methods are conservative.

### 4.2.3 The mesh

The first step in any numerical approximation is to discretize the computational domain in both space and time. For simplicity, we consider a uniform discretization of the domain along the spanwise direction $x \in [x_L, x_R]$. The discrete points are denoted as $x_j = x_L + \left(j + \frac{1}{2}\right)\Delta x$ for $j = 1, ..., N-1$, where $\Delta x = \frac{x_R - x_L}{N+1}$. We also define the midpoint values

$$x_{j-1/2} = x_j - \frac{\Delta x}{2}\ , \tag{4.45}$$

$$x_{j+1/2} = x_j + \frac{\Delta x}{2}\ , \tag{4.46}$$

for $j = 1, ..., N-1$. These values define computational cells or control volumes

$$C_j = [x_{j-1/2}, x_{j+1/2}] \tag{4.47}$$

We use also a uniform discretization in time with time step $\Delta t$. The time levels are denoted by $t^n = n\Delta t$. An illustration of the spatio temporal mesh is shown in Figure 5.6.

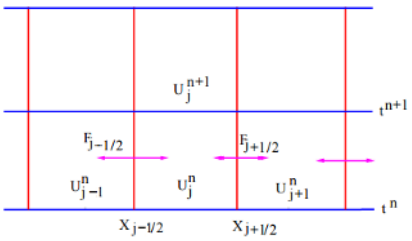


Figure 4.7: Showing the spatial discretization (red lines) and temporal discretization (blue lines). Each control volume is represented by a square delimited by these vertical and horizontal lines.

### 4.2.4 Cell averages

A classic finite difference method is based on approximating the point values of the solution of a PDE. This approach is not suitable for conservation laws as the solutions are

not continuous and point values may not make sense. Instead, we change the perspective and use the cell averages at each time level $t^n$ as the main object of interest for our approximation.

$$W_j^n \approx \frac{1}{\Delta x} \int_{x_{j-\frac{1}{2}}}^{x_{j+\frac{1}{2}}} W(x, t^n)\, dx \tag{4.48}$$

The cell average (4.48) is well defined for any integrable function, hence also for the solutions of the Saint Venant Equations (4.26) . The aim of the finite volume method is to update the cell average of the unknown at every time step.

### 4.2.5 Godunov scheme

Consider the 1D Saint Venant Equations as given in equation (4.26) with (4.27) in conservative form

$$\mathbf{W}_t + \mathbf{F}\left(\mathbf{W}\right)_x = \mathbf{b}\left(x, \mathbf{W}\right) \ , \tag{4.49}$$

where $\mathbf{W}$ is the vector of the conserved quatities, $\mathbf{F}$ is the flux function and $\mathbf{b}$ the source term.

By integrating (4.49) over a domain $[x_{j-\frac{1}{2}},\, x_{j+\frac{1}{2}}\,] \times [t^n,\, t^{n+1}\,]$

$$\int_{t^n}^{t^{n+1}} \int_{x_{j-\frac{1}{2}}}^{x_{j+\frac{1}{2}}} \mathbf{W}_t dx dt + \int_{t^n}^{t^{n+1}} \int_{x_{j-\frac{1}{2}}}^{x_{j+\frac{1}{2}}} \mathbf{F}\left(x, \mathbf{W}\right)_x dx dt = \int_{t^n}^{t^{n+1}} \int_{x_{j-\frac{1}{2}}}^{x_{j+\frac{1}{2}}} \mathbf{b}\left(x, \mathbf{W}\right) dx dt \ , \tag{4.50}$$

and using the fundamental theorem of calculus gives

$$\int_{x_{j-\frac{1}{2}}}^{x_{j+\frac{1}{2}}} \mathbf{W}(x, t^{n+1}) dx - \int_{x_{j-\frac{1}{2}}}^{x_{j+\frac{1}{2}}} \mathbf{W}(x, t^n) dx + \int_{t^n}^{t^{n+1}} \mathbf{F}\left(\mathbf{W}(x_{j+\frac{1}{2}}, t)\right) - \mathbf{F}\left(\mathbf{W}(x_{j-\frac{1}{2}}, t)\right) dt$$
$$= \int_{t^n}^{t^{n+1}} \int_{x_{j-\frac{1}{2}}}^{x_{j+\frac{1}{2}}} \mathbf{b}\left(x, \mathbf{W}\right) dx dt \tag{4.51}$$

Godunov [25] approximated the flux at each interface $x_{j+\frac{1}{2}}$ as the flux of the solution of the Riemann problem at this interface

$$\mathbf{F}^n_{j+\frac{1}{2}} = \frac{1}{\Delta t} \int_{t^n}^{t^{n+1}} \mathbf{F}\left(\mathbf{W}(x_{j+\frac{1}{2}}, t)\right) dt \ , \tag{4.52}$$

defined by

$$\mathbf{F}^n_{j+\frac{1}{2}} = \mathbf{F}\left(\mathbf{W}(x_j, t^n), \mathbf{W}(x_{j+1}, t^n)\right) \ . \tag{4.53}$$

For the source term, we simply approximate

$$\int_{t^n}^{t^{n+1}} \int_{x_{j-\frac{1}{2}}}^{x_{j+\frac{1}{2}}} \mathbf{b}\left(x, \mathbf{W}\right) dx dt \approx \Delta t \Delta x \ \mathbf{b}\left(x_j, \mathbf{W}(x_j, t^n)\right) \tag{4.54}$$

Using the cell averages definition (4.48), we can write Equation (4.49) as

$$\Delta x \left(\mathbf{W}^{n+1}_j - \mathbf{W}^n_j\right) + \Delta t \left(\mathbf{F}^n_{i+\frac{1}{2}} - \mathbf{F}^n_{j-\frac{1}{2}}\right) = \Delta t \Delta x \ \mathbf{b}^n_j \tag{4.55}$$

and so

$$\mathbf{W}^{n+1}_j = \mathbf{W}^n_j - \frac{\Delta t}{\Delta x} \left(\mathbf{F}^n_{j+\frac{1}{2}} - \mathbf{F}^n_{j-\frac{1}{2}}\right) + \Delta t \ \mathbf{b}^n_j \tag{4.56}$$

### 4.2.6 Numerical fluxes

Several numerical fluxes might be used, the most commonly used are

- Lax-Friedrichs flux [34]
- Rusanov flux [51]
- HLL flux [2]
- VFRoe-ncv flux [37]

The Lax-Friedrichs flux introduces much more diffusion than is actually required, and gives numerical results that are typically more smeared unless a very fine grid is used.

The Rusanov flux is also diffusive but more accurate and simple to implement, the kinetic one is slightly less diffusive but more computationally time consuming. VFRoencv and HLL fluxes are comparable and very accurate, but the first one is a little more time consuming due to entropy correction. All these fluxes are compared in [17] in Saint-Venant framework.

In this work, we use the Rusanov flux which is accurate and defined by

$$F(W_L, W_R) = \frac{F(W_L) + F(W_R)}{2} - \mid k \mid \frac{W_R - W_L}{2} \tag{4.57}$$

with

$$k = \sup_{u=u_L,u_R} \left( \sup_{j\in[1,2]} \mid \lambda_i(u) \mid \right) \tag{4.58}$$

where $\lambda_1(u)$ and $\lambda_2(u)$ are the eigenvalues of (4.28) and given by (4.30) and (4.31) respectively.

### 4.2.7 CFL condition

A CFL (Courant, Friedrichs, Levy) condition has to be imposed on the time step for the explicit scheme used here. The CFL allows to prevent from numerical blow up and to ensure the positivity of $a$. This classical stability condition writes

$$\Delta t \leq n_{CFL} \frac{\Delta x}{\max_i(\mid u_i \mid + c_i)} \tag{4.59}$$

where $c_i = \sqrt{\frac{ga_i}{\sigma_{\eta i}}}$ and $n_{CFL} = 1$ for the first order scheme.

### 4.2.8 Boundary and initial conditions

Two types of boundary conditions are implemented. On the outlet, all downstream waves get out of the computation domain without any reflection. On the inlet, all upstream waves are fully reflected on a wall. This condition is imposed by zero velocity

at $x = 0$, i.e. $u(x = 0) = 0$. Nevertheless, a source term at $x = 0$ on the mass conservation equation creates an inflow. When the steady state is reached, $au = Q$ where $Q$ is the specified flow rate.

All these boundary conditions are implemented as follow using ghost cells (labelled 0 and $N + 1$)

$$a_0 = a_1 \quad ,\forall t \tag{4.60}$$

$$u_0 = -u_1 \quad ,\forall t \tag{4.61}$$

$$a_N = a_{N+1} \quad ,\forall t \tag{4.62}$$

$$u_N = u_{N+1} \quad ,\forall t \tag{4.63}$$

$$\mathbf{b}(1,1) = \frac{Q(0,t)}{\Delta x} \quad ,\forall x \tag{4.64}$$

The basic initial condition would be to start with an empty channel. This could be done but without considering friction or considering a new friction model. Indeed basics friction models, as Colebrook-White model (4.39), assume a fully developed flow and so can not model a starting flow. An empty channel will introduce a new problematic for the friction terms as surface tension of the fluid. An alternative will be to impose no friction when the height of the flow is less than a minimum height. Thus we can start from an empty channel and use a simple model of friction.

### 4.2.9 Numerical results for the trapezoidal Venturi flume with the 1D unsteady flow model

Figure 4.8 represents the evolution of a water flow through the trapezoidal Venturi flume. We captured the height profile of the flow $h$ in function of the $x$ position at different time $t$. We started with an empty channel but we imposed no friction condition

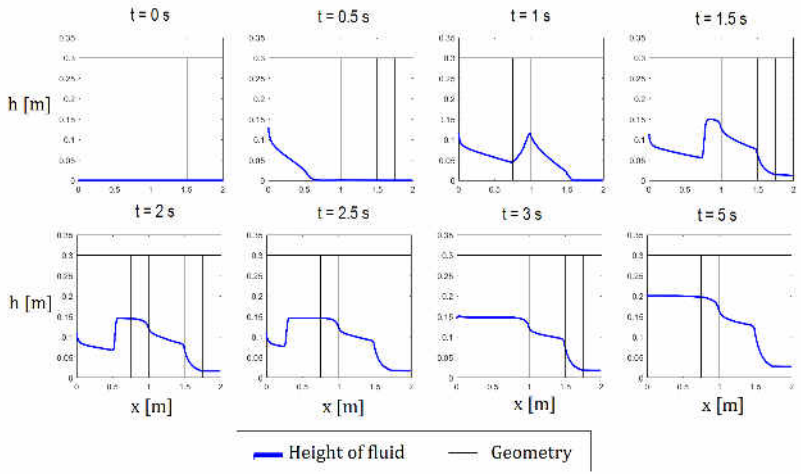


Figure 4.8: Capture at different time of a water flow along the trapezoidal Venturi flume for $Q = 500$L/min with the 1D transcient model

when $h$<1mm. Indeed, for small length scale and starting flow, other phenomenons appear as surface tension. When $h$>1mm, the friction is modelled by the Fanning friction factor described in previous part. For $t$=0.5s, the flow is still fully supercritical and we can see the formation of an hydraulic jump at $t$=1s. The hydraulic jump will go upstream the flume and makes appear a subcritical regime upstream. After 5s, the flow reached steady state and the Venturi flume works with upstream subcritical condition, and imposed a transcritical transition through the throat.

## 4.3 A 1D first order scheme for STEADY flows through a Venturi flume

### 4.3.1 Introduction to gradually varied flow

In steady steate, the flow rate is constant and the conservation of mass gives

$$\frac{dQ}{dx} = 0 \tag{4.65}$$

with $Q = au$, and the momentum equation is written

$$\left(\beta a u^2\right)_x = -gah_x - \frac{1}{2}P_w f u^2 \tag{4.66}$$

Considering $\beta$ constant, we can express the left term of Equation (4.66) as

$$\begin{aligned}
\frac{d\beta a u^2}{dx} &= \beta \frac{d}{dx}\left(\frac{Q^2}{a}\right) \\
&= \beta Q^2 \frac{d}{dx}\left(\frac{1}{bh + mh^2}\right) \\
&= -\beta Q^2 \frac{h\frac{db}{dx} + b\frac{dh}{dx} + h^2\frac{dm}{dx} + 2mh\frac{dh}{dx}}{(bh + mh^2)^2} \\
&= -\beta Q^2 \frac{h\frac{db}{dx} + h^2\frac{dm}{dx} + \sigma_\eta \frac{dh}{dx}}{a^2}
\end{aligned}$$

and then rewrite Equation (4.66) as

$$\frac{dh}{dx} = \frac{S_g - S_f}{1 - \beta Fr^2} \tag{4.67}$$

with the geometrical term source

$$S_g = \frac{\beta Q^2}{ga^3}\left(h\frac{db}{dx} + h^2\frac{dm}{dx}\right) \tag{4.68}$$

the friction term source

$$S_f = \frac{1}{2ga} P_w C_f \left(\frac{Q}{a}\right)^2 \tag{4.69}$$

and the Froude number

$$Fr = \sqrt{\frac{Q^2 \sigma_\eta}{ga^3}} \tag{4.70}$$

Equation (4.67) is the general differential equation for gradually varied flow as is currently written in the litterature, Chow [13]. It allows to obtain the slope of the fluid surface with respect to the channel bottom. The fluid surface is parallel to the channel bottom when $\frac{dh}{dx} = 0$, rising when $\frac{dh}{dx} > 0$ and lowering when $\frac{dh}{dx} < 0$. On the other hand, $\frac{dh}{dx}$ can be infinite when $Fr = \sqrt{\frac{1}{\beta}}$ (or $Fr = 1$ if $\beta = 1$) and characterized the critical state where $h = h_c$.

### 4.3.2 Characteristics of streamwise height profiles

Equation (4.67) for gradually varied flow expresses the longitudinal surface slope of the flow with respect to the channel bottom. It can therefore be used to describe the characteritics of various flow profiles. The flow profile represents the surface curve of the flow. It will represent a backwater curve if the fluid depth increases in the direction of the flow and a drawdown curve if the fluid depth decreases in the direction of flow. Therefore the streamwise height profile is a backwater curve if $\frac{\partial h}{\partial x}$ is positive and a drawdown curve if $\frac{\partial h}{\partial x}$ is negative.

When $h = h_c$, Equation (4.67) can indicate that $\frac{\partial h}{\partial x}$ is infinite, that is, that the flow profile will be vertical in crossing the critical-depth line. If the fluid depth suddenly changes from a low stage to a high stage in crossing the critical-depth line, a hydraulic jump will occur, representing a discontinuity in the height profile. If the depth changes from a high to low stage, then a transcritical transition will occur. It should be noted that, at or near the critical-depth line, the flow profile is bent to produce such great curvature that the small curvature assumption for the 1D Saint Venant equations, and

will introduce large errors. In fact, the height profile may become so curvilinear or rapidly varied so that the theory and equations developed in the preceding chapter become inapplicable. Therefore, Equation (4.67) will be inaccurate near the critical depth.

### 4.3.3 Classification of height profiles

Into a Venturi flume, when the downstream depth is high enough that the transition to subcritical flow advances upstream into the throat and the transcritical transition disappears, the flume is operating in a submerged flow regime. This regime is charactized by a submerged height $h_s$ and an upstream height bigger than this submerged height. Therefore, for a given flow rate and channel conditions, the submerged-depth and critical-depth lines divide the space in a channel into three zones

- Zone 1 : the space above the upper line
- Zone 2 : the space between the two lines
- Zone 3 : the space below the upper line

Thus, the flow profiles may be classified into six mean different types according to the nature of the conditions and the zone wich the flow surface lies. These types are designed as M1, M2, M3; S1, S2, S3; where the letter is descriptive of the condition: M for mid (subcritical) and S for steep (supercritical); and where the numerical represents the zone number. It should be noted that a continuous flow profile usually occurs only in one zone.

Figure 4.9 represents three typical flow profiles along Venturi flumes reflecting physical conditions:

- Plot 1 : M1 profile reflects a submerged flow, this occurs when fluid surface downstream from the flume is high enough to reduce flow through the flume. When the resistance to the flow in the downstream channel is sufficient to reduce the velocity

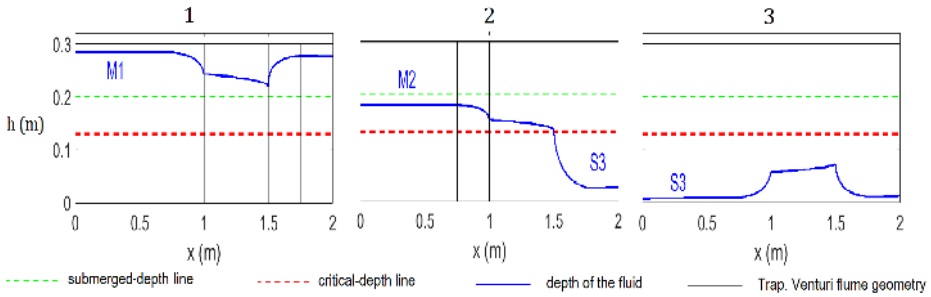


Figure 4.9: Examples of height profiles

out of the flume, flow depths increase and cause a backwater effect, as the fluid cannot exit the flume quickly enough.

- Plot 2 : M2 with S3 profiles reflects a free-flow, this occurs in the flume when there is insufficient backwater to reduce the discharge through the flume. The primary advantage of free-flow is that the level only needs to be measured in the inlet of the flume and upstream of the throat to calculate the flow rate. It is this typical configuration that we are interested.
- Plot 3 : S3 profile reflects supercritical flow, that occurs when a supercritical flow is imposed at the entrance of the flume and is used for transport and flow measurement where the flow has to be fast.

As shown in Figure 4.9 and Plot 2, we are interested on the free flow condition which allows a transcritical condition along the Venturi flume and allowing us to relate the upstream height to the flow rate. But as we can see, this transcritical transition appears when the flow cross the critical-depth line which means a critical height occurs. Using Equation (4.67), the critical height needs to be narrowly modeled.

### 4.3.4 Method of singular points

In order to solve Equation (**??**) at critical point determined by position pair $(x_c,h_c)$, one approach is to use the method of the singular point. This theory was developed by

Poincaré [46] but was first applied to flow studies in channels by Massé [38] and extended by others.

Let the numerator and denominator of Equation (4.67)be represented by two fonctions

$$\frac{dh}{dx} = \frac{S_g - S_f}{1 - \beta Fr^2} = \frac{F_1(x,h)}{F_2(x,h)} \tag{4.71}$$

Then, set each of these functions equal to zero

$$F_1(x,h) = S_g - S_f = 0 \tag{4.72}$$

$$F_2(x,h) = 1 - \beta Fr^2 = 0 \tag{4.73}$$

The solutions of theses Equations (4.72) and (4.73) are $x_c$ and $h_c$, and for this point, Equation (4.67) gives $\frac{\partial h}{\partial x} = \frac{0}{0}$, an indeterminate form. Such a point is known in mathematics as a singular point. If a critical point ($x_c$,$h_c$) exists in the domain, then the flow encounters a critical transition.

**Location of the critical point** The location of the critical point $x_c$ is determined by solving Equation (4.72). First, from Equation (4.72), we have the relation for the flow rate as

$$Q = \sqrt{\frac{g a_c^3}{\beta \sigma_{\eta,c}}} \tag{4.74}$$

where the index $c$ stands for the critical value with the critical height $h_c$. Then, we can rewrite Equation (4.72) as a function of $(x_c, hc)$ as

$$F_3(x_c, h_c) = \left( h_c \left.\frac{db}{dx}\right|_{x=x_c} + h_c^2 \left.\frac{dm}{dx}\right|_{x=x_c} \right) - \frac{1}{2\beta} P_{w,c} f_c \tag{4.75}$$

We find $(x_c, h_c)$ subject to following equation

$$F_3(x_c, h_c) = 0 \tag{4.76}$$

$$F_3(x_c - \epsilon_x, h_c + \epsilon_h) < 0 \tag{4.77}$$

$$F_3(x_c + \epsilon_x, h_c - \epsilon_h) > 0 \tag{4.78}$$

with $\epsilon_x$ is a small variation on $x$ and $\epsilon_h$ is a small variation on $h$, and which represents a change in state from subcritical to supercritical. To find $(x_c, h_c)$, one method consists on vary $x_c$ and $h_c$ and study the sign of $F_3$. So we varied $x_c$ into $[0; 2]$ and $h_c$ into $[0; 0.3]$.

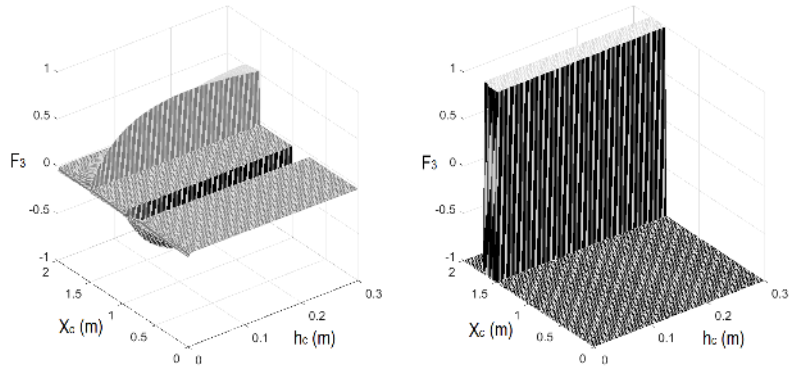


Figure 4.10: Left plot : $F_3$ as a function of $x_c$ and $h_c$; Right plot : signs of $F_3$ as a function of $x_c$ and $h_c$

The right plot on Figure 4.10 shows the sign of $F_3$, when $F_3 = 1$ then $F_3 > 0$ and when $F_3 = -1$ then $F_3 < 0$. The only location which verifies the conditions (4.76), (4.77) and (4.78) is the location $x_c = 1.5$, which is the location between the throat and the divergent part, where $b_c = 0.02m$ and $m_c = 0.15$.

**Height of the critical point** The height of the critical point is found by solving Equation (4.73) and using previous results of the critical location. Then, Equation (4.73) can be written as an equation with a polynomial on height as

$$g m_c^3 h_c^6 + 3 g b_c m_c^2 h_c^5 + 3 g b_c^2 m_c h_c^4 + g b_c^3 h_c^3 - 2\beta Q^2 m_c h_c - \beta Q^2 b_c = 0 \tag{4.79}$$

Lot of methods can be used to solve this polynomial, especially the function *roots* in matlab where the roots of the polynomial are calculated by computing the eigenvalues

of the companion matrix. The roots are six in number but only one is positive and real.

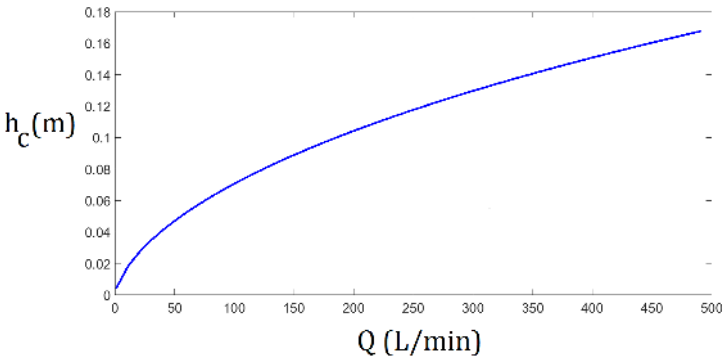


Figure 4.11: Plot of $h_c$ values in function of the flow rate $Q$ with $b_c = 0.02m$, $m_c = 0.15$, $\beta = 1$ and $g = 9.81ms^{b-2}$

O. Thual et al. [41] showed that laminar flows have the same critical height $h_c$ as that in the turbulent case. This feature is due to the existence of surface slope singularities associated to plug-like velocity profiles (Equation (4.79) with $\beta = 1$) with vanishing boundary-layer thickness. But us, we considered a normal flow for the definition of the velocity distribution and then we take into account the value of $\beta$ in Equation (4.79).

It is important to highlight that if we can measure the critical height, we can estimate directly the flow rate, thanks to Equation (4.74), and you can found the plot which represents the critical height $h_c$ in function of the flow rate $Q$ on Figure 4.11. The critical height $h_c$ is not possible to measure accurately because of the strong variation of the surface slope around the critical point.

### 4.3.5 Method of computation

The differential equation of gradually varied flow cannot be expressed explicitly in terms of $h$ for all types of channel cross-section, hence a direct and exact integration of the equation is practically impossible. Many attempts have been made either to solve the equation for a special cases or to introduce assumptions that make the equation to be analitycally integrable. Patil [47] proposed an improvement in the direct method

originally proposed by Chow [13] for integrating the equation of gradually varied flow in prismatic channels. The results obtained by this improved method compare well with the results of the numerical method.

Due to the complexity of the channel shape used here, we propose a way to integrate numerically Equation (4.67) of gradually varied flow. First, the domain is divided into three domain : subcritical, critical and supercritical. Here, only transcritical transitions are considered. In this case, the flow is subcritical prior the critical position and supercritical downstream. Equation (4.67) is therefore integrated from the critical position in both directions. In order to remove numerical singularity at ($x_c$,$h_c$), Equation (4.67) is integrated in the subcritical region from a point ($x_{c,L}$,$h_{c,L}$) just before the critical point. Similarly, we can integreate numerically Equation (4.67) from the point just after the critical point ($x_{c,R}, h_{c,R}$) to get the height profile of the supercritical regime.

$$x_{c,L} = x_c - \epsilon_{x,L} \tag{4.80}$$

$$h_{c,L} = h_c + \epsilon_{h,L} \tag{4.81}$$

$$x_{c,R} = x_c + \epsilon_{x,R} \tag{4.82}$$

$$h_{c,R} = h_c - \epsilon_{h,R} \tag{4.83}$$

where $\epsilon_{h,L}$ and $\epsilon_{h,R}$ are small variations on height just before and after the critical point, and where $\epsilon_{x,L}$ and $\epsilon_{x,R}$ are small variations on $x$ just before and after the critical point. Theses coefficient can be computed by linearising the differential equation around the critical point. With this method, we can integrate the height profile for both (subcritical and supercritical) regimes and capture the transcritical transition and solving the numerical problem due to the singular point.

### 4.3.6 Numerical results for the trapezoidal Venturi flume with the 1D steady state flow model

We used the method of computation described before to compute a complete height profile of a water flow through the trapezoidal Venturi flume, as shown in Figure 4.12. Upstream the critical point in red, we have a subcritical flow caracterized by $Fr<1$, whereas downstream the critical point we have a supercritical flow caracterized by $Fr>1$. Note that this method can be used and extended for other shapes of Venturi flume.

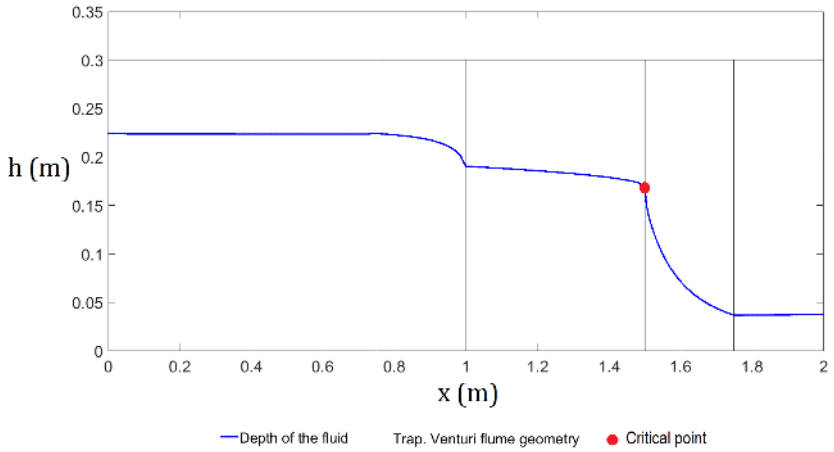


Figure 4.12: Water flow along the trapezoidal Venturi flume with $Q = 500L/min$

## 4.4 Steady solutions of the 1D models for water flows through the trapezoidal Venturi flume

We develop two strategies to compute the flow along the trapezoidale Venturi flume, but this two models are based on different numericals approaches. The purpose of this section is to compare this two models in term of performances to obtain the steady state solutions. Indeed, we wait for steady state from the unsteady computation from the 1D unsteady model to compare it with the steady computation from the 1D steady state model. The three simulations below were made with three different number of meshes : 100, 1000 and 10000; and paramaters as:

- **Fluid :** water
- **Flow rate :** 500 $L.min^{-1}$
- **Viscosity :** 0.001 $Pa.s$
- **Density :** 1000 $Kg.m^{-3}$
- $\boldsymbol{\beta}$ : 1

For figures 4.13, 4.14 and 4.15, the first plot shows the width of the trapezoidal Venturi flume, the second plot shows the depth of water along the flume, the third plot shows flow rate computed and the last plot shows the Froude number computed for each models.

**Case 1 ; number of mesh : 100**

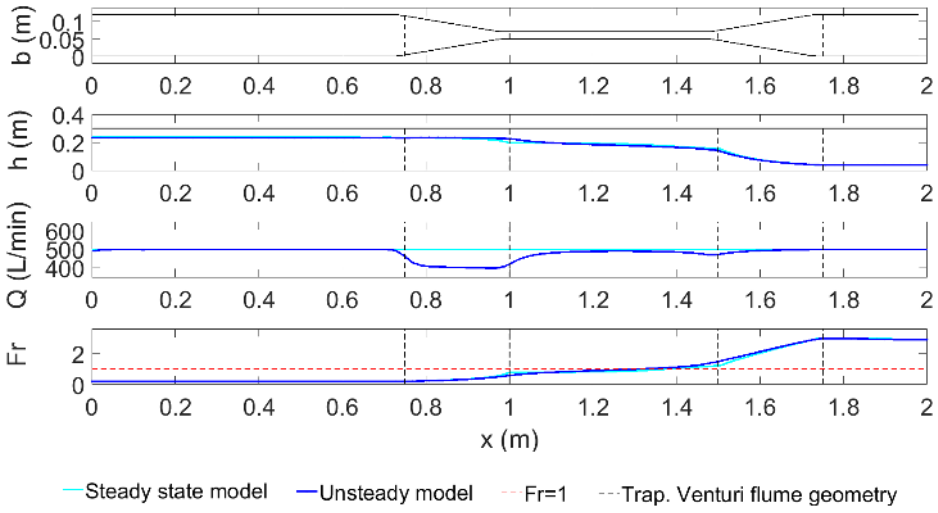


Figure 4.13: Water flow along the trapezoidale Venturi flume with $Q = 500L/min$ and a number of mesh equal to 100

**Height of the fluid** Height of fluid computed by the steady model and the unsteady model are close. The big differences are around $x$=1m and, ie. at the entrance and exit of the throat secion, where depth rapidly varies on a small distance.

**Flow rate** The flow rate computed through the Venturi flume by the steady state model is equal to the input flow rate, we have mass conservation. On the orther hand, the flow rate computed through the Venturi flume by the unsteady model is different from the input flow rate, we have not mass conservation. this discrepancy is due to the not "well balanced" scheme. The source term affects the results of the unsteady model and thus it needs to be improved.

**Froude number** Froude numbers computed by the steady model and the unsteady model are close. The main result is that we have the critical point at the same location for both models. It means that the singular point method used for the steady state

model to predict the critical position and critical height, is validated by the unsteady model where we don't impose anything to determine the critical condition.

**Case 2 ; number of mesh : 1000**

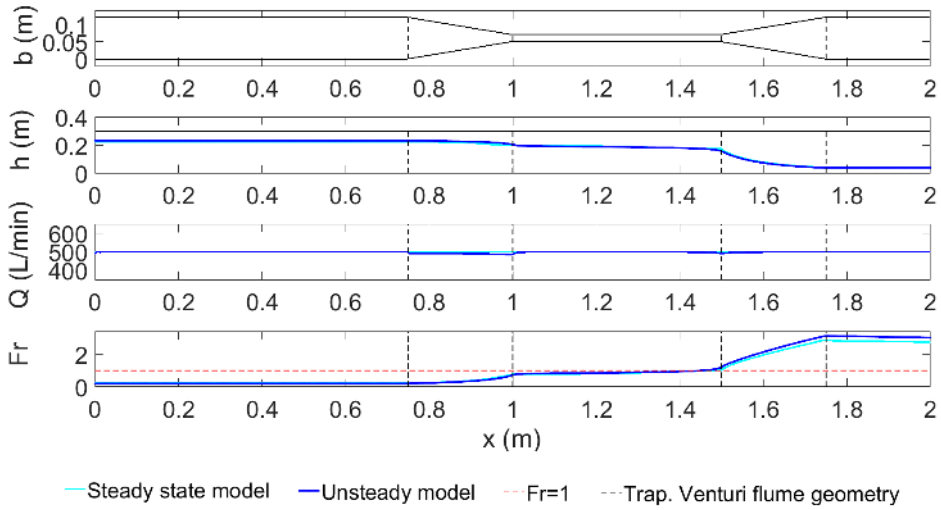


Figure 4.14: Water flow along the trapezoidale Venturi flume with $Q = 500L/min$ and a number of mesh equal to 1000

**height of the fluid** Height of fluid computed by the steady model and the unsteady model are very close. Small differences are still here, near the divergente and convergente parts.

**Flow rate** The flow rate computed through the Venturi flume by the steady state model is still equal to the input flow rate, we have mass conservation. On the other hand, the flow rate computed through the Venturi flume by the unsteady model comes closer the input flow rate. Increasing the number of meshes increases the accuracy of the unsteady model.

**Froude number** Froude numbers computed by the steady model and the unsteady model are very close. The critical point is still at the same location for both models.

**Case 3 ; number of mesh : 10000**

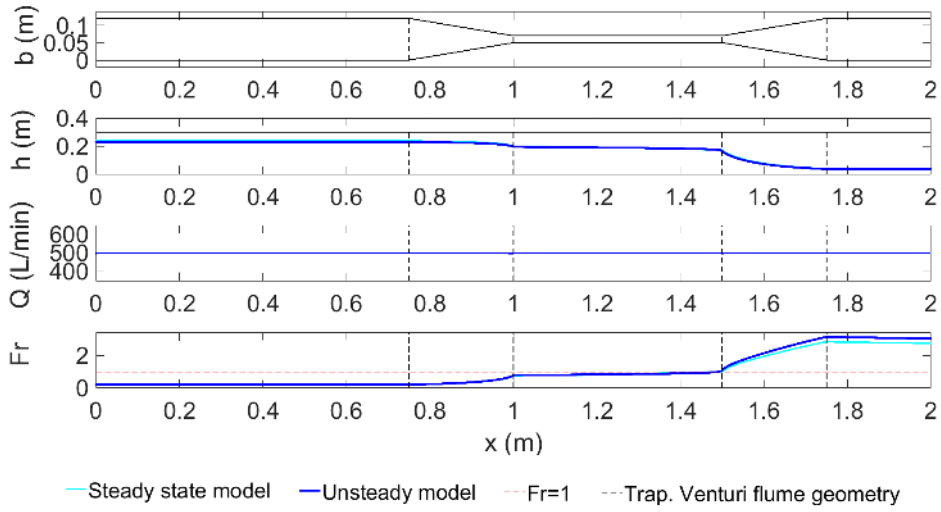


Figure 4.15: Water flow along the trapezoidale Venturi flume with $Q = 500L/min$ and a number of mesh equal to 10000

**Height of the fluid** Height of fluid computed by the steady model and the unsteady model are almost equal. The mean difference on height between boths are lesser than 5%.

**Flow rate** Flow rates computed by the steady model and the unsteady model are almost equal. The mean difference between boths are lesser than 0.03%. For this computation, we can consider that we have mass conservation for both models.

**Froude number** Froude numbers computed by the steady model and the unsteady model are almost equal and equal to 1 still at the same location.

### Conclusion

The steady state model is very accurate and ensure the mass conservation even with small number of meshes. On the other hand, the unsteady model needs a significant number of nodes to be accurate and ensure mass conservation. Moreover, the unsteady model have to compute the all evolution of the flow from empty channel to full channel and reach the steady state. Then, the computation time increases dramatically with increasing of the number of meshes, as showed in Table 4.4.

| **Models** | **Computation time** (**s**) | | |
|---|---|---|---|
| | Case 1 | Case 2 | Case 3 |
| Steady state | $< 1$ | $< 1$ | $< 1$ |
| Unsteady | 60 | 300 | 5000 |

Table 4.4: Computation time of models

## CHAPTER V

# Friction model of non-Newtonian fluids for open channels

*Free societies are societies in motion, and with motion comes friction.*

Salman Rushdie

## 5.1 Introduction to friction

The study of water flow in open channels is well documented, and a lot of friction models has been developed. On the contrary, the case of non-Newtonian fluid flows has been less explored. The lack of information for this case makes the design of open channels for complex fluid difficult. A specific attention on this point, and particularly on the development of friction models, is therefore needed. Datasets are published for non-Newtonian flow in rectangular open channels by Coussot [15], Naik [40], Haldenwang [28] and Haldenwang & Slatter [48], for non-Newtonian flow in semi-circular open channels by Fitton [20] [21] and by Burger [8] for non-Newtonian flow in semi-circular, triangular, trapezoidal and rectangular open channels. Not much of data has been available for non-Newtonian flow in channels of varying cross sections.

In the case of laminar flows of Newtonian fluids, Straub et al. [33] presented a theoretical prediction of friction laws for open channels with different cross sectional shapes and they also supplied experimental data for the flow of water and kerosene. They showed that the data in the laminar flow regime can be defined by a general relationship $f = K/Re$ where $f$ is the Fanning friction factor, $Re$ is the Newtonian Reynolds number and $K$ is a purely numerical coefficient which dependends on the channel shape. Analytical and numerical solutions for $K$ were provided for rectangular, semi-circular, elliptical, triangular and trapezoidal channels. Straub et al. [33] found that the predicted $f$ vs. $Re$ law for smooth-wall, rectangular, triangular and semi-circular shaped channels are in the good agreement with the experimental data when plotted as an $f$ vs. $Re$ plot. For rectangular channels where the water height to channel width (h/W) ratios ranges from 0.08 to 0.37, $K$ was found to vary from 19.75 to 15.25. These values compared well with the corresponding analytical values of 21.5 to 16.25. For triangular channels, K was found to be 14.25 and independent of the vertex angle. This is in excellent agreement with the analytical value of 14.23 for the 90deg triangular channel

and the numerical value of 14.15 for the other triangular channels. For semicircular channels, the $f$ vs. $Re$ plot showed the data to be grouped about the $f = K/Re$ law where $K$ was found analytically to be 16.

Chow [13] proposed a friction law $f$ as a function of$Re$for the case of water in smooth-wall, rectangular and triangular channels based on the two datasets of Straub et al. [33] . Here, $K$ was found to be approximately 24 for the rectangular channels and 14 for the triangular channels.

Only few studies have been reported in the literature for the prediction of non-Newtonian laminar friction law in open channels of arbitrary cross-section. The only method available was that proposed by Kozicki and Tiu [56]. The shape factors used by Kozicki and Tiu [56] were those evaluated from analytical solutions for flow of Newtonian fluids in the open channel of the same cross-section by Chhabra and Richardson [12]. No experimental work was carried out by Kozicki and Tiu [56] to validate their model.

Coussot [15] provided some data for the flow of a Herschel-Bulkley fluid in rectangular and trapezoidal channels. Fitton [20] [21] obtained data for flow of three different non-Newtonian fluids (carboxymethyl cellulose, carbopol and thickened tailings) in semi-circular channels. Naik [40] provided some data for turbulent flow of a Bingham fluid in a rectangular channel.

Haldenwang [28] and Haldenwang & Slatter [48] provided an extensive database for non-Newtonian flow in rectangular open channels. Burger [8] extended the database developed by Haldenwang [28] for rectangular channels to include non-Newtonian flow in semi-circular, trapezoidal and triangular channels. Using the Haldenwang [28] definition of $Re$, the effect of shape on the $f$ vs. $Re$ relationship for laminar, open channel flow of non-Newtonian fluids was investigated in some depth. During this research, Burger [8] investigated also the effect of shape on the friction factor-Reynolds number relationship for turbulent non-Newtonian flow in rectangular, trapezoidal, semi-circular

and triangular open channels.

## 5.2 Current models

### 5.2.1 Friction factor

#### Laminar friction models for open channels

We consider 4 current models used to describe laminar flows in open channels, given in Table 5.1 and namely :

- The Straub [33] model for laminar flow of Newtonian fluids in rectangular, triangular, semi-circular and trapezoidal open channels,
- The Kozicki & Tiu [56] model for laminar flow of power law and Bingham fluids in rectangular, triangular and semi-circular open channels,
- The Haldenwang et al. [28] model for laminar flow of power law, Bingham plastic and Herschel-Bulkley fluids in rectangular, triangular, semi-circular and trapezoidal open channels,
- The Burger [8] model for laminar flow of power law, Bingham plastic and Herschel-Bulkley fluids in rectangular, triangular, semi-circular and trapezoidal open channels,

| Author | Year | Shape | N | BP | PL | HB | Reynolds number | Fanning friction factor |
|---|---|---|---|---|---|---|---|---|
| Straub et al. | 1852 | Rectangular Triangular Semicircular Trapezoidal | • | | | | $Re_S = \frac{4R_h \rho u}{\mu}$ | $f_S = \frac{K_S}{Re_S}$ |
| Kozicki & Tiu | 1967 | Rectangular Triangular Semicircular | • | • | | | $Re_{K1} = \frac{R_h^n V^{2-n} \rho}{2^{n-3} k \left(\frac{a+bn}{n}\right)^n}$ | $f_{K1} = \frac{16}{Re_{K1}}$ |
| | | | • | | • | | $Re_{K2} = \frac{4R_h V}{\mu_B} \left(\frac{1}{a+b} - \frac{\chi}{b} + \frac{a\chi^{\frac{b}{a}+1}}{b(a+b)}\right)$ | $f_{K2} = \frac{16}{Re_{K2}}$ |
| Halden -wang | 2002 | Rectangular Triangular Semicircular | • | • | • | • | $Re_H = \frac{8\rho u^2}{\tau_y + k\left(\frac{2u}{R_h}\right)^n}$ | $f_H = \frac{16}{Re_H}$ |
| Burger et al. | 2014 | Rectangular Triangular Semicircular Trapezoidal | • | • | • | • | $Re_H = \frac{8\rho u^2}{\tau_y + k\left(\frac{2u}{R_h}\right)^n}$ | $f_B = \frac{K_B}{Re_H}$ |

Table 5.1: Laminar friction models for open channels and for Newtonian (N), Bingham plastic (BP), power law (PL) and Herschel Bulkley (HB) fluids.

| Shape factor | Rectangular | Semi – circular | Trapezoidal | Triangular |
|---|---|---|---|---|
| $K_S$ | 19 | 16 | 15 | 14.2 |
| $K_B$ | 16.4 | 16.2 | 17.6 | 14.6 |

Table 5.2: K shape factors used in the Straub and Burger laminar models

### Turbulent friction models for open channels

We consider 4 current models used to describe turbulent flows in open channels, namely :

- The Blasius [6] model for turbulent pipe flow of Newtonian fluid, which has been adapted for open channel flow by replacing the pipe diameter with four times the hydraulic radius,
- The Naik [40] model for turbulent open channel flow of Bingham fluids,
- The Haldenwang et al. [28] model for turbulent open channel flow of power law, Bingham plastic and Herschel-Bulkley fluids,
- The Burger [8] model for turbulent open channel flow of power law, Bingham plastic and Herschel-Bulkley fluids,

These models are given in Table 5.3.

| Author | Year | N | BP | PL | HB | Reynolds number | Fanning friction factor |
|---|---|---|---|---|---|---|---|
| Blasius* | 1913 | • | | | | $Re_S = \frac{4R_h\rho u}{\mu}$ | $f_{Bl} = \frac{0.079}{Re_S^{0.25}}$ |
| Naik | 1983 | • | • | | | $Re_N = \frac{4h\rho u}{k}$ | $\frac{1}{f_N^{0.5}} = 2.5\left(1 - \frac{8\tau_y h}{f_N\rho u^2}\right)^{\frac{1}{2}}\left(A_0 + ln\left(\frac{R_h}{k_s}\right)\right)$ |
| Halden -wang | 2003 | • | • | • | • | $Re_H = \frac{8\rho u^2}{\tau_y + k\left(\frac{2u}{R_h}\right)^n}$ | $f_H = \frac{1.32}{\left(2.5ln\left(\frac{2R_h}{k}\right) - 76.86\mu_{app(500)} - 9.45\right)^2}$ |
| Burger et al. | 2014 | • | • | • | • | $Re_H = \frac{8\rho u^2}{\tau_y + k\left(\frac{2u}{R_h}\right)^n}$ | $f_B = \frac{a}{Re_H^b}$ |

* *adapted for open channel flow by replacing the pipe diameter with four times the hydraulic radius*

Table 5.3: Turbulent friction models for open channels and for Newtonian (N), Bingham plastic (BP), power law (PL) and Herschel Bulkley (HB) fluids.

| Shape | Rectangular | Semi – circular | Trapezoidal | Triangular |
|---|---|---|---|---|
| a | 0.1200 | 0.0480 | 0.0851 | 0.0415 |
| b | 0.3297 | 0.2049 | 0.2655 | 0.20225 |

Table 5.4: Turbulent constants a and b used in the Burger turbulent model

| $\mathbf{k_s(mm)}$ | **Material** |
|---|---|
| 0.01–0.02 | PVC (plastic) |
| 0.02 | Painted pipe |
| 1–10 | Riveted steel |
| 0.25 | Cast iron (new) |
| 1–1.5 | Cast iron (rusted) |
| 0.3–3 | Concrete |
| 3–10 | Untreated shot-concrete |
| 0.6–2 | Planed wood |
| 5–10 | Rubble masonry |
| 3 | Straight uniform earth channel |

Table 5.5: Typical roughness heights

The coefficient $A_0$ for the Naik [40] turbulent model is desfined as :

$$A_0 = ln\left(\frac{30h}{R_h} exp\left(-1 - \frac{\left(\frac{b}{h}+2\right)h^2}{4a}\right)\right) \tag{5.1}$$

### 5.2.2 Momentum coefficient

Owing to the presence of a free surface and to the friction along the channel wall, the velocities in a channel are not uniformly distributed in the channel section. General patterns for velocity distribution in several channel sections for water are illustrated in Figure 5.1.

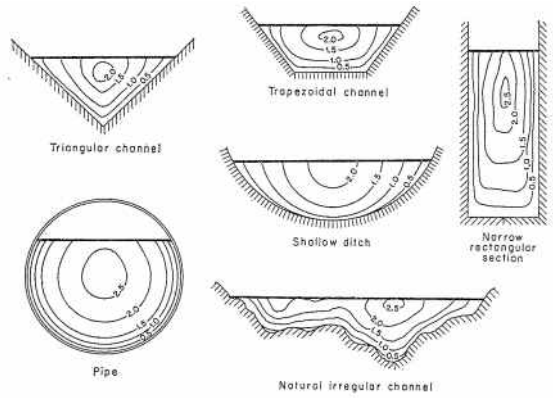


Figure 5.1: Velocity distribution in open channel flow for water

The velocity distribution in a channel section can depend also on other factors, such

as the rheology of the fluid, the unusual shape of the section and the roughness of the channel. For inviscid fluid, the velocity distribution is uniform through the section whereas the friction causes the curvature of the vertical and horizontal velocity distribution Figure 5.2.

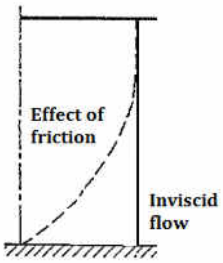


Figure 5.2: Effect of friction on velocity distribution in an open channel

The non uniform distribution of velocities affects the computation of momentum in open channel flow. From the principle of mechanics, the momentum of the fluid passing through a channel section per unit time is expressed by $\beta\rho a u^2/g$, where $\beta$ is known as the momentum coefficient or Boussiniesq coefficient, after Boussinesq [7] who first proposed it and defined as :

$$\beta = \frac{\int_a u^2 da}{a u^2} \tag{5.2}$$

**Turbulent momentum coefficient model for open channels**

As described in previous part, it is generally found that value of $\beta$, for fairly straight prismatic channels and water fluid, varies approximately from 1.01 to 1.12, as described by Chow [13]. He proposed an approximate values to estimate the momentum coefficient, for water turbulent flow assuming a uniform flow along the streamwise direction and a logarithmic distribution of velocity, as :

$$\beta = 1 + \epsilon^2 \tag{5.3}$$

where $\epsilon = u_{max}/u - 1$, $u_{max}$ being the maximum velocity and $u$ being the mean velocity. The coefficient $\epsilon$ can be estimate using the relation

$$\epsilon = \frac{9.5n}{R_h^{1/6}} \tag{5.4}$$

where $n$ is Manning's roughness coefficient and $R_h$ the hydraulic radius. The Manning's roughness can be estimated with Table 5.18.

| **Channels** | **Manning's n** |
|---|---|
| Very smooth concrete and planed timber | 0.011 |
| Smooth concrete | 0.012 |
| Ordinary concrete lining | 0.013 |
| Wood | 0.014 |
| Straight unlined earth canals in good condition | 0.02 |
| Mountain streams with rocky beds | 0.05 |

Table 5.6: Manning's roughness coefficients for various boundaries

Nothing has been reported in the literature for predicting momentum coefficient for non-Newtonian turbulent flow in open channels of arbitrary cross-section. Therefore, the model proposed by Chow [13] may be used for non-Newtonian fluids, because he related the momentum coefficient only to the hydraulic radius and the surface roughness. For example, with $h = 0.2$, $b = 0.12$ and a Mannin's roughness $n = 0.011$, the momentum coefficient $\beta = 1.03$.

### Laminar momentum coefficient model for open channels

For laminar Newtonian flow, there is not direct approximation $\beta$ but Straub et al. [33] proposed an analytical formula of the velocity distribution for several open channel shapes :

- semi-circular
- rectangular

- triangular
- trapezoidal

In this case, the flow is assumed to be uniform along the streamwise direction. Then, we can estimate the velocity distribution through the section and then estimate the coefficient $\beta$ using Equation (5.2). Figure 5.3 shows the analytical formula of the velocity distribution for open channels with rectangular section.

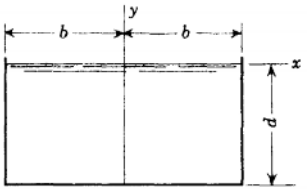


$$u(x,y) = \frac{g\,S}{2\,\nu}\,d^2\left(1 - \frac{y^2}{d^2} - \frac{32}{\pi^3}\sum_{n=0}^{\infty}\frac{(-1)^n}{(2\,n+1)^3}\,\frac{\cosh\frac{2\,n+1}{2}\frac{\pi\,x}{d}}{\cosh\frac{2\,n+1}{2}\frac{\pi\,b}{d}}\cos\frac{2\,n+1}{2}\frac{\pi\,y}{d}\right)$$

Figure 5.3: Analytical formula of the velocity distribution for open channels with rectangular section

Very little has been reported in the literature for predicting momentum coefficient for non-Newtonian laminar flow in open channels of arbitrary cross-section.

### 5.2.3 Selected friction models for open channels

**Laminar flow :** As described Straub [33] and Burger [8], the friction depends mainly on the shape of the section. Straub [33] proposed an analytical formula to estimate the friction for Newtonian fluids for different shapes, whereas Burger [8] proposed a semi-empirical formula to estimate the friction for non-Newtonian fluids for different shapes. Because of the shape variation of Venturi flumes and shape varieties, we propose a two numerical models (1D and 2D) able to estimate friction for Newtonian & non-Newtonian fluids adapted with different shapes. Thess models may compute velocity profil and may estimate Fanning friction factor and momentum coefficient for different flows.

**Transitional flow :** The transition from laminar to turbulent flow of Newtonian fluids in open channels has been reported to occur at Reynolds numbers between 2000 and 3000, as described Straub [33]. For non-Newtonian fluids, Haldenwang [48] found that the transition occurred at much lower Reynolds numbers than that for Newtonian fluids. We propose a simplification adapted for our geometry.

**Turbulent flow :** Friction is less impacted by the shape variations, therefore based on the Blasius [6] formula and the Burger [8] correction, we propose same formula adapted for our geometry.

## 5.3 Laminar theory

The wall shear stress of a liquid in steady flow in an open channel of uniform cross section under the influence of a source term is determined by making a force balance as shown in Figure 5.4.

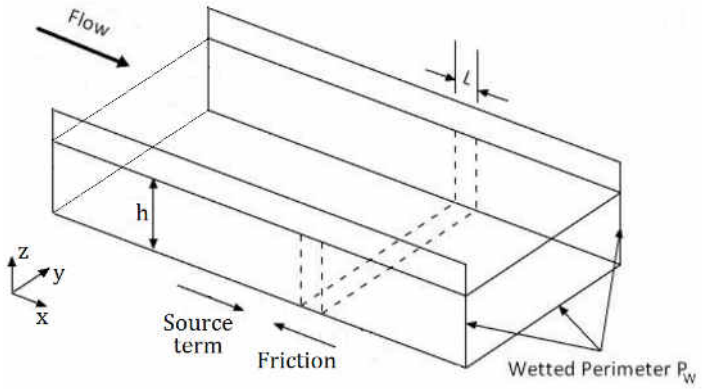


Figure 5.4: Force balance of a steady flow in an open channel of uniform cross section

A force balance between the downwards force, source term causing flow parallel to the plane and the force opposing the flow is the friction at wall. In a steady flow parallel to the plane, we consider the pressure gradient $P_g$ along the x-direction as the source term. In the other hand, the force opposing the flow is due to the wall shear stress $\tau_w$

times the wall area. Therefore, we can write the force balance in the x-direction as :

$$aLP_g = \tau_w P_w L \tag{5.5}$$

where $a$ is the cross sectional flow area, $L$ is a length of the channel and $P_w$ is the wetted perimeter. Noting the Fanning friction factor $f$ is given by :

$$\tau_w = \frac{1}{2} f \rho u^2 \tag{5.6}$$

For laminar flow, we relate the Fanning friction factor $f$ to the generalized Reynolds number $Re_g$ and the factor of shape $K$, as described Burger [8] and Straub [33].

$$f = \frac{K}{Re_g} \tag{5.7}$$

where

$$Re_g = \frac{8\rho u^2}{\tau_y + k\left(\frac{2u}{R_h}\right)^n} \tag{5.8}$$

Substituting for $\tau_w$ from Equation (5.6) and (5.7) into Equation (5.5) gives the expression of the shape factor $K$ as :

$$K = \frac{2aP_g Re_g}{P_w \rho u^2} \tag{5.9}$$

## 5.4 Laminar 1D friction model

### 5.4.1 Flow along an infinite plane

We consider a non-Newtonian laminar flow on an infinite plate, as shown in Figure 5.5. Here, the flow is driven by a pressure gradient in the x-direction, but the same problem can be solved with a flow driven by gravity on an inclined plane as did Burger [8] [30], Alireza [52], Chambon [23], Chilton [18] and Coussot [15]. In the case of a yield

stress fluid, the flow is characterized by the existence of a solid phase such that $y \in [h_y, h]$, where $h$ is the height of the fluid.

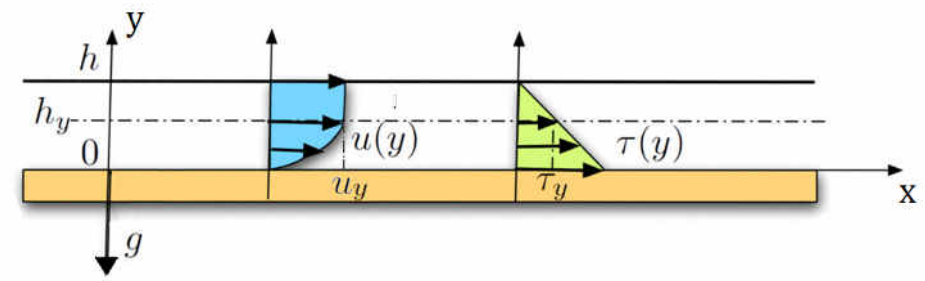


Figure 5.5: Open channel flow on an infinite plate. Velocity profil $u(y)$ and shear stress profil $\tau(y)$.

Let us consider the 2D problem, with $u(x, y, t)$ and $v(x, y, t)$ respectively parallel and orthogonal velocity fields to the flow. Navier-Stokes equations can be written as :

$$\frac{\partial u}{\partial x} + \frac{\partial v}{\partial y} = 0 \tag{5.10}$$

$$\frac{\partial u}{\partial t} + u\frac{\partial u}{\partial x} + v\frac{\partial u}{\partial y} = -\frac{1}{\rho}\frac{\partial P}{\partial x} + \frac{1}{\rho}\left(\frac{\partial \tau_{xx}}{\partial x} + \frac{\partial \tau_{xy}}{\partial y}\right) \tag{5.11}$$

$$\frac{\partial v}{\partial t} + u\frac{\partial v}{\partial x} + v\frac{\partial v}{\partial y} = -\frac{1}{\rho}\frac{\partial P}{\partial y} + \frac{1}{\rho}\left(\frac{\partial \tau_{xy}}{\partial x} + \frac{\partial \tau_{yy}}{\partial y}\right) \tag{5.12}$$

where $\rho$ denotes the density, $\tau_{xx}$, $\tau_{yy}$, and $\tau_{xy}$ are the normal stress in the x-direction, normal stress in the y-direction, and shear stress, respectively.

It is assumed that the flow is steady, incompressible, fully developed (no side effects) and is considered as being parallel to the bottom in the x-direction. This is the case when the relative slope of the free surface is nil or negligible. Therefore, we impose $\frac{\partial .}{\partial t} = 0$ and $v = 0$. We impose also $\frac{\partial .}{\partial x} = 0$ except for the pressure gradient of the x-direction, which is assumed constant and written as $P_g$. We consider only the shear

stress, and $\tau_{xy} = \tau$ , then we can write:

$$\frac{d\tau}{dy} = P_g \tag{5.13}$$

Especially, integrating Equation (5.13) on the y-direction and assuming the condition of free surface where $\tau(h) = 0$, we have the distribution of the shear stress :

$$\tau(y) = -(h - y)P_g \tag{5.14}$$

and notice that on the bottom, $\tau(0) = -hP_g$.

We express the shear stress using the Herschel Bulkley law :

$$\tau = \tau_y + k\left(\frac{du}{dy}\right)^n \tag{5.15}$$

and rewrite Equation (5.13) with the expression of the shear stress as :

$$\frac{d}{dy}\left(\tau_y + k\left(\frac{du}{dy}\right)^n\right) = P_g \tag{5.16}$$

Integrating twice Equation (5.16) results in :

$$u(y) = \frac{n}{n+1}\frac{k}{P_g}\left(\frac{P_g}{k}y + \frac{C_1 - \tau_y}{k}\right)^{\frac{n+1}{n}} + C_2 \tag{5.17}$$

where $C_1$ and $C_2$ are integration constants. Using the two boundary conditions from Equation (5.14) and the no slip condition at the bottom ($u(0) = 0$), we can write the velocity distribution as a function of the pressure gradient $P_g$ and the fluid height $h$ :

$$u(y) = \frac{n}{n+1}\frac{k}{P_g}\left[\left(\frac{P_g}{k}y - \frac{hPg + \tau_y}{k}\right)^{\frac{n+1}{n}} - \left(-\frac{hPg + \tau_y}{k}\right)^{\frac{n+1}{n}}\right] \tag{5.18}$$

But, we prefer to express the velocity distribution as a function of the flow rate $q$ per unit length in the z-direction, and the height of the fluid $h$. So, we define $h_y$ which is the height of the solid/liquid interface, $u(h_y) = u_y$ and $\tau(h_y) = \tau_y$. Then, above $h_y$, the fluid is like a solid and result are :

$$\left.\frac{du}{dy}\right|_{y=h_y} = 0 \tag{5.19}$$

$$h_y = \frac{hPg + \tau_y}{P_g} \tag{5.20}$$

$$u_y = -\frac{n}{n+1}\frac{k}{P_g}\left(-\frac{hPg + \tau_y}{k}\right)^{\frac{n+1}{n}} \tag{5.21}$$

The flow rate $q$ per unit length can be written as the sum of two partial flow rates, one part from the moving fluid below $h_y$ and the other from the moving plug above $h_y$.

$$q = \int_0^{h_y} u(y)dy + u_y(h - h_y) \tag{5.22}$$

Using Equations (5.18), (5.20) and (5.21), we can write :

$$q = \frac{n}{2n+1}\frac{k}{P_g^2}\left(-\frac{hP_g + \tau_y}{k}\right)^{\frac{n+1}{n}}\left(\frac{n\tau_y}{n+1} - hP_g\right) \tag{5.23}$$

Knowing the flow rate per unit length $q$, the rheology of the fluid $(\tau_y, k, n)$ and the height $h$, we can compute the distribution of the velocity on an infinite plate by computing the pressure gradient $P_g$ with Equation (5.23) and then computing the analytical velocity distribution with Equation (5.18).

### 5.4.2 Numerical resolution

The other way to find the velocity distribution is to solve numerically Equation (5.24)

$$\frac{d\tau}{dy} = P_g \tag{5.24}$$

We solve Equation (5.24) based on iterative method to estimate the shear stress distribution with the relation :

$$\tau = \mu_{app}\frac{du}{dy} \tag{5.25}$$

where is introduced the apparent viscosity, $\mu_{app}$, and defined on the Herschel Bulkley law as:

$$\mu_{app} = \begin{cases} \mu_{max}, & | \dot{\gamma} | \leqslant \dot{\gamma}_{min} \\ \tau_y | \dot{\gamma} |^{-1} + \ k | \dot{\gamma} |^{n-1}, & | \dot{\gamma} | > \dot{\gamma}_{min} \end{cases} \tag{5.26}$$

and the shear rate as :

$$\dot{\gamma} = \frac{du}{dy} \tag{5.27}$$

A regularization of the Herschel-Bulkley model is used in the following. Indeed, in the limit of vanishing shear rates, the apparent viscosity of a true Herschel-Bulkley fluid is infinite. This causes numerical difficulties when solving the pressure Equation (5.24) in regions of zero shear. The most common approach to deal with this difficulty is to limit the apparent viscosity to a large value, as done Frigaard & Nouar [22], Aposporidis [4], Bercovier & Engelman [5] and Papanastasiou [44]. There is, of course, an infinity of suitable functions for regularising the viscosity. The more popular is due to Bercovier & Engelman [5] whith :

$$\mu_{app} = \tau_y \left( \sqrt{\dot{\gamma}^2 + \epsilon^2} \right)^{-1} + \ k \left( \sqrt{\dot{\gamma}^2 + \epsilon^2} \right)^{n-1} \tag{5.28}$$

where $\epsilon << 1$. For our cases, best compromise between fast convergence and computation accuracy, $\epsilon = 10^{-2}$.

With the definition of the regularized apparent viscosity, Equation (5.28), Equation (5.24) reduces to :

$$\frac{d}{dy}\left(\mu_{app}\frac{du}{dy}\right) = P_g \tag{5.29}$$

The unknows of the system are $u(y)$ and $P_g$. We use finite difference method to find an approximation $u_i$ of the velocity $u(y_i)$ of the solution on a grid.

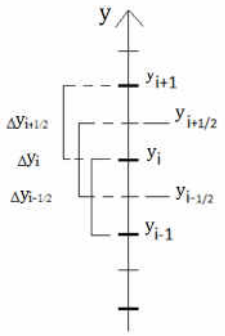


Figure 5.6: Vertical mesh and associated space steps

Using central finite difference to estimate diffusive terms, we can write :

$$\begin{aligned} \frac{d}{dy}\left(\mu\frac{du}{dy}\right)\Big|_i &= \frac{\mu_{i+\frac{1}{2}}\frac{du}{dy}\big|_{i+\frac{1}{2}} - \mu_{i-\frac{1}{2}}\frac{du}{dy}\big|_{i-\frac{1}{2}}}{\Delta y} \\ &= \frac{1}{\Delta y^2}\left(\mu_{i+\frac{1}{2}}(u_{i+1}-u_i) - \mu_{i-\frac{1}{2}}(u_i - u_{i-1})\right) \end{aligned} \tag{5.30}$$

and therefore, we find the numerical solution $u_i$ of the following equation:

$$\frac{1}{\Delta y^2}\left(\mu_{i+\frac{1}{2}}(u_{i+1}-u_i) - \mu_{i-\frac{1}{2}}(u_i - u_{i-1})\right) = P_g \tag{5.31}$$

The flow rate is imposed by a constrain on the axial velocity where N is the number of mesh.

$$\sum_{i=1}^{N} u_i \Delta y = q \tag{5.32}$$

The system take the following matrix form:

$$\begin{pmatrix} A^k & B \\ \Delta y & 0 \end{pmatrix} . \begin{pmatrix} u_i \\ P_g \end{pmatrix} = \begin{pmatrix} 0 \\ q \end{pmatrix} \tag{5.33}$$

Where $A^k$ is the diffusion matrix, with size $N \times N$,calculated with the estimate apparent viscosity at iterate $k$. The global matrix has then $(N+1)\times(N+1)$ .Equations are writen for $2 \leq i \leq N-1$. Boundary conditions are implemented as follows by completing first and last lines of diffusive matrix and right hand member.

$$\begin{array}{lll} u_1 = 0 & so & A^k_{1,1} = 1 \\ \frac{u_N - u_{N-1}}{\Delta y} = 0 & so & A^k_{N,N-1} = \frac{-1}{\Delta y}, A^k_{N,N} = \frac{1}{\Delta y} \end{array} \tag{5.34}$$

After each iteration $k$, we evaluate the new shear rate $\Pi_i^{k+1}$ and the new apparent viscosity $\mu_i^{k+1}$ with finite difference formulas.

$$\Pi_i^{k+1} = \frac{u_{i+1}^k - u_i^k}{\Delta y} \tag{5.35}$$

$$\mu_i^{k+1} = k \left(\Pi_i^{k+1}\right)^{n-1} + \tau_0 \left(\Pi_i^{k+1}\right)^{-1} \tag{5.36}$$

using zero gradient boundary condition for the shear rate as :

$$\Pi_{N-1}^{k+1} = \Pi_N^{k+1} \tag{5.37}$$

Finally the algorithm accuracy is firt order of accuracy with space step. The number of iteration required increases with the non linearity of the system.

### 5.4.3 Numerical vs. analytic solutions

The purpose of this study is to compare the analytical solution of the velocity distribution from Equation (5.18) vs. the numerical resolution of the velocity distribution from Equation (5.31). Let compare results for 3 different fluids as described in Table 5.7.

| **Case** | **Fluid** | $\tau_y$ $[Pa]$ | **k** $Pa.s^n$ | **n** $[-]$ | $\rho$ $[kg/m^3]$ |
|---|---|---|---|---|---|
| 1 | Newtonian | 0 | 0.5 | 1 | 1000 |
| 2 | Bingham | 5 | 0.5 | 1 | 1000 |
| 3 | Herschel Bulkley | 5 | 0.5 | 0.5 | 1000 |

Table 5.7: 3 different fluids of computations

For each case, we computed analytical and numerical velocity profile for $q = 0.0333m^2/s$, $h = 0.2m$ and the number of mesh $N_m = 2^{11}$. Results are shown in Figure 5.7.

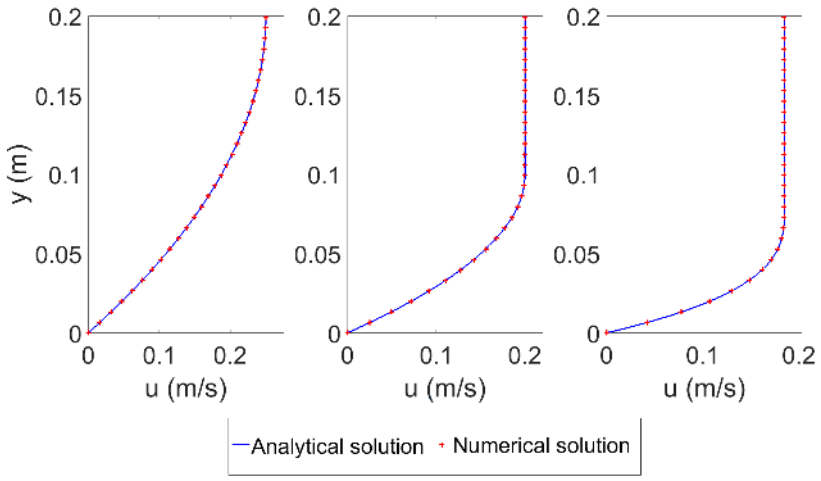


Figure 5.7: Velocity profile results from analytical and numerical solution, for the 3 different fluids : Newtonian fluid, Bingham fluid and Herschel Bulkley fluid

We summarized the maximum errors between the analytical and numerical solutions in Table 5.8.

| **Case** | **Error** [%] | **Iterations** | **Computation time** [**s**] |
|---|---|---|---|
| 1 | 0.02 | 1 | 0.5 |
| 2 | 0.13 | 88 | 20 |
| 3 | 0.32 | 83 | 19 |

Table 5.8: Maximum errors between the analytical and numerical solutions for the 3 different fluids: Newtonian fluid, Bingham fluid and Herschel Bulkley fluid

The numerical solutions have good agreement with analytical solutions. For a number of meshes equal to $2^{11}$, we can expect a maximum error on velocity between numerical and analytical solutions lesser than 0.4%. This accuracy has a cost : 88 iterations and 20s of computation for the case 2. This accuracy can be improved but it would cost too munch. For the case 1, the maximum errors between the analytical and numerical solutions were computed for various number of meshes $N_m$. The algorithm converges when increase number of meshes and the finite formulas reveal a first order accuracy in space, as shwon in Table 5.9.

| $\mathbf{N_m}$ | **Error** [%] |
|---|---|
| $2^6$ | 0.7750 |
| $2^7$ | 0.3891 |
| $2^8$ | 0.1949 |
| $2^9$ | 0.0976 |
| $2^{10}$ | 0.0488 |
| $2^{11}$ | 0.0244 |
| $2^{12}$ | 0.0121 |
| $2^{13}$ | 0.0056 |

Table 5.9: Convergence of the numerical computations for the case 1

### 5.4.4 Friction computations

#### 5.4.4.1 Friction factor computation

The computation of the friction factor for laminar flow is based on the numerical velocity profile model described on the previous part. Indeed, we can estimate the Fanning friction factor for a steady parallel flow based on the numerical velocity profile solution described on the previous part. Therefore, we can compute this friction factor using Equation (5.7), compute the generalized Reynolds number using Equation (5.8) and compute the shape factor using Equation (5.9). Based on the last 3 different cases from Table 5.7, we computed the friction factor and results are summarized in Table 5.13.

| **Case** | **Fluid** | $\tau_{\mathbf{y}}$ $[Pa]$ | **k** $Pa.s^n$ | **n** $[-]$ | $\rho$ $[kg/m^3]$ | **K** | $\mathbf{Re_g}$ | **f** |
|---|---|---|---|---|---|---|---|---|
| 1 | Newtonian | 0 | 0.5 | 1 | 1000 | 24 | 266 | 0.09 |
| 2 | Bingham | 5 | 0.5 | 1 | 1000 | 22.6 | 78 | 0.29 |
| 3 | Herschel Bulkley | 5 | 0.5 | 0.5 | 1000 | 20.1 | 84 | 0.24 |

Table 5.10: Fanning friction factor $f$ computations for the 3 different fluids

Notice that we can find analytically for Newtonian fluid that $K = 24$, by computing the mean velocity based on the analytical equation of the velocity distribution (5.18) with $\tau_y = 0$ and $n = 1$, and using Equation (5.9) with $R_h = a/P_w = h$.

### 5.4.5 Momentum coefficient computation

The computation of the momentum coefficient for laminar flow is based on the numerical velocity profile model described on the previous part. Indeed, we can estimate the momentum coefficient $\beta$ for a steady parallel flow. Therefore, we can compute this numerical momentum coefficient using Equation (5.38). Based on the last 3 different cases from Table 5.7, we computed the momentum coefficient and results are summarized in Table 5.11.

$$\beta = \frac{\frac{1}{n_i}\sum_{i=1}^{n_i} u_i^2}{\left(\frac{1}{n_i}\sum_{i=1}^{n_i} u_i\right)^2} \tag{5.38}$$

| **Case** | **Fluid** | $\tau_y$ $[Pa]$ | **k** $Pa.s^n$ | **n** $[-]$ | $\rho$ $[kg/m^3]$ | $\mathbf{Re_g}$ | $\beta$ |
|---|---|---|---|---|---|---|---|
| 1 | Newtonian | 0 | 0.5 | 1 | 1000 | 266 | 1.2 |
| 2 | Bingham | 5 | 0.5 | 1 | 1000 | 78 | 1.1 |
| 3 | Herschel Bulkley | 5 | 0.5 | 0.5 | 1000 | 84 | 1.06 |

Table 5.11: Momentum coefficient $\beta$ computations for the 3 different fluids

Notice that we can find analytically for Newtonian fluid that $\beta = 1.2$, by computing the mean velocity based on the analytical equation of the velocity distribution (5.18) with $\tau_y = 0$ and $n = 1$, and integrating it between 0 and $h$.

## 5.5 Laminar 2D friction model

### 5.5.1 Flow along a rectangular channel

We consider a non-Newtonian flow on an infinite open channel with a rectangular cross sectional shape. Here, the flow is driven by a pressure gradient in the x-direction. If we inclined the open channel, the pressure gradient can be replaced by gravity which drives the flow.

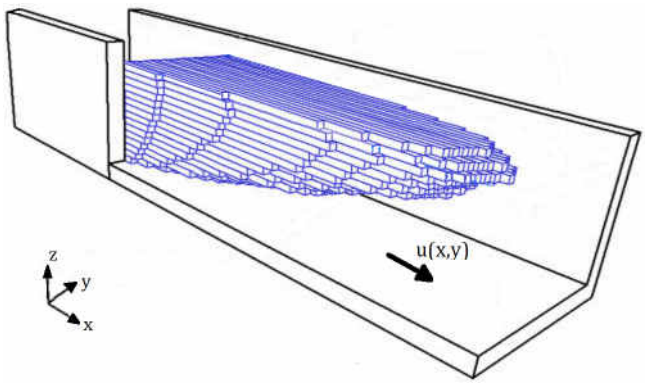


Figure 5.8: Open channel flow in a rectangular cross sectional shape

Let's consider the 2D problem, with $u(y, z)$ the parallel velocity fields to the flow. It is assumed that the flow is steady, incompressible, fully developed and is considered as being parallel to the bottom in the x-direction. Navier Stockes equations can be reduced to :

$$\frac{\partial \tau_{xy}}{\partial y} + \frac{\partial \tau_{xz}}{\partial z} = P_g \tag{5.39}$$

The shear stresses can be expressed by Herschel Bulkley laws as:

$$\tau_{xy} = \tau_y + k \left( \frac{\partial u}{\partial y} \right)^n \tag{5.40}$$

$$\tau_{xz} = \tau_y + k \left( \frac{\partial u}{\partial z} \right)^n \tag{5.41}$$

Therefore, we can rewrite Equation (5.39) with the expression of the shear stress as :

$$\frac{\partial}{\partial y} \left( \tau_y + k \left( \frac{\partial u}{\partial y} \right)^n \right) + \frac{\partial}{\partial z} \left( \tau_y + k \left( \frac{\partial u}{\partial z} \right)^n \right) = P_g \tag{5.42}$$

Equation (5.42) cannot be resolved analytically, as we did for the 1D equation, therefore numeric technics should be used.

### 5.5.2 Numerical resolution

The numerical resolution of the 2D velocity profile is based on the resolution of Equation (5.43) :

$$\frac{\partial \tau_{xy}}{\partial y} + \frac{\partial \tau_{xz}}{\partial z} = P_g \tag{5.43}$$

We solve Equation (5.43) based on iterative method to estimate the shear stresses distribution with the relations :

$$\tau_{xy} = \mu_{app,y} \frac{\partial u}{\partial y} \tag{5.44}$$

$$\tau_{xz} = \mu_{app,z} \frac{\partial u}{\partial z} \tag{5.45}$$

where are introduced the apparent viscosities defined on the Herschell Bulkley laws as :

$$\mu_{app,y/z} = \begin{cases} \mu_{max,y/z}, & \mid \dot{\gamma_{y/z}} \mid \leqslant \dot{\gamma}_{min,y/z} \\ \tau_y \mid \dot{\gamma_{y/z}} \mid^{-1} + \ k \mid \dot{\gamma_{y/z}} \mid^{n-1}, & \mid \dot{\gamma_{y/z}} \mid > \dot{\gamma}_{min,y/z} \end{cases} \tag{5.46}$$

and where shear rates are defined as :

$$\dot{\gamma_y} = \frac{\partial u}{\partial y} \tag{5.47}$$

$$\dot{\gamma_z} = \frac{\partial u}{\partial z} \tag{5.48}$$

A regularization of the Herschel-Bulkley model is used in the following. Indeed, in the limit of vanishing shear rates, the apparent viscosity of a true Herschel-Bulkley fluid is infinite. This causes numerical difficulties when solving the pressure Equation (5.43) in regions of zero shear. The most common approach to deal with this difficulty is to limit the apparent viscosity to a large value, as done Frigaard & Nouar [22], Aposporidis [4], Bercovier & Engelman [5] and Papanastasiou [44]. There is, of course, an infinity of suitable functions for regularising the viscosity. The more popular is due to Bercovier & Engelman [5] whith :

$$\mu_{app,y/z} = \tau_y \left( \sqrt{\dot{\gamma_{y/z}}^2 + \epsilon^2} \right)^{-1} + \ k \left( \sqrt{\dot{\gamma_{y/z}}^2 + \epsilon^2} \right)^{n-1} \tag{5.49}$$

where $\epsilon << 1$. For our cases, best compromise between fast convergence and computation accuracy, $\epsilon = 10^{-2}$.

With the definition of the regularized apparent viscosities, Equation (5.49), Equation (5.43) reduces to :

$$\frac{\partial}{\partial y} \left( \mu_{app,y} \frac{\partial u}{\partial y} \right) + \frac{\partial}{\partial z} \left( \mu_{app,z} \frac{\partial u}{\partial z} \right) = P_g \tag{5.50}$$

The unknows of the system are $u(y,z)$ and $P_g$. We use finite difference method to find an approximation $u_{i,j}$ of the velocity $u(y_i,z_i)$ of the solution on a control volume. Using

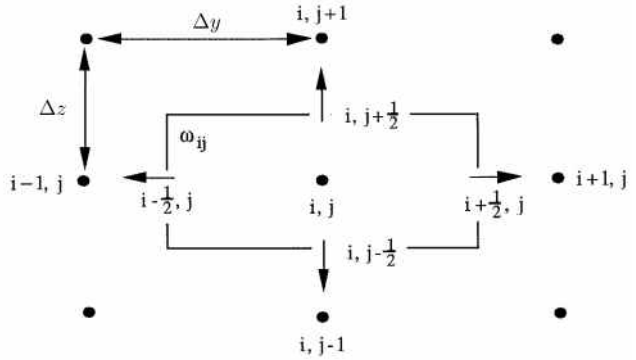


Figure 5.9: Control volume

central finite difference to estimate diffusive terms, we can write :

$$\begin{aligned}\frac{\partial}{\partial y}\left(\mu_{app,y}\frac{\partial u}{\partial y}\right)\Big|_{i,j} &= \frac{\mu_{app,R}\,\frac{\partial u}{\partial y}\big|_{i+\frac{1}{2},j}-\mu_{app,L}\,\frac{\partial u}{\partial y}\big|_{i-\frac{1}{2},j}}{\Delta y}\\ &= \frac{1}{\Delta y^2}\left[\mu_{app,R}\left(u_{i+1,j}-u_{i,j}\right)-\mu_{app,L}\left(u_{i,j}-u_{i-1,j}\right)\right]\end{aligned} \tag{5.51}$$

$$\begin{aligned}\frac{\partial}{\partial z}\left(\mu_{app,z}\frac{\partial u}{\partial z}\right)\Big|_{i,j} &= \frac{\mu_{app,U}\,\frac{\partial u}{\partial z}\big|_{i,j+\frac{1}{2}}-\mu_{app,D}\,\frac{\partial u}{\partial z}\big|_{i,j-\frac{1}{2}}}{\Delta z}\\ &= \frac{1}{\Delta z^2}\left[\mu_{app,U}\left(u_{i,j+1}-u_{i,j}\right)-\mu_{app,D}\left(u_{i,j}-u_{i,j-1}\right)\right]\end{aligned} \tag{5.52}$$

where the Up, Down, Right and Left apparent viscosities are defined respectively as :

$$\mu_{app,U} = \tau_y\,\dot{\gamma_U}^{-1} + k\,\dot{\gamma_U}^{n-1} \tag{5.53}$$

$$\mu_{app,D} = \tau_y\,\dot{\gamma_D}^{-1} + k\,\dot{\gamma_D}^{n-1} \tag{5.54}$$

$$\mu_{app,R} = \tau_y\,\dot{\gamma_R}^{-1} + k\,\dot{\gamma_R}^{n-1} \tag{5.55}$$

$$\mu_{app,L} = \tau_y\,\dot{\gamma_L}^{-1} + k\,\dot{\gamma_L}^{n-1} \tag{5.56}$$

and the Up, Down, Right and Left shear rates are defined respectively as :

$$\dot{\gamma_U} = \frac{u_{i,j+1} - u_{i,j}}{\Delta z} \tag{5.57}$$

$$\dot{\gamma_D} = \frac{u_{i,j} - u_{i,j-1}}{\Delta z} \tag{5.58}$$

$$\dot{\gamma_R} = \frac{u_{i+1,j} - u_{i,j}}{\Delta y} \tag{5.59}$$

$$\dot{\gamma_L} = \frac{u_{i,j} - u_{i-1,j}}{\Delta y} \tag{5.60}$$

Therefore, $u_{i,j}$ is the solution of the following equation:

$$\frac{1}{\Delta y^2}\left(\mu_{app,R}(u_{i+1,j} - u_{i,j}) - \mu_{app,L}(u_{i,j} - u_{i-1,j})\right) + \frac{1}{\Delta z^2}\left(\mu_{app,U}(u_{i,j+1} - u_{i,j}) - \mu_{app,D}(u_{i,j} - u_{i,j-1})\right) = P_g \tag{5.61}$$

The flow rate is imposed by a constrain on the axial velocity, where N is the number of mesh in the y and z direction.

$$\sum_{i=1}^{N}\sum_{j=1}^{N} u_{i,j}\ \Delta y \Delta z = Q \tag{5.62}$$

The system take the following matrix form:

$$\begin{pmatrix} A_1^k & & & B_1 \\ & \ddots & & \vdots \\ & & A_N^k & B_N \\ \Delta y\Delta z & \cdots & \Delta y\Delta z & 0 \end{pmatrix} \cdot \begin{pmatrix} u_{1,1} \\ \vdots \\ u_{N,N} \\ P_g \end{pmatrix} = \begin{pmatrix} 0 \\ \vdots \\ 0 \\ q \end{pmatrix} \tag{5.63}$$

where $A^k$ is the diffusion matrix, with size $N \times N$, calculated with the estimate apparent viscosities at iterate $k$. The global matrix has then $(N^2+1) \times (N^2+1)$ size. Equations are writen for $2 \leq i \leq N-1$ and $2 \leq j \leq N-1$ using boundary conditions. Boundary

conditions are implemented by completing first lines of the first diffusive matrix, last lines of the last diffusive matrix and right hand member. We impose a zero gradient on velocity for the free surface, and zero velocity on walls (left, right and bottom). After each iteration $k$, we evaluate the new shear rate $\Pi_i^{k+1}$ and the new apparent viscosity $\mu_i^{k+1}$ with finite difference formulas described before. The number of iteration required increases with the non linearity of the system.

### 5.5.3 Numerical results

#### 5.5.3.1 Newtonian flow

Straub et al. [33] presented a theory for laminar flow of Newtonian fluids in open channels of different cross-sectional shapes and they also supplied experimental data for the flow of water and kerosene. They found an analytical solutions for the velocity distribution for open channel Newtonian laminar flow in rectangular, semi-circular, elliptical, 60°, 90° and 120° triangular and trapezoidal channels. For a rectangular channel as shown in Figure 5.10, the velocity distribution is written with Equation (5.64) .

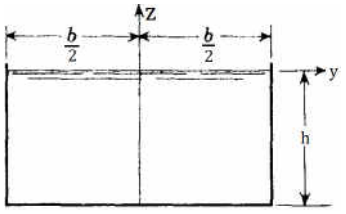


Figure 5.10: Rectangular channel

$$u(y,z) = \frac{P_g h^2}{2\mu}\left[1 - \frac{z^2}{h^2} - \frac{32}{\pi^3}\sum_{n=0}^{\infty}\frac{(-1)^n}{(2n+1)^3}\frac{cosh\left(\frac{2n+1}{2}\frac{\pi y}{h}\right)}{cosh\left(\frac{2n+1}{2}\frac{\pi b}{2h}\right)}\,cos\left(\frac{2n+1}{2}\frac{\pi z}{h}\right)\right] \tag{5.64}$$

where $P_g$ is the pressure gradient term, $h$ the height of the fluid, $\mu$ the viscosity of the fluid and $b$ the witdh of the channel.

Let's compare results for the analytical velocity profile from Straub et al [33]: $U_{analytical}$, and for the numerical velocity profile from the numerical resolution: $U_{numerical}$. We compute a flow with $Q$=200L/min, a channel width $b$=0.12, a fluid height $h$=0.2, a viscosity $\mu$=500cP, a density $\rho$=1000Kg/m$^3$ and a pressure gradient equivalent to a slope of 0.44°. The results are plotted on Figure 5.11.

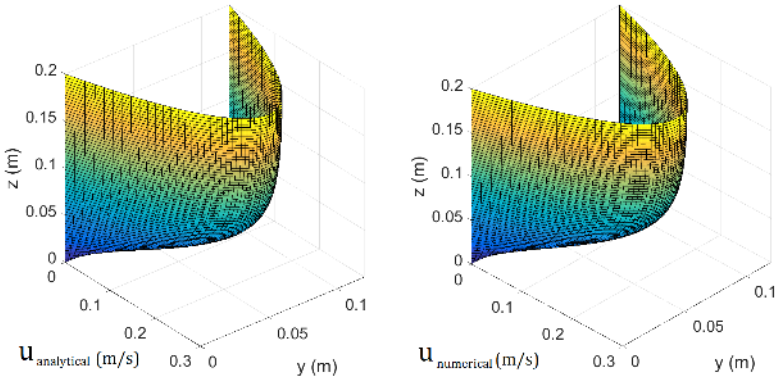


Figure 5.11: Analytical velocity profile from Straub et al [33] : $U_{analytical}$ vs. Numerical velocity profile from the numerical resolution : $U_{numerical}$

For this case, we summarized the maximum and mean errors on velocity between the analytical and numerical solutions in Table 5.12.

| **Case** | **Max. Error** [%] | **Mean Error** [%] | **Computation time** [s] | |
|---|---|---|---|---|
| | | | **Anal.** | **Num.** |
| 1 | 4.2 | 3.3 | 0.1 | 2.9 |

Table 5.12: Maximum and mean errors between the analytical and numerical solutions for the 3 different fluids: Newtonian fluid, Bingham fluid and Herschel Bulkley fluid

#### 5.5.3.2 Non-Newtonian flow

As no existing 2D velocity profile for non-Newtonian flows exists, let us compare results of the velocity profile only from the numerical resolution for 3 different fluids : Newtonian, Bingham and Herschel Bulkley fluids. Table 5.13 summarizes each fluid rheological characteristics used.

| **Case** | **Fluid** | $\tau_y$ $[Pa]$ | **k** $Pa.s^n$ | **n** $[-]$ | $\rho$ $[kg/m^3]$ |
|---|---|---|---|---|---|
| 1 | Newtonian | 0 | 0.5 | 1 | 1000 |
| 2 | Bingham | 5 | 0.5 | 1 | 1000 |
| 3 | Herschel Bulkley | 5 | 0.5 | 0.5 | 1000 |

Table 5.13: 3 different fluids of computations

For each cases, we computed numerical velocity profiles for a flow rate $Q = 0.0333m^3/s$, a height $h = 0.2m$, a channel width $b = 0.12$ and the number of mesh $N_m = 2^{12}$. Results are shown in Figure 5.12.

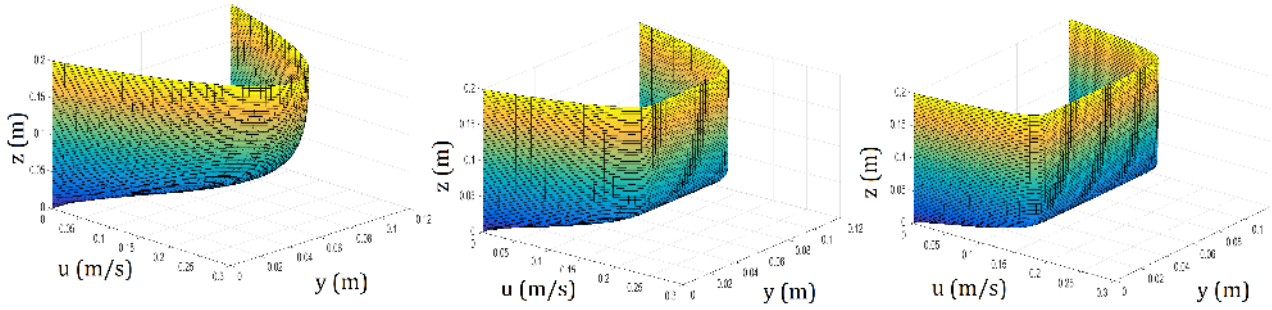


Figure 5.12: Velocity profile results from 2D numerical solutions, for the 3 different fluids : Newtonian fluid, Bingham fluid and Herschel Bulkley fluid with parameters described in Table 5.13

### 5.5.4 Friction factor

#### 5.5.4.1 Experimental measurements

**Experiments :** Burger [8] and Haldenwang [28] performed experiments where non-Newtonian fluids were circulated into flumes. Flume tests were carried out in a $10m$ long, rectangular flume designed at the Flow Process Research Center. This flume can be tilted up to 5° from the horizontal, as shown in Figure 5.13. By placing a partition insert, the flume width was changed from 300 to $75mm$. By inserting appropriate cross-sectional inserts, the rectangular flume can be changed into a triangular, semi-circular or trapezoidal cross-section. Here, the focus in on the rectangular flume.

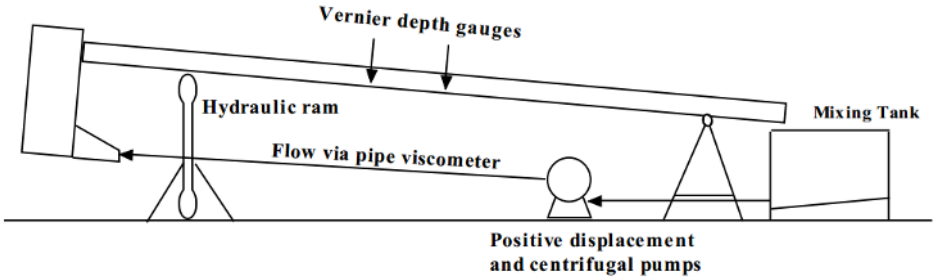


Figure 5.13: 10 m flume rig from Burger and Haldenwang experiments

The flow, provided by a $100mm$ progressive cavity, positive displacement pump and a Warmanw $4 \times 3$ centrifugal slurry pump, was monitored by an electromagnetic flow meter. The discharge capacity was $45l/s$. Flow depths were measured using digital depth gauges of $\pm 5\%$ accuracy fitted at the 5 and $6m$ positions from the flume entrance. These two positions were found to the optimum for depth measurement by Haldenwang [28]. Since the difference in fluid height between these two positions was found to be minimal, the flow in the region can therefore be taken as steady.

They used different fluid rheologies defined on Table 5.14.

| **N°** | **Fluid** | **Concentration** [%] | $\tau_y$ $[Pa]$ | **k** $[Pa.s^n]$ | **n** $[-]$ | $\rho$ $[kg/m^3]$ |
|---|---|---|---|---|---|---|
| 1 | Bentonite | 6.8 | 18.34 | 0.0078 | 1 | 1042 |
| 2 | Bentonite | 4.8 | 5.66 | 0.0036 | 1 | 1029 |
| 3 | Bentonite | 4.5 | 4.3 | 0.0036 | 1 | 1027 |
| 4 | Kaolin | 5.4 | 4.4 | 0.084 | 0.582 | 1089 |
| 5 | Kaolin | 7.1 | 11.56 | 0.148 | 0.557 | 1118 |
| 6 | Kaolin | 9 | 19 | 0.21 | 0.616 | 1148 |
| 7 | Kaolin | 5.4 | 4.4 | 0.084 | 0.582 | 1089 |
| 8 | CMC | 1.5 | 0 | 0.14 | 0.944 | 1008.2 |
| 9 | CMC | 3 | 0 | 0.145 | 0.788 | 1017.5 |
| 10 | CMC | 3.1 | 0 | 0.175 | 0.768 | 1018.2 |
| 11 | CMC | 4 | 0 | 0.33 | 0.727 | 1022.8 |
| 12 | CMC | 5.3 | 0 | 0.92 | 0.678 | 1028 |

Table 5.14: Fluids used by Burger and Haldenwang during experiments

**Results for laminar flow :** The data of all non-Newtonian fluids in four channel shapes are summarized in a database available in [8] and [28]. We are interested here by results for all non-Newtonian fluids but only for the rectangular flume, with width from 300 to $75mm$, and for the laminar regime.

Data in the laminar flow regime can be represented by a straight line of $-1$ slope in the Moody chart defined by Burger [8].

$$f = \frac{K}{Re_g} \tag{5.65}$$

where K is the numerical coefficient depending on channel shape. The average K values were obtained using

$$K = \frac{2aP_gRe_g}{P_w\rho u^2} \tag{5.66}$$

where $P_g$ corresponds here to the driving gravity term on an inclined $\theta$

$$P_g = \rho g \sin(\theta) \tag{5.67}$$

and where the generalized Reynolds number is written as

$$Re_g = \frac{8\rho u^2}{\tau_y + k\left(\frac{2u}{R_h}\right)^n} \tag{5.68}$$

Therefore, we can estimate experimentally the value of the coefficient K

$$K_{exp} = \frac{16 R_h \rho g \sin(\theta)}{\tau_y + k\left(\frac{2u}{R_h}\right)^n} \tag{5.69}$$

and the value of the Fanning friction factor

$$f_{exp} = \frac{2 R_h g \sin(\theta)}{u^2} \tag{5.70}$$

and plotted them, $f_{exp}$ and $K_{exp}$, in function of the generalized Reynolds number as shown in Figures 5.14 and 5.15.

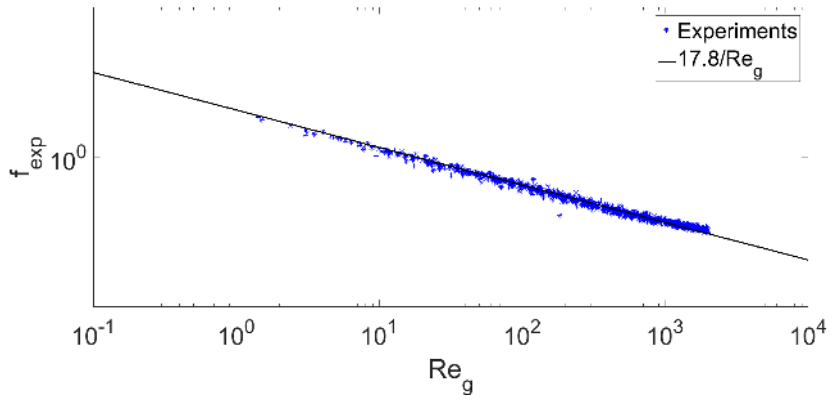


Figure 5.14: Loglog plot of $f_{exp}$ versus $Re_g$ for laminar flow of all non-Newtonian fluids in rectangular flume ,with width equal to 300, 150$mm$ and 75$mm$, at angles of 1° to 5°

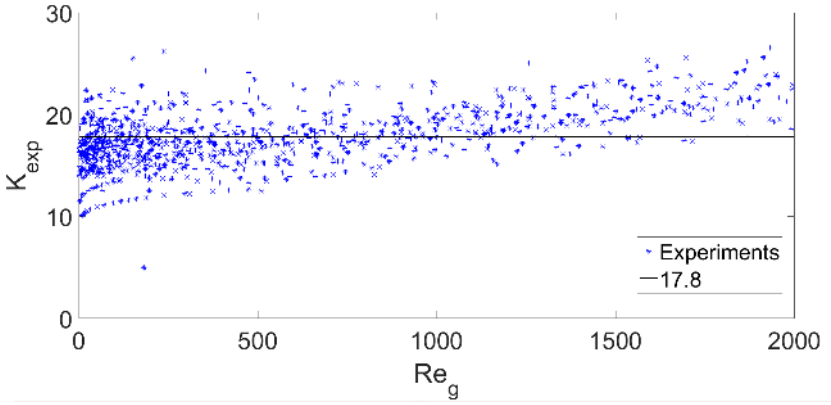


Figure 5.15: Plot of $K_{exp}$ versus $Re_g$ for laminar flow of all non-Newtonian fluids in rectangular flume ,with width equal to 300, 150$mm$ and 75$mm$, at angles of 1° to 5°

The mean value of the shape coefficient for the experiments is find to be $K_{exp} = 17.8$.

#### 5.5.4.2 Friction factor computation

**Numerical results vs. Experiments for laminar flow :** The computation of the friction factor for laminar flow is based on the numerical 2D velocity profile model described in the previous section. Indeed, we can estimate the Fanning friction factor $f_{num}$, from Equation (5.71), for a rectangular channel by computating the shape coefficient $K_{num}$, from Equation (5.72), and the generalized Reynolds number, from Equation (5.73).

$$f_{num} = \frac{K_{num}}{Re_g} \tag{5.71}$$

$$K_{num} = \frac{2aP_gRe_g}{P_w\rho u^2} \tag{5.72}$$

$$Re_g = \frac{8\rho u^2}{\tau_y + k\left(\frac{2u}{R_h}\right)^n} \tag{5.73}$$

These computations have been done by using the experimental flow rates $Q_{exp}$, the experimental height $h_{exp}$ and for the experimentale fluids from Table 5.14, and by computing the Fanning friction factor $f_{num}$ and the shape coefficient $K_{num}$. These numerical

results are shown in Figures 5.16 and 5.17 (red symbols), with the experimental results (blue symbols) as a function of the generalized Reynolds number.

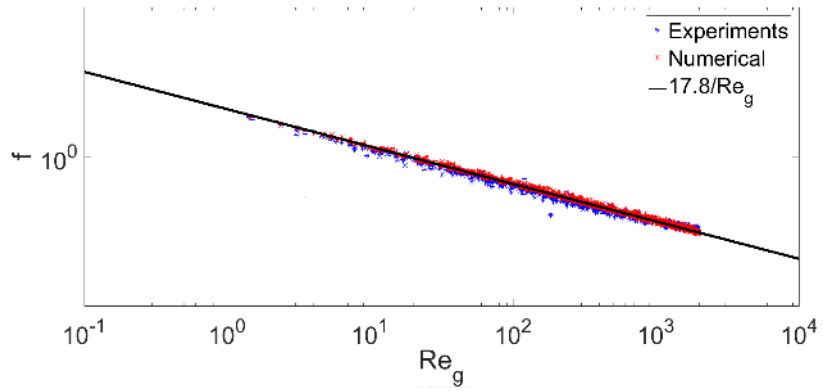


Figure 5.16: Loglog plot of $f_{exp}$ and $f_{num}$ versus $Re_g$ for laminar flow of all non-Newtonian fluids in rectangular flume ,with width equal to 300, 150$mm$ and 75$mm$, at angles of 1° to 5°

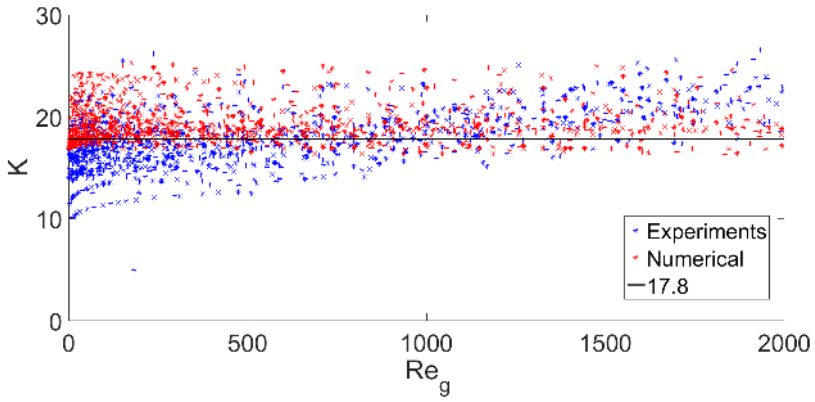


Figure 5.17: Plot of $K_{exp}$ and $K_{num}$ versus $Re_g$ for laminar flow of all non-Newtonian fluids in rectangular flume ,with width equal to 300, 150$mm$ and 75$mm$, at angles of 1° to 5°

The 2D model is shown to be in good agreement with the experiments, the mean value of the shape coefficient for the experiments is found to be $K_{exp} = 17.8$, whereas for the numerical results it is found to be $K_{exp} = 19.4$. Therefore, the error for mean value of the shape coefficien $K$ between the experimental measurements and the numerical computations is equal to 8.6%. So, we can compute the friction factor, with the 2D

velocity profile model, for laminar flow along rectangular channel with an accuracy of 8.6%.

### 5.5.5 Momentum coefficient computation

The computation of the momentum coefficient for laminar flow is based on the 2D numerical velocity profile model described previously. Indeed, we can estimate the momentum coefficient $\beta$ for a steady parallel flow on a rctangular flume. Therefore, we computed this numerical momentum coefficient using Equation (5.74). Based on the last 3 different cases from Table 5.7, we computed the momentum coefficient with the 1D model and the 2D model, and results are summarized in Table 5.15.

$$\beta = \frac{\frac{1}{n_i}\sum_{i=1}^{n_i} u_i^2}{\left(\frac{1}{n_i}\sum_{i=1}^{n_i} u_i\right)^2} \ . \tag{5.74}$$

| **Case** | **Fluid** | $\tau_{\mathbf{y}}$ $[Pa]$ | **k** $Pa.s^n$ | **n** $[-]$ | $\rho$ $[kg/m^3]$ | $\beta_{\mathbf{1D}}$ | $\beta_{\mathbf{2D}}$ |
|---|---|---|---|---|---|---|---|
| 1 | Newtonian | 0 | 0.5 | 1 | 1000 | 1.2 | 1.34 |
| 2 | Bingham | 5 | 0.5 | 1 | 1000 | 1.1 | 1.21 |
| 3 | Herschel Bulkley | 5 | 0.5 | 0.5 | 1000 | 1.06 | 1.12 |

Table 5.15: Momentum coefficient $\beta$ computations for the 3 different fluids with the 1D model and the 2D model

Note that $\beta_{1D}$ is and has to be lesser than $\beta_{2D}$, because it does not take into account of the side effect and therefore is flatter.

## 5.6 Transition friction model

The transition from laminar to turbulent flow of Newtonian fluids in open channels has been reported to occur at Reynolds numbers between 2,000 and 3,000, as described Straub [33]. Few attempts were made to predict the laminar turbulent transition of non-Newtonian fluids in open channels. The methods for predicting this transition was

reviewed by Haldenwang [28]. Of these, Haldenwang's transition model is the only available model applicable for power law, Bingham plastic and Herschel-Bulkley fluids. This model was developed for rectangular open channels based on the Froude number and the point viscosity at a shear rate of $100s^{-1}$. It was found that the transition can occurred at much lower Reynolds numbers than that for Newtonian fluids, it could start at $Re_H = 500$. Work is currently in progress to extend this work to other channel shapes. In our complex and varying geometry, we approximated that the transition occured at $Re_g = 2000$. This simplification can be improved but is a first good approximation.

## 5.7 Turbulent friction model

### 5.7.1 Friction factor computation

Only few studies have been reported in the literature for predicting non-Newtonian turbulent flow in open channels. Therefore, the computation of the friction factor for turbulent flow may be based on the Burger correlation [8], given by Equation (5.75). He adapted the Blasius equation [6] by changing the two coefficients $a$ and $b$, fitted on experiments for different channel shapes, and given in Table 5.16. Based on this method, we may fit also these two coefficients for our geometry.

$$f = \frac{a}{Re_g^b} \tag{5.75}$$

| **Shape** | **Rectangular** | **Semi − circular** | **Trapezoidal** | **Triangular** | **Venturi flume** |
|---|---|---|---|---|---|
| a | 0.1200 | 0.0480 | 0.0851 | 0.0415 | $a_v$ |
| b | 3297 | 0.2049 | 0.2655 | 0.20225 | $b_v$ |

Table 5.16: Turbulent constants a and b used in turbulent model

As the friction factor in turbulent regimehas been shown to be less dependent on the geometry than the laminar case, we compute the friction factor for turbulent flow using

the 1D steady SWE model described in Chapter 4 and the experimental data described in Chapter 2. In particular, we plot this friction factor as a function of the Reynolds number from the transition point $Re_g = 2000$, on Figure 5.18.

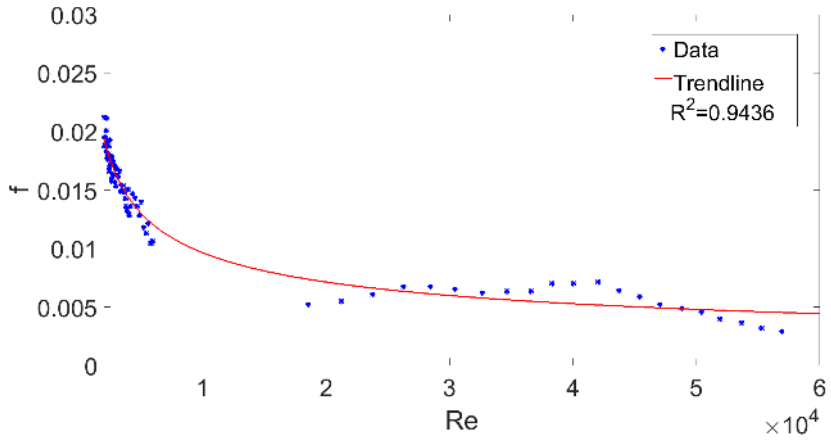


Figure 5.18: Plot of $f$ versus $Re_g$ of the turbulent flow regime for all fluids

We fit a trendline on these points and propose a new turbulent friction model with Equation **??**, and the new two coefficients for our geometry are given in Table 5.17.

$$f = \frac{a_v}{Re_g^{b_v}} \tag{5.76}$$

| **Shape** | **Trapezoidal Venturi flume** |
|---|---|
| $a_v$ | 0.52 |
| $b_v$ | 0.43 |

Table 5.17: Turbulent constants a and b used in turbulent model

### 5.7.2 Momentum coefficient computation

As described in previous part, it was generally found for Newtonian fluids that value of $\beta$, for fairly straight prismatic channels and water fluid, varies approximately from 1.01 to 1.12, as described by Chow [13]. He proposed an approximate values to estimate the momentum coefficient, for water turbulent flow assuming a logarithmic distribution

of velocity, as :

$$\beta = 1 + \epsilon^2 \tag{5.77}$$

where $\epsilon = u_{max}/u - 1$, $u_{max}$ being the maximum velocity and $u$ being the mean velocity. The coefficient $\epsilon$ can be estimate using the relation

$$\epsilon = \frac{9.5n}{R_h^{1/6}} \tag{5.78}$$

where $n$ is Manning's roughness coefficient and $R_h$ the hydraulic radius. The Manning's roughness is given in Table 5.18 for different surface texture.

| **Channels** | **Manning's n** |
|---|---|
| Very smooth concrete and planed timber | 0.011 |
| Smooth concrete | 0.012 |
| Ordinary concrete lining | 0.013 |
| Wood | 0.014 |
| Straight unlined earth canals in good condition | 0.02 |
| Mountain streams with rocky beds | 0.05 |

Table 5.18: Manning's roughness coefficients for various boundaries

Nothing has been reported in the literature for predicting momentum coefficient for non-Newtonian turbulent flow in open channels of arbitrary cross-section. Therefore, the model proposed by Chow [13] may be used for non-Newtonian fluids, because he related the momentum coefficient only to the hydraulic radius and the surface roughness. For example, with $h = 0.2$, $b = 0.12$ and a Manning's roughness $n = 0.011$, the momentum coefficient is $\beta = 1.03$.

## CHAPTER VI

# Results: Models vs. Experiments

*In theory, there is no difference between theory and practice.*

*But, in practice, there is.*

Jan L.A. van de Snepscheut (1953 - 1994)

## 6.1 Material used

### 6.1.1 Experiments

#### 6.1.1.1 Fluids database

In this study, we developed a database for water, viscous Newtonian and non-Newtonian fluids in trapezoidal Venturi flume. Prior to the publication of this database, no experimental datasets were available except for water. We provided data for the flow of water, glycerin mixtures and carbopol mixtures as described in Table 6.1.

| **Design −ation** | **Concen −tration** [%] | **Tempe −rature** [$°C$] | **Density** [$kg/m^3$] | **Rheology** | | | **Number of different flowrates** |
|---|---|---|---|---|---|---|---|
| | | | | $\tau$ [$Pa$] | $k$ [$Pa.s^n$] | $n$ [-] | |
| Water | 100 | 22 | 1000 | 0 | 0.001 | 1 | 25 |
| Gly.1 | 100 | 24 | 1256 | 0 | 0.747 | 1 | 14 |
| Gly.2 | 95 | 23 | 1249 | 0 | 0.429 | 1 | 9 |
| Gly.3 | 90 | 25 | 1237 | 0 | 0.203 | 1 | 21 |
| Gly.4 | 87.5 | 27 | 1230 | 0 | 0.128 | 1 | 22 |
| Gly.5 | 82.5 | 27.4 | 1220 | 0 | 0.074 | 1 | 23 |
| Gly.6 | 80 | 27.2 | 1215 | 0 | 0.059 | 1 | 22 |
| Gly.7 | 77.5 | 27.8 | 1209 | 0 | 0.045 | 1 | 24 |
| Gly.8 | 72.5 | 28.7 | 1197 | 0 | 0.027 | 1 | 25 |
| Gly.9 | 70 | 28 | 1215 | 0 | 0.024 | 1 | 25 |
| Gly.10 | 65 | 28.1 | 1192 | 0 | 0.016 | 1 | 25 |
| Carb.1 | 0.13 | 21 | 999.3 | 1.55 | 0.81 | 0.53 | 23 |
| Carb.2 | 0.12 | 24 | 1000.1 | 1.15 | 0.59 | 0.54 | 24 |
| Carb.3 | 0.118 | 22 | 999 | 0.83 | 0.57 | 0.55 | 21 |
| Carb.4 | 0.115 | 22 | 999 | 0.84 | 0.51 | 0.54 | 21 |
| Carb.5 | 0.11 | 23 | 1000.2 | 0.56 | 0.40 | 0.56 | 13 |
| Carb.6 | 0.10 | 22 | 999.4 | 0.01 | 0.16 | 0.61 | 24 |
| Carb.7 | 0.095 | 22 | 999.8 | 0 | 0.01 | 0.64 | 21 |
| | | | | | | **Total** : | 382 |

Table 6.1: Fluids properties used during experiments

#### 6.1.1.2 Height database

This database is a reference in this study of non-Newtonian flows in Venturi flume. For each fluid, we circulated a flow through the trapezoidal Venturi flume and we measured eight different heights along it. The location of each height sensor is shown in Figure 6.1. These eight height sensors are named from $US_1$ to $US_8$, and the eight corresponding height measured are named from $H_{1/exp}$ to $H_{8/exp}$. We developed a database with 18 different mixtures, with 382 different flow rates measured, and consequently, with 3056 different heights measured.

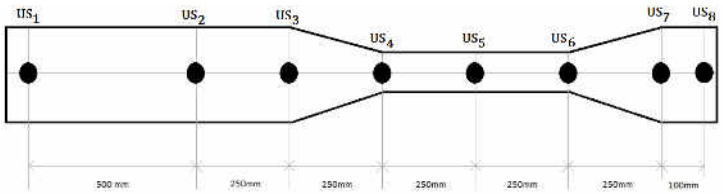


Figure 6.1: Location of the 8 ultrasonic height sensors along the trapezoidale Venturi flume

For eaches mixtures, we can plot the height measured, from $H_{1/exp}$ to $H_{8/exp}$, versus the flow rate measured $Q_{exp}$ for all data, as shown in Figures 6.2 and 6.3.

We notice that for height measured from $H_{7/exp}$ to $H_{8/exp}$, measurements are noisy. This is due to the surface of the fluid at the exit of the divergent part. Indeed, on this part of the Venturi flume, we are on supercritical regime and the surface is very agitated and not flat. Therefore, the height of the free surface is difficult to measure accurately in this region.

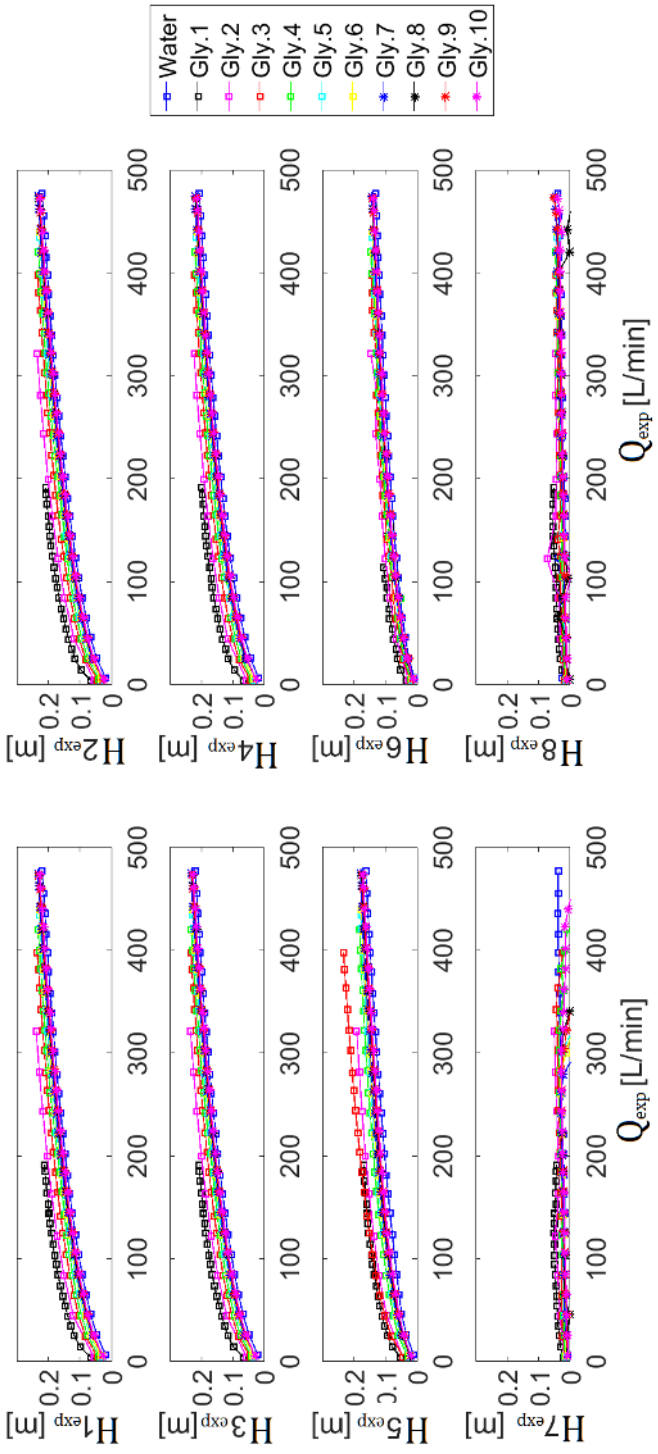


Figure 6.2: Height measured from $H_{1/exp}$ to $H_{8/exp}$ versus flow rate measured $Q_{exp}$ for all Newtonian fluids

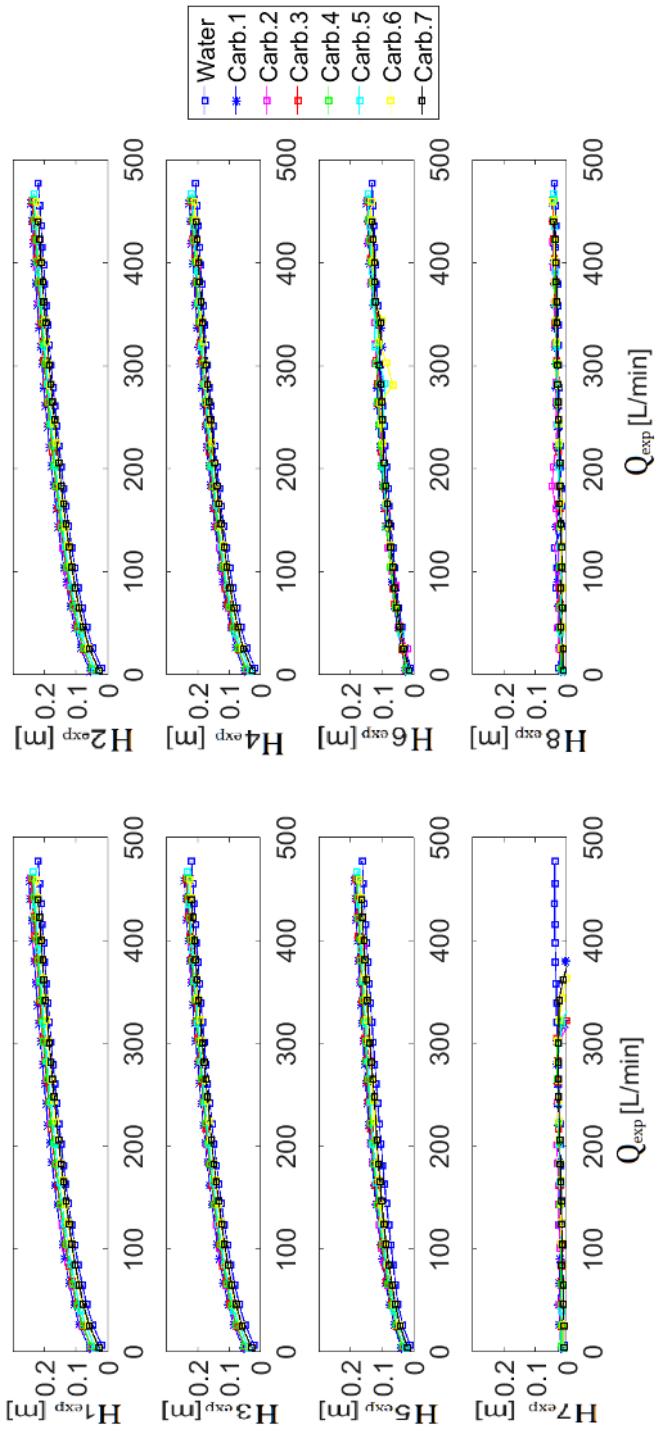


Figure 6.3: Height measured from $H_{1/exp}$ to $H_{8/exp}$ versus flow rate measured $Q_{exp}$ for all non-Newtonian fluids, with water data for comparison

### 6.1.2 3D CFD model

#### 6.1.2.1 CFD inputs/outputs

CFD enables scientists and engineers to perform numerical experiments (i.e. computer simulations) in a virtual flow laboratory. Therefore, it can be used to extend the database for fluids closest to mud. Before using it as virtual flow laboratory, we have to validate the 3D CFD model based on experimental results. First, we define the input quantities of the 3D CFD model :

- the flow rate : Q
- the fluid rheology : $\tau_y$, $k$ and $n$
- the density : $\rho$

and the output quantity of the 3D CFD model :

- the height profile in the plane of symmetry of the trapezoidale Venturi flume, shown in green on Figure 6.4.

Note that all numerical parameters and models used are described in the 3D simulation chapter.

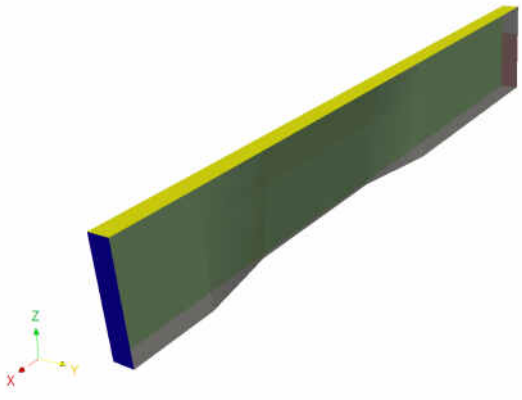


Figure 6.4: Symmetry plane in green of the trapezoidale Venturi flume

#### 6.1.2.2 CFD cases

Due to time computation cost, 3D simulations have been done for 3 specific cases:

- case 1: Newtonian turbulent flow with water fluid
- case 2: Newtonian laminar flow with glycerin fluid
- case 3: non-Newtonian lamiar flow with carbopol fluid

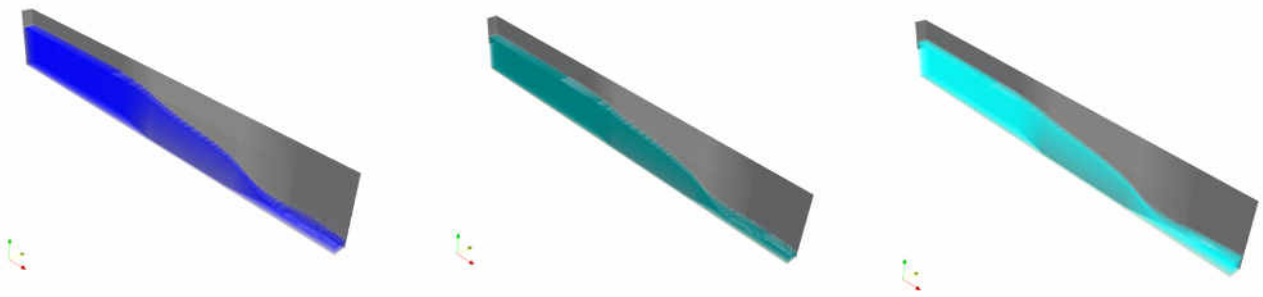

Figure 6.5: (From the left to the right: simulations of Newtonian turbulent flow, Newtonian laminar flow and non-Newtonian laminar flow

| **Case** | **Fluid** | $\tau_y$ $[Pa]$ | **k** $Pa.s^n$ | **n** $[-]$ | $\rho$ $[kg/m^3]$ | **Q** $[L/min]$ |
|---|---|---|---|---|---|---|
| 1 | Water | 0 | 0.001 | 1 | 1000 | 477.09 |
| 2 | Glycerin | 0 | 0.205 | 1 | 1237.5 | 244.5 |
| 3 | Carbopol | 1.6 | 0.81 | 0.53 | 1000 | 161.3 |

Table 6.2: 3D computation parameters

#### 6.1.2.3 Height extraction

To extract the height of the free surface, we use the height function method HF, which is a technique for calculating interface normals and curvatures from well-resolved volume fraction data $\alpha_{i,j}$, as illustrated in Figure 6.6. Consider the 2D uniform mesh used for the symmetry plane with sizes $\Delta x \times \Delta z$. For the cell $(i, j)$, illustrated in Figure

6.6, height of the free surface is constructed by summing volume fractions vertically as :

$$h_i = \sum_{j=1}^{N_z} \alpha_{i,j} \Delta z \tag{6.1}$$

where $N_z$ is the number of mesh in the z-direction.

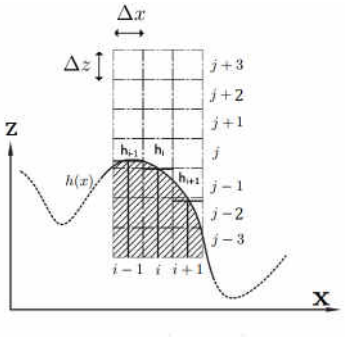


Figure 6.6: Illustration of the HF method to compute the height of the free surface

Therefore, we can plot the 3 heights of fluids extracted from the 3D simulations, as represented in Figure 6.7.

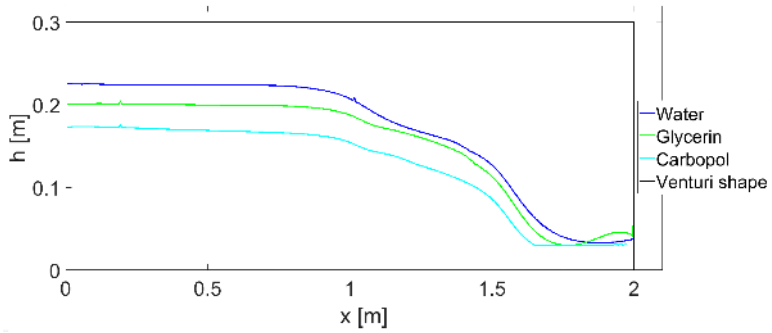


Figure 6.7: Heights of fluid extracted from the 3D simulations

### 6.1.3 1D SWE model

#### 6.1.3.1 1D model inputs/outputs

A 1D model was performed to model the flow through the trapezoidal Venturi flume, using the Shallow Water Equations as described on the 1D model for open channel flow

chapter. To compute steady flow, we focus on the 1D steady SWE model, which is faster and accurate. This model is completed by the friction model, described in friction model section. For computation time cost, we use the 1D version of the friction model for the laminar regime. First, we define the input quantities of the 1D SWE model :

- the flow rate : Q
- the fluid rheology : $\tau_y$, $k$ and $n$
- the density : $\rho$

and the output quantity of the 1D SWE model :

- the height profile in the plane of symmetry of the trapezoidale Venturi flume

Notice that all numerical parameters and models used are described in the 1D model for open channel flow chapter.

#### 6.1.3.2 1D computations

The 1D steady SWE model is so fast and accurate that we can compute quickly all the height profile for any fluids, as shown in Figure 6.8. Or, we can compute all $H_{2/1D}$ for any fluids (where $H_{2/1D}$ is the height computed by the 1D model on the location of the sensor US-2), and get quickly the relation of the height $H_{2/1D}$ vs. the flow rate Q, as shown in Figure 6.9.

### 6.1.4 0D calibrated model

#### 6.1.4.1 0D calibrated model inputs/outputs

A 0D calibrated model was developed to compute the $H_{2/0D}$ for any fluids (where $H_{2/0D}$ is the height computed by the 0D model on the US-2 sensor location). This model is based on calibration using 382 different data. First, we define the input quantities of the 0D calibrated model :

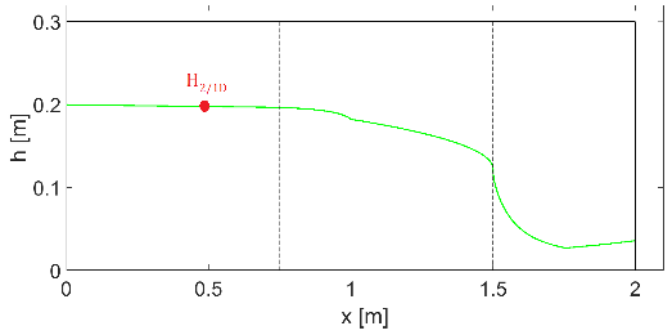


Figure 6.8: 1D computations of the height profile for a Newtonian fluid with $\mu = 0.205cP$ and $\rho = 1237.5Kg/m^3$, and for $Q = 244.5L/min$

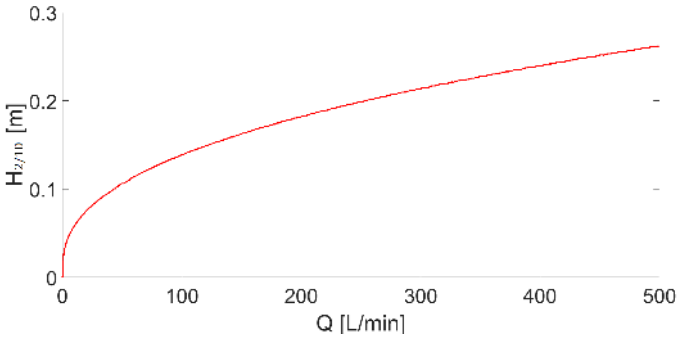


Figure 6.9: 1D computations of the relation $H_{2/1D}$ vs. Q for a Newtonian fluid with $\mu = 0.205cP$ and $\rho = 1237.5Kg/m^3$

- the flow rate : Q
- the fluid rheology : $\tau_y$, $k$ and $n$
- the density : $\rho$
- the initial relation height $H_{2/w}$ vs flow rate Q for water

and the output quantity of the 0D calibrated model :

- the height computed $H_{2/0D}$

Notice that all numerical parameters and models used are described in the experimental flow chapter.

#### 6.1.4.2 0D computations

The 0D calibrated model needs the water data, and also geometrical coefficients calibrated on an other fluid. Thus, it can model the increase of height compared to water, due to the friction. These data can be obtained by a calibration test. Here, we have a water serie of 26 different flow rates and corresponding heights. Thus, we can fit a power law trendline, or we can do a linear interpolation between each points, as shown in Figure 6.10. In this study, we focus on the linear interpolation between each points to get better accuracy. An other solution can be to use the ISO norm [1] which propose a way to get the relation of height in function of the flow rate for a Venturi flume.

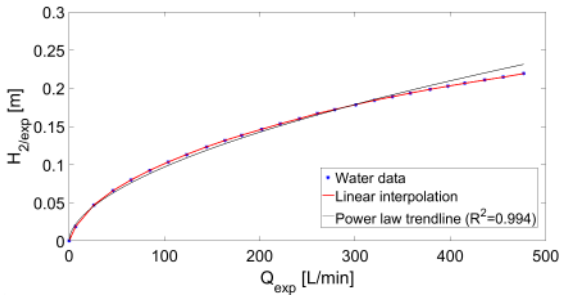


Figure 6.10: Height measured $H_{2/exp}$ versus flow rate $Q_{exp}$ for water data

Having water data, the 0D calibrated model is so fast and accurate that we can compute quickly all height $H_{2/0D}$ for any fluids, as shown in Figure 6.11.

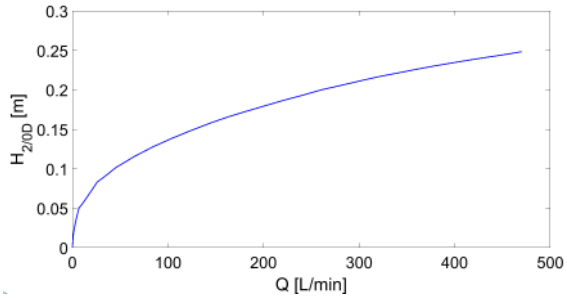


Figure 6.11: 0D computations of the relation $H_{2/0D}$ vs. Q for a Newtonian fluid with $\mu = 0.205cP$ and $\rho = 1237.5Kg/m^3$

## 6.2 Height profile modeled vs. Height profile measured

### 6.2.1 Turbulent Newtonian flow : water

| | |
|---|---|
| **Fluid** : | Water |
| **Concentration/vol** [%] : | 100 |
| **Flowrate** Q $[L/min]$ : | 477.09 |
| **Density** $\rho$ $[Kg/m^3]$ : | 1000 |
| $\tau_y$ $[Pa]$ : | 0 |
| **k** $[Pa.s^n]$ : | 0.001 |
| **n** : | 1 |

Table 6.3: Case 1 : Water flow

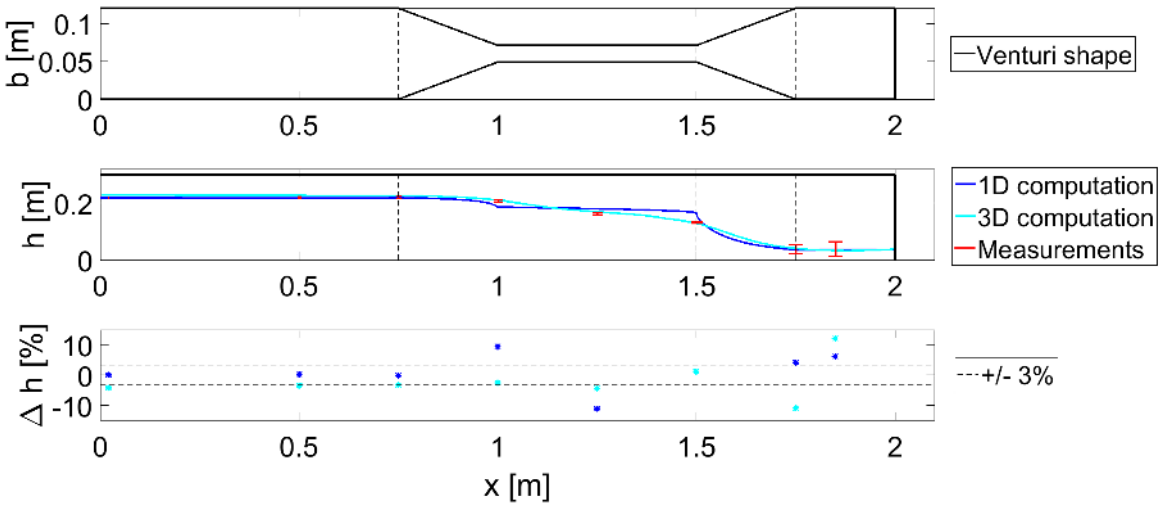


Figure 6.12: Exp. vs. 3D vs. 1D for a water flow with $\mu = 0.001Pa.s$, $\rho = 1000Kg/m^3$ and $Q = 477.09L/min$

The 3D model computes the height profile for the water flow with a good accuracy along all the length. On the other hand, the 1D model computes the height profile for the water flow with a good accuracy except around the critical point. Indeed, the 1D Saint Venant assumption of small streamline curvature is not valid around the critical point where curvatures are not small.

### 6.2.2 Laminar Newtonian flow : glycerin mixture

| | |
|---|---|
| **Fluid** : | Glycerin |
| **Concentration/vol** [%] : | 90 |
| **Flowrate** Q $[L/min]$ : | 244.5 |
| **Density** $\rho$ $[Kg/m^3]$ : | 11237.5 |
| $\tau_{\mathbf{y}}$ $[Pa]$ : | 0 |
| **k** $[Pa.s^n]$ : | 0.205 |
| **n** : | 1 |

Table 6.4: Case 2 : Glycerin flow

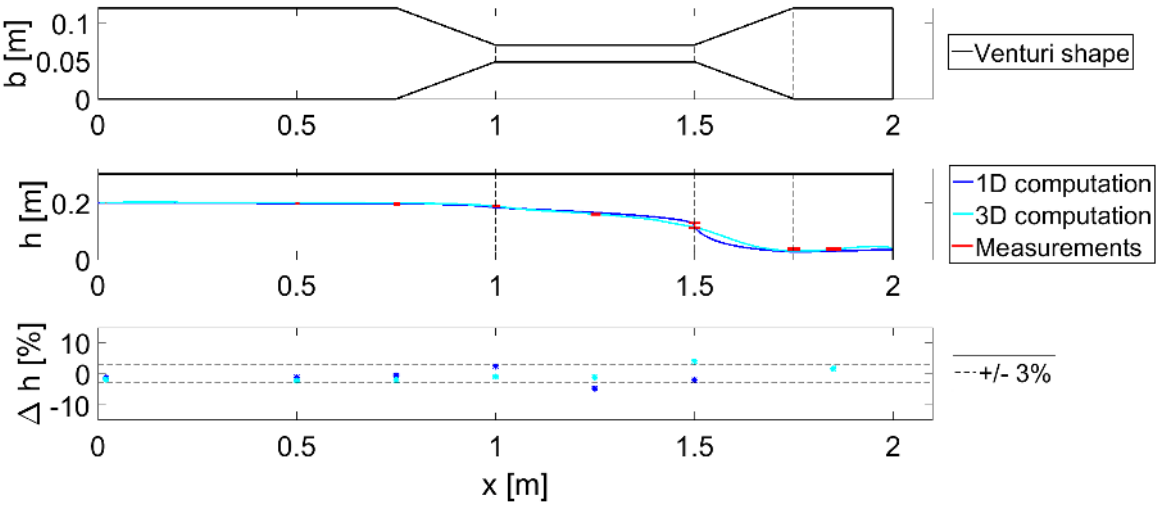


Figure 6.13: Exp. vs. 3D vs. 1D for a glycerin flow with $\mu = 0.205Pa.s$, $\rho = 1237.5Kg/m^3$ and $Q = 244.5L/min$

The 3D model computes the height profile for the laminar Newtonian flow with a good accuracy along all the length. Likewise, the 1D model computes the height profile with a good accuracy, even around the critical point. Indeed, the friction effect limits the curvature on model and on experiments.

### 6.2.3 Laminar non-Newtonian flow : carbopol mixture

| | |
|---|---|
| **Fluid** : | Carbopol |
| **Concentration/vol** [%] : | 0.13 |
| **Flowrate** Q $[L/min]$ : | 161.3 |
| **Density** $\rho$ $[Kg/m^3]$ : | 1000 |
| $\tau_{\mathbf{y}}$ $[Pa]$ : | 1.6 |
| **k** $[Pa.s^n]$ : | 0.81 |
| **n** : | 0.53 |

Table 6.5: Case 3 : Carbopol flow

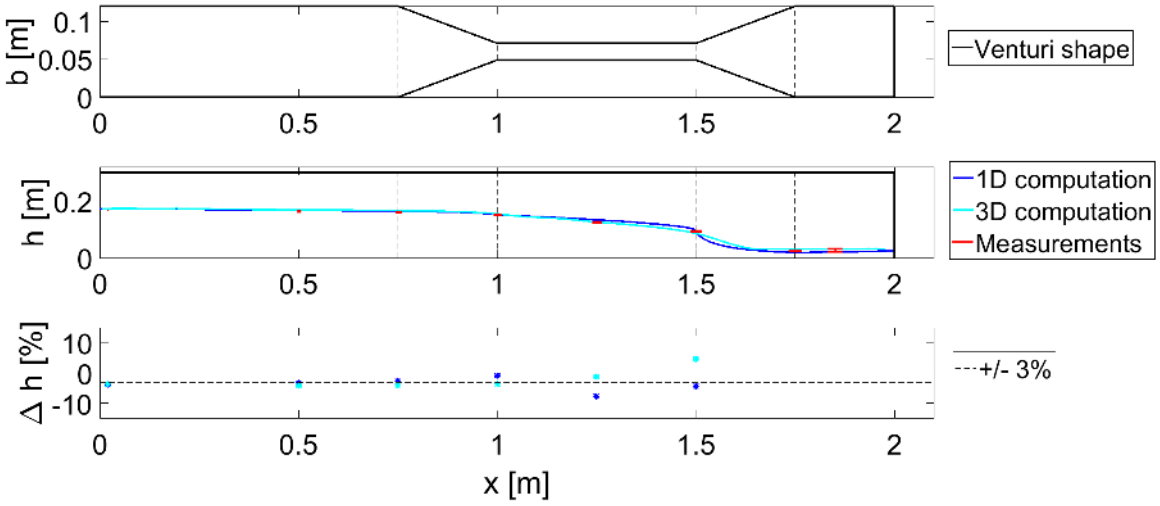


Figure 6.14: Exp. vs. 3D vs. 1D for a Carbopol flow with $\tau_y = 1.6Pa.s$, $k = 0.81Pa.s^n$, $n = 0.53$, $\rho = 1000Kg/m^3$ and $Q = 161.3L/min$

The 3D model computes the height profile for the laminar non-Newtonian flow with a good accuracy along all the length, likewise the 1D model. On downstream, accuracies are not as good because of relative errors and small heights.

## 6.3 Height modeled vs. Height measured

### 6.3.1 Turbulent Newtonian flow : water

| **Designation** : | Water |
|---|---|
| **Fluid** : | Water |
| **Concentration/vol** [%] : | 100 |

Table 6.6: Water case

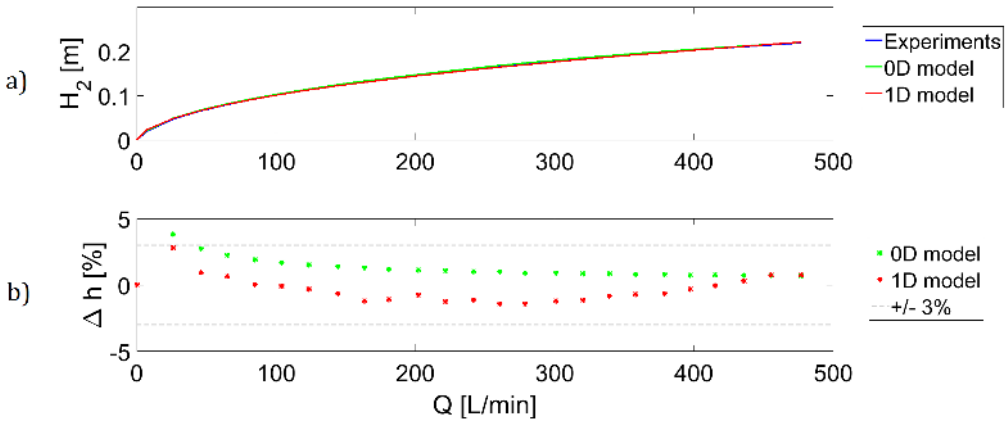


Figure 6.15: a) Upstream height $H_2$ from Experiments , 0D model and 1D model in function of flow rate $Q$ for water data, b) Error on usptream height between Experiments and 0D model, and between Experiments and 1D model.

The 1D model computes the upstream height $H_2$ with a good accuracy for Newtonian turbulent flow, note that the friction is calibrated on Newtonian turbulent measurements. On the other hand, the 0D model computes also the upstream height $H_2$ with a good accuracy, but note that it is based on calibration.

### 6.3.2 Laminar Newtonian flow : glycerin mixture

| | |
|---|---|
| **Designation** : | Gly.3 |
| **Fluid** : | Glycerin |
| **Concentration/vol** [%] : | 90 |

Table 6.7: Gly.3 case

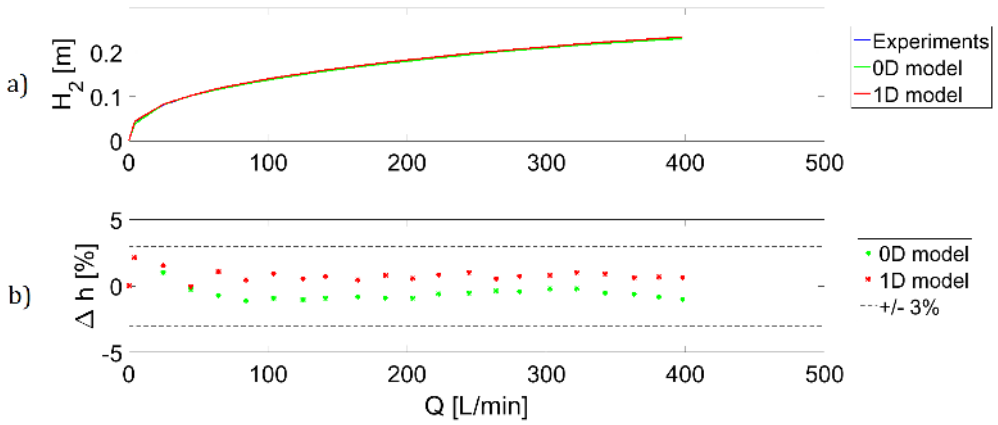


Figure 6.16: a) Upstream height $H_2$ from Experiments , 0D model and 1D model in function of flow rate $Q$ for Gly.3 data, b) Error on usptream height between Experiments and 0D model, and between Experiments and 1D model.

The 1D model computes the upstream height $H_2$ with a good accuracy for Newtonian laminar flow, note that for this computation there is none calibration. On the other hand, the 0D model computes also the upstream height $H_2$ with a good accuracy, but note that it is based on calibration.

### 6.3.3 Laminar non-Newtonian flow : carbopol mixture

| **Designation** : | Carb.1 |
|---|---|
| **Fluid** : | Carbopol |
| **Concentration/vol** [%] : | 0.13 |

Table 6.8: Carb.1 case

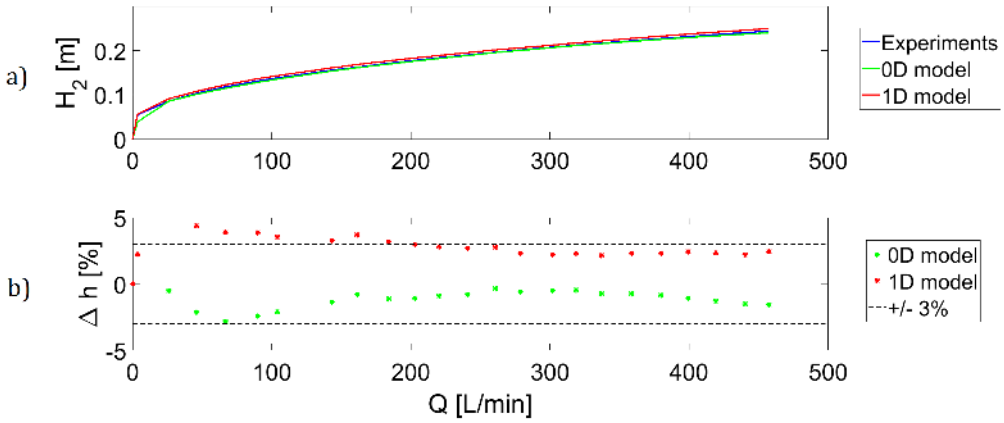


Figure 6.17: a) Upstream height $H_2$ from Experiments , 0D model and 1D model in function of flow rate $Q$ for Carb.1 data, b) Error on usptream height between Experiments and 0D model, and between Experiments and 1D model.

The 1D model computes the upstream height $H_2$ with a good accuracy for non-Newtonian laminar flow, note that for this computation there is none calibration. On the other hand, the 0D model computes also the upstream height $H_2$ with a good accuracy, but note that it is based on calibration.

## CHAPTER VII

# Venturi flume as flow meter for non-Newtonian flows

*The science of today is the technology of tomorrow.*

Edward Teller (1908 - 2003)

## 7.1 Introduction to mud flow metering

Early detection of loss of drilling fluid to the formation or of a kick is the most effective measure that can be taken to eliminate or limit the consequences of such incidents. A prerequisite for detecting loss to the formation or kick during drilling operations is monitoring the mass balance of the well, i.e. the flow of drilling fluid out of the well compared to that pumped into the well. The most basic method of monitoring the flow out of the well while drilling is using simple paddle (Figure 7.1: solution 1), which is an inaccurate measurement that limits the resolution of kick/loss detection. The other solution it to use a Coriolis flow meter (Figure 7.1: solution 2), which is quite an accurate solution but involves expensive installation costs and setup. A possible alternative is to use a Venturi flume (Figure 7.1: solution 3), which is an open channel with a constriction designed to give a jump in the fluid level that holds information about the flow rate. Venturi flumes are typically used to measure large flows of water but rarely used for other fluids. The challenge here is to extend this solution to our drilling application with non-Newtonian muds.

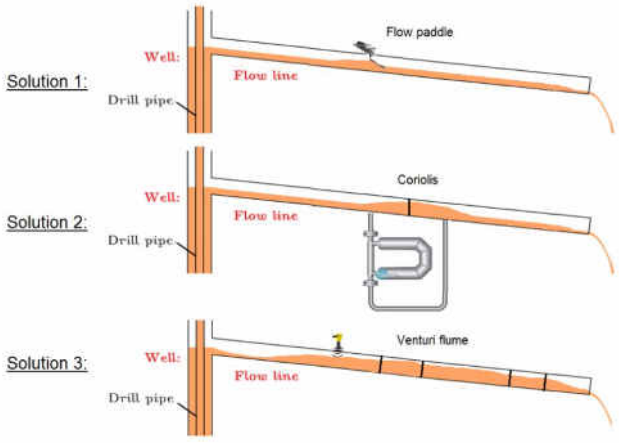


Figure 7.1: Solutions to measure the mud flow out the well

The combination of a Venturi flume with a height sensor is a very reliable method of measuring flows. The set-up can be low cost and provide good overall accuracy. The

height sensor mounted above the flow stream transmits a pulse that is reflected by the surface of the fluid. The elapsed time between sending a pulse and receiving an echo determines the fluid level in the flume. This level measurement is then converted into a flow rate in the meter through the use of a preprogrammed equation specific to the type and size of flume being used, to the density and the rheology of the fluid. For water, the ISO norm 4359 [1] propose a way to find this equation which relate the upstream height measured to the flow rate. This method is limited to water flows. In this study, we built different models able to compute the flow of any fluids throught a Venturi flume but we focus on the 1D steady SWE model. Indeed, the 1D steady SWE model can compute flow of any fluids thought a trapezoidal Venturi flume, but can be extended to all Venturi geometries.

## 7.2 Flow rate measurement

### 7.2.1 Inverse model

The 1D steady SWE model computes height of flows based on flow rate measurement, and needs to be inversed to compute the flow rate based on height measurement. The inverse model is based on optimization model which adjust the flow rate to match the height computed with the height measured, as described in Figure 7.2.

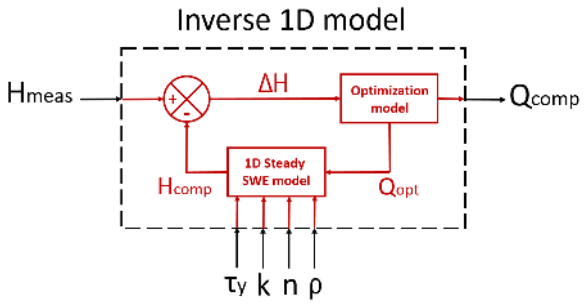


Figure 7.2: Structure of the inverse 1D steady SWE model

### 7.2.2 Accuracy

Figure 7.3 represents the error on flow rate between the 1D steady SWE inverse model and the experiments for all fluids (Newtoniand and non-Newtonian). For $Q$>250L/min, the accuracy of the Venturi flume flow meter can be taken as 5%. For $Q$<250L/min, the accuracy has to be absolute and is equal to 15L/min.

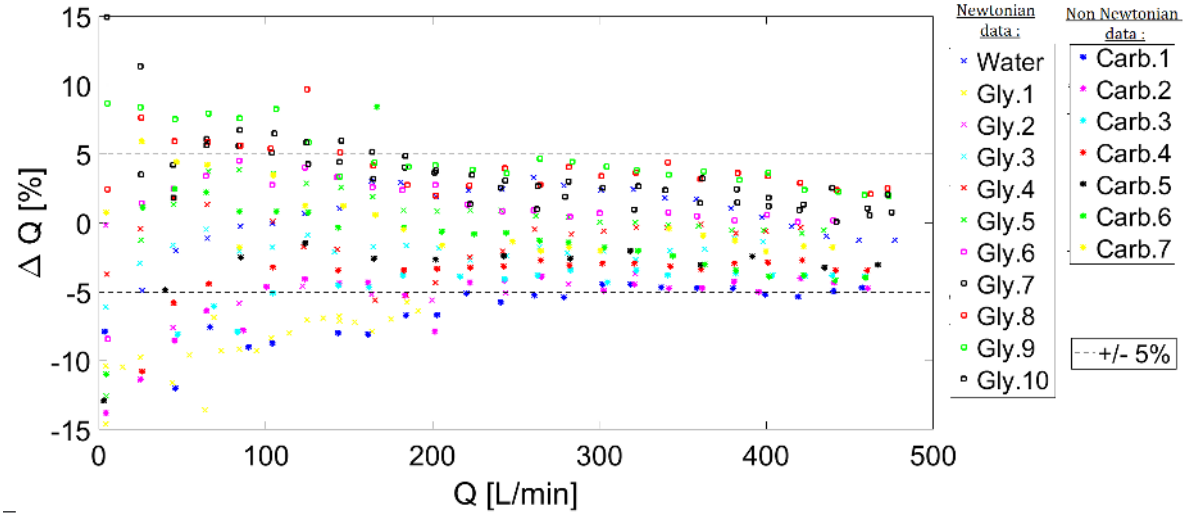


Figure 7.3: Error between the flow rate computed by the inverse 1D steady SWE model and the flow rate measured during experiments, for Newtonian and non-Newtonian data

### 7.2.3 Sensitivity analysis

The sensitivity of the model is very important for the accuracy improvement. We can know which parameter is more important than another. Indeed, first with the inverse 1D steady SWE model, we can know the impact on the flow rate for a rheology, density and height variation. This is interesting to estimate the error on the flow rate measurement due to the error of input measurements. In the other hand, we can know the impact on the flow rate for a geometry variation. This is interesting for the shape optimization to built the shape and size which is the better one for accuracy performance. Thus, for

the three cases described on Table 7.1. , Figures 7.4 and 7.5 represent respectively the sensitivity of the Venturi flow meter on physical and geometrical quatities. We can see the variation on flow rate due to each quantities variation.

| **Case** | **Fluid** | $\tau_y$ $[Pa]$ | **k** $Pa.s^n$ | **n** $[-]$ | $\rho$ $[kg/m^3]$ | **Q** $[L/min]$ |
|---|---|---|---|---|---|---|
| 1 | Water | 0 | 0.001 | 1 | 1000 | 477.09 |
| 2 | Glycerin | 0 | 0.205 | 1 | 1237.5 | 244.5 |
| 3 | Carbopol | 1.6 | 0.81 | 0.53 | 1000 | 161.3 |

Table 7.1: Three characteristic cases of computations

Due to the non linearity of the problem, computations are done with 3 characteristic cases which describe turbulent and laminar regime of Newtonian flow, and laminar regime of non-Newtonian flow, summarized in Table 7.1. Figure 7.4 shows the response on flow rate due to a height, a rheology or a density variation. Figure 7.5 shows the response on flow rate due to a width, a side slope or a length variation.

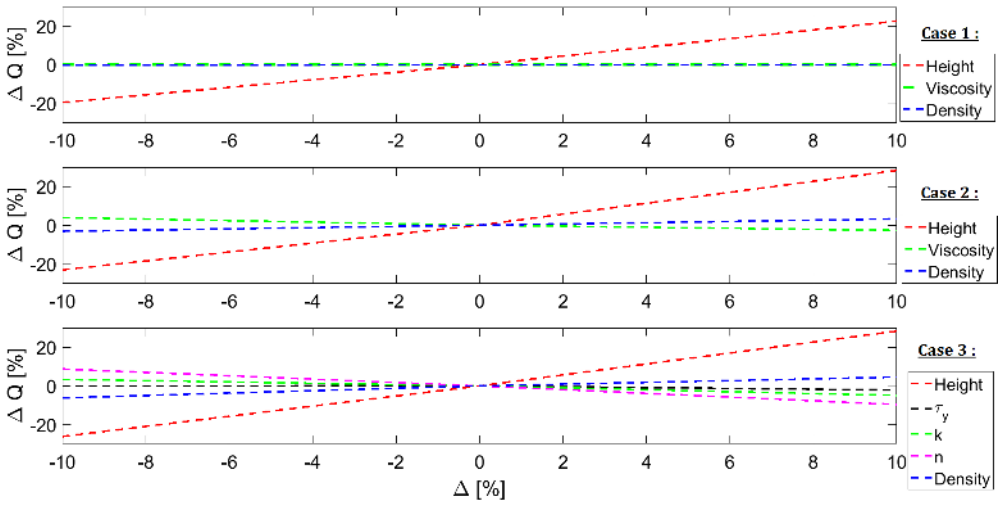


Figure 7.4: Sensitivity of the flow rate in function of height, viscosity and density.

The sensitivity of the model is approximated and summarized in Table 7.2.

In term of flow metering, we have to be accurate on height measurement. Indeed, a variation on height of 10% causes a variation on the flow rate of 30%. We have also to be careful on the width, indeed the flow rate is the most dependent on the channel

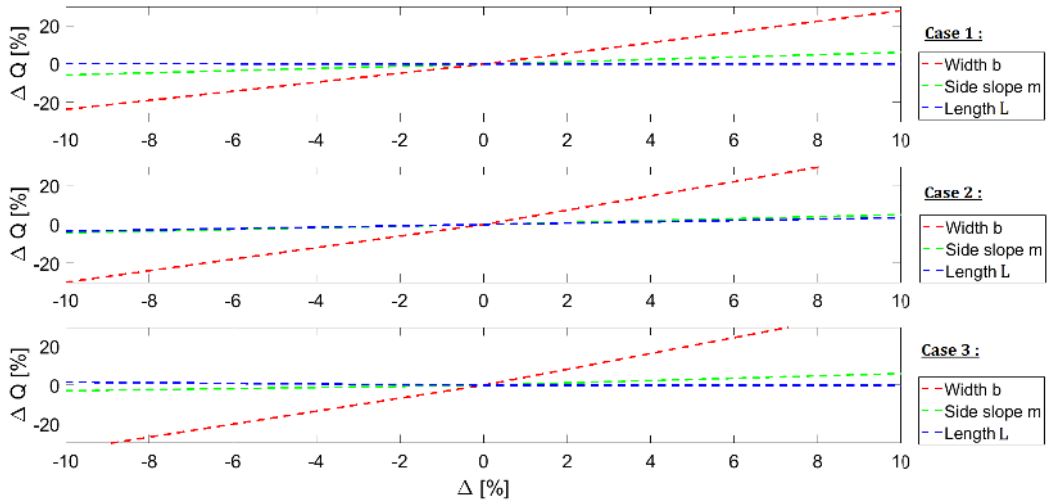


Figure 7.5: Sensitivity of the flow rate in function of width b, side slope m and length L

| Quantitie | Variation | Variation on Q |
|---|---|---|
| h | +10% | +30% |
| $\mu$ | +10% | −5% |
| $\rho$ | +10% | +5% |
| b | +10% | +40% |
| m | +10% | +5% |
| L | +10% | +0% |

Table 7.2: Sensitivity of the flow rate Q to each quantities

width. The sedimentation, which affect the height or the channel width, is very harmful for this kind of device.

## 7.3 New design for mud flow metering

With the goal of saving space in the flow line, a new geometry of Venturi was studied: H flume, shown in Figure 7.6. The H flume, so called because it was the eighth in a series of flumes investigated, combined the flow sensitivity of a narrow angle V-notch weir with the flat floor and self-cleaning properties of a flume. The H series of flumes are more modified weirs than a true flumes, with a V-shaped throat and no diverging section. The H flume design allows a wider range of flows than any other flume type,

providing low flow sensitivity as well as the ability to measure high flow rates. The constraint of using a H flume is on the need of free spilling downstream condition. This will be verified by putting it just before the tank and shale shakers.

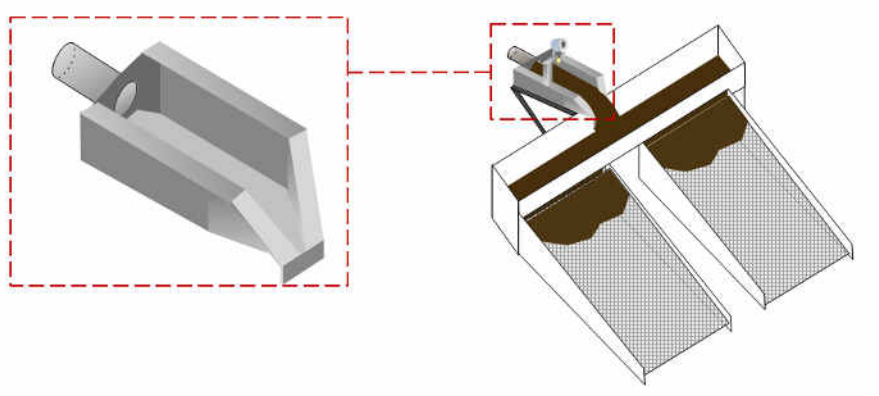

Figure 7.6: H flume in its environment

### 7.3.1 H flume geometry

Based on H flume dimensions existing, we designed own H flume shape which is able to measure the real range of flow rate from 5 to $6000 L/min$. These dimensions are based on the 2 foot H flume table. It has a throat width of 2.4" and a channel width of $3 ft$. All dimensions are shown in Figure 7.7 in the international system of units.

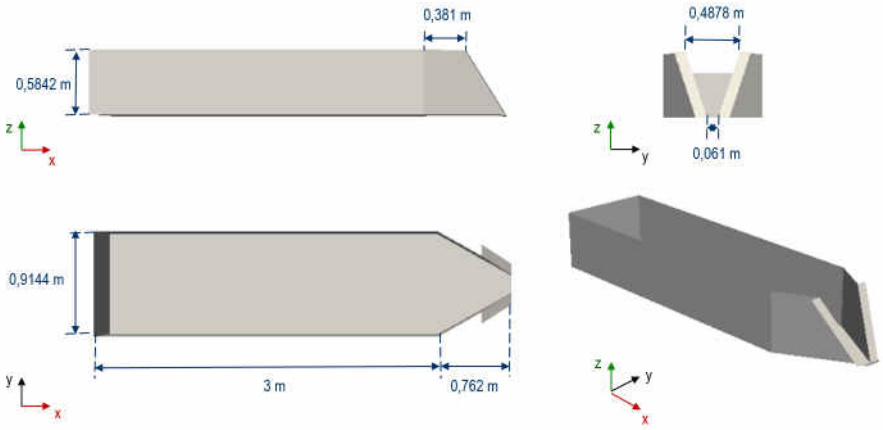


Figure 7.7: H flume dimensions

### 7.3.2 Numerical experiments

Experiments with this geometry may be interessant but for reason of time and budget, we used CFD which shows its interest. In a previous part, we showed the relevance of using the 3D CFD to model a flow through a Venturi flume. Based on this study, we developed a 3D model with the H flume geometry. The big change between the 3D model of the trapezoidal Venturi flume and the 3D model of the H flume is the adding of the tank. Indeed, the critical point may be around the throat and so we can not impose a boundary condition on it, then the adding of the tank allows a free spilling condition at the end of the H flume.

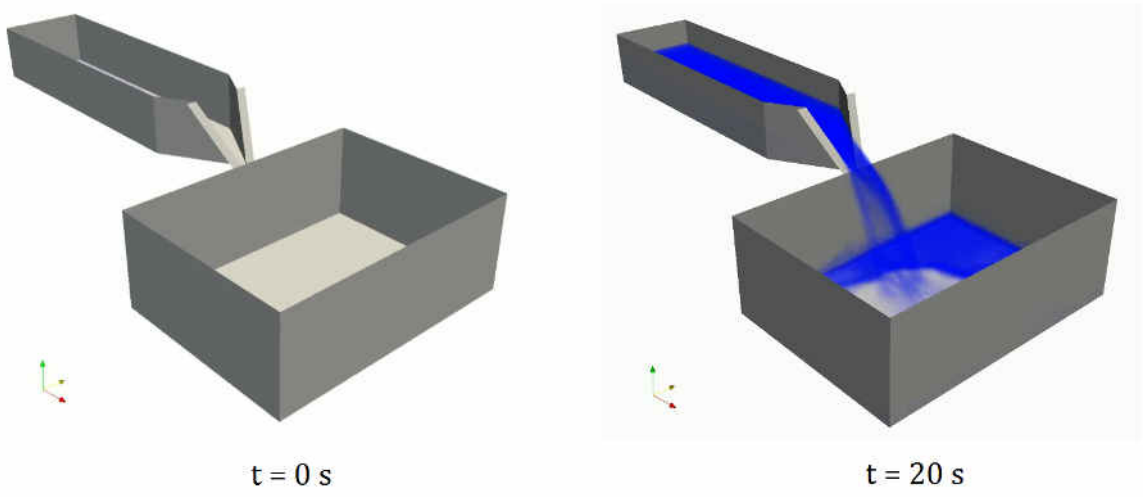


Figure 7.8: CFD computations of water flow through the H flume

### 7.3.3 Flow computation

#### 7.3.3.1 Newtonian turbulent flow

| | |
|---|---|
| **Fluid** : | Water |
| **Flowrate** Q $[L/min]$ : | 3000 |
| **Density** $\rho$ $[Kg/m^3]$ : | 1000 |
| $\tau_{\mathbf{y}}$ $[Pa]$ : | 0 |
| **k** $[Pa.s^n]$ : | 0.001 |
| **n** : | 1 |

Table 7.3: Case 1 : Newtonian turbulent flow

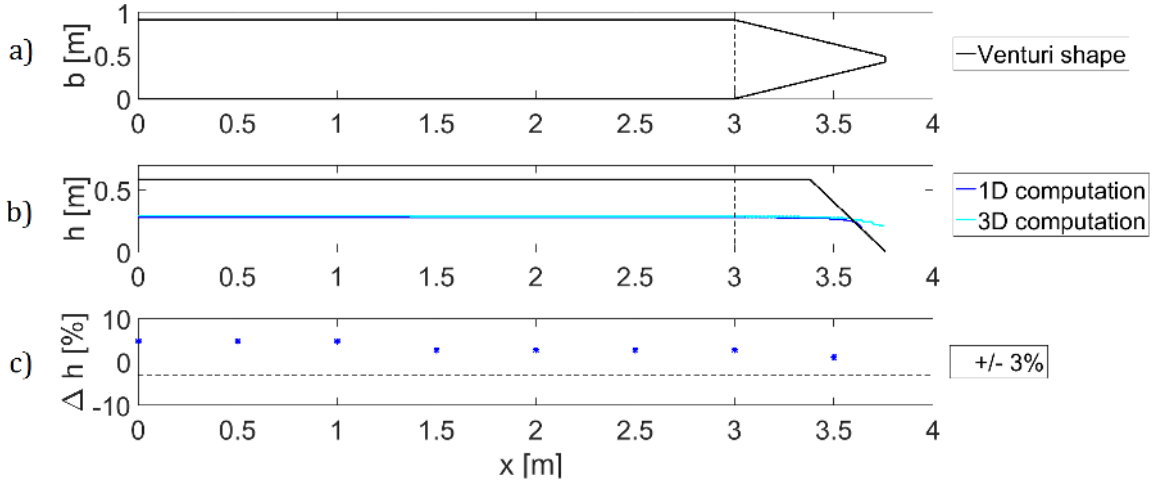


Figure 7.9: a) Venturi shape, b) 3D vs. 1D model comparison for a Newtonian turbulent flow with $\mu = 0.001Pa.s$, $\rho = 1000Kg/m^3$ and $Q = 3000L/min$, c) Error between 3D and 1D model on eight height along the Venturi flume

3D model and 1D model results are very close for turbulent Newtonian flow computation.

### 7.3.4 Newtonian laminar flow

| | |
|---|---|
| **Fluid** : | [ - ] |
| **Flowrate** Q $[L/min]$ : | 3000 |
| **Density** $\rho$ $[Kg/m^3]$ : | 1000 |
| $\tau_{\mathbf{y}}$ $[Pa]$ : | 0 |
| **k** $[Pa.s^n]$ : | 0.6 |
| **n** : | 1 |

Table 7.4: Case 2 : Newtonian laminar flow

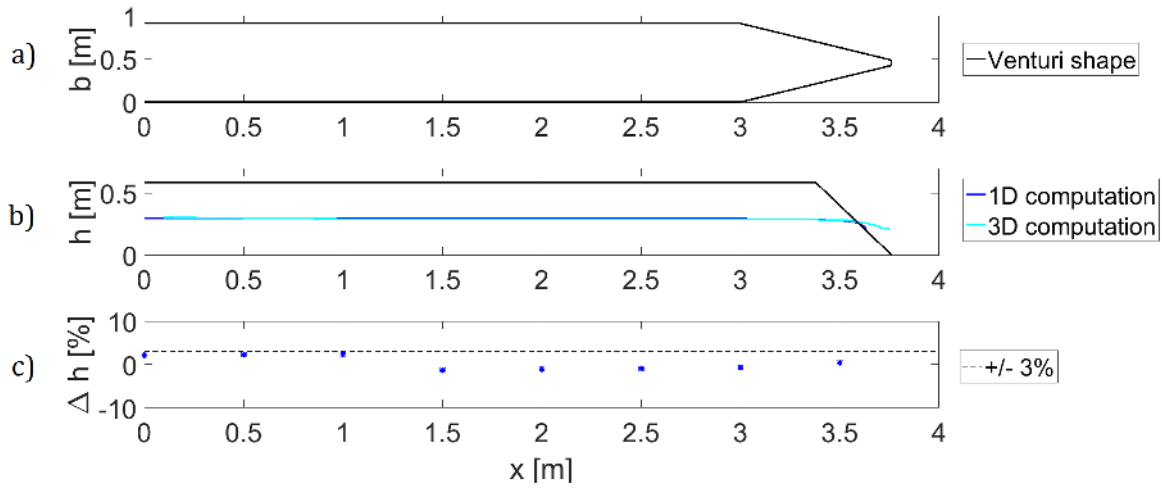


Figure 7.10: a) Venturi shape, b) 3D vs. 1D model comparison for a Newtonian laminar flow with $\mu = 0.6Pa.s$, $\rho = 1000Kg/m^3$ and $Q = 3000L/min$, c) Error between 3D and 1D model on eight height along the Venturi flume

3D model and 1D model results are also very close for laminar Newtonian flow computation.

### 7.3.5 Non-Newtonian laminar flow

| | |
|---|---|
| **Fluid** : | Rheliant mud |
| **Flowrate** Q $[L/min]$ : | 3000 |
| **Density** $\rho$ $[Kg/m^3]$ : | 1845 |
| $\tau_{\mathbf{y}}$ $[Pa]$ : | 2.8 |
| **k** $[Pa.s^n]$ : | 0.061 |
| **n** : | 0.9 |

Table 7.5: Case 3 : non-Newtonian laminar flow

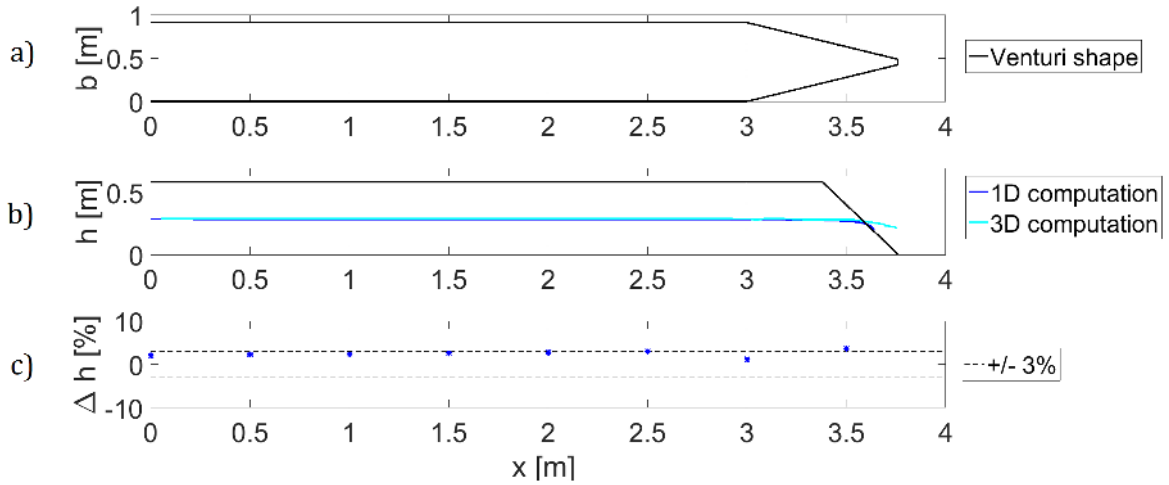


Figure 7.11: a) Venturi shape, b) 3D vs. 1D model comparison for a non-Newtonian laminar flow with $\tau_y = 2.8Pa.s$, $k = 0.061Pa.s^n$, $n = 0.9$, $\rho = 1845Kg/m^3$ and $Q = 3000L/min$, c) Error between 3D and 1D model on eight height along the Venturi flume

3D model and 1D model results are also very close for laminar non-Newtonian flow computation.

### 7.3.6 Accuracy

Table 7.6 summarizes results from 3D and 1D models. 3D model has been validated for open channel flow along a Venturi flume in a previous part. The purpose here is to take it as reference, and then quantify the accuracy of the 1D model. Thus, the 1D model has an accuracy around 4%. This kind of results is similar for what we found for the trapezoidal geometry.

| **Case** | **Fluid** | $\tau_{\mathbf{y}}$ $[Pa]$ | **k** $Pa.s^n$ | **n** $[-]$ | $\rho$ $[kg/m^3]$ | $\mathbf{Q_{3D}}$ $[L/min]$ | $\mathbf{Q_{1D}}$ $[L/min]$ | $\mathbf{\Delta Q}$ [%] |
|---|---|---|---|---|---|---|---|---|
| 1 | Water | 0 | 0.001 | 1 | 1000 | 3000 | 3180 | 6 |
| 2 | Viscous fluid | 0 | 0.6 | 1 | 1000 | 3000 | 2280 | 4 |
| 3 | Rheliant mud | 2.8 | 0.061 | 0.9 | 1845 | 3000 | 3030 | 1 |

Table 7.6: 3 characteristic cases of computations with the H flume geometry

## CHAPTER VIII

# Conclusions and recommendations

*The only exercise I excel at is jumping to conclusions.*

James Nathan Miller

## Conclusion

During drilling operations, the flow out the well has to be monitored. Thus, a flow meter has to be installed in the return line. Due to the current market, a Venturi flume can be an interesting accurate and cheap solution for monitoring the flow out the well. Even if it appears as a very good solution, this device is only used for water flows. Thus, we developed different works to extended this solution to mud flows.

Knowing the importance of experiments, a large experimental database was compiled. Indeed, we have circulated Newtonian and non-Newtonian through a trapezoidal Venturi flume. The database is composed by eighteen different fluids. During experiments, we measured flow rates and eight heights at different locations along the Venturi flume. This allowed us to estimate the height profile through the open channel for each fluids. In order to extract useful informations from these experiments, the fluid properties have to be know. For this purpose, the experiments were completed by rheology measurements.

To model the flow, a first approach may is 3D CFD. Using OpenFOAM software, 3D simulations were performed to capture the transcritical transition through the trapezoidal Venturi flume for different fluids. This 3D model was validated by comparison with experimental data. It appears robust enough to extend simulations for other geometries of Venturi and real mud properties, in order to perform real case simulations.

In the context of flow metering, we need an accurate and fast model. Thus, a simplified 1D model based on the Saint Venant Equations (SVE) has been developed with a sub-model for the friction. Two strategies were done to solve these 1D Saint Venant Equations. First, we solved them in their unsteady form using finite volume method. Next, we solved them in their steady state form using the method of singular point. These two methods have different advantages. The unsteady case allows simulating the

time evolution of the hydraulic jump and the transcritical transition along the flume. The steady state on the other hand does not give access to the transient regime but allows to extract accurately the steady state solution on a very short computational time. These two strategies were compared and converged for the same steady state results. Finally, 1D SVE solutions were found to be in good agreement with the experiments and with the 3D CFD model, but using an additional sub-model for the friction.

The development of a sub-model for the wall friction was an important step, because it expresses the impact of rheology on the flow characteristics. This sub-model of friction was performed in 1D and 2D,. The 1D version gives fast and good results, and the 2D version was found to give good agreement with the experiments done in rectangular open channel by Haldenwang [28]. The friction model computes the friction with taking into account the geometry of the channel and the rheology of the fluid.

Using the 1D steady state SVE model completed by the 1D sub-model of the friction, we built an inverse model able to compute quickly and accurately the flow rate based on upstream height, density and rheology measurements. Thus, we extended the use of Venturi device as a flow meter for different fluids: Newtonian and non-Newtonian. The accuracy of the device was found to be 5% for the high half of the flow rate range. This flow meter was found as an accurate and cheap solution provided avoiding sedimentation or anything affecting the upstream height or the throat geometry.

Considering the good agreement between experiments with 1D SVE models and 3D CFD model for the trapezoidal Venturi flume, we extended this work to another shape: H-flume. This shape appears as more adapted for some rig configurations. Thus, we performed 3D CFD and 1D SVE simulations which shown very close results. We concluded on the relevance of use 1D SVE model with the 1D sub-model of friction to model accurately non-Newtonian flows through Venturi flumes.

## Recommendations

From the outcomes achieved during this research the following recommendations can be made.

- The large experimental database compiled during this research can be used by future researchers and enginneers to further increase the understanding of non-Newtonian open channel flow through a trapezoidal Venturi flume.
- The 3D CFD model developed during this work can be used to model flow through other type of Venturi flumes.
- The 1D SVE models can be adapted to model flows through Venturi flumes, but with less accuracy around the critical point with large streamline curvatures (limitation of SVE)
- The 1D sub-model of friction appears as accurate and fast to estimate friction and momentum coefficients. But a 2D friction model was performed and compared to experimental data.
- The Venturi flume is clearly an accurate and cheap solution to measure flow rates in open channels, but limiting sedimentation.

Despite the excellent agreement of the 1D SVE model with the experimental data found for the trapezoidal Venturi flume, further work is still needed to explored effect of the yield stress. Indeed, experiments were performed for fluids with little yield stress.

The Venturi flume is an accurate and cheap solution to measure mud flow rates out the well, but limiting by sedimentation. A solution can be to inclined the flume but the gravity term has to be taking into account in the SVE. This part has been explored and gives good results. Another improvement would be to be dispensed of the rheology measurements. Indeed during drilling, mud properties can change at any time. A solution can be to have a real time rheometer. But another solution can be to measure

another(s) specific height(s) through the Venturi flume and eliminated the unknown(s) of rheology.

## Conclusion

Au cours des opérations de forage, le débit de boue sortant du puits doit être surveillé. Ainsi, un débitmètre doit être installé dans la conduite de retour. En raison du marché actuel, un canal Venturi peut être une solution précise et peu couteuse intéressante pour surveiller le débit de boue sortant du puits. Même si il apparaît comme une très bonne solution, ce dispositif est utilisé uniquement pour mesurer les débits d'eau. Ainsi, nous avons développé différents travaux afin d'étendre cette solution à des écoulements de boue.

Connaissant l'importance des expériences, une grande base de données expérimentales a été élaboré. En effet, nous avons fait circuler des fluides Newtonien et non-Newtonien à travers un canal Venturi trapézoïdal. La base de données est composé de dix-huit fluides différents. Lors des essais, nous avons mesuré les débits et huit hauteurs situé à différents emplacements le long du canal de Venturi. Cela nous a permis d'estimer le profil de hauteur le long du canal ouvert pour chaque fluides. Afin d'extraire toutes les données utiles des expériences, les propriétés des fluides doivent être connu. Pour cela, les expériences ont été complétées par la mesure de rhéologie de chaque fluides.

Pour modéliser l'écoulement, la première approche a été la CFD 3D. Avec l'utilisation d'un logiciel open source de CFD: OpenFOAM, des simulations 3D ont été réalisées afin de capturer la transition transcritique à travers le canal Venturi pour différents fluides. Ce modèle 3D a été validé par la comparaison avec les données expérimentales. Il apparait assez robuste pour étendre les simulations 3D à d'autres géométries de Venturi ainsi qu'à des fluides représentant de réelles boues, et cela dans le but d'effectuer des simulations de cas réels.

Dans le cadre de la mesure du débit, il faut un modèle précis et rapide. Ainsi, un modèle simplifié 1D basé sur les équations de Saint Venant (listé SVE) a été développé complété par un sous-modèle de frottement. Deux stratégies ont été faites pour résoudre ces équations 1D de Saint Venant. Tout d'abord, nous les avons résolu dans leur forme instationnaire en utilisant la méthode des volumes finis. Ensuite, nous les avons résolu dans leur forme stationnaire en utilisant la méthode du point singulier. Ces deux méthodes présentent des avantages différents. Le cas instationnaire permet de simuler l'évolution temporelle du ressaut hydraulique et de la transition transcritique le long du canal. D'autre part, l'état stationnaire ne donne accès au régime transitoire, mais permet d'extraire avec précision la solution d'état stable avec un temps de calcul très court. Ces deux stratégies ont été comparées et convergent vers les mêmes solutions stationnaires. Enfin, les solutions 1D SVE ont été jugées en bon accord avec les expériences et avec le modèle 3D CFD, et cela en utilisant un sous-modèle supplémentaire pour le frottement.

Le développement d'un sous-modèle, pour le frottement le long des parois, était une étape importante car elle exprime l'impact de la rhéologie sur les caractéristiques de l'écoulement. Ce sous-modèle de frottement a été réalisée en 1D, puis étendue au 2D. La version 1D donne de bons résultats mais est intéressante pour sa rapidité de calcul. Par contre la version 2D, étant en parfait accord avec les expériences réalisées par Haldenwang [28] le long d'un canal rectangulaire, s'avère précise mais couteuse en temps de calcul. Ainsi, l'élaboration d'un tel modèle de friction permet de simuler le frottement le long des parois en prenant en compte la géométrie du canal ainsi que la rhéologie du fluide.

En utilisant le modèle 1D SVE stationnaire complété du sous-modèle 1D de friction, nous avons pu construire un modèle inverse capable de calculer rapidement et avec précision le débit, et ceci en fonction de la hauteur en amont, la densité et la rhéologie du fluide. Ainsi, nous avons pu étendre l'utilisation d'un tel dispositif comme débitmètre pour différents fluides: Newtoniens et non-Newtoniens. La précision de l'appareil a été évalué à 5% pour la moitié haute de la plage de débit. Ce débitmètre s'avère donc comme une solution précise et peu chère, à condition d'éviter la sédimentation le long du canal et tout ce qui perturberait la hauteur en amont ou la géométrie de la gorge.

Compte tenu de la bonne concordance des expériences, du modèles 1D SVE et du modèle 3D CFD pour le canal Venturi à section trapézoïdal, nous avons choisi d'étendre ce travail à une autre forme de Venturi: H-flume. Cette forme apparaît comme plus adapté pour certaines configurations de plate-forme. Ainsi, nous avons réalisé différentes simulations avec le modèle CFD 3D et le modèle 1D SVE, qui ont présenté des résultats très proches. Nous avons alors conclu sur la pertinence de l'utilisation d'un modèle 1D SVE complété par un sous-modèle 1D de friction pour modéliser avec précision les écoulements non-Newtoniens les long des canaux Venturi.

## Recommandations

A partir des résultats obtenus au cours de cette recherche, les recommandations suivantes peuvent être faites.

- La large base de données expérimentales compilées au cours de cette recherche peut être utilisée par de futurs chercheurs et ingénieurs afin d'affiner la compréhension des écoulements non-Newtonien le long des canaux Venturi.
- Le modèle CFD 3D développé au cours de ce travail peut être utilisé pour modéliser l'écoulement à travers différentes formes de canaux Venturi.
- Les modèles SVE 1D peuvent être utilisé pour modéliser les écoulements le long des canaux Venturi, mais avec moins de précision autour du point critique et cela du à d'importantes courbures des lignes de courant (limitation des equations de Saint Venant)
- Le sous-modèle 1D de frottement s'avère précis et rapide pour estimer les coefficients de friction et de profile de vitesse le long d'une géométrie variable. Un modèle 2D de friction a été réalisé et validé par des données expérimentales [**?** ].
- Le canal Venturi se place clairement comme une solution précise et peu couteuse pour mesurer les écoulement le long de canaux ouverts, mais limité par le phénomène de sédimentation ou tout autre phénomène qui affecterait la hauteur en amont ou la géométrie de la gorge.

En dépit de l'excellent accord du modèle SVE 1D et des données expérimentales établies pour les canaux Venturi à sections trapézoïdales, d'autres travaux sont encore nécessaires pour étudier et mieux comprendre l'effet de la contrainte seuil de certains fluides. En effet, des expériences ont été réalisées seulement pour les fluides avec peu de contraintes seuils.

Le canal Venturi s'avère donc comme une solution précise et peu couteuse pour mesurer des débits de boue en sortie de puits, mais est limitée par le phénomène de sédimentation. Une solution à cela pourrait être l'inclinaison du canal, mais cela devra entrainer la prise en compte du terme de gravité dans les équations de Saint Venant. Cette partie a été explorée et a montré des résultats encourageants. Une amélioration de ce débitmètre consisterait à se passer des mesures de rhéologie. En effet au cours du forage, les propriétés de boue peuvent changer à tout moment. Une solution pourrait consister en l'ajout d'un rhéomètre qui permettrait de mesurer la rhéologie des boues en temps réel. Une deuxième solution, moins couteuse, pourrait être de mesurer une ou plusieurs autres hauteurs spécifiques à travers le canal Venturi et ainsi éliminer les inconnues de la rhéologie.

# WORK DONE

PAPERS :

- O. Thual, L. Lacaze, M. Mouzouri and B. Boutkhamouine. Critical slope for laminar transcritical shallow-water flows [1]. *Journal of Fluid Mechanics*, 2015
- M. Mouzouri, O. Thual, L. Lacaze and P. Varadarajan. 1D steady state Saint Venant model for mud flow in Venturi flumes [2]. *Schlumberger Journal of Modelling and Simulation*, 2016
- O. Guillet, O. Thual, L. Lacaze and M. Mouzouri. Frottement pariétal et glissement d'un écoulement viscoplastique ouvert. *22ème congrès français de Mécanique*, 2015
- M. Mouzouri and P. Varadarajan. CFD with OpenFoam to Simulate Non-Newtonian Mud Flow in a Venturi Flume. *Schlumberger Fluid Mechanics SIG Newsletter*, 2016
- M. Mouzouri and P. Varadarajan. Open Channel Flow Measurement Using A Venturi Flume. *Schlumberger Fluid Mechanics SIG Newsletter*, 2015

SEMINARS :

- M. Mouzouri. Mud flow in Venturi flume. *Modelling and Simulation Eureka Workshop*, 2016
- M. Mouzouri. Mud flow in Venturi flume. *Schlumberger Fluid Mechanics SIG Webinar*, 2016
- M. Mouzouri. Venturi flume as a new low cost and accurate flowmeter for kick and loss detection during drilling. *Schlumberger Symposium*, 2015 (winner of the best abstract video)

[1] Appendix B
[2] Appendix C

# APPENDICES

# APPENDIX A

# Dataset

| **N°** | **Q** $[L/min]$ | $\tau_{\mathbf{y}}$ $[Pa]$ | **k** $Pa.s^n$ | **n** $[-]$ | $\rho$ $[kg/m^3]$ | **US1** $[m]$ | **US2** $[m]$ | **US3** $[m]$ | **US4** $[m]$ | **US5** $[m]$ | **US6** $[m]$ | **US7** $[m]$ | **US8** $[m]$ |
|---|---|---|---|---|---|---|---|---|---|---|---|---|---|
| 1 | 6.9 | 0.0 | 0.001 | 1.00 | 1000.0 | 0.018 | 0.019 | 0.019 | 0.017 | 0.012 | 0.010 | 0.008 | 0.026 |
| 2 | 26.1 | 0.0 | 0.001 | 1.00 | 1000.0 | 0.046 | 0.047 | 0.047 | 0.043 | 0.034 | 0.026 | 0.015 | 0.023 |
| 3 | 46.1 | 0.0 | 0.001 | 1.00 | 1000.0 | 0.066 | 0.066 | 0.067 | 0.061 | 0.049 | 0.037 | 0.019 | 0.025 |
| 4 | 65.0 | 0.0 | 0.001 | 1.00 | 1000.0 | 0.080 | 0.080 | 0.080 | 0.074 | 0.056 | 0.046 | 0.019 | 0.026 |
| 5 | 84.8 | 0.0 | 0.001 | 1.00 | 1000.0 | 0.093 | 0.093 | 0.093 | 0.087 | 0.064 | 0.054 | 0.018 | 0.034 |
| 6 | 104.0 | 0.0 | 0.001 | 1.00 | 1000.0 | 0.104 | 0.103 | 0.104 | 0.097 | 0.071 | 0.060 | 0.020 | 0.032 |
| 7 | 123.5 | 0.0 | 0.001 | 1.00 | 1000.0 | 0.114 | 0.113 | 0.114 | 0.107 | 0.078 | 0.066 | 0.026 | 0.039 |
| 8 | 144.4 | 0.0 | 0.001 | 1.00 | 1000.0 | 0.124 | 0.123 | 0.124 | 0.117 | 0.086 | 0.072 | 0.018 | 0.016 |
| 9 | 163.5 | 0.0 | 0.001 | 1.00 | 1000.0 | 0.132 | 0.132 | 0.132 | 0.125 | 0.092 | 0.076 | 0.018 | 0.017 |
| 10 | 181.0 | 0.0 | 0.001 | 1.00 | 1000.0 | 0.139 | 0.138 | 0.139 | 0.131 | 0.097 | 0.081 | 0.020 | 0.018 |
| 11 | 202.1 | 0.0 | 0.001 | 1.00 | 1000.0 | 0.147 | 0.146 | 0.147 | 0.138 | 0.103 | 0.085 | 0.022 | 0.022 |
| 12 | 221.7 | 0.0 | 0.001 | 1.00 | 1000.0 | 0.154 | 0.153 | 0.154 | 0.145 | 0.108 | 0.090 | 0.023 | 0.020 |
| 13 | 241.7 | 0.0 | 0.001 | 1.00 | 1000.0 | 0.160 | 0.160 | 0.160 | 0.151 | 0.113 | 0.093 | 0.027 | 0.023 |
| 14 | 260.6 | 0.0 | 0.001 | 1.00 | 1000.0 | 0.167 | 0.167 | 0.167 | 0.157 | 0.118 | 0.097 | 0.026 | 0.026 |
| 15 | 278.9 | 0.0 | 0.001 | 1.00 | 1000.0 | 0.172 | 0.172 | 0.172 | 0.162 | 0.122 | 0.100 | 0.028 | 0.025 |
| 16 | 300.8 | 0.0 | 0.001 | 1.00 | 1000.0 | 0.179 | 0.179 | 0.179 | 0.168 | 0.127 | 0.105 | 0.030 | 0.027 |
| 17 | 320.2 | 0.0 | 0.001 | 1.00 | 1000.0 | 0.184 | 0.184 | 0.184 | 0.173 | 0.132 | 0.108 | 0.032 | 0.028 |
| 18 | 339.2 | 0.0 | 0.001 | 1.00 | 1000.0 | 0.188 | 0.189 | 0.189 | 0.177 | 0.136 | 0.111 | 0.032 | 0.027 |
| 19 | 358.1 | 0.0 | 0.001 | 1.00 | 1000.0 | 0.193 | 0.194 | 0.194 | 0.182 | 0.140 | 0.114 | 0.034 | 0.029 |
| 20 | 379.0 | 0.0 | 0.001 | 1.00 | 1000.0 | 0.198 | 0.199 | 0.199 | 0.186 | 0.144 | 0.117 | 0.036 | 0.029 |
| 21 | 397.4 | 0.0 | 0.001 | 1.00 | 1000.0 | 0.202 | 0.203 | 0.203 | 0.190 | 0.148 | 0.120 | 0.037 | 0.033 |
| 22 | 415.2 | 0.0 | 0.001 | 1.00 | 1000.0 | 0.206 | 0.206 | 0.207 | 0.194 | 0.151 | 0.123 | 0.038 | 0.036 |
| 23 | 436.0 | 0.0 | 0.001 | 1.00 | 1000.0 | 0.211 | 0.211 | 0.211 | 0.198 | 0.155 | 0.126 | 0.039 | 0.033 |
| 24 | 455.5 | 0.0 | 0.001 | 1.00 | 1000.0 | 0.215 | 0.215 | 0.215 | 0.201 | 0.159 | 0.128 | 0.038 | 0.036 |
| 25 | 477.1 | 0.0 | 0.001 | 1.00 | 1000.0 | 0.219 | 0.219 | 0.219 | 0.206 | 0.162 | 0.131 | 0.037 | 0.038 |

Table A.1: Water data

| **N°** | **Q** $[L/min]$ | $\tau_{\mathbf{y}}$ $[Pa]$ | **k** $Pa.s^n$ | **n** $[-]$ | $\rho$ $[kg/m^3]$ | **US1** $[m]$ | **US2** $[m]$ | **US3** $[m]$ | **US4** $[m]$ | **US5** $[m]$ | **US6** $[m]$ | **US7** $[m]$ | **US8** $[m]$ |
|---|---|---|---|---|---|---|---|---|---|---|---|---|---|
| 1 | 4.2 | 0.0 | 0.885 | 1.00 | 1258.1 | 0.066 | 0.065 | 0.065 | 0.064 | 0.053 | 0.034 | 0.022 | 0.020 |
| 2 | 14.2 | 0.0 | 0.881 | 1.00 | 1258.3 | 0.098 | 0.097 | 0.096 | 0.095 | 0.079 | 0.052 | 0.030 | 0.027 |
| 3 | 25.2 | 0.0 | 0.853 | 1.00 | 1258.2 | 0.117 | 0.115 | 0.115 | 0.113 | 0.094 | 0.063 | 0.035 | 0.031 |
| 4 | 34.4 | 0.0 | 0.847 | 1.00 | 1257.6 | 0.127 | 0.125 | 0.124 | 0.122 | 0.102 | 0.065 | 0.038 | 0.034 |
| 5 | 44.2 | 0.0 | 0.801 | 1.00 | 1257.4 | 0.138 | 0.135 | 0.134 | 0.131 | 0.110 | 0.075 | 0.040 | 0.036 |
| 6 | 54.3 | 0.0 | 0.769 | 1.00 | 1257.4 | 0.147 | 0.144 | 0.143 | 0.139 | 0.117 | 0.079 | 0.042 | 0.039 |
| 7 | 63.8 | 0.0 | 0.808 | 1.00 | 1257.2 | 0.155 | 0.152 | 0.151 | 0.146 | 0.124 | 0.086 | 0.043 | 0.041 |
| 8 | 73.6 | 0.0 | 0.758 | 1.00 | 1256.9 | 0.161 | 0.158 | 0.157 | 0.153 | 0.129 | 0.088 | 0.045 | 0.042 |
| 9 | 84.1 | 0.0 | 0.756 | 1.00 | 1256.7 | 0.169 | 0.165 | 0.164 | 0.159 | 0.135 | 0.095 | 0.048 | 0.043 |
| 10 | 94.7 | 0.0 | 0.751 | 1.00 | 1256.7 | 0.175 | 0.172 | 0.171 | 0.165 | 0.140 | 0.096 | 0.049 | 0.043 |
| 11 | 103.4 | 0.0 | 0.731 | 1.00 | 1256.3 | 0.180 | 0.176 | 0.175 | 0.169 | 0.144 | 0.101 | 0.050 | 0.045 |
| 12 | 114.0 | 0.0 | 0.724 | 1.00 | 1256.2 | 0.185 | 0.182 | 0.180 | 0.174 | 0.148 | 0.107 | 0.050 | 0.048 |
| 13 | 124.9 | 0.0 | 0.712 | 1.00 | 1255.8 | 0.191 | 0.187 | 0.185 | 0.179 | 0.153 | -0.015 | 0.051 | 0.050 |
| 14 | 134.5 | 0.0 | 0.698 | 1.00 | 1255.5 | 0.195 | 0.191 | 0.189 | 0.183 | 0.156 | -0.008 | 0.051 | 0.053 |
| 15 | 144.1 | 0.0 | 0.690 | 1.00 | 1255.3 | 0.199 | 0.195 | 0.193 | 0.186 | 0.159 | 0.051 | 0.050 | 0.054 |
| 16 | 144.3 | 0.0 | 0.677 | 1.00 | 1254.8 | 0.198 | 0.194 | 0.193 | 0.186 | 0.158 | 0.103 | 0.049 | 0.054 |
| 17 | 153.4 | 0.0 | 0.643 | 1.00 | 1254.1 | 0.200 | 0.197 | 0.195 | 0.188 | 0.160 | 0.072 | 0.046 | 0.054 |
| 18 | 163.8 | 0.0 | 0.631 | 1.00 | 1253.9 | 0.204 | 0.200 | 0.199 | 0.191 | 0.163 | 0.111 | 0.046 | 0.055 |
| 19 | 175.4 | 0.0 | 0.618 | 1.00 | 1253.9 | 0.208 | 0.204 | 0.203 | 0.194 | 0.166 | 0.022 | 0.045 | 0.054 |
| 20 | 184.6 | 0.0 | 0.606 | 1.00 | 1253.8 | 0.210 | 0.207 | 0.206 | 0.197 | 0.168 | 0.025 | 0.044 | 0.053 |
| 21 | 191.3 | 0.0 | 0.587 | 1.00 | 1253.3 | 0.212 | 0.208 | 0.207 | 0.198 | 0.169 | 0.045 | 0.043 | 0.052 |

Table A.2: Gly.1 data

| **N°** | **Q** $[L/min]$ | $\tau_{\mathbf{y}}$ $[Pa]$ | **k** $Pa.s^n$ | **n** $[-]$ | $\rho$ $[kg/m^3]$ | **US1** $[m]$ | **US2** $[m]$ | **US3** $[m]$ | **US4** $[m]$ | **US5** $[m]$ | **US6** $[m]$ | **US7** $[m]$ | **US8** $[m]$ |
|---|---|---|---|---|---|---|---|---|---|---|---|---|---|
| 1 | 4.3 | 0.0 | 0.450 | 1.00 | 1249.5 | 0.055 | 0.055 | 0.055 | 0.054 | 0.045 | 0.028 | 0.020 | 0.018 |
| 2 | 44.4 | 0.0 | 0.449 | 1.00 | 1249.4 | 0.120 | 0.118 | 0.118 | 0.115 | 0.096 | 0.066 | 0.033 | 0.032 |
| 3 | 84.1 | 0.0 | 0.443 | 1.00 | 1249.3 | 0.150 | 0.148 | 0.147 | 0.142 | 0.120 | 0.085 | 0.039 | 0.036 |
| 4 | 122.2 | 0.0 | 0.440 | 1.00 | 1249.2 | 0.171 | 0.169 | 0.168 | 0.162 | 0.137 | 0.100 | 0.048 | 0.073 |
| 5 | 163.4 | 0.0 | 0.437 | 1.00 | 1249.0 | 0.190 | 0.187 | 0.186 | 0.179 | 0.152 | 0.112 | 0.036 | 0.045 |
| 6 | 199.7 | 0.0 | 0.431 | 1.00 | 1248.6 | 0.203 | 0.201 | 0.199 | 0.191 | 0.163 | 0.117 | 0.037 | 0.045 |
| 7 | 243.7 | 0.0 | 0.421 | 1.00 | 1248.0 | 0.218 | 0.215 | 0.214 | 0.204 | 0.174 | 0.131 | 0.043 | 0.043 |
| 8 | 281.5 | 0.0 | 0.403 | 1.00 | 1247.3 | 0.228 | 0.226 | 0.224 | 0.214 | 0.183 | 0.126 | 0.047 | 0.047 |
| 9 | 321.6 | 0.0 | 0.383 | 1.00 | 1246.3 | 0.238 | 0.235 | 0.234 | 0.223 | 0.191 | 0.146 | 0.051 | 0.047 |

Table A.3: Gly.2 data

| **N°** | **Q** $[L/min]$ | $\tau_{\mathbf{y}}$ $[Pa]$ | **k** $Pa.s^n$ | **n** $[-]$ | $\rho$ $[kg/m^3]$ | **US1** $[m]$ | **US2** $[m]$ | **US3** $[m]$ | **US4** $[m]$ | **US5** $[m]$ | **US6** $[m]$ | **US7** $[m]$ | **US8** $[m]$ |
|---|---|---|---|---|---|---|---|---|---|---|---|---|---|
| 1 | 4.4 | 0.0 | 0.216 | 1.00 | 1238.7 | 0.044 | 0.043 | 0.043 | 0.042 | 0.034 | 0.021 | 0.017 | 0.015 |
| 2 | 24.7 | 0.0 | 0.217 | 1.00 | 1238.6 | 0.082 | 0.081 | 0.081 | 0.079 | 0.066 | 0.044 | 0.023 | 0.022 |
| 3 | 44.6 | 0.0 | 0.217 | 1.00 | 1238.5 | 0.104 | 0.102 | 0.102 | 0.099 | 0.082 | 0.054 | 0.026 | 0.025 |
| 4 | 64.5 | 0.0 | 0.217 | 1.00 | 1238.5 | 0.119 | 0.117 | 0.117 | 0.113 | 0.095 | 0.067 | 0.028 | 0.027 |
| 5 | 84.1 | 0.0 | 0.214 | 1.00 | 1238.5 | 0.132 | 0.130 | 0.130 | 0.125 | 0.105 | 0.076 | 0.028 | 0.031 |
| 6 | 103.9 | 0.0 | 0.214 | 1.00 | 1238.5 | 0.142 | 0.141 | 0.140 | 0.136 | 0.114 | 0.079 | 0.024 | 0.031 |
| 7 | 125.2 | 0.0 | 0.214 | 1.00 | 1238.4 | 0.153 | 0.151 | 0.151 | 0.145 | 0.122 | 0.090 | 0.026 | 0.030 |
| 8 | 141.3 | 0.0 | 0.214 | 1.00 | 1238.3 | 0.161 | 0.159 | 0.158 | 0.152 | 0.128 | 0.095 | 0.028 | 0.040 |
| 9 | 164.5 | 0.0 | 0.212 | 1.00 | 1238.2 | 0.170 | 0.168 | 0.168 | 0.161 | 0.136 | 0.102 | 0.028 | 0.032 |
| 10 | 184.2 | 0.0 | 0.210 | 1.00 | 1238.0 | 0.177 | 0.176 | 0.175 | 0.169 | 0.142 | 0.107 | 0.030 | 0.031 |
| 11 | 203.7 | 0.0 | 0.209 | 1.00 | 1237.9 | 0.184 | 0.183 | 0.182 | 0.175 | 0.147 | 0.112 | 0.031 | 0.032 |
| 12 | 222.5 | 0.0 | 0.207 | 1.00 | 1237.7 | 0.190 | 0.188 | 0.188 | 0.181 | 0.152 | 0.116 | 0.034 | 0.034 |
| 13 | 244.5 | 0.0 | 0.205 | 1.00 | 1237.5 | 0.197 | 0.195 | 0.195 | 0.186 | 0.158 | 0.120 | 0.036 | 0.036 |
| 14 | 264.0 | 0.0 | 0.202 | 1.00 | 1237.1 | 0.203 | 0.201 | 0.201 | 0.192 | 0.162 | 0.124 | 0.037 | 0.036 |
| 15 | 280.8 | 0.0 | 0.199 | 1.00 | 1236.9 | 0.207 | 0.206 | 0.205 | 0.196 | 0.166 | 0.128 | 0.039 | 0.037 |
| 16 | 302.6 | 0.0 | 0.194 | 1.00 | 1236.5 | 0.213 | 0.211 | 0.211 | 0.201 | 0.170 | 0.126 | 0.040 | 0.038 |
| 17 | 321.8 | 0.0 | 0.190 | 1.00 | 1236.2 | 0.217 | 0.216 | 0.216 | 0.206 | 0.173 | 0.130 | 0.040 | 0.039 |
| 18 | 342.1 | 0.0 | 0.186 | 1.00 | 1235.9 | 0.222 | 0.221 | 0.221 | 0.210 | 0.177 | 0.136 | 0.044 | 0.041 |
| 19 | 363.2 | 0.0 | 0.179 | 1.00 | 1235.4 | 0.227 | 0.226 | 0.225 | 0.214 | 0.180 | 0.142 | 0.040 | 0.043 |
| 20 | 380.8 | 0.0 | 0.174 | 1.00 | 1235.0 | 0.231 | 0.230 | 0.229 | 0.218 | 0.183 | 0.142 | 0.029 | 0.043 |
| 21 | 397.9 | 0.0 | 0.166 | 1.00 | 1234.5 | 0.234 | 0.233 | 0.233 | 0.221 | 0.186 | 0.144 | 0.023 | 0.045 |

Table A.4: Gly.3 data

| **N°** | **Q** $[L/min]$ | $\tau_{\mathbf{y}}$ $[Pa]$ | **k** $Pa.s^n$ | **n** $[-]$ | $\rho$ $[kg/m^3]$ | **US1** $[m]$ | **US2** $[m]$ | **US3** $[m]$ | **US4** $[m]$ | **US5** $[m]$ | **US6** $[m]$ | **US7** $[m]$ | **US8** $[m]$ |
|---|---|---|---|---|---|---|---|---|---|---|---|---|---|
| 1 | 4.9 | 0.0 | 0.136 | 1.00 | 1232.3 | 0.040 | 0.040 | 0.040 | 0.037 | 0.030 | 0.019 | 0.016 | 0.014 |
| 2 | 25.2 | 0.0 | 0.137 | 1.00 | 1231.8 | 0.075 | 0.074 | 0.074 | 0.072 | 0.059 | 0.040 | 0.020 | 0.020 |
| 3 | 44.9 | 0.0 | 0.136 | 1.00 | 1231.7 | 0.095 | 0.094 | 0.094 | 0.090 | 0.075 | 0.053 | 0.022 | 0.022 |
| 4 | 65.0 | 0.0 | 0.134 | 1.00 | 1231.7 | 0.111 | 0.109 | 0.110 | 0.105 | 0.087 | 0.063 | 0.022 | 0.024 |
| 5 | 83.8 | 0.0 | 0.133 | 1.00 | 1231.7 | 0.122 | 0.121 | 0.121 | 0.098 | 0.097 | 0.052 | 0.021 | 0.023 |
| 6 | 104.2 | 0.0 | 0.133 | 1.00 | 1231.7 | 0.132 | 0.131 | 0.132 | 0.127 | 0.106 | 0.078 | 0.024 | 0.025 |
| 7 | 122.8 | 0.0 | 0.133 | 1.00 | 1231.7 | 0.141 | 0.140 | 0.140 | 0.135 | 0.113 | 0.084 | 0.027 | 0.025 |
| 8 | 143.1 | 0.0 | 0.133 | 1.00 | 1231.4 | 0.149 | 0.148 | 0.148 | 0.144 | 0.120 | 0.090 | 0.023 | 0.024 |
| 9 | 165.3 | 0.0 | 0.133 | 1.00 | 1231.4 | 0.156 | 0.156 | 0.156 | 0.152 | 0.128 | 0.097 | 0.025 | 0.027 |
| 10 | 183.9 | 0.0 | 0.132 | 1.00 | 1231.3 | 0.164 | 0.163 | 0.163 | 0.159 | 0.133 | 0.101 | 0.027 | 0.028 |
| 11 | 201.8 | 0.0 | 0.132 | 1.00 | 1231.2 | 0.171 | 0.170 | 0.170 | 0.165 | 0.138 | 0.106 | 0.028 | 0.029 |
| 12 | 222.2 | 0.0 | 0.131 | 1.00 | 1231.1 | 0.179 | 0.178 | 0.178 | 0.172 | 0.143 | 0.111 | 0.030 | 0.030 |
| 13 | 242.1 | 0.0 | 0.131 | 1.00 | 1231.0 | 0.186 | 0.185 | 0.185 | 0.178 | 0.148 | 0.115 | 0.031 | 0.031 |
| 14 | 261.2 | 0.0 | 0.129 | 1.00 | 1230.6 | 0.193 | 0.192 | 0.192 | 0.183 | 0.153 | 0.119 | 0.034 | 0.033 |
| 15 | 283.2 | 0.0 | 0.128 | 1.00 | 1230.4 | 0.200 | 0.199 | 0.198 | 0.189 | 0.158 | 0.123 | 0.035 | 0.034 |
| 16 | 302.7 | 0.0 | 0.127 | 1.00 | 1230.2 | 0.205 | 0.204 | 0.204 | 0.194 | 0.162 | 0.125 | 0.035 | 0.036 |
| 17 | 322.2 | 0.0 | 0.123 | 1.00 | 1229.7 | 0.210 | 0.209 | 0.209 | 0.198 | 0.165 | 0.128 | 0.034 | 0.037 |
| 18 | 340.7 | 0.0 | 0.121 | 1.00 | 1229.4 | 0.215 | 0.213 | 0.213 | 0.202 | 0.169 | 0.129 | 0.028 | 0.039 |
| 19 | 360.7 | 0.0 | 0.120 | 1.00 | 1229.3 | 0.219 | 0.218 | 0.218 | 0.207 | 0.173 | 0.133 | 0.021 | 0.040 |
| 20 | 381.7 | 0.0 | 0.118 | 1.00 | 1229.0 | 0.224 | 0.223 | 0.223 | 0.212 | 0.177 | 0.137 | 0.028 | 0.043 |
| 21 | 399.6 | 0.0 | 0.115 | 1.00 | 1228.6 | 0.228 | 0.227 | 0.227 | 0.216 | 0.179 | 0.143 | 0.018 | 0.043 |
| 22 | 420.5 | 0.0 | 0.111 | 1.00 | 1228.2 | 0.232 | 0.231 | 0.231 | 0.219 | 0.183 | 0.146 | 0.011 | 0.048 |

Table A.5: Gly.4 data

| N° | Q $[L/min]$ | $\tau_y$ $[Pa]$ | k $Pa.s^n$ | n $[-]$ | $\rho$ $[kg/m^3]$ | US1 $[m]$ | US2 $[m]$ | US3 $[m]$ | US4 $[m]$ | US5 $[m]$ | US6 $[m]$ | US7 $[m]$ | US8 $[m]$ |
|---|---|---|---|---|---|---|---|---|---|---|---|---|---|
| 1 | 4.6 | 0.0 | 0.075 | 1.00 | 1221.6 | 0.031 | 0.032 | 0.032 | 0.030 | 0.024 | 0.016 | 0.014 | 0.013 |
| 2 | 25.2 | 0.0 | 0.076 | 1.00 | 1220.6 | 0.066 | 0.066 | 0.066 | 0.064 | 0.053 | 0.037 | 0.015 | 0.016 |
| 3 | 44.8 | 0.0 | 0.076 | 1.00 | 1220.6 | 0.085 | 0.085 | 0.085 | 0.082 | 0.068 | 0.049 | 0.016 | 0.018 |
| 4 | 65.6 | 0.0 | 0.073 | 1.00 | 1220.7 | 0.101 | 0.101 | 0.101 | 0.097 | 0.080 | 0.058 | 0.015 | 0.019 |
| 5 | 84.3 | 0.0 | 0.073 | 1.00 | 1220.7 | 0.113 | 0.112 | 0.113 | 0.108 | 0.089 | 0.066 | 0.018 | 0.018 |
| 6 | 104.7 | 0.0 | 0.073 | 1.00 | 1220.7 | 0.125 | 0.124 | 0.124 | 0.116 | 0.095 | 0.065 | 0.018 | 0.019 |
| 7 | 124.6 | 0.0 | 0.074 | 1.00 | 1220.7 | 0.134 | 0.134 | 0.134 | 0.128 | 0.107 | 0.080 | 0.020 | 0.014 |
| 8 | 145.2 | 0.0 | 0.074 | 1.00 | 1220.6 | 0.144 | 0.143 | 0.143 | 0.136 | 0.114 | 0.086 | 0.023 | 0.024 |
| 9 | 164.1 | 0.0 | 0.074 | 1.00 | 1220.6 | 0.152 | 0.150 | 0.151 | 0.144 | 0.120 | 0.091 | 0.024 | 0.024 |
| 10 | 182.6 | 0.0 | 0.074 | 1.00 | 1220.5 | 0.159 | 0.158 | 0.158 | 0.151 | 0.125 | 0.096 | 0.025 | 0.025 |
| 11 | 202.8 | 0.0 | 0.074 | 1.00 | 1220.4 | 0.166 | 0.165 | 0.165 | 0.158 | 0.131 | 0.101 | 0.027 | 0.026 |
| 12 | 222.6 | 0.0 | 0.074 | 1.00 | 1220.4 | 0.173 | 0.172 | 0.172 | 0.164 | 0.136 | 0.105 | 0.028 | 0.028 |
| 13 | 241.2 | 0.0 | 0.074 | 1.00 | 1220.3 | 0.179 | 0.178 | 0.178 | 0.169 | 0.140 | 0.109 | 0.029 | 0.029 |
| 14 | 262.0 | 0.0 | 0.074 | 1.00 | 1220.1 | 0.185 | 0.184 | 0.184 | 0.175 | 0.144 | 0.114 | 0.030 | 0.031 |
| 15 | 281.5 | 0.0 | 0.073 | 1.00 | 1219.8 | 0.191 | 0.190 | 0.190 | 0.180 | 0.149 | 0.118 | 0.031 | 0.032 |
| 16 | 300.3 | 0.0 | 0.073 | 1.00 | 1219.7 | 0.196 | 0.195 | 0.195 | 0.185 | 0.153 | 0.121 | 0.026 | 0.034 |
| 17 | 321.4 | 0.0 | 0.073 | 1.00 | 1219.4 | 0.202 | 0.201 | 0.201 | 0.191 | 0.157 | 0.124 | -0.005 | 0.035 |
| 18 | 341.2 | 0.0 | 0.072 | 1.00 | 1219.2 | 0.207 | 0.206 | 0.206 | 0.196 | 0.162 | 0.127 | -0.013 | 0.036 |
| 19 | 359.2 | 0.0 | 0.071 | 1.00 | 1218.8 | 0.211 | 0.211 | 0.211 | 0.200 | 0.165 | 0.130 | -0.033 | 0.037 |
| 20 | 379.3 | 0.0 | 0.071 | 1.00 | 1218.7 | 0.216 | 0.216 | 0.216 | 0.204 | 0.169 | 0.133 | -0.033 | 0.038 |
| 21 | 398.3 | 0.0 | 0.069 | 1.00 | 1218.2 | 0.221 | 0.220 | 0.220 | 0.209 | 0.172 | 0.135 | -0.024 | 0.040 |
| 22 | 421.1 | 0.0 | 0.069 | 1.00 | 1218.0 | 0.226 | 0.225 | 0.225 | 0.213 | 0.176 | 0.139 | -0.030 | 0.042 |
| 23 | 434.4 | 0.0 | 0.068 | 1.00 | 1217.8 | 0.229 | 0.228 | 0.228 | 0.216 | 0.178 | 0.141 | -0.035 | 0.043 |

Table A.6: Gly.5 data

| N° | Q $[L/min]$ | $\tau_y$ $[Pa]$ | k $Pa.s^n$ | n $[-]$ | $\rho$ $[kg/m^3]$ | US1 $[m]$ | US2 $[m]$ | US3 $[m]$ | US4 $[m]$ | US5 $[m]$ | US6 $[m]$ | US7 $[m]$ | US8 $[m]$ |
|---|---|---|---|---|---|---|---|---|---|---|---|---|---|
| 1 | 5.6 | 0.0 | 0.060 | 1.00 | 1216.6 | 0.032 | 0.033 | 0.033 | 0.032 | 0.024 | 0.015 | 0.014 | 0.012 |
| 2 | 25.6 | 0.0 | 0.061 | 1.00 | 1215.7 | 0.064 | 0.064 | 0.065 | 0.062 | 0.051 | 0.035 | 0.014 | 0.014 |
| 3 | 44.7 | 0.0 | 0.060 | 1.00 | 1215.7 | 0.082 | 0.082 | 0.083 | 0.080 | 0.065 | 0.047 | 0.015 | 0.016 |
| 4 | 64.2 | 0.0 | 0.059 | 1.00 | 1215.7 | 0.098 | 0.097 | 0.098 | 0.094 | 0.077 | 0.056 | 0.013 | 0.017 |
| 5 | 84.1 | 0.0 | 0.059 | 1.00 | 1215.8 | 0.111 | 0.110 | 0.110 | 0.106 | 0.087 | 0.065 | 0.022 | 0.023 |
| 6 | 103.8 | 0.0 | 0.059 | 1.00 | 1215.7 | 0.121 | 0.120 | 0.120 | 0.115 | 0.096 | 0.071 | 0.019 | 0.019 |
| 7 | 123.4 | 0.0 | 0.059 | 1.00 | 1215.7 | 0.131 | 0.130 | 0.131 | 0.125 | 0.104 | 0.078 | 0.020 | 0.019 |
| 8 | 142.9 | 0.0 | 0.059 | 1.00 | 1215.7 | 0.140 | 0.139 | 0.140 | 0.133 | 0.111 | 0.084 | 0.022 | 0.022 |
| 9 | 164.1 | 0.0 | 0.059 | 1.00 | 1215.6 | 0.149 | 0.148 | 0.149 | 0.142 | 0.118 | 0.090 | 0.023 | 0.023 |
| 10 | 182.1 | 0.0 | 0.059 | 1.00 | 1215.5 | 0.156 | 0.155 | 0.156 | 0.149 | 0.123 | 0.095 | 0.025 | 0.023 |
| 11 | 201.7 | 0.0 | 0.059 | 1.00 | 1215.5 | 0.163 | 0.163 | 0.163 | 0.155 | 0.128 | 0.100 | 0.026 | 0.025 |
| 12 | 221.0 | 0.0 | 0.059 | 1.00 | 1215.4 | 0.170 | 0.169 | 0.169 | 0.161 | 0.133 | 0.104 | 0.028 | 0.027 |
| 13 | 241.8 | 0.0 | 0.059 | 1.00 | 1215.3 | 0.177 | 0.176 | 0.176 | 0.168 | 0.138 | 0.108 | 0.029 | 0.028 |
| 14 | 260.6 | 0.0 | 0.059 | 1.00 | 1215.0 | 0.183 | 0.181 | 0.182 | 0.173 | 0.142 | 0.112 | 0.030 | 0.030 |
| 15 | 282.4 | 0.0 | 0.059 | 1.00 | 1214.9 | 0.189 | 0.188 | 0.188 | 0.180 | 0.146 | 0.115 | 0.031 | 0.031 |
| 16 | 300.2 | 0.0 | 0.059 | 1.00 | 1214.7 | 0.194 | 0.193 | 0.193 | 0.184 | 0.150 | 0.119 | 0.012 | 0.032 |
| 17 | 341.2 | 0.0 | 0.059 | 1.00 | 1214.3 | 0.205 | 0.204 | 0.204 | 0.194 | 0.159 | 0.126 | -0.023 | 0.035 |
| 18 | 358.3 | 0.0 | 0.058 | 1.00 | 1214.2 | 0.209 | 0.208 | 0.208 | 0.198 | 0.162 | 0.128 | -0.028 | 0.037 |
| 19 | 380.8 | 0.0 | 0.058 | 1.00 | 1213.9 | 0.214 | 0.214 | 0.214 | 0.203 | 0.166 | 0.131 | -0.031 | 0.038 |
| 20 | 400.2 | 0.0 | 0.057 | 1.00 | 1213.7 | 0.219 | 0.218 | 0.218 | 0.207 | 0.170 | 0.134 | -0.027 | 0.040 |
| 21 | 418.9 | 0.0 | 0.057 | 1.00 | 1213.3 | 0.223 | 0.223 | 0.223 | 0.211 | 0.173 | 0.138 | -0.030 | 0.041 |
| 22 | 439.9 | 0.0 | 0.056 | 1.00 | 1213.1 | 0.228 | 0.227 | 0.227 | 0.215 | 0.176 | 0.141 | -0.035 | 0.042 |

Table A.7: Gly.6 data

| N° | Q $[L/min]$ | $\tau_y$ $[Pa]$ | k $Pa.s^n$ | n $[-]$ | $\rho$ $[kg/m^3]$ | US1 $[m]$ | US2 $[m]$ | US3 $[m]$ | US4 $[m]$ | US5 $[m]$ | US6 $[m]$ | US7 $[m]$ | US8 $[m]$ |
|---|---|---|---|---|---|---|---|---|---|---|---|---|---|
| 1 | 25.2 | 0.0 | 0.048 | 1.00 | 1209.9 | 0.061 | 0.062 | 0.062 | 0.059 | 0.048 | 0.034 | 0.015 | 0.015 |
| 2 | 44.8 | 0.0 | 0.046 | 1.00 | 1209.9 | 0.079 | 0.079 | 0.080 | 0.078 | 0.063 | 0.046 | 0.014 | 0.015 |
| 3 | 64.5 | 0.0 | 0.045 | 1.00 | 1210.0 | 0.095 | 0.095 | 0.096 | 0.092 | 0.075 | 0.055 | 0.015 | 0.016 |
| 4 | 84.0 | 0.0 | 0.045 | 1.00 | 1210.0 | 0.108 | 0.108 | 0.108 | 0.104 | 0.084 | 0.063 | 0.023 | 0.024 |
| 5 | 103.6 | 0.0 | 0.045 | 1.00 | 1210.0 | 0.119 | 0.118 | 0.119 | 0.114 | 0.094 | 0.070 | 0.020 | 0.017 |
| 6 | 125.4 | 0.0 | 0.045 | 1.00 | 1210.0 | 0.130 | 0.129 | 0.130 | 0.124 | 0.103 | 0.077 | 0.021 | 0.020 |
| 7 | 144.4 | 0.0 | 0.045 | 1.00 | 1210.0 | 0.138 | 0.138 | 0.139 | 0.132 | 0.109 | 0.084 | 0.022 | 0.022 |
| 8 | 164.6 | 0.0 | 0.046 | 1.00 | 1209.9 | 0.147 | 0.146 | 0.147 | 0.140 | 0.116 | 0.089 | 0.024 | 0.022 |
| 9 | 183.4 | 0.0 | 0.046 | 1.00 | 1209.8 | 0.154 | 0.153 | 0.154 | 0.147 | 0.121 | 0.094 | 0.025 | 0.024 |
| 10 | 201.2 | 0.0 | 0.046 | 1.00 | 1209.7 | 0.160 | 0.160 | 0.161 | 0.153 | 0.126 | 0.097 | 0.027 | 0.026 |
| 11 | 222.6 | 0.0 | 0.046 | 1.00 | 1209.7 | 0.168 | 0.167 | 0.168 | 0.160 | 0.131 | 0.103 | 0.028 | 0.027 |
| 12 | 240.8 | 0.0 | 0.046 | 1.00 | 1209.6 | 0.174 | 0.173 | 0.174 | 0.166 | 0.135 | 0.107 | 0.029 | 0.029 |
| 13 | 262.4 | 0.0 | 0.046 | 1.00 | 1209.4 | 0.181 | 0.180 | 0.180 | 0.172 | 0.140 | 0.111 | 0.030 | 0.030 |
| 14 | 279.4 | 0.0 | 0.045 | 1.00 | 1209.3 | 0.186 | 0.185 | 0.185 | 0.176 | 0.143 | 0.114 | 0.020 | 0.031 |
| 15 | 302.3 | 0.0 | 0.045 | 1.00 | 1209.1 | 0.192 | 0.191 | 0.192 | 0.182 | 0.148 | 0.118 | -0.018 | 0.033 |
| 16 | 320.8 | 0.0 | 0.045 | 1.00 | 1209.0 | 0.197 | 0.197 | 0.197 | 0.187 | 0.152 | 0.122 | -0.031 | 0.034 |
| 17 | 342.5 | 0.0 | 0.045 | 1.00 | 1208.7 | 0.203 | 0.202 | 0.203 | 0.193 | 0.157 | 0.124 | -0.027 | 0.036 |
| 18 | 360.3 | 0.0 | 0.045 | 1.00 | 1208.5 | 0.207 | 0.207 | 0.207 | 0.197 | 0.160 | 0.126 | -0.033 | 0.037 |
| 19 | 382.7 | 0.0 | 0.044 | 1.00 | 1208.3 | 0.213 | 0.213 | 0.213 | 0.202 | 0.164 | 0.130 | -0.034 | 0.039 |
| 20 | 401.5 | 0.0 | 0.044 | 1.00 | 1208.1 | 0.218 | 0.217 | 0.217 | 0.206 | 0.168 | 0.133 | -0.034 | 0.041 |
| 21 | 419.9 | 0.0 | 0.044 | 1.00 | 1207.9 | 0.222 | 0.221 | 0.222 | 0.210 | 0.171 | 0.134 | -0.035 | 0.042 |
| 22 | 441.9 | 0.0 | 0.043 | 1.00 | 1207.6 | 0.227 | 0.226 | 0.226 | 0.214 | 0.174 | 0.138 | -0.032 | 0.043 |
| 23 | 462.0 | 0.0 | 0.043 | 1.00 | 1207.4 | 0.231 | 0.230 | 0.230 | 0.218 | 0.178 | 0.141 | -0.033 | 0.047 |
| 24 | 475.0 | 0.0 | 0.042 | 1.00 | 1207.0 | 0.234 | 0.233 | 0.233 | 0.220 | 0.180 | 0.144 | -0.031 | 0.048 |

Table A.8: Gly.7 data

| **N°** | **Q** $[L/min]$ | $\tau_{\mathbf{y}}$ $[Pa]$ | **k** $Pa.s^n$ | **n** $[-]$ | $\rho$ $[kg/m^3]$ | **US1** $[m]$ | **US2** $[m]$ | **US3** $[m]$ | **US4** $[m]$ | **US5** $[m]$ | **US6** $[m]$ | **US7** $[m]$ | **US8** $[m]$ |
|---|---|---|---|---|---|---|---|---|---|---|---|---|---|
| 1 | 5.1 | 0.0 | 0.027 | 1.00 | 1198.5 | 0.027 | 0.027 | 0.028 | 0.025 | 0.021 | 0.015 | 0.010 | 0.002 |
| 2 | 25.4 | 0.0 | 0.027 | 1.00 | 1198.3 | 0.057 | 0.058 | 0.059 | 0.056 | 0.046 | 0.033 | 0.010 | 0.013 |
| 3 | 45.4 | 0.0 | 0.027 | 1.00 | 1198.3 | 0.077 | 0.077 | 0.078 | 0.074 | 0.060 | 0.045 | 0.002 | 0.012 |
| 4 | 65.3 | 0.0 | 0.027 | 1.00 | 1198.3 | 0.092 | 0.092 | 0.092 | 0.087 | 0.072 | 0.054 | 0.018 | 0.036 |
| 5 | 84.8 | 0.0 | 0.027 | 1.00 | 1198.3 | 0.105 | 0.104 | 0.105 | 0.100 | 0.081 | 0.061 | 0.017 | 0.025 |
| 6 | 103.0 | 0.0 | 0.027 | 1.00 | 1198.3 | 0.115 | 0.114 | 0.115 | 0.110 | 0.090 | 0.068 | 0.016 | 0.007 |
| 7 | 124.8 | 0.0 | 0.027 | 1.00 | 1198.3 | 0.125 | 0.125 | 0.126 | 0.120 | 0.099 | 0.074 | 0.018 | 0.015 |
| 8 | 144.7 | 0.0 | 0.027 | 1.00 | 1198.2 | 0.134 | 0.134 | 0.135 | 0.128 | 0.105 | 0.081 | 0.019 | 0.020 |
| 9 | 164.4 | 0.0 | 0.027 | 1.00 | 1198.1 | 0.143 | 0.142 | 0.143 | 0.136 | 0.111 | 0.086 | 0.021 | 0.021 |
| 10 | 185.0 | 0.0 | 0.027 | 1.00 | 1198.0 | 0.151 | 0.150 | 0.151 | 0.143 | 0.116 | 0.091 | 0.022 | 0.023 |
| 11 | 201.7 | 0.0 | 0.027 | 1.00 | 1197.9 | 0.157 | 0.156 | 0.157 | 0.149 | 0.121 | 0.095 | 0.024 | 0.024 |
| 12 | 222.0 | 0.0 | 0.027 | 1.00 | 1197.8 | 0.164 | 0.163 | 0.164 | 0.156 | 0.125 | 0.100 | 0.025 | 0.025 |
| 13 | 243.4 | 0.0 | 0.027 | 1.00 | 1197.7 | 0.171 | 0.170 | 0.171 | 0.162 | 0.130 | 0.104 | 0.027 | 0.027 |
| 14 | 264.6 | 0.0 | 0.027 | 1.00 | 1197.5 | 0.178 | 0.177 | 0.177 | 0.168 | 0.135 | 0.109 | 0.027 | 0.027 |
| 15 | 281.7 | 0.0 | 0.027 | 1.00 | 1197.3 | 0.183 | 0.182 | 0.182 | 0.173 | 0.138 | 0.111 | 0.029 | 0.028 |
| 16 | 301.3 | 0.0 | 0.027 | 1.00 | 1197.1 | 0.188 | 0.187 | 0.188 | 0.178 | 0.142 | 0.114 | 0.027 | 0.029 |
| 17 | 321.7 | 0.0 | 0.027 | 1.00 | 1196.9 | 0.194 | 0.193 | 0.193 | 0.183 | 0.147 | 0.118 | 0.020 | 0.031 |
| 18 | 341.0 | 0.0 | 0.027 | 1.00 | 1196.6 | 0.199 | 0.198 | 0.199 | 0.188 | 0.151 | 0.121 | 0.001 | 0.032 |
| 19 | 360.3 | 0.0 | 0.027 | 1.00 | 1196.3 | 0.204 | 0.203 | 0.204 | 0.193 | 0.155 | 0.124 | -0.012 | 0.033 |
| 20 | 383.0 | 0.0 | 0.026 | 1.00 | 1196.0 | 0.210 | 0.209 | 0.209 | 0.198 | 0.159 | 0.127 | -0.027 | 0.034 |
| 21 | 401.2 | 0.0 | 0.026 | 1.00 | 1195.8 | 0.214 | 0.213 | 0.213 | 0.202 | 0.163 | 0.128 | -0.036 | 0.035 |
| 22 | 420.3 | 0.0 | 0.026 | 1.00 | 1195.5 | 0.219 | 0.218 | 0.218 | 0.206 | 0.166 | 0.131 | -0.035 | 0.002 |
| 23 | 441.9 | 0.0 | 0.026 | 1.00 | 1195.2 | 0.223 | 0.223 | 0.223 | 0.210 | 0.170 | 0.136 | -0.035 | 0.009 |
| 24 | 462.4 | 0.0 | 0.026 | 1.00 | 1194.7 | 0.228 | 0.227 | 0.227 | 0.214 | 0.174 | 0.139 | -0.032 | -0.002 |
| 25 | 472.5 | 0.0 | 0.025 | 1.00 | 1194.4 | 0.230 | 0.229 | 0.229 | 0.216 | 0.176 | 0.140 | -0.034 | -0.009 |

Table A.9: Gly.8 data

| **N°** | **Q** $[L/min]$ | $\tau_y$ $[Pa]$ | **k** $Pa.s^n$ | **n** $[-]$ | $\rho$ $[kg/m^3]$ | **US1** $[m]$ | **US2** $[m]$ | **US3** $[m]$ | **US4** $[m]$ | **US5** $[m]$ | **US6** $[m]$ | **US7** $[m]$ | **US8** $[m]$ |
|---|---|---|---|---|---|---|---|---|---|---|---|---|---|
| 1 | 5.3 | 0.0 | 0.023 | 1.00 | 1193.0 | 0.028 | 0.027 | 0.028 | 0.026 | 0.020 | 0.014 | 0.009 | 0.011 |
| 2 | 25.1 | 0.0 | 0.023 | 1.00 | 1192.9 | 0.057 | 0.057 | 0.057 | 0.052 | 0.041 | 0.027 | 0.011 | 0.012 |
| 3 | 45.8 | 0.0 | 0.023 | 1.00 | 1192.9 | 0.077 | 0.076 | 0.077 | 0.074 | 0.058 | 0.045 | 0.010 | 0.013 |
| 4 | 65.7 | 0.0 | 0.023 | 1.00 | 1192.9 | 0.091 | 0.092 | 0.092 | 0.088 | 0.070 | 0.054 | 0.016 | 0.018 |
| 5 | 84.4 | 0.0 | 0.023 | 1.00 | 1192.9 | 0.103 | 0.103 | 0.104 | 0.099 | 0.078 | 0.061 | 0.016 | 0.017 |
| 6 | 106.4 | 0.0 | 0.023 | 1.00 | 1192.9 | 0.115 | 0.115 | 0.116 | 0.111 | 0.090 | 0.069 | 0.017 | 0.016 |
| 7 | 125.8 | 0.0 | 0.023 | 1.00 | 1192.9 | 0.125 | 0.125 | 0.126 | 0.120 | 0.097 | 0.075 | 0.018 | 0.019 |
| 8 | 144.4 | 0.0 | 0.023 | 1.00 | 1192.8 | 0.133 | 0.133 | 0.134 | 0.128 | 0.103 | 0.080 | 0.019 | 0.020 |
| 9 | 165.2 | 0.0 | 0.023 | 1.00 | 1192.7 | 0.142 | 0.142 | 0.143 | 0.136 | 0.109 | 0.086 | 0.021 | 0.021 |
| 10 | 185.7 | 0.0 | 0.023 | 1.00 | 1192.6 | 0.149 | 0.149 | 0.150 | 0.143 | 0.114 | 0.091 | 0.022 | 0.023 |
| 11 | 201.9 | 0.0 | 0.023 | 1.00 | 1192.6 | 0.156 | 0.155 | 0.156 | 0.148 | 0.118 | 0.095 | 0.023 | 0.024 |
| 12 | 224.1 | 0.0 | 0.023 | 1.00 | 1192.5 | 0.163 | 0.163 | 0.164 | 0.156 | 0.123 | 0.099 | 0.025 | 0.026 |
| 13 | 244.4 | 0.0 | 0.023 | 1.00 | 1192.3 | 0.170 | 0.170 | 0.170 | 0.162 | 0.128 | 0.104 | 0.026 | 0.027 |
| 14 | 264.1 | 0.0 | 0.023 | 1.00 | 1192.3 | 0.177 | 0.176 | 0.176 | 0.167 | 0.133 | 0.108 | 0.028 | 0.028 |
| 15 | 283.7 | 0.0 | 0.023 | 1.00 | 1192.1 | 0.182 | 0.182 | 0.182 | 0.173 | 0.137 | 0.111 | 0.028 | 0.030 |
| 16 | 304.3 | 0.0 | 0.023 | 1.00 | 1192.0 | 0.188 | 0.188 | 0.188 | 0.178 | 0.141 | 0.115 | 0.019 | 0.032 |
| 17 | 322.4 | 0.0 | 0.023 | 1.00 | 1191.8 | 0.193 | 0.193 | 0.193 | 0.183 | 0.145 | 0.118 | 0.013 | 0.033 |
| 18 | 341.5 | 0.0 | 0.023 | 1.00 | 1191.6 | 0.198 | 0.198 | 0.199 | 0.188 | 0.149 | 0.120 | -0.002 | 0.034 |
| 19 | 362.3 | 0.0 | 0.023 | 1.00 | 1191.3 | 0.204 | 0.203 | 0.204 | 0.192 | 0.154 | 0.124 | -0.016 | 0.035 |
| 20 | 383.8 | 0.0 | 0.023 | 1.00 | 1191.2 | 0.209 | 0.208 | 0.209 | 0.197 | 0.158 | 0.127 | -0.032 | 0.037 |
| 21 | 401.2 | 0.0 | 0.023 | 1.00 | 1191.0 | 0.213 | 0.213 | 0.213 | 0.201 | 0.161 | 0.127 | -0.037 | 0.038 |
| 22 | 422.7 | 0.0 | 0.023 | 1.00 | 1190.7 | 0.218 | 0.217 | 0.218 | 0.205 | 0.165 | 0.132 | -0.037 | 0.040 |
| 23 | 442.9 | 0.0 | 0.023 | 1.00 | 1190.4 | 0.223 | 0.222 | 0.222 | 0.209 | 0.169 | 0.135 | -0.037 | 0.040 |
| 24 | 458.7 | 0.0 | 0.022 | 1.00 | 1189.9 | 0.226 | 0.225 | 0.226 | 0.212 | 0.171 | 0.138 | -0.037 | 0.044 |
| 25 | 473.2 | 0.0 | 0.022 | 1.00 | 1189.7 | 0.229 | 0.228 | 0.229 | 0.216 | 0.174 | 0.140 | -0.037 | 0.051 |

Table A.10: Gly.9 data

| **N°** | **Q** $[L/min]$ | $\tau_{\mathbf{y}}$ $[Pa]$ | **k** $Pa.s^n$ | **n** $[-]$ | $\rho$ $[kg/m^3]$ | **US1** $[m]$ | **US2** $[m]$ | **US3** $[m]$ | **US4** $[m]$ | **US5** $[m]$ | **US6** $[m]$ | **US7** $[m]$ | **US8** $[m]$ |
|---|---|---|---|---|---|---|---|---|---|---|---|---|---|
| 1 | 4.9 | 0.0 | 0.016 | 1.00 | 1181.4 | 0.026 | 0.025 | 0.027 | 0.025 | 0.019 | 0.012 | 0.008 | 0.008 |
| 2 | 25.1 | 0.0 | 0.016 | 1.00 | 1181.3 | 0.055 | 0.056 | 0.056 | 0.053 | 0.042 | 0.031 | 0.009 | 0.010 |
| 3 | 44.6 | 0.0 | 0.016 | 1.00 | 1181.3 | 0.074 | 0.074 | 0.075 | 0.070 | 0.056 | 0.043 | 0.010 | 0.011 |
| 4 | 64.8 | 0.0 | 0.015 | 1.00 | 1181.3 | 0.089 | 0.089 | 0.089 | 0.083 | 0.066 | 0.052 | 0.013 | 0.015 |
| 5 | 84.4 | 0.0 | 0.016 | 1.00 | 1181.3 | 0.101 | 0.101 | 0.102 | 0.097 | 0.077 | 0.060 | 0.015 | 0.015 |
| 6 | 105.4 | 0.0 | 0.016 | 1.00 | 1181.3 | 0.113 | 0.113 | 0.114 | 0.107 | 0.087 | 0.067 | 0.016 | -0.002 |
| 7 | 124.3 | 0.0 | 0.016 | 1.00 | 1181.3 | 0.122 | 0.122 | 0.123 | 0.117 | 0.094 | 0.073 | 0.018 | 0.017 |
| 8 | 145.4 | 0.0 | 0.015 | 1.00 | 1307.8 | 0.131 | 0.131 | 0.132 | 0.124 | 0.100 | 0.080 | 0.019 | 0.019 |
| 9 | 163.8 | 0.0 | 0.016 | 1.00 | 1181.2 | 0.139 | 0.139 | 0.140 | 0.133 | 0.106 | 0.084 | 0.020 | 0.019 |
| 10 | 183.7 | 0.0 | 0.016 | 1.00 | 1181.1 | 0.147 | 0.147 | 0.148 | 0.140 | 0.111 | 0.090 | 0.022 | 0.021 |
| 11 | 202.0 | 0.0 | 0.016 | 1.00 | 1181.1 | 0.154 | 0.154 | 0.154 | 0.146 | 0.115 | 0.094 | 0.023 | 0.022 |
| 12 | 223.6 | 0.0 | 0.016 | 1.00 | 1181.1 | 0.161 | 0.161 | 0.162 | 0.153 | 0.120 | 0.098 | 0.025 | 0.023 |
| 13 | 243.6 | 0.0 | 0.016 | 1.00 | 1181.0 | 0.168 | 0.168 | 0.168 | 0.160 | 0.125 | 0.102 | 0.026 | 0.025 |
| 14 | 263.3 | 0.0 | 0.016 | 1.00 | 1180.9 | 0.174 | 0.174 | 0.174 | 0.166 | 0.129 | 0.107 | 0.028 | 0.026 |
| 15 | 281.5 | 0.0 | 0.016 | 1.00 | 1180.8 | 0.180 | 0.179 | 0.180 | 0.170 | 0.134 | 0.110 | 0.028 | 0.027 |
| 16 | 301.8 | 0.0 | 0.016 | 1.00 | 1180.6 | 0.186 | 0.185 | 0.185 | 0.176 | 0.137 | 0.111 | 0.028 | 0.026 |
| 17 | 323.4 | 0.0 | 0.016 | 1.00 | 1180.5 | 0.192 | 0.191 | 0.192 | 0.182 | 0.143 | 0.117 | 0.023 | 0.028 |
| 18 | 339.5 | 0.0 | 0.016 | 1.00 | 1180.1 | 0.196 | 0.196 | 0.196 | 0.185 | 0.146 | 0.119 | 0.021 | 0.028 |
| 19 | 361.6 | 0.0 | 0.016 | 1.00 | 1179.9 | 0.202 | 0.201 | 0.202 | 0.190 | 0.151 | 0.122 | 0.019 | 0.030 |
| 20 | 382.3 | 0.0 | 0.016 | 1.00 | 1179.7 | 0.207 | 0.206 | 0.207 | 0.195 | 0.155 | 0.125 | 0.014 | 0.031 |
| 21 | 401.5 | 0.0 | 0.016 | 1.00 | 1179.4 | 0.211 | 0.211 | 0.212 | 0.199 | 0.159 | 0.128 | 0.015 | 0.032 |
| 22 | 422.1 | 0.0 | 0.016 | 1.00 | 1178.9 | 0.216 | 0.216 | 0.216 | 0.204 | 0.163 | 0.130 | 0.016 | 0.033 |
| 23 | 439.4 | 0.0 | 0.016 | 1.00 | 1178.8 | 0.220 | 0.220 | 0.220 | 0.207 | 0.166 | 0.134 | 0.007 | 0.027 |
| 24 | 460.7 | 0.0 | 0.016 | 1.00 | 1178.3 | 0.225 | 0.224 | 0.224 | 0.212 | 0.170 | 0.136 | -0.008 | 0.033 |
| 25 | 472.8 | 0.0 | 0.016 | 1.00 | 1178.0 | 0.227 | 0.227 | 0.227 | 0.214 | 0.172 | 0.138 | -0.037 | 0.039 |

Table A.11: Gly.10 data

| **N°** | **Q** $[L/min]$ | $\tau_{\mathbf{y}}$ $[Pa]$ | **k** $Pa.s^n$ | **n** $[-]$ | $\rho$ $[kg/m^3]$ | **US1** $[m]$ | **US2** $[m]$ | **US3** $[m]$ | **US4** $[m]$ | **US5** $[m]$ | **US6** $[m]$ | **US7** $[m]$ | **US8** $[m]$ |
|---|---|---|---|---|---|---|---|---|---|---|---|---|---|
| 1 | 3.5 | 1.3 | 0.912 | 0.51 | 1000.3 | 0.058 | 0.055 | 0.053 | 0.049 | 0.038 | 0.026 | 0.017 | 0.017 |
| 2 | 26.1 | 1.4 | 0.866 | 0.52 | 1000.4 | 0.089 | 0.086 | 0.084 | 0.079 | 0.061 | 0.037 | 0.023 | 0.024 |
| 3 | 45.9 | 1.4 | 0.843 | 0.52 | 1000.4 | 0.107 | 0.103 | 0.101 | 0.094 | 0.075 | 0.050 | 0.026 | 0.025 |
| 4 | 66.8 | 1.5 | 0.820 | 0.53 | 1000.4 | 0.122 | 0.118 | 0.116 | 0.108 | 0.088 | 0.060 | 0.023 | 0.026 |
| 5 | 89.8 | 1.5 | 0.818 | 0.53 | 1000.3 | 0.135 | 0.131 | 0.129 | 0.120 | 0.099 | 0.070 | 0.022 | 0.030 |
| 6 | 104.1 | 1.6 | 0.816 | 0.53 | 1000.3 | 0.142 | 0.138 | 0.136 | 0.127 | 0.104 | 0.071 | 0.019 | 0.026 |
| 7 | 143.2 | 1.6 | 0.816 | 0.53 | 1000.0 | 0.160 | 0.156 | 0.154 | 0.144 | 0.119 | 0.087 | 0.023 | 0.034 |
| 8 | 161.3 | 1.6 | 0.815 | 0.53 | 999.9 | 0.167 | 0.162 | 0.160 | 0.150 | 0.124 | 0.092 | 0.022 | 0.026 |
| 9 | 184.0 | 1.6 | 0.815 | 0.53 | 999.7 | 0.176 | 0.171 | 0.169 | 0.158 | 0.131 | 0.098 | 0.024 | 0.026 |
| 10 | 202.9 | 1.6 | 0.816 | 0.53 | 999.6 | 0.182 | 0.178 | 0.175 | 0.164 | 0.137 | 0.103 | 0.025 | 0.026 |
| 11 | 220.2 | 1.6 | 0.816 | 0.53 | 999.6 | 0.188 | 0.184 | 0.181 | 0.169 | 0.141 | 0.106 | 0.027 | 0.029 |
| 12 | 240.8 | 1.6 | 0.816 | 0.53 | 999.2 | 0.194 | 0.190 | 0.187 | 0.176 | 0.146 | 0.111 | 0.029 | 0.030 |
| 13 | 260.9 | 1.6 | 0.816 | 0.53 | 999.1 | 0.201 | 0.196 | 0.194 | 0.181 | 0.151 | 0.115 | 0.029 | 0.031 |
| 14 | 278.8 | 1.6 | 0.816 | 0.53 | 999.1 | 0.206 | 0.201 | 0.199 | 0.186 | 0.155 | 0.115 | 0.031 | 0.033 |
| 15 | 301.8 | 1.6 | 0.803 | 0.53 | 999.0 | 0.212 | 0.207 | 0.205 | 0.192 | 0.160 | 0.111 | 0.032 | 0.035 |
| 16 | 318.6 | 1.6 | 0.797 | 0.54 | 998.9 | 0.217 | 0.212 | 0.210 | 0.196 | 0.163 | 0.100 | 0.006 | 0.036 |
| 17 | 337.0 | 1.6 | 0.793 | 0.54 | 998.6 | 0.222 | 0.217 | 0.215 | 0.200 | 0.167 | 0.103 | -0.019 | 0.037 |
| 18 | 358.8 | 1.6 | 0.790 | 0.54 | 998.5 | 0.227 | 0.222 | 0.220 | 0.205 | 0.170 | 0.126 | -0.026 | 0.038 |
| 19 | 379.7 | 1.6 | 0.790 | 0.54 | 998.3 | 0.232 | 0.227 | 0.225 | 0.210 | 0.174 | 0.133 | 0.005 | 0.040 |
| 20 | 399.5 | 1.6 | 0.790 | 0.54 | 998.2 | 0.236 | 0.232 | 0.229 | 0.214 | 0.178 | 0.138 | -0.033 | 0.041 |
| 21 | 419.1 | 1.6 | 0.790 | 0.54 | 998.0 | 0.241 | 0.236 | 0.234 | 0.218 | 0.181 | 0.143 | -0.037 | 0.043 |
| 22 | 440.4 | 1.6 | 0.790 | 0.54 | 997.8 | 0.245 | 0.240 | 0.238 | 0.223 | 0.184 | 0.144 | -0.030 | 0.044 |
| 23 | 457.4 | 1.6 | 0.790 | 0.54 | 997.5 | 0.249 | 0.244 | 0.242 | 0.226 | 0.187 | 0.148 | -0.037 | 0.045 |

Table A.12: Carb.1 data

| N° | Q $[L/min]$ | $\tau_y$ $[Pa]$ | k $Pa.s^n$ | n $[-]$ | $\rho$ $[kg/m^3]$ | US1 $[m]$ | US2 $[m]$ | US3 $[m]$ | US4 $[m]$ | US5 $[m]$ | US6 $[m]$ | US7 $[m]$ | US8 $[m]$ |
|---|---|---|---|---|---|---|---|---|---|---|---|---|---|
| 1 | 4.3 | 1.1 | 0.571 | 0.55 | 1000.8 | 0.050 | 0.049 | 0.048 | 0.042 | 0.033 | 0.022 | 0.018 | 0.019 |
| 2 | 25.1 | 1.1 | 0.577 | 0.55 | 1000.7 | 0.080 | 0.078 | 0.077 | 0.071 | 0.055 | 0.020 | 0.020 | 0.023 |
| 3 | 45.6 | 1.1 | 0.587 | 0.55 | 1000.7 | 0.099 | 0.097 | 0.096 | 0.089 | 0.070 | 0.047 | 0.024 | 0.029 |
| 4 | 64.7 | 1.1 | 0.597 | 0.54 | 1000.7 | 0.112 | 0.110 | 0.109 | 0.102 | 0.082 | 0.056 | 0.019 | 0.026 |
| 5 | 86.6 | 1.1 | 0.573 | 0.55 | 1000.6 | 0.125 | 0.123 | 0.122 | 0.113 | 0.094 | 0.055 | 0.018 | 0.027 |
| 6 | 100.7 | 1.1 | 0.579 | 0.55 | 1000.6 | 0.133 | 0.130 | 0.129 | 0.121 | 0.100 | 0.067 | 0.020 | 0.026 |
| 7 | 123.4 | 1.1 | 0.584 | 0.55 | 1000.5 | 0.143 | 0.141 | 0.140 | 0.130 | 0.109 | 0.079 | 0.025 | 0.029 |
| 8 | 143.9 | 1.1 | 0.581 | 0.55 | 1000.5 | 0.152 | 0.149 | 0.148 | 0.139 | 0.116 | 0.086 | 0.027 | 0.030 |
| 9 | 161.5 | 1.2 | 0.577 | 0.55 | 1000.4 | 0.159 | 0.156 | 0.154 | 0.142 | 0.118 | 0.084 | 0.026 | 0.035 |
| 10 | 183.3 | 1.1 | 0.588 | 0.55 | 1000.3 | 0.167 | 0.164 | 0.163 | 0.152 | 0.128 | 0.096 | 0.029 | 0.046 |
| 11 | 201.6 | 1.1 | 0.598 | 0.55 | 1000.3 | 0.172 | 0.168 | 0.169 | 0.158 | 0.133 | 0.098 | 0.031 | 0.043 |
| 12 | 222.3 | 1.1 | 0.589 | 0.54 | 1000.1 | 0.181 | 0.177 | 0.176 | 0.165 | 0.138 | 0.100 | 0.027 | 0.033 |
| 13 | 242.9 | 1.2 | 0.585 | 0.54 | 1000.2 | 0.187 | 0.184 | 0.182 | 0.171 | 0.143 | 0.107 | 0.028 | 0.031 |
| 14 | 265.4 | 1.2 | 0.582 | 0.54 | 1000.2 | 0.194 | 0.190 | 0.189 | 0.177 | 0.147 | 0.107 | 0.029 | 0.034 |
| 15 | 283.1 | 1.2 | 0.580 | 0.54 | 1000.2 | 0.198 | 0.194 | 0.189 | 0.173 | 0.136 | 0.103 | 0.030 | 0.034 |
| 16 | 302.4 | 1.2 | 0.590 | 0.54 | 1000.0 | 0.204 | 0.201 | 0.199 | 0.186 | 0.154 | 0.120 | 0.026 | 0.035 |
| 17 | 321.0 | 1.2 | 0.595 | 0.54 | 999.9 | 0.209 | 0.206 | 0.204 | 0.191 | 0.158 | 0.120 | -0.011 | 0.036 |
| 18 | 341.7 | 1.2 | 0.598 | 0.54 | 999.7 | 0.215 | 0.211 | 0.210 | 0.196 | 0.162 | 0.122 | -0.037 | 0.037 |
| 19 | 361.4 | 1.2 | 0.599 | 0.54 | 999.5 | 0.220 | 0.216 | 0.214 | 0.200 | 0.166 | 0.125 | -0.036 | 0.039 |
| 20 | 380.7 | 1.2 | 0.599 | 0.54 | 999.4 | 0.224 | 0.221 | 0.219 | 0.205 | 0.169 | 0.133 | -0.034 | 0.040 |
| 21 | 395.3 | 1.2 | 0.600 | 0.54 | 999.4 | 0.229 | 0.224 | 0.220 | 0.200 | 0.160 | 0.131 | -0.035 | 0.042 |
| 22 | 420.6 | 1.2 | 0.600 | 0.54 | 999.3 | 0.234 | 0.230 | 0.228 | 0.213 | 0.176 | 0.140 | -0.036 | 0.043 |
| 23 | 440.8 | 1.2 | 0.600 | 0.54 | 999.1 | 0.238 | 0.234 | 0.233 | 0.217 | 0.180 | 0.143 | -0.037 | 0.044 |
| 24 | 460.7 | 1.2 | 0.600 | 0.54 | 999.0 | 0.242 | 0.239 | 0.237 | 0.222 | 0.183 | 0.146 | -0.037 | 0.044 |

Table A.13: Carb.2 data

| **N°** | **Q** $[L/min]$ | $\tau_{\mathbf{y}}$ $[Pa]$ | **k** $Pa.s^n$ | **n** $[-]$ | $\rho$ $[kg/m^3]$ | **US1** $[m]$ | **US2** $[m]$ | **US3** $[m]$ | **US4** $[m]$ | **US5** $[m]$ | **US6** $[m]$ | **US7** $[m]$ | **US8** $[m]$ |
|---|---|---|---|---|---|---|---|---|---|---|---|---|---|
| 1 | 5.2 | 0.8 | 0.568 | 0.55 | 999.2 | 0.052 | 0.049 | 0.048 | 0.045 | 0.034 | 0.023 | 0.017 | 0.016 |
| 2 | 24.3 | 0.8 | 0.568 | 0.55 | 984.5 | 0.077 | 0.075 | 0.073 | 0.069 | 0.055 | 0.036 | 0.019 | 0.020 |
| 3 | 47.4 | 0.8 | 0.568 | 0.55 | 999.9 | 0.099 | 0.096 | 0.095 | 0.089 | 0.071 | 0.045 | 0.019 | 0.020 |
| 4 | 69.0 | 0.8 | 0.568 | 0.55 | 999.8 | 0.113 | 0.111 | 0.110 | 0.103 | 0.084 | 0.059 | 0.018 | 0.022 |
| 5 | 83.3 | 0.8 | 0.568 | 0.55 | 999.8 | 0.122 | 0.119 | 0.119 | 0.111 | 0.091 | 0.064 | 0.017 | 0.022 |
| 6 | 104.3 | 0.8 | 0.568 | 0.55 | 999.8 | 0.133 | 0.130 | 0.129 | 0.121 | 0.100 | 0.073 | 0.018 | 0.021 |
| 7 | 143.6 | 0.8 | 0.571 | 0.55 | 999.6 | 0.151 | 0.148 | 0.147 | 0.138 | 0.114 | 0.084 | 0.020 | 0.022 |
| 8 | 161.7 | 0.8 | 0.572 | 0.55 | 999.5 | 0.158 | 0.155 | 0.154 | 0.145 | 0.120 | 0.090 | 0.022 | 0.023 |
| 9 | 182.3 | 0.8 | 0.572 | 0.55 | 999.5 | 0.166 | 0.163 | 0.162 | 0.152 | 0.126 | 0.095 | 0.023 | 0.025 |
| 10 | 216.7 | 0.8 | 0.573 | 0.55 | 999.5 | 0.178 | 0.175 | 0.174 | 0.163 | 0.136 | 0.103 | 0.025 | 0.026 |
| 11 | 243.1 | 0.8 | 0.573 | 0.55 | 999.4 | 0.187 | 0.183 | 0.182 | 0.171 | 0.142 | 0.109 | 0.028 | 0.029 |
| 12 | 263.0 | 0.8 | 0.573 | 0.55 | 999.3 | 0.193 | 0.189 | 0.188 | 0.176 | 0.146 | 0.113 | 0.029 | 0.030 |
| 13 | 282.7 | 0.8 | 0.572 | 0.55 | 999.3 | 0.198 | 0.195 | 0.194 | 0.182 | 0.150 | 0.114 | 0.030 | 0.031 |
| 14 | 304.9 | 0.8 | 0.571 | 0.55 | 999.3 | 0.204 | 0.201 | 0.200 | 0.187 | 0.155 | 0.117 | 0.031 | 0.033 |
| 15 | 322.2 | 0.9 | 0.570 | 0.55 | 999.2 | 0.209 | 0.206 | 0.205 | 0.192 | 0.158 | 0.108 | 0.002 | 0.035 |
| 16 | 340.8 | 0.9 | 0.576 | 0.55 | 999.2 | 0.214 | 0.211 | 0.210 | 0.196 | 0.162 | 0.112 | -0.031 | 0.036 |
| 17 | 381.5 | 0.9 | 0.579 | 0.55 | 999.0 | 0.223 | 0.221 | 0.219 | 0.205 | 0.169 | 0.132 | -0.023 | 0.039 |
| 18 | 403.9 | 0.9 | 0.581 | 0.55 | 998.9 | 0.229 | 0.226 | 0.225 | 0.210 | 0.173 | 0.136 | -0.037 | 0.040 |
| 19 | 423.3 | 0.9 | 0.582 | 0.55 | 998.9 | 0.233 | 0.230 | 0.229 | 0.214 | 0.176 | 0.140 | -0.037 | 0.043 |
| 20 | 439.6 | 0.9 | 0.582 | 0.55 | 998.7 | 0.237 | 0.234 | 0.232 | 0.217 | 0.179 | 0.142 | -0.037 | 0.044 |
| 21 | 459.2 | 0.9 | 0.582 | 0.55 | 998.6 | 0.241 | 0.238 | 0.237 | 0.221 | 0.182 | 0.145 | -0.037 | 0.044 |

Table A.14: Carb.3 data

| **N°** | **Q** $[L/min]$ | $\tau_{\mathbf{y}}$ $[Pa]$ | **k** $Pa.s^n$ | **n** $[-]$ | $\rho$ $[kg/m^3]$ | **US1** $[m]$ | **US2** $[m]$ | **US3** $[m]$ | **US4** $[m]$ | **US5** $[m]$ | **US6** $[m]$ | **US7** $[m]$ | **US8** $[m]$ |
|---|---|---|---|---|---|---|---|---|---|---|---|---|---|
| 1 | 6.1 | 1.0 | 0.487 | 0.55 | 999.9 | 0.052 | 0.050 | 0.049 | 0.044 | 0.035 | 0.024 | 0.018 | 0.020 |
| 2 | 25.9 | 1.0 | 0.487 | 0.55 | 999.9 | 0.078 | 0.076 | 0.075 | 0.070 | 0.056 | 0.034 | 0.017 | 0.018 |
| 3 | 44.9 | 1.0 | 0.487 | 0.55 | 999.9 | 0.095 | 0.093 | 0.092 | 0.085 | 0.068 | 0.045 | 0.019 | 0.021 |
| 4 | 65.9 | 0.9 | 0.519 | 0.54 | 999.9 | 0.110 | 0.108 | 0.107 | 0.099 | 0.081 | 0.058 | 0.018 | 0.022 |
| 5 | 104.4 | 0.8 | 0.535 | 0.54 | 999.8 | 0.132 | 0.129 | 0.128 | 0.119 | 0.098 | 0.072 | 0.017 | 0.020 |
| 6 | 143.2 | 0.8 | 0.543 | 0.53 | 999.6 | 0.149 | 0.146 | 0.145 | 0.136 | 0.113 | 0.084 | 0.021 | 0.022 |
| 7 | 183.0 | 0.8 | 0.551 | 0.53 | 999.5 | 0.164 | 0.161 | 0.160 | 0.150 | 0.125 | 0.094 | 0.023 | 0.024 |
| 8 | 202.9 | 0.8 | 0.525 | 0.54 | 999.5 | 0.171 | 0.168 | 0.167 | 0.156 | 0.131 | 0.099 | 0.025 | 0.026 |
| 9 | 222.6 | 0.9 | 0.512 | 0.54 | 999.5 | 0.178 | 0.175 | 0.173 | 0.163 | 0.135 | 0.104 | 0.026 | 0.027 |
| 10 | 242.8 | 0.9 | 0.499 | 0.54 | 999.3 | 0.184 | 0.181 | 0.180 | 0.168 | 0.140 | 0.109 | 0.028 | 0.029 |
| 11 | 265.1 | 0.9 | 0.510 | 0.54 | 999.2 | 0.191 | 0.188 | 0.186 | 0.175 | 0.144 | 0.113 | 0.029 | 0.030 |
| 12 | 282.1 | 0.9 | 0.515 | 0.54 | 999.1 | 0.195 | 0.193 | 0.191 | 0.179 | 0.148 | 0.110 | 0.031 | 0.032 |
| 13 | 302.0 | 0.9 | 0.517 | 0.54 | 999.1 | 0.201 | 0.198 | 0.197 | 0.184 | 0.151 | 0.117 | 0.030 | 0.034 |
| 14 | 321.0 | 0.9 | 0.520 | 0.54 | 998.8 | 0.206 | 0.203 | 0.202 | 0.189 | 0.155 | 0.107 | 0.022 | 0.034 |
| 15 | 342.6 | 0.8 | 0.511 | 0.54 | 998.8 | 0.211 | 0.208 | 0.207 | 0.194 | 0.159 | 0.116 | -0.035 | 0.035 |
| 16 | 360.6 | 0.8 | 0.507 | 0.54 | 998.6 | 0.216 | 0.213 | 0.212 | 0.198 | 0.163 | 0.126 | -0.037 | 0.037 |
| 17 | 380.7 | 0.8 | 0.502 | 0.54 | 998.5 | 0.220 | 0.217 | 0.216 | 0.202 | 0.166 | 0.131 | -0.027 | 0.038 |
| 18 | 401.0 | 0.8 | 0.488 | 0.54 | 998.2 | 0.225 | 0.222 | 0.221 | 0.207 | 0.170 | 0.135 | -0.033 | 0.040 |
| 19 | 421.7 | 0.8 | 0.474 | 0.55 | 997.9 | 0.229 | 0.226 | 0.225 | 0.211 | 0.173 | 0.139 | -0.037 | 0.040 |
| 20 | 441.9 | 0.7 | 0.498 | 0.54 | 997.6 | 0.233 | 0.230 | 0.230 | 0.215 | 0.176 | 0.141 | -0.037 | 0.042 |
| 21 | 460.5 | 0.5 | 0.521 | 0.53 | 997.4 | 0.237 | 0.234 | 0.233 | 0.218 | 0.179 | 0.144 | -0.037 | 0.043 |

Table A.15: Carb.4 data

| **N°** | **Q** $[L/min]$ | $\tau_{\mathbf{y}}$ $[Pa]$ | **k** $Pa.s^n$ | **n** $[-]$ | $\rho$ $[kg/m^3]$ | **US1** $[m]$ | **US2** $[m]$ | **US3** $[m]$ | **US4** $[m]$ | **US5** $[m]$ | **US6** $[m]$ | **US7** $[m]$ | **US8** $[m]$ |
|---|---|---|---|---|---|---|---|---|---|---|---|---|---|
| 1 | 3.3 | 0.5 | 0.429 | 0.55 | 1000.9 | 0.039 | 0.038 | 0.038 | 0.031 | 0.023 | 0.016 | 0.014 | 0.014 |
| 2 | 39.8 | 0.5 | 0.429 | 0.55 | 1000.8 | 0.085 | 0.084 | 0.084 | 0.078 | 0.060 | 0.040 | 0.017 | 0.018 |
| 3 | 85.1 | 0.6 | 0.380 | 0.57 | 1000.7 | 0.116 | 0.115 | 0.114 | 0.106 | 0.086 | 0.061 | 0.015 | 0.018 |
| 4 | 123.9 | 0.6 | 0.390 | 0.57 | 1000.6 | 0.135 | 0.134 | 0.134 | 0.124 | 0.103 | 0.075 | 0.018 | 0.021 |
| 5 | 164.7 | 0.6 | 0.399 | 0.56 | 1000.5 | 0.152 | 0.151 | 0.150 | 0.140 | 0.117 | 0.089 | 0.021 | 0.023 |
| 6 | 201.6 | 0.6 | 0.403 | 0.56 | 1000.4 | 0.166 | 0.164 | 0.163 | 0.153 | 0.128 | 0.095 | 0.024 | 0.026 |
| 7 | 242.7 | 0.5 | 0.407 | 0.56 | 1000.4 | 0.179 | 0.177 | 0.176 | 0.166 | 0.137 | 0.096 | 0.026 | 0.028 |
| 8 | 282.4 | 0.6 | 0.404 | 0.56 | 1000.3 | 0.191 | 0.189 | 0.188 | 0.177 | 0.145 | 0.091 | 0.029 | 0.031 |
| 9 | 318.5 | 0.6 | 0.401 | 0.56 | 1000.1 | 0.201 | 0.199 | 0.198 | 0.186 | 0.152 | 0.121 | 0.017 | 0.033 |
| 10 | 360.9 | 0.6 | 0.404 | 0.56 | 1000.0 | 0.212 | 0.210 | 0.209 | 0.196 | 0.160 | 0.125 | -0.036 | 0.036 |
| 11 | 391.6 | 0.6 | 0.405 | 0.56 | 999.8 | 0.219 | 0.217 | 0.216 | 0.203 | 0.166 | 0.131 | -0.037 | 0.037 |
| 12 | 435.1 | 0.6 | 0.406 | 0.56 | 999.5 | 0.229 | 0.227 | 0.226 | 0.211 | 0.173 | 0.139 | -0.037 | 0.040 |
| 13 | 467.0 | 0.6 | 0.409 | 0.56 | 999.1 | 0.235 | 0.234 | 0.233 | 0.218 | 0.178 | 0.144 | -0.037 | 0.041 |

Table A.16: Carb.5 data

| N° | Q $[L/min]$ | $\tau_y$ $[Pa]$ | k $Pa.s^n$ | n $[-]$ | $\rho$ $[kg/m^3]$ | US1 $[m]$ | US2 $[m]$ | US3 $[m]$ | US4 $[m]$ | US5 $[m]$ | US6 $[m]$ | US7 $[m]$ | US8 $[m]$ |
|---|---|---|---|---|---|---|---|---|---|---|---|---|---|
| 1 | 4.4 | 0.0 | 0.157 | 0.60 | 999.7 | 0.029 | 0.028 | 0.028 | 0.025 | 0.020 | 0.013 | 0.011 | 0.011 |
| 2 | 26.4 | 0.0 | 0.149 | 0.61 | 999.7 | 0.060 | 0.060 | 0.061 | 0.055 | 0.045 | 0.033 | 0.012 | 0.018 |
| 3 | 45.4 | 0.1 | 0.145 | 0.61 | 999.7 | 0.078 | 0.078 | 0.078 | 0.073 | 0.059 | 0.044 | 0.011 | 0.013 |
| 4 | 64.5 | 0.1 | 0.141 | 0.62 | 999.6 | 0.091 | 0.091 | 0.092 | 0.085 | 0.070 | 0.053 | 0.012 | 0.015 |
| 5 | 84.1 | 0.0 | 0.152 | 0.61 | 999.6 | 0.103 | 0.104 | 0.104 | 0.097 | 0.079 | 0.060 | 0.015 | 0.015 |
| 6 | 106.5 | 0.0 | 0.157 | 0.61 | 999.6 | 0.115 | 0.115 | 0.116 | 0.108 | 0.089 | 0.068 | 0.017 | 0.017 |
| 7 | 125.5 | 0.0 | 0.162 | 0.60 | 999.6 | 0.125 | 0.125 | 0.126 | 0.118 | 0.097 | 0.074 | 0.018 | 0.017 |
| 8 | 143.4 | 0.0 | 0.161 | 0.60 | 999.6 | 0.132 | 0.132 | 0.133 | 0.125 | 0.103 | 0.079 | 0.019 | 0.019 |
| 9 | 166.9 | 0.0 | 0.160 | 0.60 | 999.5 | 0.142 | 0.142 | 0.143 | 0.134 | 0.109 | 0.085 | 0.020 | 0.020 |
| 10 | 183.0 | 0.0 | 0.159 | 0.60 | 999.5 | 0.148 | 0.148 | 0.149 | 0.140 | 0.113 | 0.089 | 0.021 | 0.021 |
| 11 | 205.6 | 0.0 | 0.157 | 0.61 | 999.5 | 0.156 | 0.156 | 0.156 | 0.147 | 0.118 | 0.094 | 0.023 | 0.022 |
| 12 | 225.0 | 0.0 | 0.154 | 0.61 | 999.5 | 0.163 | 0.163 | 0.163 | 0.153 | 0.123 | 0.098 | 0.024 | 0.023 |
| 13 | 244.0 | 0.0 | 0.159 | 0.61 | 999.5 | 0.169 | 0.169 | 0.169 | 0.159 | 0.127 | 0.103 | 0.026 | 0.025 |
| 14 | 264.3 | 0.0 | 0.161 | 0.60 | 999.5 | 0.176 | 0.175 | 0.175 | 0.165 | 0.131 | 0.107 | 0.028 | 0.027 |
| 15 | 281.3 | 0.0 | 0.162 | 0.60 | 999.5 | 0.181 | 0.181 | 0.180 | 0.170 | 0.136 | 0.065 | 0.028 | 0.028 |
| 16 | 303.0 | 0.0 | 0.163 | 0.60 | 999.4 | 0.187 | 0.187 | 0.187 | 0.175 | 0.140 | 0.085 | 0.029 | 0.029 |
| 17 | 323.0 | 0.0 | 0.164 | 0.60 | 999.3 | 0.192 | 0.192 | 0.192 | 0.181 | 0.145 | 0.110 | 0.025 | 0.031 |
| 18 | 344.0 | 0.0 | 0.164 | 0.60 | 999.3 | 0.198 | 0.198 | 0.198 | 0.186 | 0.149 | 0.100 | 0.014 | 0.034 |
| 19 | 363.0 | 0.0 | 0.158 | 0.61 | 999.2 | 0.202 | 0.202 | 0.202 | 0.190 | 0.153 | 0.121 | 0.002 | 0.036 |
| 20 | 381.8 | 0.0 | 0.155 | 0.61 | 999.1 | 0.207 | 0.207 | 0.207 | 0.194 | 0.156 | 0.125 | -0.028 | 0.036 |
| 21 | 401.7 | 0.0 | 0.154 | 0.61 | 999.0 | 0.212 | 0.211 | 0.212 | 0.198 | 0.160 | 0.128 | -0.036 | 0.038 |
| 22 | 422.4 | 0.0 | 0.152 | 0.61 | 998.7 | 0.216 | 0.216 | 0.216 | 0.203 | 0.164 | 0.131 | -0.037 | 0.039 |
| 23 | 441.3 | 0.0 | 0.155 | 0.61 | 998.5 | 0.220 | 0.220 | 0.220 | 0.206 | 0.167 | 0.135 | -0.037 | 0.039 |
| 24 | 459.3 | 0.0 | 0.158 | 0.61 | 998.3 | 0.224 | 0.224 | 0.224 | 0.210 | 0.171 | 0.134 | -0.037 | 0.043 |

Table A.17: Carb.6 data

| **N°** | **Q** $[L/min]$ | $\tau_{\mathbf{y}}$ $[Pa]$ | **k** $Pa.s^n$ | **n** $[-]$ | $\rho$ $[kg/m^3]$ | **US1** $[m]$ | **US2** $[m]$ | **US3** $[m]$ | **US4** $[m]$ | **US5** $[m]$ | **US6** $[m]$ | **US7** $[m]$ | **US8** $[m]$ |
|---|---|---|---|---|---|---|---|---|---|---|---|---|---|
| 1 | 4.6 | 0.0 | 0.097 | 0.64 | 1000.0 | 0.027 | 0.027 | 0.028 | 0.024 | 0.020 | 0.013 | 0.009 | 0.012 |
| 2 | 25.6 | 0.0 | 0.093 | 0.65 | 1000.0 | 0.058 | 0.058 | 0.058 | 0.054 | 0.042 | 0.031 | 0.008 | 0.012 |
| 3 | 46.4 | 0.0 | 0.091 | 0.65 | 1000.0 | 0.077 | 0.076 | 0.077 | 0.071 | 0.058 | 0.043 | 0.012 | 0.019 |
| 4 | 64.9 | 0.0 | 0.089 | 0.65 | 1000.0 | 0.090 | 0.089 | 0.090 | 0.084 | 0.068 | 0.052 | 0.012 | 0.015 |
| 5 | 84.5 | 0.0 | 0.094 | 0.65 | 1000.0 | 0.102 | 0.102 | 0.103 | 0.095 | 0.078 | 0.059 | 0.015 | 0.018 |
| 6 | 104.8 | 0.0 | 0.096 | 0.64 | 999.9 | 0.113 | 0.113 | 0.113 | 0.106 | 0.087 | 0.066 | 0.015 | 0.015 |
| 7 | 123.8 | 0.0 | 0.102 | 0.63 | 999.9 | 0.121 | 0.121 | 0.122 | 0.114 | 0.094 | 0.071 | 0.017 | 0.017 |
| 8 | 146.5 | 0.0 | 0.100 | 0.64 | 999.9 | 0.132 | 0.132 | 0.132 | 0.123 | 0.101 | 0.078 | 0.017 | 0.019 |
| 9 | 165.9 | 0.0 | 0.099 | 0.64 | 999.9 | 0.140 | 0.140 | 0.140 | 0.131 | 0.106 | 0.084 | 0.019 | 0.025 |
| 10 | 182.8 | 0.0 | 0.098 | 0.64 | 999.9 | 0.146 | 0.146 | 0.147 | 0.137 | 0.110 | 0.087 | 0.021 | 0.021 |
| 11 | 205.9 | 0.0 | 0.105 | 0.63 | 999.8 | 0.155 | 0.155 | 0.155 | 0.145 | 0.116 | 0.093 | 0.022 | 0.022 |
| 12 | 248.0 | 0.0 | 0.108 | 0.62 | 1184.4 | 0.168 | 0.168 | 0.168 | 0.156 | 0.123 | 0.099 | 0.026 | 0.026 |
| 13 | 265.0 | 0.0 | 0.109 | 0.62 | 999.8 | 0.174 | 0.174 | 0.174 | 0.164 | 0.129 | 0.100 | 0.027 | 0.028 |
| 14 | 281.8 | 0.0 | 0.111 | 0.62 | 999.8 | 0.179 | 0.179 | 0.179 | 0.168 | 0.133 | 0.104 | 0.028 | 0.029 |
| 15 | 300.4 | 0.0 | 0.101 | 0.64 | 999.8 | 0.184 | 0.184 | 0.184 | 0.173 | 0.138 | 0.108 | 0.026 | 0.030 |
| 16 | 341.8 | 0.0 | 0.102 | 0.64 | 999.7 | 0.196 | 0.196 | 0.196 | 0.184 | 0.147 | 0.103 | 0.025 | 0.032 |
| 17 | 362.1 | 0.0 | 0.097 | 0.64 | 999.7 | 0.201 | 0.201 | 0.201 | 0.188 | 0.150 | 0.121 | 0.012 | 0.033 |
| 18 | 381.1 | 0.0 | 0.093 | 0.65 | 999.5 | 0.206 | 0.206 | 0.206 | 0.192 | 0.154 | 0.124 | -0.006 | 0.034 |
| 19 | 399.8 | 0.0 | 0.097 | 0.64 | 999.5 | 0.210 | 0.210 | 0.210 | 0.197 | 0.157 | 0.123 | -0.003 | 0.034 |
| 20 | 422.6 | 0.0 | 0.099 | 0.64 | 999.2 | 0.215 | 0.215 | 0.215 | 0.202 | 0.162 | 0.127 | -0.019 | 0.037 |
| 21 | 439.8 | 0.0 | 0.101 | 0.64 | 999.1 | 0.219 | 0.219 | 0.219 | 0.205 | 0.165 | 0.130 | -0.020 | 0.041 |

Table A.18: Carb.7 data

# APPENDIX B

# Critical slope for laminar transcritical shallow-water flows

doi:10.1017/jfm.2015.559

# Critical slope for laminar transcritical shallow-water flows

**O. Thual[1,2,†], L. Lacaze[1,2], M. Mouzouri[1,2] and B. Boutkhamouine[1,2]**

[1]Université de Toulouse; INPT, UPS; IMFT, Allée Camille Soula, F-31400 Toulouse, France
[2]CNRS; IMFT; F-31400 Toulouse, France

Backwater curves denote the depth profiles of steady flows in a shallow open channel. The classification of these curves for turbulent regimes is commonly used in hydraulics. When the bottom slope $I$ is increased, they can describe the transition from fluvial to torrential regimes. In the case of an infinitely wide channel, we show that laminar flows have the same critical height $h_c$ as that in the turbulent case. This feature is due to the existence of surface slope singularities associated to plug-like velocity profiles with vanishing boundary-layer thickness. We also provide the expression of the critical surface slope as a function of the bottom curvature at the critical location. These results validate a similarity model to approximate the asymptotic Navier–Stokes equations for small slopes $I$ with Reynolds number $Re$ such that $Re\, I$ is of order 1.

**Key words:** interfacial flows (free surface), low-Reynolds-number flows, thin films

## 1. Introduction

Shallow-flow modelling usually eliminates one or two spatial dimensions by considering average properties over the depth of a thin fluid layer. This modelling approach is current in hydraulics (Chow 1959), dealing with turbulent open-channel flows. In this context, backwater curves denote 1D steady depth profiles $h(x)$ and obey the backwater equation $(1 - Fr)h' = I - J$ where $Fr$ is a Froude number, $I$ is the bottom slope and $J$ is the lineic head loss due to bottom friction. When $I > 0$ is constant, the relative values of the critical height $h_c$, such that $Fr = 1$, and the normal height $h_n$, such that $I = J$, lead to three $M$-curve types in the weak slope regime $h_c < h_n$ and to three $S$-curve types in the strong slope regime $h_n < h_c$. When $I(x)$ varies with space, transitions between the fluvial ($Fr < 1$) and the torrential ($Fr > 1$) regimes can occur through hydraulic jumps or transcritical transition (e.g. Bukreev, Gusev & Lyapidevskii 2002 or Zerihun & Fenton 2006). These backwater curves can

† Email address for correspondence: thual@imft.fr

be viewed as steady solutions of the Saint-Venant equations (de Saint-Venant 1871), also called the shallow-water equations.

The laminar flows of thin viscous liquid layers are also modelled by shallow-flow equations. Benney (1966) and Shkadov (1967) derived such models by retaining only a parabolic velocity profile in a Galerkin approximation of the 2D vertical Navier–Stokes equations and justified it by the good agreement with the experiments of Kapitsa & Kapitsa (1949). Numerous subsequent works have proposed asymptotic expansion leading to a 1D partial differential equation for the depth $h(x, t)$ and the lineic discharge flux $q(x, t)$, often taking into account the effect of surface tension and considering various bottom slopes (Lin 1969; Gjevik 1970; Nakaya 1975; Pumir, Manneville & Pomeau 1983; Alekseenko, Nakoryakov & Pokusaev 1985; Roberts 1996; Oron, Davis & Bankoff 1997; Ruyer-Quil & Manneville 1998, 2000, 2005; Nguyen & Balakotaiah 2000; Shkadov & Sisoev 2004; Boutounet *et al.* 2008; Sadiq & Usha 2008; Fernàndez-Nieto, Noble & Vila 2010; Samanta, Ruyer-Quil & Goyeau 2011; Noble & Vila 2013; Chakraborty *et al.* 2014, ...). Starting with the so-called 'boundary-layer equation', similar to Prandtl's equations (Schlichting 1955), the difficulty of these modelling approaches lies in the information required about the velocity profile in the integration direction. Most works suggest fixed shapes such as the parabolic one in the laminar cases. More elaborate approaches, such as the weighted-residual method of Ruyer-Quil & Manneville (1998), are based on well suited Galerkin approximation functions that minimize the number of resulting equations. Following a different approach, we present an approximation method that leads to a single backwater equation associated with similarity solutions for the velocity profiles.

Here, we consider laminar flows of Newtonian fluids with negligible surface tension effects in the presence of a small and slowly varying bottom slope such that the product $\Gamma = Re\, I$ of the slope $I$ and the Reynolds number $Re$ is of order one, while $I$ is small. For instance, the case $I = 0.01$ and $Re = 100$ satisfies this requirement while ensuring that the flow is laminar. As for most asymptotic expansions, this choice aims to balance a maximum of terms in the equations, that is, for the present case, acceleration, pressure, bottom slope and friction in the momentum equations.

Under this asymptotic expansion, we express the steady solution velocities in the form $u = T/h$ and $v = L(\mathrm{d}h/\mathrm{d}X)/h - \partial M/\partial X$ where $T$, $L$ and $M$ are functions of $X = x/Re$ and $Y = y/h$, being related through $L = YT$ and $\partial M/\partial Y = T$. This leads to the 'TLM model' in which the $X$ dependency of the $T$ profiles is contained in the term $h[(\partial M/\partial X)(\partial T/\partial Y) - (\partial T/\partial X)T]$ that appears to be often small compared to the others. When it is so, the steady flow is described by the similarity model in which $T$ and $L$ no longer depend on $X$ (STL model). Such a similarity assumption for the velocity profiles was introduced by Serre (1953), but the shape of the velocity profiles had to be imposed eventually. Instead of using a Galerkin approximation and averaging over the vertical, as is often done in the literature, our TLM and STL models involve an implicit relation for $h$ and $\mathrm{d}h/\mathrm{d}X$ through a nonlinear 1D eigenvalue problem, as explained in § 2. These models are then compared to each other in § 3 in the case of transcritical flows.

## 2. Three shallow-water steady models

### 2.1. *The TLM shallow-water model*

We consider an infinitely wide channel whose bottom is defined by the equation $z = Z_f(x)$ where $(x, z)$ are respectively the horizontal and vertical coordinates in the

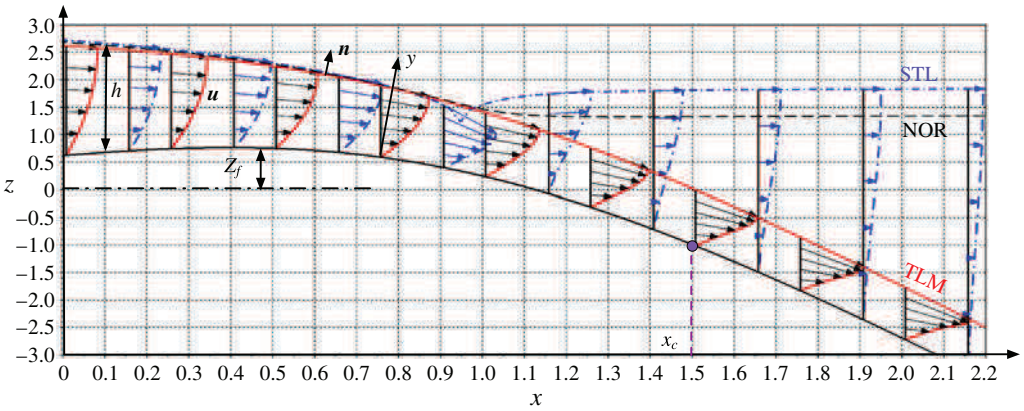


FIGURE 1. 2D flow $\boldsymbol{u}$ of a layer of depth $h$ over a slowly variable bottom $z = Z_f(x)$. Comparison of three shallow-water steady models for a transcritical flow: TLM in plain red, STL in dash-dotted blue and NOR in dashed black. The TLM backwater curve is critical at $x = x_c$.

presence of gravity $g$ (figure 1). If $y$ denotes the coordinate perpendicular to the bottom at some location, we suppose that the slope $I = -Z_f'(x)$ is small enough to consider that $x$ is also the coordinate in the direction tangential to the bottom. Within this approximation and denoting by $\varphi_x$ the derivatives $(\partial\varphi/\partial x)(x, y)$ or $\varphi'(x)$ of a quantity $\varphi$, the steady 2D incompressible Navier–Stokes equations read

$$\left.\begin{aligned} \widetilde{u}_x + \widetilde{v}_y = 0, \quad \widetilde{u}\widetilde{u}_x + \widetilde{v}\widetilde{u}_y &= -\widetilde{p}_x + I + Re^{-1}(\widetilde{u}_{xx} + \widetilde{u}_{yy}), \\ \widetilde{u}\widetilde{v}_x + \widetilde{v}\widetilde{v}_y &= -\widetilde{p}_y - 1 + Re^{-1}(\widetilde{v}_{xx} + \widetilde{v}_{yy}), \end{aligned}\right\} \tag{2.1}$$

where the velocities $\widetilde{u}$ and $\widetilde{v}$ are made non-dimensional by $q^{1/3}g^{1/3}$ and all spatial coordinates by $q^{2/3}g^{-1/3}$, with $q$ denoting the constant lineic discharge flux. The Reynolds number is $Re = q/\nu$ where $\nu$ is the kinematic viscosity.

The boundary conditions at the bottom, defined by the equation $y = 0$, are $\widetilde{u} = \widetilde{v} = 0$. On the free surface, defined by the equation $y = \widetilde{h}(x)$, the kinematic and dynamic boundary conditions are respectively $\widetilde{u}\widetilde{h}_x = \widetilde{v}$ and $(\widetilde{p} - \widetilde{p}_a)\boldsymbol{n} = 2Re^{-1}\widetilde{\boldsymbol{d}} \cdot \boldsymbol{n}$ where $p_a$ is the constant atmospheric pressure, $\boldsymbol{n}$ is the normal to the free surface and $\widetilde{\boldsymbol{d}}$ is the strain rate tensor.

Since the slope $I$ is small, we consider the following asymptotic expansion with $\epsilon \ll 1$:

$$\left.\begin{aligned} \epsilon = Re^{-1}, \quad \Gamma = Re\, I, \quad \widetilde{h} = h(\epsilon x) + O(\epsilon), \\ \widetilde{u} = u(\epsilon x, y) + O(\epsilon), \quad \widetilde{v} = \epsilon v(\epsilon x, y) + O(\epsilon^2), \quad \widetilde{p} = p(\epsilon x, y) + O(\epsilon), \end{aligned}\right\} \tag{2.2}$$

where $\Gamma$, $h$, $v$ and $p$ are of order one. Since $I = O(\epsilon)$, the coordinate $x$ can be considered to refer to the direction tangential to the bottom. We denote by $X = \epsilon x$ the slow streamwise coordinate. At the leading order of the expansion, one gets the following system for $u(X, y)$, $v(X, y)$ and $h(X)$:

$$u_X + v_y = 0, \quad uu_X + vu_y = -h_X + \Gamma + u_{yy}, \tag{2.3a,b}$$

with $u(X, 0) = v(X, 0) = 0$, $u(X, h)h_X = v(X, h)$ and $u_y(X, h) = 0$ for the boundary conditions, with $\int_0^h u(X, y)\,\mathrm{d}y = 1$ as a constraint to express the constant dimensionless discharge flux. Note that the pressure $p$ is hydrostatic in the framework of this analysis.

We look at solutions of (2.3*a*,*b*) with the general form

$$u(X, y) = \frac{1}{h(X)} T\left(X, \frac{y}{h(X)}\right), \tag{2.4}$$

which leads to the 'TLM model' for $T(X, Y)$ and $h(X)$:

$$0 = T_{YY} + h^3(\Gamma - h_X) + h_X T^2 + h(M_X T_Y - T_X T), \tag{2.5}$$

where $M(X, Y) = \int_0^Y T(X, Z)\,\mathrm{d}Z$, with $T(X, 0) = T_Y(X, 1) = 0$ and $M(X, 1) = 1$. The vertical velocity reads $v = (h_X/h)L(X, y/h) - M_X$ with $L(X, Y) = YT(X, Y)$.

This equation with its three constraints determines one unknown scalar. If we impose a bathymetry $Z_f(X)$ of slope $\Gamma(X) = -Z_f'(X)$, we can compute $h'(X) = \Sigma$ where $\Sigma$ is the solution of (2.5) and then integrate to obtain the backwater curve $h(X)$.

### 2.2. *The one-parameter family profiles of the STL model*

We denote by 'STL' the model obtained by ignoring the $h$ term $(M_X T_Y - T_X T)$ in the TLM model. Similarity solutions $u(X, y) = T[y/h(X)]/h(X)$ are thus described by this STL model. Denoting $\Delta = h^3(\Gamma - \Sigma)$, this model reduces to the ordinary differential equation $0 = T'' + \Delta + \Sigma T^2$, subject to the three constraints $T(0) = T'(1) = 0$ and $\int_0^1 T(Y)\,\mathrm{d}Y = 1$. We use a finite difference scheme $(N-1)^2(T_{n+1} - 2T_n + T_{n-1})$ for $n = 2, \ldots, N-1$ to approximate $T''$, where the $T_n$ values are the values of $T$ at $N$ equally distributed points in the interval $Y \in [0, 1]$. The three constraints of (2.5) read $T_1 = T_N - T_{N-1} = 0$ and $\sum_1^N T_n = N$. The function `fsolve` of `Scilab` (Scilab Enterprises 2012) is used with $\Sigma$ considered as a control parameter to determine a branch of solutions $\Sigma = \mathscr{S}(\Delta)$. We have checked that the resolution $N = 101$ provided sufficient accuracy for most of the cases presented here.

Part of the branch of solutions $\Sigma = \mathscr{S}(\Delta)$ passing through the linear case $(\Sigma, \Delta) = (0, 3)$ is displayed in figure 2. The corresponding velocity profiles $T_\Delta(Y)$ range from a shear profile for $\Delta = -\infty$ up to a plug-like profile ($T_\infty = 1$ with a boundary layer at $Y = 0$) for $\Delta = \infty$, passing through the parabolic profile $T_3(Y) = (3/2)Y(2 - Y)$ for the linear case.

In order to obtain a synthetic overview of our STL model, we integrate the equation $0 = T'' + \Delta + \Sigma T^2$ over the interval $Y \in [0, 1]$ to obtain

$$[h^3 - \beta(\Delta)]h'(X) = h^3\Gamma(X) - \alpha(\Delta) \quad \text{with } \Delta = h^3[\Gamma(X) - h'(X)], \tag{2.6}$$

where $\alpha(\Delta) = T_\Delta'(0)$ and $\beta(\Delta) = \int_0^1 T_\Delta^2(Y)\,\mathrm{d}Y$ are plotted in figure 3(*a*). When the velocity profile $T_\Delta$ is the parabolic solution $T_3$, one recovers the values $\alpha(3) = 3$ and $\beta(3) = 1.2$ that are commonly used for laminar shallow flows. The solutions $\Sigma = h'(X)$ of the implicit (2.6) are displayed in figure 3(*b*) as functions of $h$ for various values of $\Gamma$. For $\Gamma \in [1.82, 3]$, the resulting backwater curves exhibit more complex topologies than the usual one obtained with constant values of $\alpha$ and $\beta$.

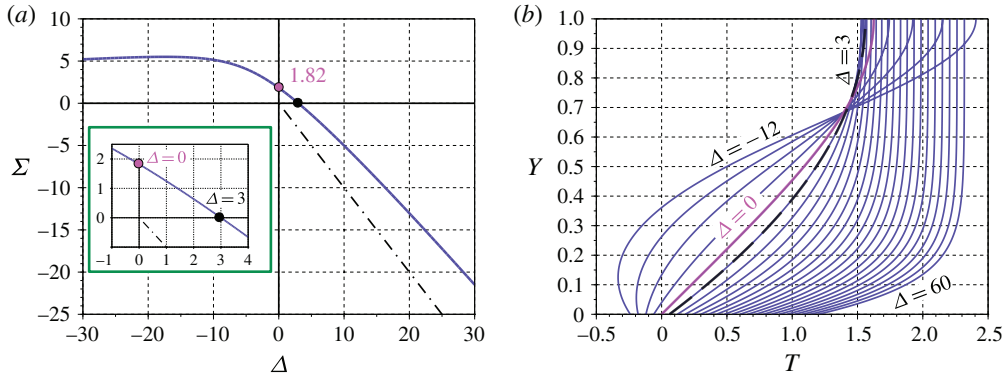


FIGURE 2. (*a*) Branch of solutions $\Sigma = \mathscr{S}(\Delta)$ for $\Delta \in [-30, 30]$ and (*b*) corresponding profiles $T_\Delta(Y) + \Delta/50$ (the shift is for clarity) for $\Delta \in [-12, 60]$. The special value $\mathscr{S}(0) \sim 1.82$ is shown in magenta.

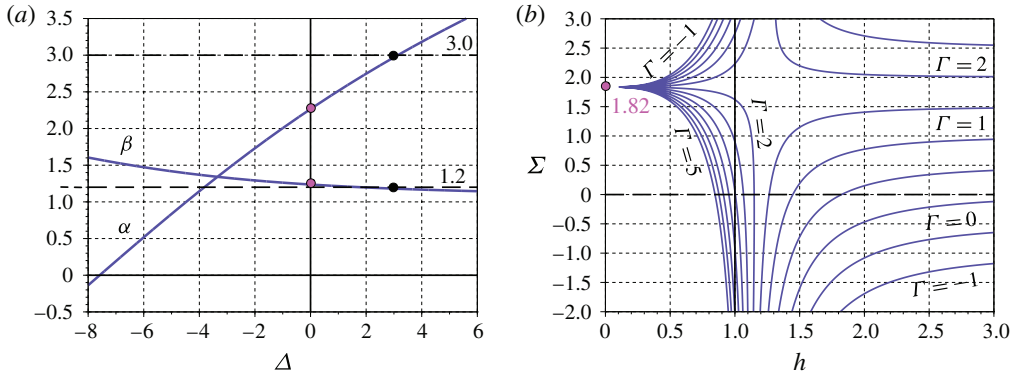


FIGURE 3. (*a*) Plot of $\alpha(\Delta)$ and $\beta(\Delta)$. (*b*) Slope $\Sigma = h_X$ as a function of $h$ for $\Gamma \in [-1, 5]$.

### 2.3. *Determination of the transcritical point with the NOR and STL models*

We denote by NOR the model for which $\alpha = 3$ and $\beta = 1.2$ are kept constant, as if the velocity profiles were stuck to the parabola of the normal flow that would be obtained for $h = h_n = (3/\Gamma)^{1/3}$. The backwater curves are thus solutions of the ordinary differential equation $h'(X) = [h^3\Gamma(X) - 3](h^3 - 1.2)^{-1}$. The general solutions of the NOR model can be sought by considering the family of trajectories $[X(s), h(s)]$ that are solutions of the system $\dot{X} = D(h)$ and $\dot{h} = N(X, h)$ with $D(h) = h^3 - 1.2$ and $N(X, h) = h^3\Gamma(X) - 3$. The critical point $(X_c, h_c)$, forming a saddle node for the phase portrait of the dynamical system, is obtained for $D(h_c) = N(X_c, h_c) = 0$, leading to $h_c = 1.2^{1/3}$ and $\Gamma_c(X_c) = \Gamma_c = 2.5$. The linearization of the dynamical system around the critical point leads to the matrix $\boldsymbol{A}$ with the components $A_{11} = 0$, $A_{12} = D'(h_c) = 3h_c^2$, $A_{21} = h_c^3\xi$ and $A_{22} = 3h_c^2\Gamma_c$ where $\xi = \Gamma'(X_c)$ measures the curvature of the bottom at the critical point. The 'eigenslopes' of $\boldsymbol{A}$, that is the slope of its eigenvectors, read

$$\Sigma_\pm(\xi) = \frac{\Gamma_c}{2}\left(1 \pm \sqrt{1 + \frac{4\xi h_c}{3\Gamma_c^2}}\right). \tag{2.7}$$

It appears that this expression is also valid for the STL model (2.6) with $h_c = 1$ and $\Gamma_c = 3$. To prove it, we consider, as for the NOR model, the following dynamical system:

$$\left.\begin{aligned} \dot{X} &= D[X, h, \dot{h}/\dot{X}] \quad \text{with } D(X, h, \Sigma) = h^3 - \beta(h^3[\Gamma(X) - \Sigma]), \\ \dot{h} &= N[X, h, \dot{h}/\dot{X}] \quad \text{with } N(X, h, \Sigma) = h^3\Gamma(X) - \alpha(h^3[\Gamma(X) - \Sigma]). \end{aligned}\right\} \tag{2.8}$$

At first, the critical point is at the intersection of the lines $\dot{h} = 0$ and $\dot{X} = 0$ in the $(X, h)$ plane. The first condition reads $\Delta = \alpha(\Delta)$, leading to $\Delta = 3$ and $h = h_n(X) = [3/\Gamma(X)]^{1/3}$. It describes the lines of the normal heights as $\Sigma = 0$. The second condition can be satisfied only when $h'(X) \to -\infty$ and leads to $h = 1$ since it can be numerically checked that $(1 - \beta)/\alpha \to 0$ when $\Delta \to +\infty$. As announced, we find $h_c = 1$ and $\Gamma(X_c) = 3$ when both conditions are met.

We now determine whether a straight line trajectory with the equation $X_\Sigma(s) = X_c + \eta(s)$ and $h_\Sigma(s) = h_c + \Sigma\eta(s)$, where $\Sigma$ is a constant and $\eta(s) = \exp(\lambda s)$ is a small parameter, can satisfy (2.8) at the dominant order of $\eta \ll 1$. Such a property is equivalent to

$$\left.\begin{aligned} \boldsymbol{L}(\Sigma)\cdot\phi = \lambda\phi \quad &\text{with } \phi = \begin{pmatrix} 1 \\ \Sigma \end{pmatrix}, \quad \boldsymbol{L}(\Sigma) = \boldsymbol{A} + \boldsymbol{B}(\Sigma), \\ \boldsymbol{A} = \begin{pmatrix} 0 & 3h_c^2 \\ h_c^3\xi & 3h_c^2\Gamma_c \end{pmatrix} \quad &\text{and} \quad \boldsymbol{B}(\Sigma) = \begin{pmatrix} -h_c^3\xi\beta' & -3h_c^2(\Gamma_c - \Sigma)\beta' \\ -h_c^3\xi\alpha' & -3h_c^2(\Gamma_c - \Sigma)\alpha' \end{pmatrix}, \end{aligned}\right\} \tag{2.9}$$

where $\xi = \Gamma'(X_c)$, $\alpha' = \alpha'[h_c^3(\Gamma_c - \Sigma)]$ and $\beta' = \beta'[h_c^3(\Gamma_c - \Sigma)]$. We have $\boldsymbol{A}\cdot\phi = \lambda\phi$ under the conditions $\lambda = 3h_c^2\Sigma$ and $h_c^3\xi + 3h_c^2\Gamma_c\Sigma = 3h_c^2\Sigma^2$. In that case, we see that $\boldsymbol{B}(\Sigma)\cdot\phi = \boldsymbol{0}$. This shows that if $\Sigma$ is a critical slope of $\boldsymbol{A}$, it is also a critical slope of $\boldsymbol{L}(\Sigma)$ while being given by (2.7). We note that this property is independent of the functions $\alpha(\Delta)$ and $\beta(\Delta)$, whose roles are confined to the determination of $h_c$ and $\Gamma_c$.

## 3. Numerical simulations of critical transitions over obstacles

### 3.1. *Numerical method for the TLM model and constant slope comparison*

In order to solve (2.5) numerically, we discretize the variables $X$ and $h$ into successive values $X^i$ and $h^i$ for $i = 1, \ldots, H$. Choosing two positive weights $\theta$ and $\zeta$ such that $\theta + \zeta = 1$, we build an implicit finite difference scheme to solve for the system (2.5) in the form

$$\begin{aligned} 0 \;=\; & (\theta T_{YY}^{i-1} + \zeta T_{YY}^{i}) + (h^{i-1} + \zeta\,\mathrm{d}h^i)^3(\Gamma - \Sigma) + \Sigma[\theta(T^{i-1})^2 + \zeta(T^i)^2] \\ & + \frac{h^{i-1} + \zeta\,\mathrm{d}h^i}{\mathrm{d}h^i}\Sigma[(M^i - M^{i-1})(\theta T_Y^{i-1} + \zeta T_Y^i) - (T^i - T^{i-1})(\theta T^{i-1} + \zeta T^i)], \end{aligned} \tag{3.1}$$

where the bottom slope is $\Gamma = \theta\Gamma(h^{i-1}) + \zeta\Gamma(h^i)$. The surface slope $\Sigma$ that results from this implicit equation must be considered as $\Sigma = \theta\Sigma^{i-1} + \zeta\Sigma^i$. As $\mathrm{d}h^i = h^i - h^{i-1}$, we then set $\mathrm{d}h^i = \Sigma\,\mathrm{d}X^i$ with $\mathrm{d}X^i = X^i - X^{i-1}$ to simulate the differential equation $h_X = \Sigma$ with an explicit Euler scheme. These steps are modified near singularities. The vertical scheme is the same as the one used for the STL model. We denote by $T^0(Y) = T_0(Y)$ the initial condition. A centred scheme $\theta = \zeta = 1/2$ has been chosen.

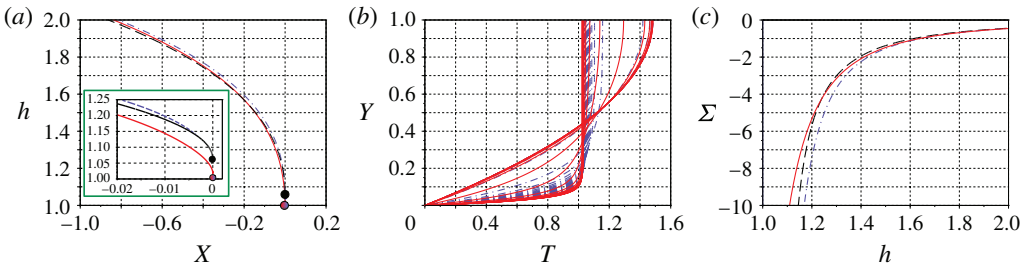


FIGURE 4. Comparison of the TLM (plain red), STL (dash-dotted blue) and NOR (dashed black) models near a surface slope singularity at $X = 0$ for $\Gamma = 0$. ($a$) Backwater curve $h(X)$. ($b$) Associated velocity profiles $T(X)$. ($c$) Corresponding curves $\Sigma = h'(X)$ as functions of $h$.

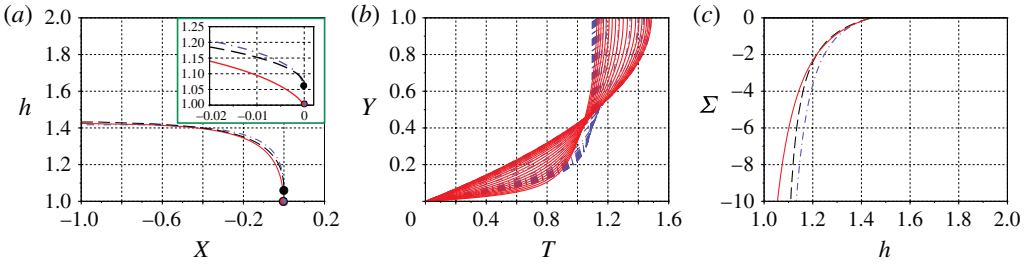


FIGURE 5. Same as figure 4 for $\Gamma = 1$. In contrast to the $\Gamma = 0$ case, $h_n \sim 1.44$ is bounded.

A first comparison between the TLM, STL and NOR models is made for the case of constant slope $\Gamma = 0$. We start with an initial condition with $h_0$ high enough that $T_0(Y)$ can be approximated by a parabola. A singularity at finite length is expected as shown in figure 4. The singularities of the three models have been translated to $X = 0$ in order to compare them. The heights of these backwater curves differ by only 5 %, which is also the order of magnitude of the difference between the critical height $h_c = 1$ of the TLM and STL models and the critical height $h_c \sim 1.06$ of the NOR model. Similar results are found with non-vanishing slopes $\Gamma \neq 0$ (e.g. figure 5). These flows can be viewed as the fluvial regime of a transcritical transition through a bottom slope discontinuity.

### 3.2. *Phase portraits for semi-parabolic bottom shapes*

We now choose a semi-parabolic bottom profile $Z_f(X)$ such that $\Gamma(X) = -Z_f'(X)$ reads $\Gamma(X) = \xi X$ for $X \geqslant 0$ and $\Gamma(X) = 0$ for $X \leqslant 0$. A comparison of the phase portrait for the TLM, STL and NOR models is shown in figure 6 for two values of $\xi$. The initial conditions, taken at $X = -1$, are set to explore the vicinity of the TLM critical point reached for $X = 3$ for $\xi = 1$ and $X = 0.3$ for $\xi = 10$. The initial velocity profile for the TLM is computed from the STL model for the same value of initial height $h_0$. A fine tuning of these values (up to twelve digits) shows that $(\Gamma_c, h_c) \sim (3, 1)$ as predicted by our theory.

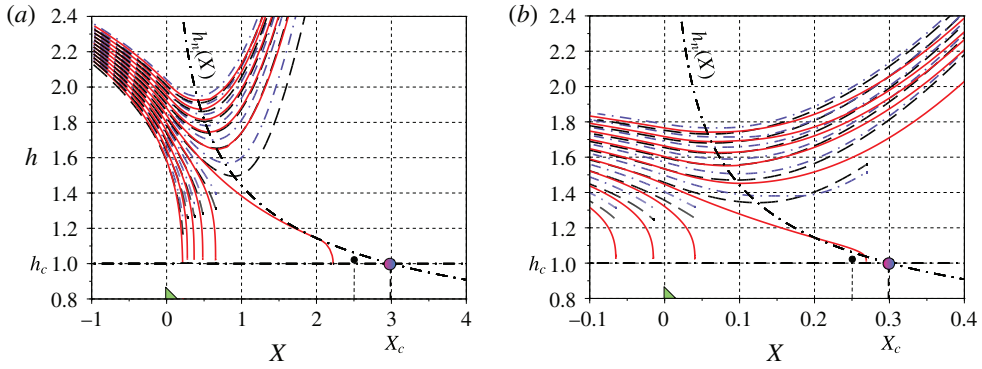


FIGURE 6. Phase portrait comparison between the TLM (plain red), the STL (dash-dotted blue) and the NOR (dashed black) models for a parabolic bottom ramp $Z_f(X) = -\xi X^2/2$ for $X \geqslant 0$ and $Z_f(X) = 0$ for $X \leqslant 0$. The normal heights $h_n(X)$, defined for $X > 0$, are shown by dashed-dotted lines. Determination of the critical point for (*a*) $\xi = 1$ and (*b*) $\xi = 10$.

The negative slope of the critical trajectory in the $(X, h)$ plane can be compared to the expression (2.7) that reads here

$$\Sigma_-(\xi) = \frac{3}{2}\left(1 - \sqrt{1 + \frac{4\xi}{27}}\right) = -\frac{1}{9}\xi + \frac{1}{243}\xi^2 + O(\xi^3). \tag{3.2}$$

This can be done visually by considering the curve of the normal height profiles $h_n(X) = [\Gamma(X)/3]^{1/3}$ and noticing that $h_n'(X_c) = -\xi/9$. For $\xi = 1$, the proximity of the slopes $\Sigma_-(1) \sim h_n'(X_c) \sim -0.11$ can be seen in figure 6. For $\xi = 10$, the discrepancy between $\Sigma_-(10) = -0.86$ and $h_n'(X_c) = -1.11$ can be discerned visually.

These backwater phase portraits help to explain why the NOR model fails to catch the correct values of $\Gamma_c$ and $h_c$. Indeed, the singularities of the phase portraits are associated with plug-like velocity profiles $T(Y)$ with $\beta = \int_0^1 T^2\,\mathrm{d}Y \to 1$ while this shape factor is stuck at $\beta = 1.2$ for the NOR model.

### 3.3. *Bottom shape inverse problem and validation of the critical slope relation*

Rather than computing the unique critical backwater $h(X)$ that links the fluvial and torrential regimes for a given bottom slope profile $\Gamma(X)$, which is cumbersome, we consider the inverse problem of computing the latter, given the former. This is done by considering that $\Sigma$ and $\Gamma$ are respectively known and unknown in the implicit (3.1).

We choose $h(X) = \overline{h} + \Delta h \tanh(X/L)$ with $\overline{h} = (h_1 + h_2)/2$ and $\Delta h = (h_2 - h_1)/2$ such that $h_1 = (3/\Gamma_1)^{1/3}$ and $h_2 = (3/\Gamma_2)^{1/3}$ are the normal heights associated with the bottom slopes $\Gamma_2 > \Gamma_1$. The corresponding $\Gamma(X)$ in the cases $\Gamma_1 = 1$, $\Gamma_2 = 4$ and $L = 0.8$ is displayed in figure 7(*a*) for both the TLM and STL models. Further numerical experiments show that the discrepancy between the two models disappears when $L$ increases. We also observe that $\Gamma \sim 3$ when $h = 1$, which confirms the value of the critical slope $\Gamma_c = 3$. This defines the location $X_c$ of the critical point. For each value of $L$, we then compute $\xi = \Gamma'(X_c)$, which traces back the curvature of the bottom at the critical point. Its relation with the critical slope $\Sigma_c = \Sigma(X_c)$ is shown in figure 7(*b*) and compared (dashed-dotted blue curve) with the function $\Sigma_-(\xi)$ of (3.2), derived from the STL model. We observe a satisfactory agreement compared to

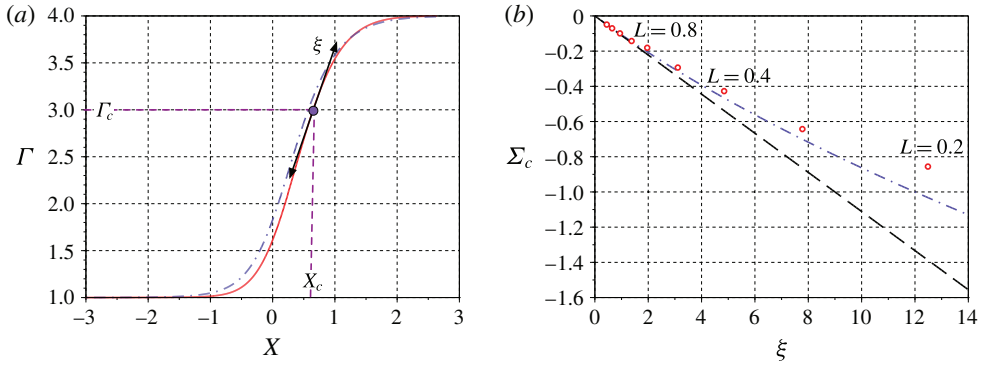


FIGURE 7. Slope $\Gamma(X)$ such that $h(X) = \overline{h} + \Delta h \tanh(X/L)$ is the critical backwater curve in the cases $\Gamma_1 = 1$ and $\Gamma_2 = 4$. (*a*) Comparison between the TLM (plain red) and the STL (dash-dotted blue) for $L = 0.8$. (*b*) Critical surface slope $\Sigma_c = h'(X_c)$ as a function of the bottom curvature $\xi = \Gamma'(X_c)$ for $L = 2^{k/2}/10$ and $k = 2, 3, \ldots, 11$. Comparison with the theoretical functions for the STL (dash-dotted blue) and the NOR (dashed black) models.

the NOR model, which can only predict a critical slope $\Sigma_c = h_n'(X) = -\xi/9$ given by the normal height profile $h_n(X)$.

## 4. Conclusion

We have shown that the STL model, based on a similarity assumption $u = T(y/h)/h$ for the streamwise velocity $u(X, y)$, could provide a reasonable approximation of the TLM model that takes into account the $X$-dependency of $u = T(X, y/h)/h$ beyond that of the height profile $h(X)$. We proved this to be the case for the critical transition of a laminar shallow-water flow in the presence of a bottom with increasing slope $\Gamma(X)$. Through numerical simulations of the TLM model, which involve the resolution of an implicit nonlinear differential equation, we have checked the validity of the relation (3.2) between the critical surface slope $\Sigma_c = h'(X_c)$ and the bottom curvature factor $\xi = \Gamma'(X_c)$ computed at the critical location $X = X_c$.

We have shown that the critical values were $h_c = 1$ and $\Gamma_c = 3$ for a Newtonian rheology in the laminar case, contrarily to the commonly used NOR model that leads to $h_c = 1.2^{1/3} \sim 1.06$ and $\Gamma_c = 2.5$, as shown in § 2.3. Other rheologies would provide different values in the framework of the STL approach. Indeed, these generalizations lead to different functions $\alpha(\Delta) = T'(0)$, related to the bottom friction, and $\beta(\Delta) = \int_0^1 T^2 \, \mathrm{d}Y$, related to the shape of the velocity profiles. These functions provide the values of $h_c^3 = \lim_{\Delta \to \infty} \beta(\Delta)$ and $\Gamma_c$ as the solution of $\Delta_n = \alpha(\Delta_n)$ with $\Delta_n = h_c^3 \Gamma_c$. But there is a universality of the critical slope expression through (2.7) that involves only $h_c$, $\Gamma_c$ and $\xi = \Gamma'(X_c)$.

The STL model is likely to provide a good approximation of the TLM model for other shallow-water regimes, as is suggested by comparison of the backwater curves of the two models, for instance in the $(h, \Sigma)$ representation of figure 3. Such an exhaustive plot in the case of the TLM model could not be shown here due to numerical problems that lead to instabilities or failure of the implicit problem resolution for some regions of the $(h, \Sigma)$ plane. Numerical methods to overcome this difficulty are to be explored. This could validate the complex classification of the backwater curves associated with the STL model, due to multiple values of $\Sigma = h'(X)$ as a function of $h$ for $\Gamma \in [1.82, 3]$.

An extension of our approach to unsteady flows is under way. This could improve the temporal and spatial stability analysis of the normal flows (Thual, Plumerault & Astruc 2010, and references therein). We think that numerous flow analyses, such as roll waves or hydraulic jumps (Thual 2013, and references therein), could be enriched in the light of these TLM and STL shallow-water models. Their generalization to non-Newtonian rheologies and turbulence parameterization is possible. Finally, taking into account capillarity effects in these models is worth pursuing in order to address, with our approach, the vast literature devoted to thin viscous films.

## Acknowledgement

This work was performed in the framework of the PHYSCALE project of the RTRA STAE foundation (http://www.fondation-stae.net).

## References

ALEKSEENKO, S. V., NAKORYAKOV, V. YE. & POKUSAEV, B. G. 1985 Wave formation on a vertical falling liquid film. *AIChE J.* **31** (9), 1446–1460.

BENNEY, D. J. 1966 Long waves on liquid films. *J. Math. Phys.* **45** (2), 50–155.

BOUTOUNET, M., CHUPIN, L., NOBLE, P. & VILA, J.-P. 2008 Shallow water viscous flows for arbitrary topopgraphy. *Commun. Math. Sci.* **6** (1), 29–55.

BUKREEV, V. I., GUSEV, A. V. & LYAPIDEVSKII, V. YU. 2002 Transcritical flow over a ramp in an open channel. *Fluid Dyn.* **37** (6), 896–902.

CHAKRABORTY, S., NGUYEN, P.-K., RUYER-QUIL, C. & BONTOZOGLOU, V. 2014 Extreme solitary waves on falling liquid films. *J. Fluid Mech.* **745**, 564–591.

CHOW, V. T. 1959 *Open-channel Hydraulics*. McGraw-Hill.

FERNÀNDEZ-NIETO, E. D., NOBLE, P. & VILA, J.-P. 2010 Shallow water equations for non-newtonian fluids. *J. Non-Newtonian Fluid Mech.* **165** (1314), 712–732.

GJEVIK, B. 1970 Occurrence of finite amplitude surface waves on falling liquid films. *Phys. Fluids* **13** (8), 1918–1925.

KAPITSA, P. L. & KAPITSA, S. P. 1949 Wave flow of thin layers of a viscous liquid. *Zh. Eksp. Teor. Fiz.* **19**, 105–120.

LIN, S. P. 1969 Finite-amplitude stability of a parallel flow with a free surface. *J. Fluid Mech.* **36**, 113–126.

NAKAYA, C. 1975 Long waves on a thin fluid layer flowing down an inclined plane. *Phys. Fluids* **18** (11), 1407–1412.

NGUYEN, L. T. & BALAKOTAIAH, V. 2000 Modeling and experimental studies of wave evolution on free falling viscous films. *Phys. Fluids* **12** (9), 2236–2256.

NOBLE, P. & VILA, J.-P. 2013 Thin power-law film flow down an inclined plane: consistent shallow-water models and stability under large-scale perturbations. *J. Fluid Mech.* **735**, 29–60.

ORON, A., DAVIS, S. H. & BANKOFF, S. G. 1997 Long-scale evolution of thin liquid films. *Rev. Mod. Phys.* **69**, 931–980.

PUMIR, A., MANNEVILLE, P. & POMEAU, Y. 1983 On solitary waves running down an inclined plane. *J. Fluid Mech.* **135**, 27–50.

ROBERTS, A.J. 1996 Low-dimensional models of thin film fluid dynamics. *Phys. Lett.* A **212** (12), 63–71.

RUYER-QUIL, C. & MANNEVILLE, P. 1998 Modeling film flows down inclined planes. *Eur. Phys. J.* B **6** (2), 277–292.

RUYER-QUIL, C. & MANNEVILLE, P. 2000 Improved modeling of flows down inclined planes. *Eur. Phys. J.* B **15** (2), 357–369.

RUYER-QUIL, C. & MANNEVILLE, P. 2005 On the speed of solitary waves running down a vertical wall. *J. Fluid Mech.* **531**, 181–190.

SADIQ, I. M. R. & USHA, R. 2008 Thin newtonian film flow down a porous inclined plane: stability analysis. *Phys. Fluids* **20** (2), 022105.

# APPENDIX C

# 1D steady state Saint Venant model for mud flow in Venturi flumes

# 1D Steady State Saint Venant model for mud flow in Venturi flumes

**Miloud Mouzouri[1,2], Olivier Thual [2], Laurent Lacaze[2] and Prasanna Amur Varadarajan[1]**

[1]Geoservices, Roissy-en-France, 95700, FRANCE
[2]Institut de Mecanique des Fluides de Toulouse, Toulouse, 31400, FRANCE

***Abstract*—A Venturi flume is an open channel flowmeter, which is a flow line with a constrict in that causes a drop in the hydraulic grade line, creating a critical depth. This critical state appears when the flow transitions from subcritical to supercritical state. This solution is commonly used in water engineering to measure the flow rate. The challenge here is to extend this solution to non-Newtonian mud flows. Venturi flume flows have been simulated using a simplified 1D model based on Shallow Water theory and a friction model taking into account the rheology of the fluid and the variation of the geometry along the open channel. The model is validated by series of experiments with both Newtonian & non-Newtonian fluids, and also validated by using 3D CFD.**

***Keywords*—Venturi flume, Flow rate measurement, Open channel flow, 1D Saint Venant/Shallow water Equations, Non-Newtonian fluids, CFD, OpenFoam.**

## I. Introduction

### A. Background & Motivation

CONTROL of the downhole pressure is critical in drilling operations. If the downhole pressure exceeds the strength of the formation, the wellbore can be fractured, causing a loss of drilling fluid to the formation and possibly damaging the reservoir. In the worst case, such a damage may cause an uncontrolled reduction in the downhole pressure. If, on the other hand, the downhole pressure reduces below the formation pore pressure, this may cause an unwanted influx of formation fluid into the wellbore and up the annulus, referred to as a kick, which in the worst case could escalate to a blow-out of hydrocarbons on the rig, e.g. the Deepwater Horizon incident in 2012 [1]. For safe operations, the downhole pressure should thus be kept within a window defined by the formation fracture pressure and the formation pore pressure.

Early detection of loss of drilling fluid to the formation or of a kick is the most effective measure that can be taken to eliminate or limit the consequences of such incidents. A prerequisite for detecting loss to the formation or kick during drilling operations is monitoring the mass balance of the well, i.e. the flow of drilling fluid out of the well compared to that pumped into the well.

The most basic method of monitoring the flow out of the well while drilling is using simple paddle (Figure 1 : solution 1) which is an inaccurate measurement that limits the resolution of kick/loss detection. The other solution it to use a Coriolis flow meter (Figure 1 : solution 2) which is quite an accurate solution but involves expensive installation costs and setup. A possible alternative is to use a Venturi flume (Figure 1 : solution 3) which is an open channel with a constriction designed to give a jump in the fluid level which holds information about the flow rate. Venturi flumes are typically used to measure large flows of water but rarely used for other fluids. The challenge here is to extend this solution to our drilling application.

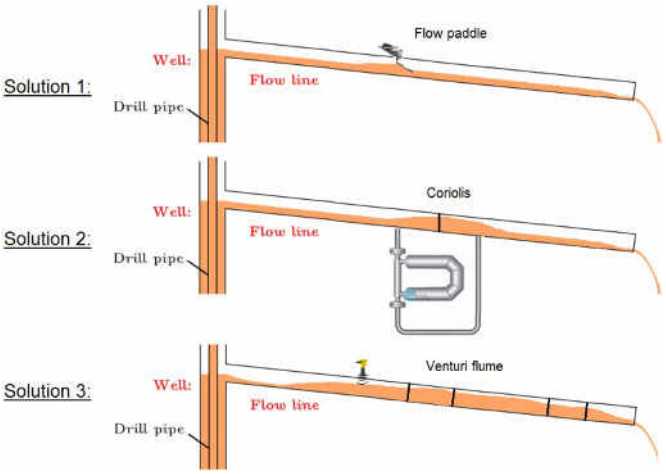


Fig. 1: Solution to measure the flow out the well.

The summary of this paper is as follows, we describe a 1D model for the non-Newtonian mud flow in Venturi flume to provide the relationship of the flow rate with the free surface height of the flow. The steady-state 1D Saint Venant Equations were extended for mud flow through flume including the non-Newtonian flow friction model. The numerical strategy to solve the equations are described by adressing the technical challenge near the critical point for the transcritical flows. The 1D model is validated against a series of experiments with both Newtonian and non Newtonian fluids. Few computations are done using 3D CFD with OpenFoam. The results are compared and validated with good accuracy.

Manuscript received May 10, 2016; revised May 15, 2016. Corresponding author: Miloud Mouzouri (MMouzouri@slb.com)

This paper is organized as follows, we described the principle of the flume on section I. Section II describes the governing equations of the 1D model, the numerical strategy for solving the model. Serction III describes in details the friction term for the 1D model. Section IV describes experimental setup and the series of experiments. Section V describes the 3D CFD model using open source software. Section VI compares and validates models with experiments.

### B. Principle

The principle behind Venturi flume is to impose a critical condition in the flow regime (since it is an open channel flow, the critical condition is obtained when Froude number is equal to 1). This is obtained by having a subcritical flow at the inlet of the flume and accelerating it to supercritical flow at the outlet. The flume is designed with a convergent part, throat and a divergent part to obtain the above mentioned flow configuration. The reason for making the flow critical is that, once we have a measurement of critical height we can relate it directly to the flowrate without measuring the velocity. However, it is difficult to measure the critical height with sufficient accuracy because of its location and the slope in the height along the flume at the critical point. Instead, we must measure the height upstream ($h$ in Figure 2), relate it to the critical height ($h_c$ in Figure 2) and compute the flow rate ($Q$). This is done by modelling the height variation along the flume.

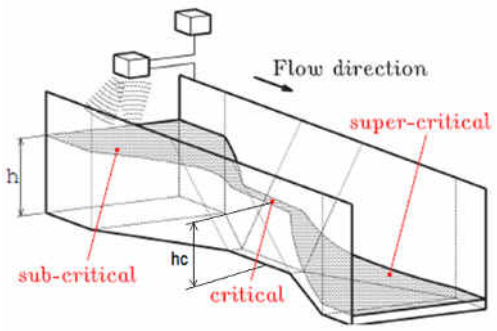


Fig. 2: Transitional flow along a trapezoidal venturi flume.

### C. Earlier works

Flume has been mainly used in the water industry as described in the ISO standard [2], but we wish to extend this device to measure mudflow rates in our drilling environment which means that we have to take into account the rheology of the mud. Thus to use this device and relate the height measurement to flow rate, we require more detailed model than the ISO standard that describes the flow through this device. One method is to model free surface flow using 1D Saint Venant Equations for our device.

## II. Governing equations

Saint Venant Equations (SVE), from Saint Venant [18], can be derived by averaging the three dimensional Navier-Stokes equations over the cross-section of the channel, as described Aldrighetti [3]. The basic assumptions for the analytical derivation of the Saint Venant Equations are

- the flow is one-dimensional, i.e. the velocity is uniform over the cross-section and the fluid level across the section is represented by a horizontal line,
- the streamline curvature is small and the vertical accelerations are negligible, so that the pressure can be taken as hydrostatic.

The detailed analysis of transient Saint Venant Equations and its appropriate numerical solvers are discussed in the works of Leveque [13]. Since we are interested in the steady state conditions, the equations in the 1D approximation for our vayring geometry along the flume can be written as Chow [8]

$$au = Q \tag{1}$$

$$\partial_x(\beta a u^2) = -ga\partial_x(h) + ga\partial_x(z_b) - \frac{1}{2} f P_w u^2 \tag{2}$$

Where $Q$ is the flow rate, $u$ the mean velocity of the fluid, $a$ the cross section area occupied by the fluid, $h$ the height of the fluid, $g$ acceleration due to gravity, $z_b$ the bottom level of the flume, $P_w$ the wetted perimeter, $f$ the fanning friction coefficient and $\beta$ the momentum coefficient.

There are different geometries of Venturi flume, as described in the ISO standard, but we have chosen to use a trapezoidal shape. Indeed, trapezoidal Venturi flumes are more adapted to measure large range of flow rates and even small flow rates with good accuracy. We introduce parameters ($b$ and $m$) to characterise our trapezoidal geometry as described in the figure 3.

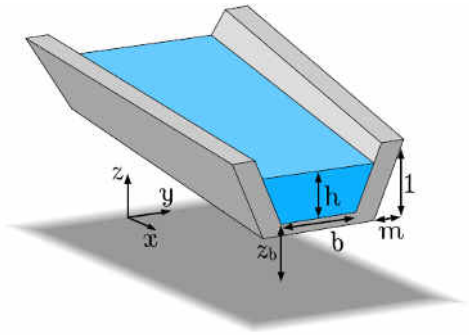


Fig. 3: Venturi flume parameters.

Where $b$ is the bottom width and $m$ the side slope of the flume. Then, we can rewrite the equations (1) and (2) as a function of height $h$ and the other geometrical parameters $b$ and $m$, as currently done in the literature with Thual [4].

$$\frac{\partial h}{\partial x} = \frac{\beta Fr^2 Ig_1 - \partial_x(z_b) - Fr^2 f(Re) Ig_2}{1 - \beta Fr^2} \tag{3}$$

where non-dimension numbers in the above equations are

- $Fr$ : Froude number

$$Fr = \frac{u}{g\frac{a}{b+2mh}} \tag{4}$$

- $Re$ : Generalized Reynolds number

$$Re_g = \frac{8\rho u^2}{\tau_0 + k\left(\frac{8u}{D_h}\right)^n} \tag{5}$$

- $Ig_1$ : Geometrical number 1

$$Ig_1 = \frac{h\partial_x(b) + h^2\partial_x(m)}{b+2mh} \tag{6}$$

- $Ig_2$ : Geometrical number 2

$$Ig_2 = \frac{b+2h\sqrt{1+m^2}}{b+2mh} \tag{7}$$

where $D_h$ is the hydraulic diamater (equal to $4a/P_w$) and $(\tau_0, k, n)$ are the parameters of the Herschel Bulkley model used to characterise non-Newtonian fluids. When $\beta = 1$, we see directly that in equation 3 the denominator is equal to 0 at $Fr = 1$ indicating the three regimes of the flow which are

- $Fr < 1$ : subcritical flow, where the fluid velocity is smaller than the wave velocity
- $Fr = 1$ : critical flow, where the fluid velocity is equal to the wave velocity
- $Fr > 1$ : supercritical flow, where the fluid velocity is bigger than the wave velocity

The form of the equation (3) is currently used to model transcritical transition. It is an ordinary differential equation on height but needs to be solved taking into account the singularity, i.e. when the denominator is equal to 0. In our case, this singularity happens when the flow transitions from subcritical to supercritical regime.

*Numerical strategy*

To avoid the difficulty of the singularity, we have to solve separately the three regimes : subcritical flow, critical flow and supercritical flow. Then the singularity will happen only on the critical flow. The critical flow appears when the derivative of $h$ is undefined, which is when

$$numerator : \beta Fr^2 Ig_1 - \partial_x(z_b) - Fr^2 f(Re) Ig_2 = 0 \tag{8}$$

$$denominator : 1 - \beta Fr^2 = 0 \tag{9}$$

These equations 8 and 9 are solved to get the critical height $h_c$ and the critical location $x_c$. In our configuration and our range of flow rates, the location of the critical point $x_c$ is always found at the end of the throat and before the divergent part. Then we can define the critical flow at $x_c$ with values of height $h_c$ computed for each flows.

To solve the subcritical flow, we have to integreate the differential equation 3 from $(x_c - \epsilon_x, h_c + \epsilon_h)$ and the supercritical flow from $(x_c + \epsilon_x, h_c - \epsilon_h)$. Values of $\epsilon_x$ and $\epsilon_h$ are small variations of $x$ and $h$ and need to be determined by doing a Taylor series expension around the critical point. With this strategy, we can solve for transcritical flows along Venturi flume.

We use matlab and ode45 function solver to solve the equation 3 using the strategy defined before. Ode45 is based on an explicit Runge-Kutta formula as the Dormand-Prince pair [17]. That means the numerical solver ode45 combines a fourth order method and a fifth order method, both of which are similar to the classical fourth order Runge-Kutta method. This solver appears accurate and faster with computation time less than 1 seconde for 1000 spatial points along $2m$ length.

The other difficulty is to model the friction. Indeed, the friction will model the effect of rheology on the flow and will have an important impact on results. So we have to model it properly and estimate it at each location along the flume because of the change in geometry. So we will use the SVE model to compute the height profile along the Venturi flume with a sub-model for friction, with estimation of $f$ and $\beta$, taking into account the rheology and change of geometry. The details are given bellow.

## III. Friction model

The biggest challenge is to model the friction coefficients $f$ and $\beta$ for a change of geometry and rheology, which capture the 3D nature of the flow, in 1D. These are well known for closed channel pipe flows and rectangular channel flows but not for open channel flows with changing geometry.

### A. Fanning friction coefficient

The fanning friction coefficient $f$, named after J. T. Fanning, is a non dimensional number that relates shear stress at the wall $\tau$ to the velocity $u$.

$$\tau = \frac{1}{2}\rho f u^2 \tag{10}$$

It can be relat to the pressure loss due to the friction. This friction factor is one-fourth of the commonly used Darcy friction factor. For laminar flow, this friction factor can be written as

$$f = \frac{K}{Re_g} \tag{11}$$

With a coefficient $K$ depending on the geometry, as described Burger [5], and is equal to 14.6 for triangular flumes with a vertex angle of 90°, 16.2 for semi-circular flumes, 16.4 for rectangular flumes and 17.6 for trapezoidal flumes with 60° sides. For simple geometries like circular pipes, this coefficient can be computed analytically and is equal to 16, but still difficult to compute analytically for complex geometries.

For turbulent flow, there are a lot of models based on pipes experiments and correlations to approximate this factor. The best known is the implicit relation of Colebrook [6]. Various explicit approximations of this relation have been developed. Churchill [7] developed a formula that covers the friction factor for both laminar and turbulent flow for pipe. This was originally produced to describe the Moody chart, which plots the Darcy friction factor as a function of Reynolds number. The idea here is to adapt the Churchill relation given for pipe to a general relation working for other shape using the $K$ coefficient, working for non-Newtonian fluids using the

generalized Reynolds number $Re_g$ and adapt to open channel flow with the hydraulic diameter $D_h$ and surface roughness $\epsilon$

$$f = \left( \left( \frac{K}{Re_g} \right)^{12} + 2^{12} \left( A + B \right)^{-1.5} \right)^{\frac{1}{12}} \tag{12}$$

$$A = \left( 2.457 ln \left( \left( \left( \frac{7}{Re_g} \right)^{0.9} + 0.27 \frac{\epsilon}{D_h} \right)^{-1} \right) \right)^{16} \tag{13}$$

$$B = \left( \frac{37530}{Re_g} \right)^{16} \tag{14}$$

### B. Momentum coefficient $\beta$

The momentum coefficient is a dimensionless number based on the velocity profile and is defined as

$$\beta = \frac{\frac{1}{a} \int u^2 dS}{\left( \frac{1}{a} \int u dS \right)^2} \tag{15}$$

Few experimental investigations on the computation of $\beta$ has been done by Chow [8] who proposed a way to estimate this coefficient for simple velocity distribution like linear or logarithmic but for water flows in turbulent regime. It was found, as in Al-Khatib [16], that $\beta$ is around 1 but still depends of the channel geometry. Typically, for an ideal inviscid fluid $\beta$ is equal to 1, and for Newtonian turbulent flows currently $\beta$ is assumed to be 1. But for other fluids, as muds in laminar regime, we cannot assume $\beta = 1$ and it needs to be modeled.

### C. Velocity profile model

To estimate the friction, a first approximation would be to take $K$ and $\beta$ constant and calibrate on experiments. A better approximation would be to relate them to the velocity profile based on rheology and geometry. So we consider a steady flow with constant free stream velocity (similar to Blasius assumption of flat plate flow), which corresponds to a flow over a flat plate that is oriented parallel to the free surface flow.

With this assumption, consider a laminar non-Newtonian fluid flow on an infinite plane, inclined with an angle $\theta$ with the horizontal direction as shown in the figure 4. In the case of a yield stress fluid, the flow is characterized by the existence of a solid phase in a field such that $y \in [h_y, h]$, where $h_y$ denotes the height of the sheared fluid layer and $h$ the height of the free surface. We consider a normal flow with velocity $u(y)$ along $x$ and a constant height.

We solve the momentum equation (16) considering only the pressure gradient and the shear stress terms as

$$0 = -\frac{\partial p}{\partial x} + \frac{\partial \tau}{\partial y} \tag{16}$$

with an hydrostatic pressure defined as

$$p = \rho g (h - y_0) + p_{atm} \tag{17}$$

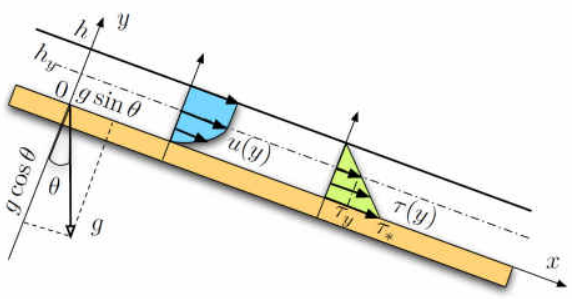


Fig. 4: Free surface flow on an inclined plane with a velocity profile $u(y)$ and a shear stress $\tau(y)$.

and a shear stress following the Herschel-Bulkley law as

$$\tau = \tau_0 + k \left( \frac{\partial u}{\partial y} \right)^n \tag{18}$$

We solve the equation (16) using an implicit scheme to find a solution $u(y)$ as described by Guillet [14]. For a turbulent flow, the velocity profile is more flat and we approximate $\beta$ to be 1.

### D. $\beta$ and $f$ computation

Using the previous model, we can compute $\beta$ using the equation (15), $f$ using the equation (12) and $K$ using the equation 19.

$$K = \frac{-2b \frac{\partial p}{\partial x} Re_g}{\rho u^2} \tag{19}$$

To compute $f$ and $\beta$ consider scenarios of three different fluids over a flat plate of width $b = 0.12$, height $h = 0.2m$ and flow rate $Q = 200L/min$.

- **Fluid 1** : Newtonian fluid with $\tau_0 = 0Pa$, $k = 0.2Pa.s^n$ and $n = 1$
- **Fluid 2** : Bingham fluid with $\tau_0 = 1Pa$, $k = 0.2Pa.s^n$ and $n = 1$
- **Fluid 3** : Herschel Bulkley fluid with $\tau_0 = 1Pa$, $k = 0.2Pa.s^n$ and $n = 0.5$

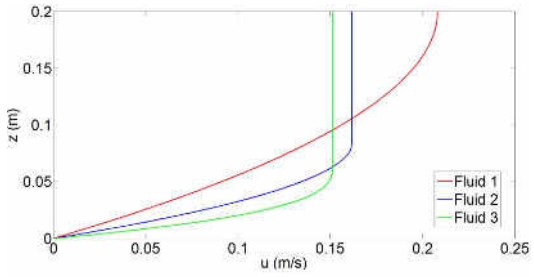


Fig. 5: Velocity profile computed for the 3 different fluids.

Based on this theory, we find for a Newtonian fluid and a laminar flow $K = 24$ and $\beta = 1.2$ (which is approximately known for laminar flows). But for an other fluid, the value of $K$ and $\beta$ vary and depend on the rheology, on the height and fluid velocity.

| | K | $Re_g$ | f | $\beta$ |
|---|---|---|---|---|
| **Fluid 1** | 24 | 555 | 0.04 | 1.2 |
| **Fluid 2** | 22 | 120 | 0.18 | 1.09 |
| **Fluid 3** | 20 | 124 | 0.16 | 1.05 |

TABLE I: Value of friction coefficients computed for the 3 different fluids

As mentioned earlier, we use this sub-model of friction to estimate $f$ and $\beta$ and then taking into account the rheology and change of geometry in the SVE model.

## IV. Experiments for validation

At Geoservices, we have a flow loop that allows us to circulate fluids through the Venturi flume, shown in figure 6. The flow loop works by pumping the fluid with pumps (1), measuring the flow rate with Coriolis flow meter (2) for reference and measuring heights of the fluid with eight height sensors (3) at different locations along the Venturi flume. This flow loop was designed with scale down version of the geometry in the field (with the geometrical ratio of 1:3) and to match the required flowrates (with the flow rate ratio of 1:12). The scaling is based on the conservation of the non dimensional numbers which are governing the flow.


Fig. 6: Flow loop at Geoservices equiped with a Coriolis flow meter and eight ultra-sonic height sensors.

The experimental campaign carried out to circulate different fluids into the loop, measure the flow rate at different steady state, measure the density, measure the 8 height along the Venturi flume and measure the rheology of the fluid few times a day.

| Sensor | Measurement | Accuracy |
|---|---|---|
| CMF 200 | Flow rate | +/- 0.1 % |
| CMF 200 | Density | +/- 0.2 $kg/m^3$ |
| UNAM12 | Height | +/- 1 $mm$ |

TABLE II: Performance specifications of sensors used

We conducted experiments with the trapezoidal Venturi flume for differents fluids: water, viscous Newtonian fluids (mixture of glycerin & water) and non-Newtonian mud-like fluids (mixture of carbopol & water). We conclude on a dataset of 17 different fluids and for each series of fluid 20 different flow rates and for each flow rates we measure the all 8 heights along the Venturi flume.

| N° | Mixture | Conc. [%] | App. Viscosity [cP] |
|---|---|---|---|
| 1 | Water | - | 1 |
| 2 to 11 | Glycerin | 60 to 100 | 17 to 900 |
| 12 to 17 | Carbopol | 0.095 to 0.13 | 10 to 300 |

TABLE III: Fluids and range of viscosities studied

The plot show in figure 7 an upstream height measured by the ultra-sonic sensor on the Venturi flume versus the flow rate measured by the Coriolis flow meter for only 6 different fluids.

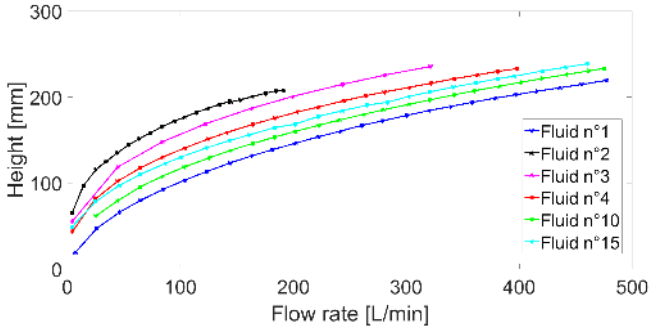


Fig. 7: Upstream height vs. flow rate for different fluids for our trapezoidal Venturi flume

The fluid number 2 (in black on the figure 7) is the more viscous that we have, opposed to the fluid number 1 (in blue on the figure 7) which is water. Figure 7 show the big impact of the rheology on the relation height versus flow rate.

In addition to the experiments we study the flow using 3D computation. This is done for two purposes one to establish and validate the 3D features not modelled by by 1D model and to establish further database of flume characteristics for different geometries.

## V. 3D CFD model

The 3D open channel flow simulation was done using the Open source CFD software OpenFoam [15]. This software uses a large library of solver for the fluid flow models and that can be found on OpenFoam user guide. For our 3D simulation, we use the solver InterFoam which is used to model incompressible multiphase flow. This solver uses the volume of fluid (VOF) method for tracking and locating the free surface of the flow. This method is based on the idea of fraction function, a scalar defined as the integral of the fluid in the control volume. In our case, when the cell is empty of liquid (so only air), this fraction function is equal to 0 and when the cell is full of liquid, this fraction function is equal to 1. Then the interface is tracked when the fraction function is between 0 and 1, as shown in the figure 8.

The computational domain in 3D consists of a Venturi flume and a flow line upstream as shown in the figure (9). This rectangular channel upstream is important to maintain a length of stabilisation of the flow. The boundary conditions are described such that we have a flow rate at the inlet, means at the entrance of the flow line.

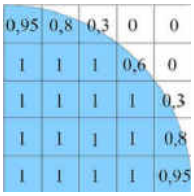


Fig. 8: Fraction function value.

The open surface is described with air at atmospheric pressure and no slip condition is described for the velocity along the walls. At the outlet a zeroGradient on height is described which allows the flow to evacuate whitout affecting the flow upstream.

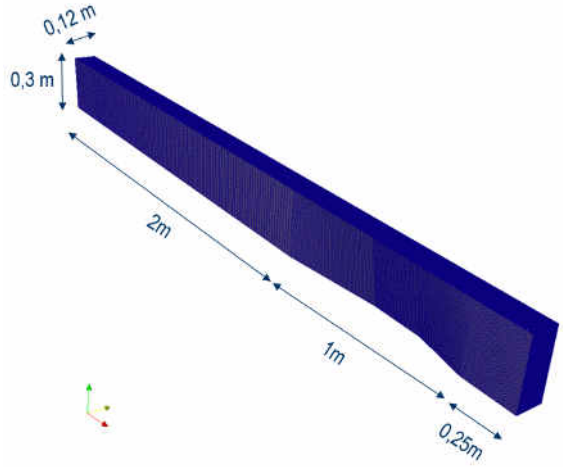


Fig. 9: 3D geometry composed by a rectangular channel and a trapezoidal Venturi flume.

We choose non uniform rectangular meshes along the domain with fine mesh along the Venturi flume and coarser mesh away from the Venturi, to increase computational efficiency. Along the Venturi flume, the size of the mesh along x direction equals 11 mm, along y direction equals 12mm and along z direction equals 6mm, with a total around 100 000 meshes. The computation time step is chosen automatically with using the adjustTimeStep option in OpenFoam, this function adjusts the time step during the simulation according to the Courant number and ensure the time step for wave stability. All numerical residuals are checked to ensure the convergence of the computations to ensure steady solution. We used $k-\omega$ model for turbulent flows.

## VI. Results : 1D-SWE Vs. EXP Vs. CFD

### A. Height profile comparison

*1) Newtonian case:* water

We considered the water serie and selected data for the flow rate equal to $477L/min$ where the flow is turbulent.

The plot of eight height measured by the ultra-sonic sensors from the experiments, the height profile computed by the 1D steady state Saint Venant model and the medium height profile

| Properties | Fluid |
|---|---|
| density, $\rho$ $[kg/m^3]$ | 1000 |
| yield stress, $\tau_0$ $[Pa]$ | 0 |
| fluid behaviour index, $k$ $[Pa.s^n]$ | $10^{-3}$ |
| fluid power index, n [-] | 1 |

TABLE IV: Water properties

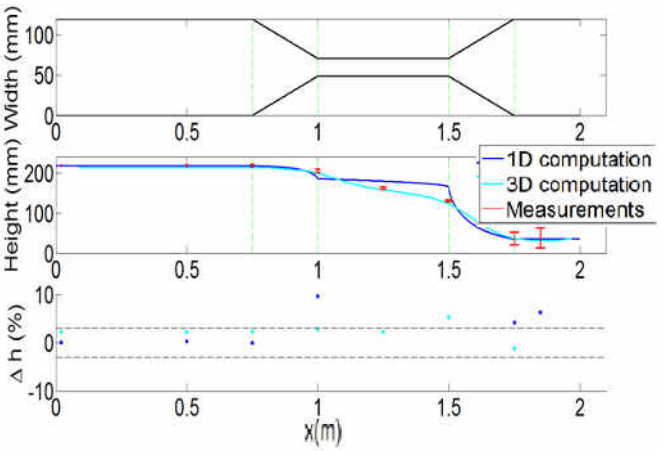


Fig. 10: Plots comparing experiments, 1D computation and 3D computation of a water flow along the trapezoidal Venturi flume.

computed by the 3D CFD model for this Newtonian flow is shown in figure 10.

*2) Non-Newtonian case:* carbopol mixture

Now we consider the mixture of carbopol series, which has a rheology closer of drilling muds, and selected data for the flow rate equal to $440L/min$ where the flow is laminar.

| Properties | Fluid |
|---|---|
| density, $\rho$ $[kg/m^3]$ | 1000 |
| yield stress, $\tau_0$ $[Pa]$ | 1.6 |
| fluid behaviour index, $k$ $[Pa.s^n]$ | 0.79 |
| fluid power index, n [-] | 0.54 |

TABLE V: Carbopol mixture properties

The plot of the eight height measured by the ultra-sonic sensors during the experiments, the height profile computed by the 1D steady state Saint Venant model and the medium height profile computed by the 3D CFD model for this non-Newtonian flow is shown in figure 11.

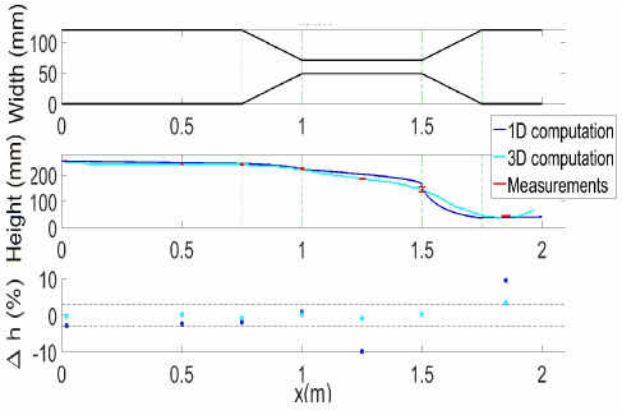


Fig. 11: Plots comparing experiments, a 1D computation and a 3D computation of a non-Newtonian flow along the trapezoidal Venturi flume.

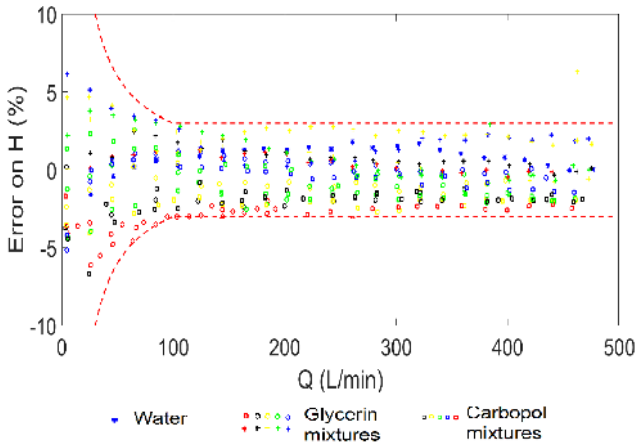


Fig. 12: Error on height between experiments and 1D computations for all fluids.

*3) Discussion:* The 1D model is able to capture accurately the real height profile of the flow, for Newtonian and non-Newtonian fluid, but has less accuracy around the critical point. As described earlier this could be based on the lack of diffusion term, higher order term orturbulent dissipation present in the 1D model and also the condition for the critical point which is derived for the inviscid assumption. In terms of our application of flow metering, the important height is the upstream height and the accuracy is described in the following section.

For the 3D model, we have accurate results along the Venturi flume (2%) and also around the critical point. There is no assumption of the location of the critical point and any empirical relation for the friction terms in the 3D model which are the possible uncertainties in the 1D model.

### B. Upstream height comparison

The figure 12 show the error between upstream height measured and computed by the 1D model for all fluids, at the location $x = 0.5m$.

$$error_h = \frac{h_{comp}(x = 0.5) - h_{exp}(x = 0.5)}{h_{exp}(x = 0.5)} \times 100 \quad (20)$$

For all the data, we establish an envelope of error that we have on upstream height shown by red dotted line in figure 12.

- if $Q < 100L/min$, $max(|error_h|) < 3mm$
- if $Q > 100L/min$, $max(|error_h|) < 3\%$

Then, we can quantify that our 1D model is able to predict upstream height of Venturi flume with an accuracy of 3% on height (for flow rates bigger than $100L/min$).

## VII. Conclusion

A simplified 1D model based on the Saint Venant Equations (SVE) has been developed with a sub-model for the friction. It is found to give good agreement with the experiments and with the 3D CFD model. The study was done for 17 different fluids (for both Newtonian & non-Newtonian fluids) and 20 different flow rates for each fluid (in both laminar & turbulent regimes). The 3D simulation is also a reference to quantify our simplification, indeed we can compare the friction and the momentum coefficient with our friction model and improve it.

In terms of our application the important height is the upstream height and the 1D model is very accurate at this location, because our assumptions seems to be valid far of the critical point and are possibly absorbed by the modelled friction terms. We have a good 1D model able to predict the height with a good accuracy. Based on this 1D steady state model, we develop an inverse model to predict the flow rate based on the upstream height measured and the fluid properties. Then we quantified this solution in term of flow rate measurement with an accuracy of 5% based on 340 different flow rates and 17 different fluids. This study highlights the potential of using a Venturi flume as a new low cost flow meter for drilling operations [11].

## Acknowledgment

The authors would like to thank Florian Leblay (FLAG team), Aurore Lafond (FLAG team) and Maurice Ringer (M& S team), from Geoservices, for their suggestions and support of this study.

## REFERENCES


[1] Hauge S.(2012). *Deepwater horizon: Lessons learned for the norwegian petroleum industry with focus on technical aspects.* Chemical Engineering transactions, 26, 621-626.

[2] ISO (2013). *Flow measurement structures-rectangular, trapezoidal and u-shaped flumes.* Technical Report ISO, 4359 International Organization for Standardization, Switzerland.

[3] Aldrighetti E. (2007). *Computational hydraulic techniques for the Saint Venant Equations in arbitrarily shaped geometry.* Ph.D. thesis, Universita degli Studi di Trento, Dipartimento di Matematica.

[4] Thual O. (2010). *Hydrodynamique de l'environnement.* Edition Polytechnique.

[5] Burger J.H. (2014). *Non-Newtonian open channel flow : the effect of shape.* Ph.D. thesis. Cape Peninsula University of Technology.

[6] Colebrook, C. F. and White, C. M. (1937). *Experiments with Fluid Friction in Roughened Pipes.* Proceedings of the Royal Society of London. Mathematical and Physical Sciences.

[7] Churchill, S.W. (1977). *Friction-factor equation spans all fluid-flow regimes.* Chemical Engineering: 91?92.

[8] Chow V.T. (1959). *Open-Channel Hydraulics.* McGrawHill.

[9] Hirt, C. and Nichols, B. (1981). Volume of fluid (vof) method for the dynamics of free boundaries. *Journal of Computational Physics.* 39(1), 201 ? 225.

[10] O. Thual, L. Lacaze, M. Mouzouri and B. Boutkhamouine (2015). *Critical slope for laminar transcritical shallow-water flows.* Journal of fluid mechanics.

[11] M. Mouzouri and P.A. Varadarajan (2015). *Open Channel Flow Measurement Using A Venturi Flume.* Schlumberger Fluid Mechanics Newsletter #1.

[12] M. Mouzouri and P.A. Varadarajan (2016). *CFD with OpenFoam to simulate non Newtonian mud flow in a Venturi flume.* Schlumberger Fluid Mechanics Newsletter #1.

[13] Randall J. Leveque (2004). *Finite Volume Methods for Hyperbolic Problems.* University of Washington.

[14] O. Guillet,O. Thual, L. Lacaze, M. Mouzouri (2015). *Frottement parital et glissement d?un coulement viscoplastique ouvert.* 22ème Congrès Français de Mécanique.

[15] OpenFoam (2004). *http://www.openfoam.com/.* OpenCFD Ltd and OpenFOAM Foundation.

[16] I. A. Al-Khatib, M. GOGUS (1999). *Momentum and Kinetic Energy Coefficients in Symmetrical Rectangular Compound Cross Section Flumes.* Tr. J. of Engineering and Environmental Science.

[17] Dormand J. R., Prince P. J. (1980). *A family of embedded Runge-Kutta formulae.* Journal of Computational and Applied Mathematics.

[18] B. de Saint Venant (1871). *Théorie du mouvement non-permanent des eaux avec appplication aux crues des riviéres et introdution des marées dans leur lit.* Acad. Sci. Comptes Rendus Paris.



**M. Mouzouri** will receive his Ph.D. in Fluid Mechanics from IMFT. He joined Schlumbeger in 2013, and is working on free-surface flows of non-newtonian fluids.

**O. Thual** is the Ph.D. advisor of M. Mouzouri. He is from IMFT and supervises M. Mouzouri's work at Geoservices. He is working on free-surface flows of non-newtonian fluids, stratified flows and sediment transports.

**L. Lacaze** is the Ph.D. co-advisor of M. Mouzouri. He is from IMFT and supervises also M. Mouzouri's work at Geoservices. He is working on granular media, numerical modelling of solid particles, free-surface flows of non-newtonian fluids, geophysical fluid mechanics and coastal flows.

**P. A. Varadarajan** received his Ph.D. in Aerospace Engineering in 2011 from University of Michigan. He joined Schlumbeger in 2011, and is working on free-surface flows of non-newtonian fluids and 1D transcient models for mud circulation.

# APPENDIX D

# Various flume shapes

| **Section** | **Area**<br><br>**a** | **Wetted perimeter**<br>$\mathbf{P_w}$ | **Hydraulic radius**<br>$\mathbf{R_h}$ | **Surface width**<br>$\sigma_\eta$ |
|---|---|---|---|---|
| 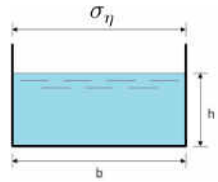 | $bh$ | $b + 2h$ | $\frac{bh}{b+2h}$ | $b$ |
| 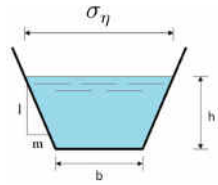 | $bh + mh^2$ | $b + 2h\sqrt{1+m^2}$ | $\frac{bh+mh^2}{b+2h\sqrt{1+m^2}}$ | $b + 2mh$ |
| 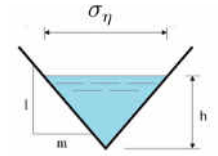 | $mh^2$ | $2h\sqrt{1+m^2}$ | $\frac{mh}{2\sqrt{1+m^2}}$ | $2mh$ |
| 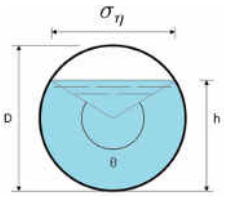 | $\frac{1}{8}(\theta - \sin\theta)D^2$ | $\frac{1}{2}\theta D$ | $\frac{1}{4}\left(1 - \frac{\sin\theta}{\theta}\right)D$ | $2\sqrt{h(D-h)}$ |

Table D.1: Various flumes shapes with their area, wetted perimeter, hydraulic radius and surface width

# BIBLIOGRAPHY

# BIBLIOGRAPHY


[1] International Standar ISO 4359. Liquid flow measurement in open channels - rectangular, trapezoidal and u-shapped flumes. Technical report, 1983.

[2] P. D. Lax A. Harten and B. van Leer. On upstream differencing and godunov-type schemes for hyperbolic conservation laws. *SIAM Review*, 1983.

[3] E. Aldrighetti. *Computational hydraulic techniques for the Saint Venant Equations in arbitrarily shaped geometry.* PhD thesis, Universita degli Studi di Trento, 2007.

[4] A. Aposporidis. *Numerical analysis of mixed formulations for Bingham fluids.* PhD thesis, Emory University, 2012.

[5] M. Bercovier and M. Engelman. A finite element for the numerical solution of viscous incompressible flows. *Journal of Computational Physics*, 1979.

[6] P. R. H. Blasius. Das aehnlichkeitsgesetz bei reibungsvorgangen in flüssigkeiten. *Forschungsheft 131, 1-41*, 1913.

[7] J. Boussinesq. Essaie sur la theory des eaux courantes. *Mémoires présentés par divers savants à l'Academie des Sciences, Paris*, 1877.

[8] J. H. Burger. *Non Newtonian open channel flow : the effect of shape.* PhD thesis, Faculty of Eng, Cape Peninsula University of Technology, 2014.

[9] B. D. Nichols C. W. Hirt. Volume of fluid (vof) method for the dynamics of free boundaries. *Journal of Computational Physics*, 1981.

[10] H. Chanson. The hydraulics of open channel flow. *John Wiley & Sons Ltd*, 1999.

[11] M. H. Chaudhry. Open channel flow. *Springer*, 2008.

[12] R. P. Richardson Chhabra. Non-newtonian flow and applied rheology. *2nd edition. Oxford: Butterworth-Heinemann*, 2008.

[13] V. T. Chow. *Open-channel hydraulics.* PhD thesis, University of Illinois, 1959.

[14] C.F. Colebrook and White. Experiments with fluid friction roughened pipes. *Proc. R.Soc.(A), 161*, 1937.

[15] P. Coussot. Steady, laminar, flow of concentrated mud suspensions in open channel. *Journal of Hydraulic Research*, 1994.

[16] B. de Saint Venant. Théorie du mouvement non-permanent des eaux avec appplication aux crues des riviéres et introdution des marées dans leur lit. *Acad. Sci. Comptes Rendus Paris*, 1871.

[17] O. Delestre. *Simulation du ruissellement d'eau de pluie sur des surfaces agricoles / rain water overland flow on agricultural fields simulation*. PhD thesis, Université d'Orléans, 2010.

[18] R. Chilton et D. Gregory-Smith. Steady, laminar, flow of concentrated mud suspensions in open channel. *Journal of Hydraulic Research*, 1995.

[19] J. Fenton. Open channel hydraulics. *Engineering Hydraulics and Hydrology*, 2005.

[20] T. G. Fitton. *Tailings beach slope prediction*. PhD thesis, Royal Melbourne Institute of Technology, University, Melbourne, Australia, 2007.

[21] T. G. Fitton. A simple method of estimation of laminar/turbulent transition and flow resistance. *Paste*, 2008.

[22] I. Frigaard and C. Nouar. On the usage of viscosity regularisation methods for viscoplastic fluid flow computation. *J. Non-Newtonian Fluid Mech.*, 2005.

[23] A. Ghemmour G. Chambon and M. Naaim. Experimental investigation of viscoplastic free-surface flows in a steady uniform regime. *Journal of Fluid Mechanics*, 2014.

[24] Céline Gabard. *Déplacements de fluides miscibles non-newtoniens en conduite cylindrique verticale*. PhD thesis, Université Paris VI, 2001.

[25] S. K. Godunov. A difference scheme for numerical solution of discontinuous solution of hydrodynamic equations. *Math. Sbornik*, 1969.

[26] W. Malalasekera H. K. Versteeg. An introduction to computational fluid dynamics: the finite volume method. *Longman Scientific & Technical*, 1995.

[27] SE Haaland. Simple and explicit formulas for the friction factor in turbulent flow. *Journal of Fluids Engineering (ASME) 105 (1): 89/90*, 1983.

[28] R. Haldenwang. *Flow of non Newtonian fluids in open channel*. PhD thesis, Civ Eng, Cape Technikon, 2003.

[29] American Petroleum Institute. Recommended practice on the rheology and hydraulics of oil-well drilling fluids. Technical report, 2003.

[30] R. Haldenwang J. Burger and N. Alderman. Experimental database for non-newtonian flow in four channel shapes. *J. Hydraul. Res.*, 2010.

[31] M. Sokolov J. Kestin and W. Wakeham. Viscosity of liquid water in the range -8 °c to 150 °c. *Brown University, Providence, Rhode Island 02912*, 1978.

[32] C. Fagot J. Vazquez. Using 3d modelling to design a venturi channel. *NOVATECH*, 2010.

[33] E. Silberman L. G. Straub, M. ASCE and H. C. Nelson. Open channel flow at small reynolds number. *American Society of Civil Engineers*, 1852.

[34] R. J. Leveque. Numerical methods for conservation laws. *Birkhauser Verlag*, 1992.

[35] R. J. Leveque. Finite volume methods for hyperbolic problems. *Cambridge University Press*, 2002.

[36] J. A. Ligget. Fluid mechanics. *McGraw-Hill, New York*, 1994.

[37] F. Marche and C. Berthon. A positive preserving high order vfroe scheme for shallow water equations: A class of relaxation schemes. *SIAM Journal on Scientific Computing*, 2008.

[38] P. Massé. Ressaut et lignes d'eau dans les cours d'eau à pente variable. *Revues générale de l'hydraulique, Paris*, 1938.

[39] A. Samsuri M.Zoveidavianpoor and S. R. Shadizadeh. Overview of environmental management by drill cutting re-injection through hydraulic fracturing in upstream oil and gas industry. *INTECH Open Access Publisher*, 2012.

[40] B. Naik. *Mechanics of mudflow treated as the flow of a Bingham fluid*. PhD thesis, Washington State University, 1983.

[41] M. Mouzouri O. Thual, L. Lacaze and B. Boutkhamouine. Critical slope for laminar transcritical shallow-water flows. *Journal of Fluid Mechanics, vol. 783*, 2015.

[42] F. Bertrand P. Coussot and B. Herzhaft. Rheological behavior of drilling muds, characterization using mri visualization. *Oil & Gas Science and Technology – Rev. IFP*, 2004.

[43] M.E. Vazquez-Cendon P. Garcia-Navarro. On numerical treatment of the source terms in the shallow water equations. *Computers & Fluids*, 2000.

[44] T. C. Papanastasiou. Flows of materials with yield. *Journal of Rheology*, 1987.

[45] Ralph L. Parshall. The improved venturi flume. Technical report, 1928.

[46] H. Poincaré. Mémoire sur les courbes définies par une équation différentielle. *Journal de mathématiques pures et appliquées, Paris*, 1881.

[47] V. N. Diwanji R. G. Patil and R. M. Khatsuria. Integrating equation of gradually varied flow. *JOURNAL OF HYDRAULIC ENGINEERING*, 2001.

[48] P. T. Slatter R. Haldenwang. Experimental procedure and database for non-newtonian open channel flow. *Journal of Hydraulic Research*, 2006.

[49] Jr. K.R. R. Smith, D. Chery and W. Gwinn. Supercritical flow flumes for measuring sediment-laden flow. Technical report, 1981.

[50] T. H. Rehbock. The determination of the position of the energy line in flowing water with the o.id of velocity-head adjustment. *Der Bauingenieu T, Berlin, vol. 3*, 1929.

[51] V. V. Rusanov. Calculation of interaction of non-steady shock waves with obstacles. *J. Comput. Math. Phys.*, 1961.

[52] C. Martin et A. Magnin S. Alireza. Effects of surface properties on the impact process of a yield stress fluid drop. *Experiments in Fluids*, 2011.

[53] H. Schlichting. Boundary layer theory. *7th ed., McGraw Hill, New York, U.S.A*, 1979.

[54] R.E. Hayes S.J. Curran and A. Afacan. Properties of carbopol solutions as models for yield-stress fluids. *Journal of Food Science*, 2002.

[55] M.E. Vazquez-Cendon. Improved treatment of source terms in upwind schemes for the shallow water equations in channels with irregular geometry. *Journal of Computational Physics*, 1999.

[56] C. Tiu W. Kozicki. Non newtonian flow through open channels. *The Canadian journal of chemecal engineering*, 1967.

[57] U. G. Wali. Kinetic energy and momentum correction coefficients for a small irrigation channel. *International Journal of Emerging Technology and Advanced Engineering*, 2013.